

Visualisation and Evaluation of Electrical Contact Spots and Asperities of a  
Given Contact System Using X-ray Computed Tomography

Constantinos C. Roussos

Submitted for the degree of Doctor of Philosophy

Heriot-Watt University

School of Engineering and Physical Sciences / Institute of Mechanical,  
Process and Energy Engineering

September 2016

The copyright in this thesis is owned by the author. Any quotation from the thesis or use of any of the information contained in it must acknowledge this thesis as the source of the quotation or information.

## **Abstract**

The electrical contact is identified as the most common factor as to why electrical and electronic devices fail. The electrical contacts fail due to a variation of factors such as the normal-force (force perpendicular to the surface) and the general contact design, the wear and the environmental and electrical parameters. This research attempts to address these factors by introducing an innovative inspection method to investigate a contact system connection without the need to prior dismantle it. The X-ray Computed Tomography (CT) is used and several Contact Analysis Techniques (CAT\*) are developed and implemented with a suite of tools in MATLAB in order to accurately analyse the acquired images from the X-ray CT. The CAT\* produce visualisation of the contact interface (contact spots) between the conductors of the contact system as well as the visualisation of their contact asperities (structures above and below the contact spots). Furthermore, the CAT\* produce visualisation of any cross-section slice of the contact system and show from which voxels the electric current flows through. These visualisations can be analysed to evaluate the degradation process of contact spots and contact asperities under different current loading tests. An in depth appraisal of X-ray CT as a non-destructive visualisation technique for investigating electrical contacts is performed and procedures enhancing the deliverables of the technique are introduced. The outcomes of this research confirm that the use of X-ray CT visualisation technique in the field of electrical contacts can improve our understanding in the field. Moreover, the CAT\* could help the manufacture companies of contact systems to develop more reliable contact systems examining their features for different contact materials under different applied forces and different environmental and electrical parameters.

*To my parents*

## **Acknowledgements**

The procedure and completion of a PhD thesis is both a hard and rewarding experience. Having completed this thesis I realise that this was a fruitful personal effort, but at the same time it was the contribution and support of many people, whom I want to thank and express my sincere thankfulness.

Firstly, I would like to thank my supervisor, Dr Jonathan Swingler for giving me the opportunity to work in this research. His knowledge on the related field and his logical way of thinking were of great value to me as his useful advice inspired and changed my critical thinking.

My parents, my whole family and my friends deserve my respect and love as they were always supporting me in this difficult but worthwhile and unique experience in my life. I honestly thank them.

ACADEMIC REGISTRY  
**Research Thesis Submission**



Name:	Constantinos C. Roussos		
School:	EPS / IMPEE		
Version: <i>(i.e. First, Resubmission, Final)</i>	Final	Degree Sought:	PhD in Electrical Engineering

**Declaration**

In accordance with the appropriate regulations I hereby submit my thesis and I declare that:

- 1) the thesis embodies the results of my own work and has been composed by myself
- 2) where appropriate, I have made acknowledgement of the work of others and have made reference to work carried out in collaboration with other persons
- 3) the thesis is the correct version of the thesis for submission and is the same version as any electronic versions submitted\*.
- 4) my thesis for the award referred to, deposited in the Heriot-Watt University Library, should be made available for loan or photocopying and be available via the Institutional Repository, subject to such conditions as the Librarian may require
- 5) I understand that as a student of the University I am required to abide by the Regulations of the University and to conform to its discipline.
- 6) I confirm that the thesis has been verified against plagiarism via an approved plagiarism detection application e.g. Turnitin.

\* Please note that it is the responsibility of the candidate to ensure that the correct version of the thesis is submitted.

Signature of Candidate:		Date:	22/09/2016
-------------------------	---	-------	------------

**Submission**

Submitted By <i>(name in capitals)</i> :	
Signature of Individual Submitting:	
Date Submitted:	

**For Completion in the Student Service Centre (SSC)**

Received in the SSC by <i>(name in capitals)</i> :	
Method of Submission <i>(Handed in to SSC; posted through internal/external mail)</i> :	
E-thesis Submitted <b>(mandatory for final theses)</b>	
Signature:	Date:

# Table of Contents

<b>Abstract</b> .....	<b>i</b>
<b>Dedication</b> .....	<b>ii</b>
<b>Acknowledgements</b> .....	<b>iii</b>
<b>Declaration Statement</b> .....	<b>iv</b>
<b>Table of Contents</b> .....	<b>v</b>
<b>List of Figures</b> .....	<b>x</b>
<b>List of Tables</b> .....	<b>xvi</b>
<b>Nomenclature</b> .....	<b>xix</b>
<b>List of Publications by the Candidate</b> .....	<b>xxiv</b>
<b>Chapter 1 – Introduction</b> .....	<b>1</b>
1.1 The Electrical Contact in Engineering and its Importance.....	1
1.2 Research Initiative .....	2
1.3 The Experimental Equipment – X-ray CT .....	2
1.3.1 Brief description of X-ray CT .....	2
1.3.2 How X-ray CT has been used in the past.....	3
1.4 Why use X-ray CT to Visualise and Characterise Electrical Contact Systems..	4
1.5 Electrical Contact System Characteristics and X-ray CT Technique.....	5
1.6 The Scope of Research .....	6
1.7 The Objectives of Research.....	7
1.8 Research Summary .....	9
<b>Chapter 2 – Electrical Contact</b> .....	<b>11</b>
2.1 Introduction .....	11
2.2 Surface Characterisation.....	12
2.2.1 Surface categories .....	12
2.2.2 Surface parameters measurement.....	13
2.2.3 Modern methods of surface parameters measurement.....	15
2.3 Contact Interface Characterisation .....	16
2.3.1 Elastic deformation of contact system .....	17
2.3.2 Plastic deformation of contact system.....	19
2.3.3 Elastic-plastic deformation of contact system.....	20
2.3.4 Contact interface models.....	20
2.3.5 Fractals in contact interface .....	21
2.3.6 Area of contact interface .....	22
2.3.7 Electrical contact interface.....	24
2.3.8 Reliability of electrical contact interface .....	27
2.4 Classification of Electrical Contacts .....	29

2.4.1	Stationary contacts .....	29
2.4.2	Moving contacts .....	30
2.5	Conclusion.....	31
<b>Chapter 3 – Visualisation Methods .....</b>		<b>33</b>
3.1	Introduction .....	33
3.2	Destructive Visualisation Techniques .....	33
3.3	Non-Destructive Visualisation Techniques .....	34
3.4	X-ray CT in Engineering and the Sciences .....	35
3.4.1	The use of the X-ray CT.....	35
3.4.2	Historical use.....	36
3.4.3	X-radiation .....	36
3.4.4	Basic operation of X-ray CT .....	38
3.4.5	Image reconstruction.....	40
3.4.6	Quality of the X-ray CT scan .....	46
3.4.7	Artifacts.....	51
3.5	Conclusion.....	51
<b>Chapter 4 – Methodology .....</b>		<b>52</b>
4.1	Introduction .....	52
4.2	Selection of Contact System.....	52
4.3	The Selected Contact System .....	53
4.4	Experimental Equipment – X-ray CT.....	54
4.4.1	Equipment characteristics .....	54
4.4.2	Test environment.....	56
4.4.3	X-ray CT system configuration to ensure a good quality of scan.....	56
4.4.4	From 2D X-ray images acquisition to 3D reconstructed volume .....	58
4.4.5	From 3D reconstructed volume to 2D cross-section slice images .....	62
4.5	Post-Processing and Analysis of Experimental Data .....	65
4.5.1	Threshold calculation .....	67
4.5.2	Same sample X-ray CT scans .....	69
4.5.3	3D reconstructed volume orientation .....	73
4.5.4	Validation method of pixel length.....	75
4.6	Conclusion.....	76
<b>Chapter 5 – The 3D Nature of a Real Un-Dismantled Electrical Contact Interface .....</b>		<b>77</b>
5.1	Introduction .....	77
5.2	A Suite of Contact Analysis Techniques Tools.....	77

5.3	Contact Analysis and Modelling Techniques.....	79
5.4	Results of 2D and 3D Mapping Techniques.....	82
5.4.1	Contact maps.....	82
5.4.2	Total Mechanical area of contact.....	85
5.4.3	Contact resistance calculation.....	85
5.5	Additional Investigations Using the Contact Spots of 3D Contact Maps.....	87
5.5.1	Contact spot area distribution.....	87
5.5.2	Contact spot angle distribution.....	87
5.6	3D Voids Visualisation and Their Volume Distribution.....	92
5.6.1	Voids visualisation.....	92
5.6.2	Void volume distribution.....	93
5.7	Conductors Visualisation and Their Fractal Characteristics.....	95
5.7.1	Conductors visualisation.....	95
5.7.2	Conductors fractal characteristics.....	96
5.8	Discussion.....	104
5.8.1	The X-ray CT technique.....	104
5.8.2	The 2D and 3D mapping techniques.....	104
5.8.3	Loss of information with 2D contact maps.....	106
5.8.4	Total mechanical area of contact findings.....	109
5.8.5	Contact resistance findings.....	109
5.8.6	Contact spot area distribution findings.....	110
5.8.7	Contact spot angle distribution findings.....	111
5.8.8	Void volume distribution findings.....	112
5.8.9	Conductors fractal characteristics findings.....	113
5.9	Conclusion.....	120

**Chapter 6 – Towards a 3D Technique to Determine the Geometric Path of Electric Current Flow through a Contact System..... 122**

6.1	Introduction.....	122
6.2	Contact Analysis and Modelling Techniques.....	123
6.2.1	The concept and characteristics of a resistor network model system.....	123
6.2.2	Development of Open/Closed and Closed resistor network models.....	123
6.3	Results and Analysis.....	132
6.3.1	Contact system.....	132
6.3.2	2D and 3D contact maps.....	132
6.3.3	Resistor network model of the contact system.....	133
6.3.4	Electric current path maps.....	134



6.3.5	Total cross-sectional area of slice asperities .....	134
6.4	Discussion.....	139
6.4.1	X-ray CT technique.....	139
6.4.2	Contact analysis techniques .....	139
6.4.3	Resistor network model of the contact system findings.....	142
6.4.4	Total resistance and total conductance of the contact system.....	148
6.4.5	Electric current maps findings .....	151
6.4.6	Total cross-sectional area of slice asperities findings .....	152
6.4.7	Electric current constriction .....	155
6.5	Conclusion.....	156

## **Chapter 7 – The 3D Contact Analysis Approach for the Visualisation and**

### **Characterisation of the Electrical Contact Asperities ..... 158**

7.1	Introduction .....	158
7.2	Contact Analysis and Modelling Techniques.....	159
7.3	Results and Analysis.....	167
7.3.1	Contact system .....	167
7.3.2	2D and 3D contact maps .....	168
7.3.3	3D contact asperities visualisation .....	169
7.3.4	3D contact asperities volume distribution.....	171
7.3.5	3D contact asperities surface area distribution.....	174
7.3.6	Bottom surface area distribution of 3D contact asperities .....	174
7.3.7	Top surface area distribution of 3D contact asperities.....	174
7.3.8	Ratio of top/ bottom surface areas of 3D contact asperities distribution	175
7.3.9	3D contact asperities height distribution.....	175
7.3.10	Ratio of top/bottom surface areas with height .....	175
7.3.11	Hemispherical 3D contact asperities.....	183
7.4	Discussion.....	183
7.4.1	X-ray CT technique.....	183
7.4.2	Contact analysis approach.....	184
7.4.3	3D contact asperities findings .....	185
7.4.4	3D contact asperity volume distribution findings .....	188
7.4.5	3D contact asperity surface area distribution findings.....	189
7.4.6	3D contact asperity bottom surface area distribution findings.....	190
7.4.7	3D contact asperity top surface area distribution findings.....	191
7.4.8	Ratio of top and bottom surface areas findings.....	192
7.4.9	3D contact asperity height distribution findings .....	193

7.4.10	Ratio of top/bottom surface areas with height findings .....	194
7.4.11	Hemispherical 3D contact asperities findings .....	196
7.5	Conclusion .....	198
<b>Chapter 8 – Conclusion .....</b>		<b>199</b>
8.1	Scope of this Research.....	199
8.2	Novelties of this Research .....	199
8.3	Main Findings.....	200
8.3.1	Chapter 4 .....	200
8.3.2	Chapter 5 .....	200
8.3.3	Chapter 6 .....	200
8.3.4	Chapter 7 .....	201
8.4	The X-ray CT Technique.....	201
8.5	The Contact Analysis Techniques .....	202
8.6	Future Work.....	203
<b>References .....</b>		<b>204</b>

## List of Figures

Figure 2.1. Archard’s surface roughness model [97].....	12
Figure 2.2. Categories of surface profile [23].....	13
Figure 2.3. 2D profile of a surface [23] .....	14
Figure 2.4. Ranges of vertical-lateral resolution for different methods of roughness measurement [23].....	16
Figure 2.5. (a) Cross-section of schematic contact system of bodies A and B which are in mechanical contact, (b) Zoom-in at a part of the contact interface.....	17
Figure 2.6. Top view of schematic contact interface .....	17
Figure 2.7. Hertz contact system of elastic bodies [104] .....	18
Figure 2.8. Electric current flowing through contact systems [132].....	25
Figure 2.9. Schematic diagram of electric current flowing through contact interface....	26
Figure 2.10. Classification of electrical contacts [23].....	29
Figure 3.1. The effect of different absorption layers on the intensity of an X-ray beam	37
Figure 3.2. (a) Basic principle of X-ray CT, (b) Detector.....	38
Figure 3.3. X-ray beam transmitting through a cross-section of the sample .....	39
Figure 3.4. X-ray CT process.....	41
Figure 3.5. Projections are taken by measuring the rays of the sample for three different angles [163].....	42
Figure 3.6. The function $g, k, l$ describes the projection of the function $f(x, y)$ at angle $\theta$ .....	43
Figure 3.7. Back-projection. Sample cross-section slice image using (a) 3 projections and (b) many projections [163].....	45
Figure 3.8. Filtered back-projection. Sample cross-section slice image using (a) 3 projections and (b) many projections [163] .....	45
Figure 3.9. Fourier slice theorem in (a) spatial domain and (b) frequency domain [163] .....	46
Figure 3.10. X-ray source, turntable and detector arrangement.....	47
Figure 3.11. Image resolution in pixels. (a) $20 \times 20$ , (b) $50 \times 50$ and (c) $100 \times 100$ ....	48
Figure 3.12. X-ray source power loadings. (a) Multi-focus [169], (b) Micro-focus [170] .....	49
Figure 3.13. Cross-section slice image for different number of projections using back-projection method.....	50
Figure 4.1. Schematic diagram of the single pole rocker switch [175].....	53

Figure 4.2. Dimensions of the single pole rocker. (a) Side-view [175], (b) Top-view...	53
Figure 4.3. HMX 225 X-ray CT system scanner (Abertay University, Dundee, UK) [177]	
.....	55
Figure 4.4. Installed softwares along with the equipment [75].....	56
Figure 4.5. 2D X-ray image of the 16 A rated AC single pole rocker switch.....	59
Figure 4.6. Projection of the 16 A rated AC single pole rocker switch.....	60
Figure 4.7. Positions of the X-ray image and the projection in the 3D volume of X-ray images .....	61
Figure 4.8. 3D reconstructed volume of the 16 A rated AC single pole rocker switch...	61
Figure 4.9. Colour histogram of the 3D reconstructed volume .....	62
Figure 4.10. Colour histogram of the 2D cross-section slice images .....	64
Figure 4.11. 2D cross-section slice image of the 16 A rated AC single pole rocker switch .....	64
Figure 4.12. Position of the 2D cross-section slice image in the 3D reconstructed volume .....	65
Figure 4.13. (a) 16-bit grayscale 2D cross-section slice image, (b) Colour values of the section .....	66
Figure 4.14. 1-bit 2D cross-section slice image of the 16 A rated AC single pole rocker switch .....	67
Figure 4.15. 3D volume of interest of the 16 A rated AC single pole rocker switch.....	68
Figure 4.16. (a) Schematic cross-section slice of rectangular parallelepiped on the detector at $\theta_1 = 0^\circ$ , (b) Schematic 2D grayscale X-ray images of rectangular parallelepiped at $\theta_1 = 0^\circ$ with grid.....	71
Figure 4.17. (a) Schematic cross-section slice of rectangular parallelepiped on the detector at $\theta_2 = -90^\circ$ , (b) Schematic 2D grayscale X-ray images of rectangular parallelepiped at $\theta_2 = -90^\circ$ with grid .....	71
Figure 4.18. (a) Schematic cross-section slice of rectangular parallelepiped on the detector at $\theta_2 = 30^\circ$ , (b) Schematic 2D grayscale X-ray images of rectangular parallelepiped at $\theta_2 = 30^\circ$ with grid.....	72
Figure 4.19. Orientation of the 3D reconstructed volume of the 16 A rated AC single pole rocker switch.....	74
Figure 4.20. Orientation of the 3D volume of interest of the 16 A rated AC single pole rocker switch.....	74
Figure 4.21. Length measurement between particular characteristics of the Conductor B using a standard micro-meter .....	75

Figure 4.22. Top-view of the Conductor B .....	76
Figure 5.1. Flowchart of software tool.....	78
Figure 5.2. Schematic cross-section of (a) Bodies A and B, (b) 2D contact mapping technique and (c) 3D contact mapping technique [75] .....	80
Figure 5.3. Schematic cross-section slice of a contact spot [75] .....	81
Figure 5.4. Schematic contact spots [75] .....	82
Figure 5.5. 2D contact maps of 16 A rated AC single pole rocker switch after four different current loading tests using CATVis .....	83
Figure 5.6. 3D contact maps of 16 A rated AC single pole rocker switch after the four different current loading tests using CATVis .....	84
Figure 5.7. Contact spot area distribution after the four different current loading tests ..	89
Figure 5.8. Contact spot angle distribution after the four different current loading tests .....	90
Figure 5.9. (a) 2D angle map of 16 A rated AC single pole rocker switch at 64 A, (b) Close-up view of the red box of 2D angle map .....	91
Figure 5.10. Schematic top view of contact spot <i>i</i> . Explanation of angle calculation ....	92
Figure 5.11. 3D voids of 16 A rated AC single pole rocker switch after the 64 A current loading test with bounding box dimensions of $1.69 \times 0.42 \times 2.61$ mm.....	92
Figure 5.12. Close-up view of the largest void of the 16 A rated AC single pole rocker switch after the 64 A current loading test with bounding box dimensions of $0.42 \times 0.20 \times 0.36$ mm .....	93
Figure 5.13. Void volume distribution after the four different current loading tests.....	94
Figure 5.14. Conductor A of the 16 A rated AC single pole rocker switch after the first current loading test at 0 A with bounding box dimensions of $3.95 \times 1.52 \times 3.62$ mm ..	95
Figure 5.15. Conductor B of the 16 A rated AC single pole rocker switch after the first current loading test at 0 A with bounding box dimensions of $3.95 \times 1.52 \times 3.62$ mm ..	96
Figure 5.16. Total mechanical area of contact in each x-z cross-section slice image of the oriented 3D volume of interest after the 0 A current loading test .....	97
Figure 5.17. Cross-section slice images of Conductor A for the three different height levels selection after the 0 A current loading test.....	98
Figure 5.18. Cross-section slice images of Conductor B for the three different height levels selection after the 0 A current loading test.....	99
Figure 5.19. Contact spot area cumulative distributions according to different scales of Conductor A after the four different current loading tests. Where <i>K</i> , is the slope of the fitting line.....	100

Figure 5.20. Contact spot area cumulative distributions according to different scales of Conductor B after the four different current loading tests. Where $K$ , is the slope of the fitting line.....	101
Figure 5.21. Contact spot spatial cumulative distributions according to different scales of Conductor A after the four different current loading tests. Where $Kd$ , is the slope of the fitting line.....	102
Figure 5.22. Contact spot spatial cumulative distributions according to different scales of Conductor B after the four different current loading tests. Where $Kd$ , is the slope of the fitting line.....	103
Figure 5.23. Peak and side contact spots. Schematic cross-section slice of (a) Bodies A and B, (b) 2D contact mapping technique and (c) 3D contact mapping technique [75] .....	107
Figure 5.24. Schematic contact spots in (a) 2D contact map and (b) 3D contact map [75] .....	108
Figure 5.25. Contact spots with angle values equal with (a) $-45^\circ$ and (b) $45^\circ$ .....	112
Figure 6.1. Schematic contact system with its characteristics .....	124
Figure 6.2. Schematic oriented 3D volume of interest of contact system with its resistor network.....	125
Figure 6.3. Schematic 3D contact source model of the schematic oriented 3D volume of interest of contact system with its resistor network .....	126
Figure 6.4. (a) 3D constriction asperities map. (b) x-z contact slice [132].....	127
Figure 6.5. 3D source model of the 16 A rated AC single pole rocker switch after the first current loading test at 0 A with bounding box dimensions of $3.22 \times 0.71 \times 3.31$ mm	132
Figure 6.6. 2D cross-sections of x-z contact slices of the 3D source model after each current loading test using CATVis.....	133
Figure 6.7. Number of resistors in each x-z cross-section slice image of the 3D source model for Open/Closed and Closed Circuits after the four different current loading tests .....	135
Figure 6.8. Cross-section area of the 33 <sup>rd</sup> x-z cross-section slice of the 3D source model at 0 A .....	136
Figure 6.9. Cross-section area of the 35 <sup>th</sup> x-z cross-section slice of the 3D source model at 16 A .....	136
Figure 6.10. Cross-section area of the 36 <sup>th</sup> x-z cross-section slice of the 3D source model at 32 A .....	137

Figure 6.11. Cross-section area of the 35<sup>th</sup> x-z cross-section slice of the 3D source model at 64 A ..... 137

Figure 6.12. Total cross-section area in each x-z cross-section slice image of the 3D source model for Open/Closed and Closed Circuits after the four different current loading tests..... 138

Figure 6.13. Total mechanical area of contact in each x-z cross-section slice image of the oriented 3D volume of interest after the first current loading test at 0 A..... 141

Figure 6.14. (a) Schematic diagram of a contact system. (b) Schematic diagram of resistors of a contact system in each x-z cross-section slice..... 155

Figure 7.1. (a) Schematic oriented 3D volume of interest. (b) Schematic oriented 3D contact volume of interest. (c) 2<sup>nd</sup> x-z cross-section slice of the schematic oriented 3D contact volume of interest [186] ..... 161

Figure 7.2. (a) 3D constriction asperities map. (b) x-z contact slice [186]..... 162

Figure 7.3. Three different 3D contact asperities with their full extensions to the two bodies A and B [186] ..... 165

Figure 7.4. (a) Summation of the voxels of 3D contact asperities with their extensions to bodies A and B. (b) 3D contact asperities [186] ..... 166

Figure 7.5. 3D source model of the 16 A rated AC single pole rocker switch after the second current loading test at 16 A with bounding box dimensions of  $3.22 \times 0.69 \times 3.40$  mm ..... 167

Figure 7.6. Part from 3D contact source model of the 16 A rated AC single pole rocker switch after the second current loading test at 16 A with bounding box dimensions of  $2.78 \times 0.58 \times 2.62$  mm..... 168

Figure 7.7. (a) 2D cross-section of x-z contact slice after the 16 A current loading test. (b) Close-up view of the red box of 2D cross-section of x-z contact slice..... 169

Figure 7.8. 3D contact asperities of the 16 A rated AC single pole rocker switch after four different current loading tests with bounding box dimensions of  $2.52 \times 0.31 \times 2.82$  mm ..... 170

Figure 7.9. Four different contact spots of the x-z contact slice with their full extensions to the two conductors after the 16 A current loading test with bounding box dimensions of  $2.61 \times 0.25 \times 2.59$  mm..... 171

Figure 7.10. 3D contact asperities *ii*, *jj*, *kk* and *ll* with bounding boxes dimensions of  $0.12 \times 0.11 \times 0.11$  mm..... 172

Figure 7.11. 3D contact asperities volume distribution after the four different current loading tests [195]..... 173

Figure 7.12. 3D contact asperities surface area distribution after four different current loading tests [195].....	176
Figure 7.13. 3D contact asperities bottom surface area distribution after the four different current loading tests .....	177
Figure 7.14. 3D contact asperities top surface area distribution after four different current loading tests.....	178
Figure 7.15. 3D contact asperities ratio of top and bottom surface area distribution after four different current loading tests .....	179
Figure 7.16. 3D contact asperities height distribution after four different current loading tests.....	180
Figure 7.17. 3D contact asperities ratio of top and bottom surface area with height distribution after four different current loading tests .....	181
Figure 7.18. 3D contact asperities ratio distribution of equal bottom and top surface areas with height squared and multiplied by $4/\pi$ after four different current loading tests....	182
Figure 7.19. Schematic types of 3D contact asperities .....	196



## List of Tables

Table 4.1. Threshold values for four different sections for four different x-y 16-bit grayscale 2D cross-section slice images .....	69
Table 4.2. Threshold value at 16-bit greyscale and volume for each X-ray CT scan .....	70
Table 4.3. Measured values for the validation of pixel length.....	75
Table 5.1. Nomenclature of CAT* .....	79
Table 5.2. Characteristics of 2D contact maps.....	86
Table 5.3. Characteristics of 3D contact maps.....	86
Table 5.4. Characteristics of 3D voids .....	95
Table 5.5. Characteristics of the first regime of the contact spot area distribution after each current loading test at 0 A, 16 A, 32 A and 64 A .....	111
Table 5.6. Characteristics of the first regime of the voids volume distribution after each current loading tests .....	113
Table 5.7. Korcak exponent and constant values for each contact spot area cumulative distribution graph of Conductor A .....	116
Table 5.8. Average Korcak exponent and average contact spots area fractal dimension of Conductor A .....	116
Table 5.9. Korcak exponent and constant values for each contact spot area cumulative distribution graph of Conductor B .....	117
Table 5.10. Average Korcak exponent and average contact spots area fractal dimension of Conductor B after each current loading test .....	117
Table 5.11. Slope of contact spot spatial distribution and constant values for each contact spot spatial cumulative distribution graph of Conductor A .....	118
Table 5.12. Average slope of contact spots spatial distribution of Conductor A.....	119
Table 5.13. Slope of contact spot spatial distribution and constant values for each contact spot spatial cumulative distribution graph of Conductor B .....	119
Table 5.14. Average slope of contact spots spatial distribution of Conductor B.....	119
Table 6.1. Number of x-z cross-section slice images in y-direction of 3D source model after the four different current loading tests.....	141
Table 6.2. The total number of resistors for a x-z cross-section slice image with the maximum number of resistors for the Open/Closed Circuit resistor network model after the four different current loading tests .....	143
Table 6.3. Limits of each main region of the Open/Closed Circuit resistor network model after the four different current loading tests.....	143

Table 6.4. Second region characteristics of the Open/Closed Circuit resistor network model after the four different current loading tests.....	144
Table 6.5. Electric current map characteristics in Open/Closed and Closed Circuit resistor network models after the four different current loading tests .....	145
Table 6.6. Limits of each main region of the Closed Circuit resistor network model after the four different current loading tests .....	146
Table 6.7. Second region characteristics of the Closed Circuit resistor network model after the four different current loading tests .....	147
Table 6.8. Resistance values in each zone and the total resistance across the 1 <sup>st</sup> and 3 <sup>rd</sup> zone of the 3D contact source model after the four different current loading tests .....	149
Table 6.9. Conductance values in each zone and the total conductance across the 1 <sup>st</sup> and 3 <sup>rd</sup> zone of the 3D contact source model after the four different current loading tests.	151
Table 6.10. Number of x-z cross-section slice image with the smallest total cross-section area and its total cross-section area for the Open/Closed Circuit resistor network model after the four different current loading tests.....	152
Table 6.11. Number of x-z cross-section slice image with the smallest total cross-section area and its total cross-section area for the Closed Circuit resistor network model after the four different current loading tests .....	153
Table 6.12. Total volume of resistors at the second region of the Open/Closed Circuit resistor network model after the four different current loading tests.....	153
Table 6.13. Total volume of resistors at the second region of the Closed Circuit resistor network model after the four different current loading tests.....	154
Table 7.1. Characteristics of 3D contact asperities <i>ii</i> , <i>jj</i> , <i>kk</i> and <i>ll</i> .....	187
Table 7.2. Total volume and total surface area exposed to the air of the 3D contact asperities after the four different current loading tests.....	188
Table 7.3. Characteristics of the first regime of the 3D contact asperities volume distribution after the four different current loading tests .....	189
Table 7.4. Characteristics of the first regime of the 3D contact asperities surface area exposed to the air distribution after the four different current loading tests.....	190
Table 7.5. Characteristics of the first regime of the 3D contact asperities bottom surface area distribution after the four different current loading tests.....	191
Table 7.6. Characteristics of the first regime of the 3D contact asperities top surface area distribution after the four different current loading tests .....	192
Table 7.7. Number of 3D contact asperities with equal bottom (Conductor A) and top (Conductor B) surface areas after the four different current loading tests.....	193

Table 7.8. Number of 3D contact asperities with bottom (Conductor A) surface area bigger or smaller than top (Conductor B) surface area after the four different current loading tests.....	193
Table 7.9. Characteristics of the exponential graphs of 3D contact asperities height distribution after the four different current loading tests .....	194
Table 7.10. Number of 3D contact asperities with equal bottom and top surface areas divided by the minimum height (5 $\mu\text{m}$ ) after the four different current loading tests ..	194
Table 7.11. Number of 3D contact asperities with equal bottom and top surface areas with height between them bigger than 5 $\mu\text{m}$ after the four different current loading tests...	195
Table 7.12. Number of 3D contact asperities with volume equal with 1 voxel after the four different current loading tests .....	195
Table 7.13. Number of 3D contact asperities with volume bigger than 1 voxel and height equals with 1 pixel length after the four different current loading tests .....	195
Table 7.14. Number of 3D contact asperities with ratio equal, smaller or larger than 1 after each current loading test .....	197

## Nomenclature

$1D$	1-Dimension
$2D$	2-Dimensions
$3D$	3-Dimensions
$A$	Cross section area of the contact system ( $m^2$ )
$A_{A_i}$	Surface area of the top of 3D contact asperity $i$ ( $m^2$ )
$A_{B_i}$	Surface area of the bottom of 3D contact asperity $i$ ( $m^2$ )
$A_e$	Area of contact (under elastic deformation) ( $m^2$ )
$AFM$	Atomic Force Microscopy
$A_i$	Total cross section area of contact spot or contact slice $i$ ( $m^2$ )
$A'_i$	Surface area which is equal with the top and bottom surface area of 3D contact asperity $i$ ( $m^2$ )
$A''_i$	Total surface area exposed to the air of the largest contact asperity across the fit-line ( $m^2$ )
$A_j$	Cross section area of contact spot or contact slice $j$ ( $m^2$ )
$A_L$	Area of the largest contact spot ( $m^2$ )
$A_l$	Area of the largest contact spot across the fit-line ( $m^2$ )
$A''_L$	Surface area exposed to the air of the largest contact asperity ( $m^2$ )
$A''_l$	Surface area exposed to the air of the largest contact asperity ( $m^2$ )
$A_p$	Area of contact (under plastic deformation) ( $m^2$ )
$A_{ref}$	Reference area ( $m^2$ )
$ASME$	American Society of Mechanical Engineers
$ASTM$	American Society for Testing and Materials
$A_{sur}$	Total surface area of 3D contact asperity $i$ ( $m^2$ )
$A_T$	Total mechanical area of contact ( $m^2$ )
$A''_T$	Total surface area of 3D contact asperities exposed to the air ( $m^2$ )
$b$	Cluster radius (m)
$C$	Constant
$CAA *$	Contact Analysis Approaches
$CAACHR$	Contact Analysis Approach for Cooper Resistance
$CAAGR$	Contact Analysis Approach for Greenwood Resistance
$CAT *$	Contact Analysis Techniques
$CAT2DCM$	Contact Analysis Technique for 2D Contact Map

<i>CAT3DCM</i>	Contact Analysis Technique for 3D Contact Map
<i>CATA</i>	Contact Analysis Technique for Asperities
<i>CATC</i>	Contact Analysis Technique for Comparison
<i>CATCM</i>	Contact Analysis Technique for Contact Map
<i>CATHR</i>	Contact Analysis Technique for Holm Resistance
<i>CATTCHR</i>	Contact Analysis Technique for Total Cooper Holm Resistance
<i>CATV</i>	Contact Analysis Technique for Contact Voxels
<i>CATVis</i>	Contact Analysis Technique for Visualization
<i>ConA<sub>max</sub></i>	Maximum colour value of Conductor A
<i>ConB<sub>max</sub></i>	Maximum colour value of Conductor B
<i>CT</i>	Computed Tomography
<i>D</i>	Fractal dimension
<i>d<sub>ij</sub></i>	Distance between the contact spots <i>i</i> and <i>j</i> (m)
<i>D<sub>K</sub></i>	Korcak dimension
<i>d<sub>ref</sub></i>	Reference distance (m)
<i>d<sub>res</sub></i>	Resolution of pixel length (m)
<i>d<sub>sd</sub></i>	Distance between sample and detector (m)
<i>d<sub>xs</sub></i>	Distance between X-ray source and sample (m)
<i>e</i>	Charge of electron ( $1.602 \times 10^{-19}$ C)
<i>E*</i>	Composite Young's modulus (Pa)
<i>E<sub>A</sub></i>	Young's moduli of contact Body A (Pa)
<i>E<sub>B</sub></i>	Young's moduli of contact Body B (Pa)
<i>EMI</i>	Electrical and Musical Instruments
<i>F</i>	Normal force (N)
<i>Fe</i>	Iron
<i>F<sub>g</sub></i>	Form great spacing (m)
<i>F<sub>s</sub></i>	Form small spacing (m)
<i>F<sub>sp</sub></i>	Force of the spring (N)
<i>G</i>	Scaling parameter
<i>Gap<sub>min</sub></i>	Minimum colour value between the two conductors
<i>H</i>	Material hardness (N/m <sup>2</sup> )
<i>H<sub>i</sub></i>	Height of 3D contact asperity <i>i</i> (m)
<i>i</i>	Contact spot of interest
<i>I'</i>	Final intensity (W/m <sup>2</sup> )

$I_0$	Incident intensity (W/m <sup>2</sup> )
<i>ISO</i>	International Organisation for Standardization
$j$	Contact spot of interest
$K$	Korcak exponent
$k_B$	Boltzmann constant ( $1.380 \times 10^{-23}$ J/K)
$K_S$	Slope of contact spot spatial distribution
$L$	Traverse measuring length (m)
$l$	Length (m)
$m_a$	Number of contact spots per unit area
$m_d$	Number of contact spots per unit distance
$m_e$	Mass of electron ( $9.109 \times 10^{-31}$ Kg)
<i>MEMS</i>	Micro-Electro-Mechanical Systems
<i>MRI</i>	Magnetic Resonance Imaging
$N$	Number of contact spots of a particular area
$n$	Total number of contact spots, 3D contact asperities, constriction asperities
<i>NCSAE</i>	Neighbouring Contact Spot Aggregation Error
$N_d$	Number of contact spots of a particular distance
$n_e$	Number of electrons
$Ni$	Nickel
$N_r$	Total number of resistors
$n_r$	Number of resistors
$n_{res}$	Number of contact spots $i$ , separated from contact spots $j$ by $d_{res}$
$n_v$	Total number of voids
<i>OVDE</i>	Overlapping Void Disaggregation Error
$p_0$	Maximum contact pressure (Pa)
$P_F$	Fermi momentum (kg · m/s)
$p_l$	Pixel length (m)
$P_\theta$	Projection of sample for angle $\theta$
$q$	Slope
$r_i$	Radius of contact asperity $i$ (m)
$R$	Resistance ( $\Omega$ )
$R_a$	Mean surface roughness (m)
$R_A$	Radius of curvature contact Body A (m)

$R_{AB}$	Composite radius of curvature of contact Bodies A and B (m)
$R_B$	Radius of curvature contact Body B (m)
$R_c$	Contact resistance ( $\Omega$ )
$R_g$	Roughness great spacing (m)
$R_j$	Contact resistance of contact spot $j$ ( $\Omega$ )
$R_s$	Roughness small spacing (m)
$S$	Total number of slice asperities
$SEM$	Scanning Electron Microscopy
$Si$	Silicon
$STM$	Scanning Tunnel Microscopy
$T$	Threshold
$T_F$	Fermi temperature (K)
$TT$	Thermographic Technique
$\nu_A$	Poisson's ratio of contact Body A
$\nu_B$	Poisson's ratio of contact Body B
$V_F$	Fermi velocity (m/s)
$V'_i$	Total volume of void $i$ ( $m^3$ )
$V''_i$	Total volume of contact asperity $i$ ( $m^3$ )
$V'_L$	Volume of the largest void ( $m^3$ )
$V'_l$	Volume of the largest void across the fit-line ( $m^3$ )
$V''_L$	Volume of the largest contact asperity ( $m^3$ )
$V''_l$	Volume of the largest contact asperity across the fit-line ( $m^3$ )
$V_R$	Total volume of resistors ( $m^3$ )
$V'_T$	Total volume of voids ( $m^3$ )
$V''_T$	Total volume of 3D contact asperities ( $m^3$ )
$W_g$	Waviness great spacing (m)
$W_s$	Waviness small spacing (m)
$\alpha$	Contact spot radius (m)
$\bar{a}$	Average value of contact spot radii (m)
$a_i$	Radius of contact spot or contact slice or contact asperity $i$ (m)
$a_j$	Radius of contact spot or contact slice $j$ (m)
$\delta$	Dirac's delta function
$\delta_A$	Displace distance of contact Body A (m)
$\delta_{AB}$	Deflection of contact Bodies A and B (m)

$\delta_B$	Displace distance of contact Body B (m)
$\theta$	Angle (rad)
$\mu$	Attenuation coefficient vector
$\xi$	Exponent
$\rho$	Electrical resistivity ( $\Omega \cdot \text{m}$ )
$\sigma$	Standard deviation
$\sigma_d$	Projection's image blurring due to the finite pixel length
$\sigma_s$	Standard deviation of summits
$\omega$	Angular spatial frequency (Hz)



## List of Publications by the Candidate

### Peer-Reviewed Journals:

1. **C. C. Roussos** and J. Swingler, "A 3D contact analysis approach for the visualization of the electrical contact asperities," *submitted to AIP Advances (accepted for publication)*, 2016.
2. **C. C. Roussos** and J. Swingler, "Towards a 3D technique to determine the geometric path of electric current flow through a contact system," *submitted to IEEE Transactions on Components, Packaging and Manufacturing Technology (accepted for publication)*, 2016.
3. **C. Roussos** and J. Swingler, "The 3D nature of a real un-dismantled electrical contact interface," *Wear*, vol. 328–329, pp. 115-122, 2015.

### Conference Proceedings:

4. **C. C. Roussos** and J. Swingler, "Visualisation and characterisation of 3D electrical contact asperities for different current values using an X-ray computed tomography," in *28th International Conference on Electrical Contacts (ICEC 2016)*, Edinburgh, UK, June, 2016, pp. 15-20.
5. **C. C. Roussos** and J. Swingler, "Calculation of the electrical parameters from 3D visualisation data of non-disassembled contact interfaces," in *61st IEEE Holm Conference on Electrical Contacts*, San Diego, CA, Oct., 2015, pp. 82-89.
6. **C. Roussos** and J. Swingler, "Visualisation and characterisation of electrical contact spots for different current values using an X-Ray Computer Tomography," in *12th International Conference on Computational Methods and Experiments in Surface and Contact Mechanics including Tribology*, Valencia, Spain, April, 2015, pp. 59-69.

7. **C. Roussos** and J. Swingler, "Evaluation of electrical contacts using an X-Ray CT 3D visualisation technique," in *27th International Conference on Electrical Contacts (ICEC 2014)*, Dresden, Germany, June, 2014, pp. 326-331.

# **Chapter 1– Introduction**

## **1.1 The Electrical Contact in Engineering and its Importance**

The electrical and electronic industry has made a marvellous progression over the past decades. The cost value of the materials used has meaningfully decreased while the demand for new devices is further away from any comparison to those of the mid of the previous century.

The electrical contact is an important component in many fields of engineering and science as it is an integral part of all electrical and micro-electronic devices [1-5]. This component consists of two conductive surfaces brought together which allows an electric current to flow through it.

The conductive surfaces of the bodies in contact play an important role in the reliability of devices due to the contact normal force, material hardness and surface roughness. The roughness of the surfaces causes a distribution of small peaks or asperities within the apparent area to be in mechanical and electrical contact.

The classification of electrical contacts in general can be divided into two main categories: the stationary and moving. The stationary contacts are connected elastically or rigidly to the stationary part of the device in order to provide the permanent connection. Regarding the moving contacts, commonly one contact part is moving and the other one is static. These main categories of contacts (stationary and moving) contacts are divided into sub-categories according to their operation conditions. More details concerning these sub-categories and examples are given in Section 2.4.

The electrical contacts fail due to a variation of factors such as film formation, corrosion, oxidation, stress relaxation, fretting and diffusion [6-16]. All these failures reduce the actual mechanical area of contact and increase the total contact resistance. The electrical contact is identified as the most common factor as to why electrical and electronic devices fail. According to statistics, the most common cause of electrical failures is credited to connection failures [7, 17-19]. Moreover, the high current flowing through a limited space accelerates the degradation of electrical contact [6]. The total

contact resistance increases localised temperature at the contact interface and primarily softens the contact materials. The thermal cycling hastens stress relaxation and ageing of contact materials causing failure of the electrical contact.

According to the above, the electrical contact is an essential factor that should be considered to achieve better performance and long term reliability for the design of devices. Having more detailed knowledge of the physics and mechanisms of electrical contacts and their material properties helps in the design of these devices with a better performance.

## **1.2 Research Initiative**

Notwithstanding the extensive research into the field of contact mechanics and electrical contacts since the mid of last century [20-23], electrical contacts still face several problems affecting their performance and long term reliability. Due to the limitation of optical imaging, methods and techniques for the contact mechanics and electrical contacts measurement characteristics are only suitable for open or transparent contact systems.

For most of the practical situations that require contact mechanics and electrical contact measurements characteristics in non-transparent or enclosed contact systems, the traditional methods are not effective. Based upon these requirements, a technique suitable for the electrical contact characteristics in non-transparent contact systems is developed by using X-ray Computed Tomography (CT). The main advantage of this technique is the ability to acquire 3-Dimensional (3D) views of contact systems keeping the features intact. The technique could corroborate an irreplaceable tool for researchers, scientists when designing new or improving current electrical devices.

## **1.3 The Experimental Equipment – X-ray CT**

### *1.3.1 Brief description of X-ray CT*

The X-ray CT belongs to the radiography investigations and is considered to be one of the very few non-destructive visualisation techniques available in nowadays. The X-ray CT makes use of electromagnetic radiation in order to yield an X-ray image. An X-

ray is electromagnetic energy in the form of wave. The photons of X-rays have very high energy which can travel through virtually any material.

For the characterisation of X-ray CT, it could be divided into three main parts: the X-ray source, the turntable and the detector. Firstly, the sample is placed on the turntable and illuminated with X-rays from the X-ray source and an X-ray image is acquired from the detector. Every time the turntable rotates the sample by very small interval angle, an X-ray image is acquired and this is repeated until the sample has been rotated around one complete revolution.

Each X-ray image records the level of X-ray intensity across an x-y plane which relates to the level of admittance of X-rays along the z-direction through the whole sample. Thus, each X-ray image contains information about the X-ray admittance characteristic of the materials through the whole sample. A more detailed description and analysis concerning the X-ray CT equipment in engineering and science, as well as its basic operation is given in Section 3.4.

### *1.3.2 How X-ray CT has been used in the past*

The X-ray CT technique was initially used for medical diagnosis. This technique is based on radiography and is used widely to identify e.g. cracked bones, harmed nerves, traumatic vascular as well as tumours [24-30]. The X-ray CT technique is a powerful tool for doctors when the visualisation and characterisation of an inner part of the body is required. Nevertheless, due to the porousness of different materials, the use of the X-ray CT technique was consequently protracted and adapted to a varied range of industrial and scientific fields. Some examples are given below.

In manufacturing industries, the X-ray CT technique has been used widely for fault diagnosis and quality assurance in a variety of different applications. For instance, the use of the X-ray CT technique is supported expressively the food industry. Primarily, the X-ray CT technique was used in order to inspect the grouping of meat with small bones or to identify contaminants hidden within the vegetables or fruits [31-33].

Moreover, the X-ray CT has been used widely for the integrated circuit development industry. The development of silicon integrated circuits is a very complex process. This

process requires correctness during all the development stages. The miniaturisation of electrical and electronic devices in combination with the increased complexity of new designs requires fast and correct non-destructive inspection methods in order to identify failure localization in microscopic and nanoscopic scale ranges and ensure the superiority of the device [34-36]. The X-ray CT technique is adopted by many integrated circuit developers.

In addition, the X-ray CT technique has the ability to visualise voids and residuals in on-chip metal interconnects without physical modification of the chip [37]. The importance of synchrotron radiation experiments is essential to study procedures and materials used in the semiconductor industry.

The aircraft development and maintenance is also benefiting from the abilities of X-ray CT technique as the safety critical components are scanned in order to identify possible defects during the development or failures caused in the field [7, 38, 39]. The X-ray CT technique nowadays is the main non-destructive method which has the ability to identify and visualise internal failure localization or structural defects which are not externally visible [7].

#### **1.4 Why use X-ray CT to Visualise and Characterise Electrical Contact Systems**

As mentioned before in Section 1.1, the electrical contact which occurs between the conductors of an electrical contact system is an important component in many fields of engineering and science as it is an integral part of all electrical and micro-electronic devices [1-4]. This component consists of two conductive surfaces brought together which allows an electric current to flow through it. The conductive surfaces of the bodies play an important role in the reliability of devices due to the contact normal force, material hardness and surface roughness. The roughness of the surfaces causes a distribution of small peaks or asperities within the apparent area of contact.

The contact asperities of a contact system have been considered for decades due to their significant importance in several branches of science and engineering such as surface science [40-42], tribology [43-45], heat transfer [46-49] and recently in Micro-Electro-Mechanical Systems (MEMS) [50-56]. Due to this significant importance, several models [57-62] are developed using simulation of simplified data or statistically

using estimates of the contact area or imaginary data in order to provide information about their features. These features include the contact asperity dimensions, number, distribution material properties, surface profiles and operating conditions. One of the most popular models has been developed by Greenwood-Williamson [63]. According to this model, it assumes the contact asperities on a surface are hemispherical in shape with the same radius. The peak of each contact asperity is assumed to be located at different heights following a random Gaussian distribution. When a flat plane is brought into contact with the Greenwood-Williamson surface, the contact asperities deform elastically with consideration of plastic deformation under particular limits.

More interesting studies in recent times are focused on non-destructive visualisation techniques (a more detailed description and analysis concerning these techniques is given in Section 3.3). In this research, the X-ray CT which belongs to the non-destructive visualisation techniques is selected because it gives the ability to visualise and characterise the experimental data of a real electrical contact system keeping its features intact.

## **1.5 Electrical Contact System Characteristics and X-ray CT Technique**

The characteristics of an electrical contact system in this research are classified into three main categories: the contact interface, the resistor network model and the 3D contact asperities. The contact interface is found to be very important by many researchers which are visualized using different techniques. Nowadays, the only valuable alternative technique has been developed by Lalechos [7] which presented a “2D Contact Map” on a 2D contact profile from experimental data collected using the X-ray CT technique. In this research, the “3D Contact Map” of an electrical contact interface is developed demonstrating the 3D nature of the contact interface of a contact system from experimental data collected using the X-ray CT technique. The 3D contact map gives information on where the electrical contact spots in a 3D profile are located. Chapter 5 focuses on the 3D contact map showing its advantages over the 2D contact map.

The resistor network model has been developed in this research using the cross-section slices of the contact system from experimental data collected using the X-ray CT technique. The resistor network model development is based on the contact interface of the contact system which is presented as 3D contact map. The 3D contact map consists

of contact spots which have been extended across the two conductors of the contact system as asperities. In this modelling process, a technique is developed which pictures any cross-section slice of the contact system and shows in which spots the electric current flows. It is important to note that no attempts have been made to date to introduce the resistor network model of a contact system and to show from which resistors (the pathway) the electric current flows. A more detailed description and analysis concerning the resistor network model of a contact system is given in Chapter 6.

The visualisation of 3D contact asperities of the contact system has been developed in this research using the contact interface which has been visualised as a 3D contact map. The 3D contact asperities describe the extensions above and below this contact interface (3D contact map) to the two conductors which consist the contact system. Nowadays, several studies have attempted to visualise a single 3D contact asperity using different methods and techniques [64, 65]. A contact analysis approach which has been developed and introduced in this research shows the way to the 3D visualization of all the contact asperities of a given contact system. A more detailed description and analysis concerning this contact analysis approach of a contact system is given in Chapter 7.

## **1.6 The Scope of Research**

The research presented in this thesis uses the X-ray CT visualisation technique for the collection of experimental data of a contact system. The nature of this visualisation technique is very promising as it has the ability to acquire 2D and 3D views of the contact system keeping its features intact. Nevertheless, a more scientific approach is required in order to verify all assumptions.

This research illustrates the usefulness or the uselessness of X-ray CT technique as a means for visualising electrical contact systems and characterising their different mechanical and electrical parameters with the main advantage of not needing to disassemble them. The experimental data (images of the contact system) which are acquired using the X-ray CT technique provide a good foundation for better understanding the characteristics of mechanical and electrical contacts as well as their extensions above and below to the two conductors which consist of the contact system. The extensions above and below of contacts to the two conductors are called contact asperities.



## 1.7 The Objectives of Research

The main objectives of this research are listed below:

- i. Survey the literature of Electrical Contact and X-ray CT scanning technique
  - Surface characterisation
  - Contact Interface characterisation
  - Classification of electrical contacts
  - Destructive and non-destructive visualisation techniques
  - The X-ray CT in Engineering and Science
  
- ii. Use an X-ray CT technique to investigate characteristics in Contact Systems
  - Selection of contact system
  - The selected contact system
  - Experimental equipment (X-ray CT)
  - Post-processing and analysis of experimental data
  - Calculation of the error of experimental data
  
- iii. Development of Contact Analysis Techniques (CAT\*) for the 2D contact mapping
  - Visualisation of 2D contact map
  - Calculation of the mechanical area of contact of each contact spot
  - Calculation of the total mechanical area of contact
  
- iv. Development of CAT\* for the 3D contact mapping
  - Visualisation of 3D contact map
  - Calculation of the mechanical area of contact of each contact spot
  - Calculation of the total mechanical area of contact
  - Calculation of the angle of each contact spot
  - Development and visualisation of 2D angle map
  
- v. Development of CAT\* for the 3D voids identification
  - Visualisation of 3D voids
  - Calculation of the volume of each void
  - Calculation of the total volume of voids

- vi. Development of CAT\* for the conductors separation
  - Visualisation of each conductor
  - Calculation of the conductors fractal characteristics
  
- vii. Development of CAT\* for the resistor network modelling
  - Visualisation of current flowing through the spots of any cross-section slice of the contact system
  - Calculation of the number of resistors in each cross-section slice (Open/Closed Circuit resistor network model)
  - Calculation of the number of resistors in each cross-section slice (Closed Circuit resistor network model)
  - Calculation of the total area of spots (resistors) in each cross-section slice (Open/Closed Circuit resistor network model)
  - Calculation of the total area of spots (resistors) in each cross-section slice (Closed Circuit resistor network model)
  - Calculation of the total volume of resistors in Open/Closed Circuit resistor network model
  - Calculation of the total volume of resistors in Closed Circuit resistor network model
  - Calculation of the total resistance across any two points of the contact system
  - Calculation of the total conductance across any two points of the contact system
  
- viii. Development of CAT\* for the 3D contact asperities analysis
  - Visualisation of 3D contact asperities
  - Visualisation of a selected 3D contact asperity
  - Calculation of the volume of each 3D contact asperity
  - Calculation of the total volume of 3D contact asperities
  - Calculation the surface area exposed to air of each 3D contact asperity
  - Calculation the total surface area exposed to air of all 3D contact asperities
  - Calculation of the top surface area of each 3D contact asperity
  - Calculation of the bottom surface area of each 3D contact asperity
  - Calculation of the ratio of top and bottom surface areas of each 3D contact asperity
  - Calculation of the ratio of top and bottom surface areas with the height of each 3D contact asperity

- Calculation of the height of each 3D contact asperity

In brief, this research evaluates whether X-ray CT scanning technique could be potentially used to visualise and characterise a given electrical contact system.

## **1.8 Research Summary**

A 16 A rated AC single pole rocker switch is selected as the contact system for investigation and it was scanned using the X-ray CT technique after four different current loading tests at 0 A, 16 A, 32 A and 64 A. In the process, several CAT\* are developed and implemented with a suite of tools in MATLAB and Image Processing Toolbox in order to help with the analysis of experimental data (data which are acquired from X-ray CT technique scan). These CAT\* consist of a variety of tools which are categorised into visualisation tools and calculation tools.

The visualisation tools have the ability to visualise the contact interface of the contact system (2D contact map and 3D contact map), the 2D angle contact map (show the contact spot with equal contact angle with same colour), the 3D voids between the conductors of the contact system, the 3D contact asperities (the structures of contact spots above and below the two conductors of the contact system) and the geometric path of electric current which flows through the contact system.

The calculation tools have the ability to calculate the contact resistance using two different approaches (Greenwood [66] and Holm [20]), the number of contact spots, the area of each contact spot and the total mechanical area of contact of a given contact system. Moreover, the calculation tools can calculate the angle of each contact spot in 3D contact interface and the number of voids which are located between the two conductors of the contact system. In addition, the calculation of the volume of each void and the total volume of voids are conducted to the calculation tools.

Concerning the 3D contact asperities, the calculation tools have the ability to calculate the number of contact asperities, the height and the volume of each contact asperity and the total volume of all contact asperities as well as the surface area of each contact asperity which is exposed to air and the total surface area of all contact asperities which are exposed to air.

Another ability of the calculation tools is the calculation of the number of contact spots (number of resistors in resistor network model, for open and closed circuits) in each cross-section slice (perpendicular to normal force of the contact system) from which the electric current flows through them and from which does not flow.

The CAT\* give the possibility to examine and characterise the contact system under different conditions and operations. This possibility may be useful and beneficial for contact users, their suppliers and electrical device system design engineers as it visualises and characterises different features of the contact system.

## Chapter 2 – Electrical Contact

### 2.1 Introduction

It is a very difficult issue to create surfaces which are really flat. Even on carefully polished surfaces, peaks and valleys are presented at the microscopic scale illustrating a roughness with fractal behaviour which is found to be very interesting by many researchers [67-74]. On this scale when two surfaces are brought together this roughness influences mechanical contact which occurs only in a specific number of areas on the apparent area of contact. These areas, which are a result of mechanical contact are called contact spots and the aggregate of contact spots is called the contact interface. In addition, the slight projections from a surface (the result of roughness) are called asperities.

Electrical contacts provide electrical connection of two conjoining conductors. The main objective of an electrical connection is to allow the flow of electric current through the contact interface. It is evident that this can only be achieved if a good conductor-to-conductor contact is established. The electrical contact is an important factor in many fields of engineering and the sciences as it is an integral part of all electrical and micro-electronic devices [1, 2, 20, 66, 75, 76].

According to Braunovic *et al.* [23], the processes occurring in the contact region are nontrivial and are not fully explained within the limits of present knowledge. Although the nature of these processes may differ, they are all governed by the same fundamental phenomena. An understanding of these phenomena that occur at a contact region is crucial to achieve better performance and long-term reliability of devices constituting such contact interfaces.

This chapter includes surface characterisation, contact interface characterisation and classification of electrical contacts. The surface characterisation refers to the surface categories, the surface parameters measurement and the modern methods of surface parameters measurement. The contact interface characterisation refers to the elastic, plastic and elastic-plastic deformation of the contact system as well as the contact interface models, fractals and area of contact interface and electrical contact interface and its reliability. The classification of electrical contacts refers to the two main categories of electrical contacts which are stationary and moving.

## 2.2 Surface Characterisation

Surface characterisation is an important factor in many fields of engineering and the sciences by elucidating the fundamental aspects of chemistry and physics occurring at a wide range of surfaces and interfaces [10, 77-86]. Surface characterisation can be used to develop techniques in a wide range of functional properties including physical [87, 88], chemical [89, 90], electronic [91, 92], mechanical [93, 94], magnetic [95, 96], wear and corrosion resistance properties [13, 14] at the required substrate surface.

### 2.2.1 Surface categories

Real surfaces show roughness on the microscopic scale. This roughness in engineered surfaces consists of peaks and valleys whose high variations in shape, average separation and other geometrical characteristics depending on the manufacturing process and material used. Archard [74] in the 50's of the 20<sup>th</sup> century provide a model of surface roughness. According to this model all surfaces consist of “protrusions on protrusion on protrusion”. Therefore, as the zoom in on the image is increasing, different levels of roughness can be detected as illustrated in Figure 2.1.

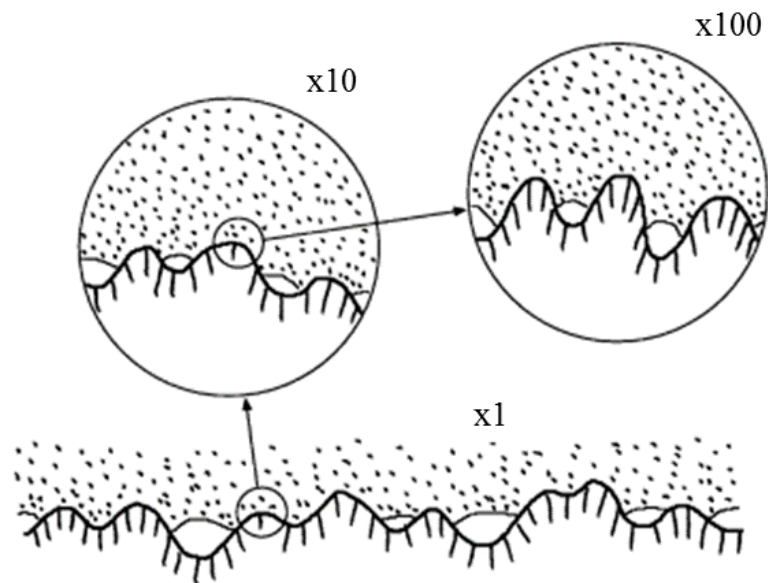


Figure 2.1. Archard's surface roughness model [97]

In engineering, real surfaces are produced by a variety of material removal process. Archard [74], reported that the total resulting geometry of these real surfaces can be better

considered to be divided into three categories: form, waviness and roughness. Figure 2.2 illustrates these three categories in a surface profile.

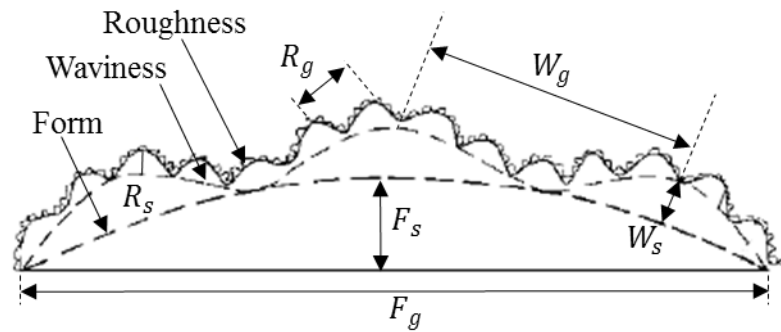


Figure 2.2. Categories of surface profile [23]

The form describes the macroscopic shape of the surface. Braunovic *et al.* [23] reported that the macroscopic shapes in this category have a great spacing ( $F_g$ ) between 1-5,000 mm and relatively small height ( $F_s$ ) between 1-50  $\mu\text{m}$ . Different combinations of form shapes produce different shapes of contact spots.

The waviness describes the shape of the surface at the microscopic scale. The microscopic shapes in this category have a great spacing ( $W_g$ ) between 0.8-10 mm and relatively small height ( $W_s$ ) between 0.01-500  $\mu\text{m}$  [23]. Waviness is included in the International Organisation for Standardization (ISO), standards ISO 4287 [98] and ISO 16610 [99] as well as the American Society of Mechanical Engineers (ASME), standard ASME B46.1 [100].

The roughness describes the fine detail of the surface in the microscopic scale. Such details include the asperities height and spacing. Typically, such details can be visualised in the sub of 1  $\mu\text{m}$  range and therefore very high precision is required.

### 2.2.2 Surface parameters measurement

For the surface topographical characterisation geometry, a 2D profile of the surface is required. For the acquisition of this 2D profile an optical Surface 3D Profiler could be used. Figure 2.3 shows an example of a 2D profile of the surface. The height (y-direction) of each asperity is indicated together with the reference position across the 2D profile (x-

direction). The mean roughness line indicates the mean  $y$ -value across the 2D profile ( $x$ -direction).

The 2D profile in Figure 2.3 is divided into consecutive and equal sampling lengths ( $l$ ), which are long enough to include a statistically reliable amount of roughness, yet short enough to exclude waviness from the roughness measurement. It is important to note that  $l$  corresponds to a filter cut-off length. Measurements on the deviation of the mean roughness line are taken over a number of consecutive samples and often used to estimate the waviness. The traverse measuring length ( $L$ ) is defined as the length of 2D profile used for the measurement of surface roughness parameters (usually containing several sampling lengths; five consecutive sampling lengths are taken as standard).

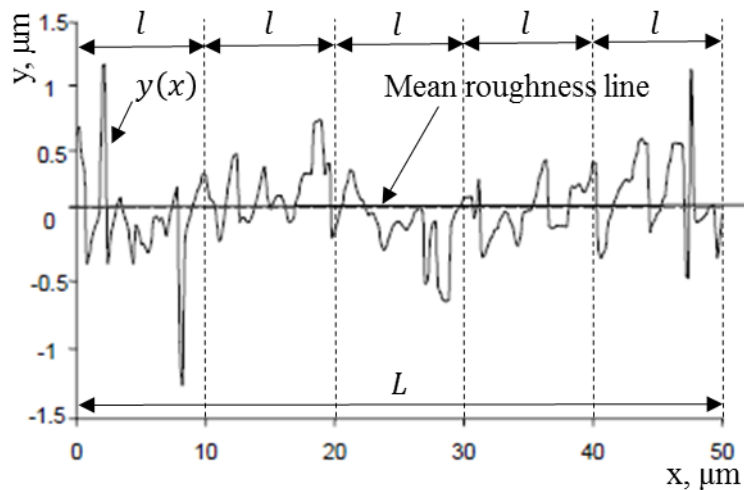


Figure 2.3. 2D profile of a surface [23]

The most familiar surface roughness parameter is the surface mean roughness. The mean surface roughness ( $R_a$ ) of the 2D profile of Figure 2.3 is given from the area enclosed by the  $x$ -axis and curve of the roughness ( $y(x)$ ) as described in Eq. (2.1).

$$R_a = \frac{1}{L} \int_0^L |y(x)| dx \quad (2.1)$$

A less common, but statistically more meaningful measure of mean surface roughness, is the standard deviation ( $\sigma$ ) of the height of the surface from the mean



roughness line. The standard deviation of the 2D profile of Figure 2.3 is given by Eq. (2.2).

$$\sigma^2 = \frac{1}{L} \int_0^L y^2(x) dx \quad (2.2)$$

Greenwood and Williamson [63] considered that the mechanical contact occurs only between the summits and not between the slopes or edges of asperities. According to this consideration, they reported that the use of the standard deviation of summits ( $\sigma_s$ ) is more reliable than the use of the standard deviation ( $\sigma$ ) of the surface profile. The standard deviation of summits of the 2D profile of Figure 2.3 is given by Eq. (2.3).

$$\sigma_s^2 = \frac{1}{L} \int_0^L y^2(x)_s dx \quad (2.3)$$

The relationship between the mean surface roughness and standard deviation of the summits is given by Eq. (2.4).

$$\sigma_s = R_a \sqrt{\frac{\pi}{2}} \quad (2.4)$$

### 2.2.3 Modern methods of surface parameters measurement

Nowadays there are many different methods to study the surface parameters [101, 102]. The most popular of these methods are the stylus whose results have been the foundation of modern standards. According to Braunovic *et al.* [23], optical methods using electromagnetic radiation have become phenomena and heat transfer through the surface. The capabilities of different methods for measuring the surface parameters are illustrated in Figure 2.4. These methods include the stylus profilometry, optical profilometry, Scanning Electron Microscopy (SEM) based methods, large and small scan Atomic Force Microscopy (AFM) and Scanning Tunnel Microscopy (STM).

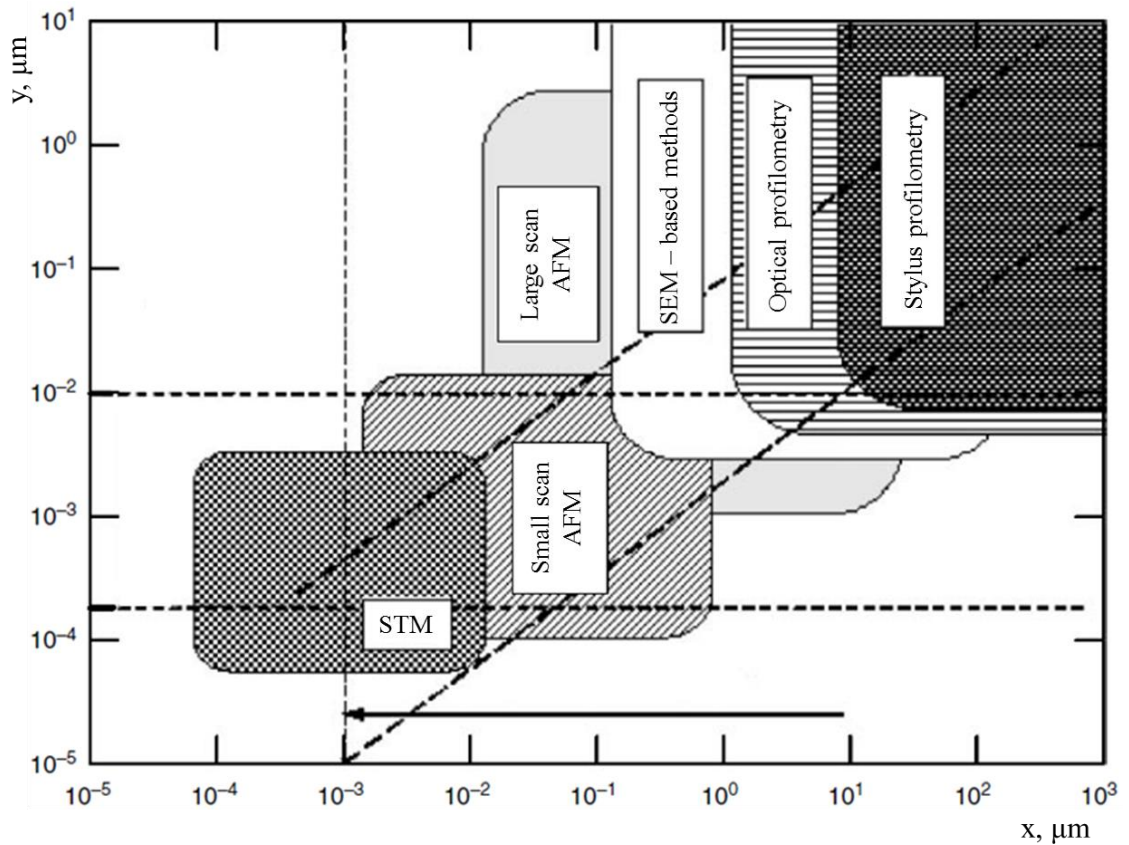


Figure 2.4. Ranges of vertical-lateral resolution for different methods of roughness measurement [23]

### 2.3 Contact Interface Characterisation

As mentioned before, real surfaces contain peaks and valleys on the microscopic scale presenting a roughness. On this scale when two surfaces are brought together this roughness influences mechanical contact. The red arrows in Figure 2.5 show the mechanical contact which occurs between the rough surfaces of bodies A and B (side view, x-y - direction). The mechanical contact occurs only in a specific number of areas on the apparent area of contact. These areas, which are a result of mechanical contact called contact spots and the aggregate of contact spots is called the contact interface. Figure 2.6 shows the top view (x-z - direction) of a contact interface consisting of contact spots.

The mechanical contact is a result of a load force which holds the two bodies of the contact system in touch. When a load force is applied to a contact system, it results in the change of the shape of these two bodies. This result is called deformation and is categorized into elastic, plastic and elastic-plastic.

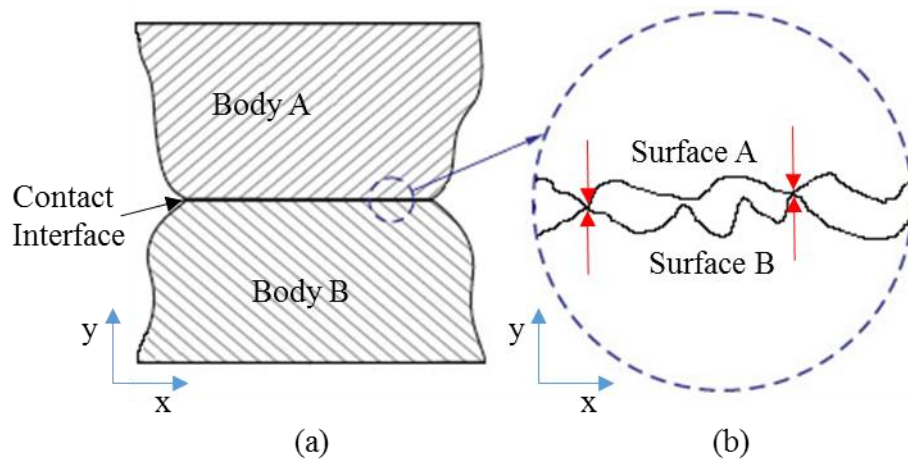


Figure 2.5. (a) Cross-section of schematic contact system of bodies A and B which are in mechanical contact, (b) Zoom-in at a part of the contact interface

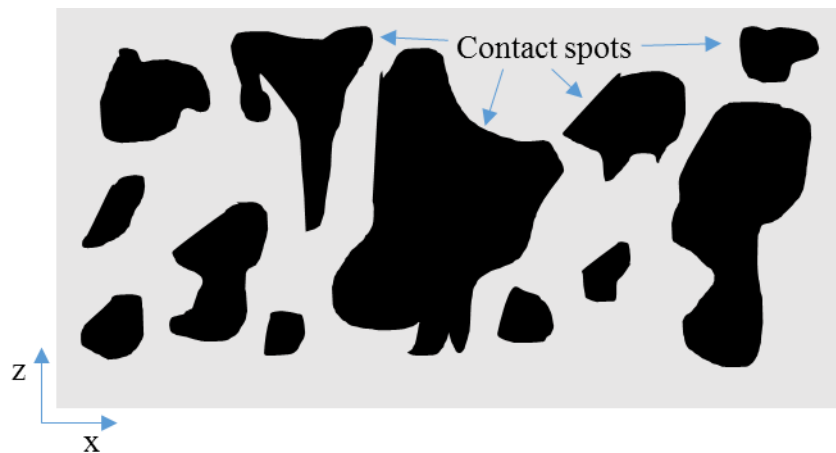


Figure 2.6. Top view of schematic contact interface

### 2.3.1 Elastic deformation of contact system

Elastic deformation results in changes of shapes of the contact bodies which could self-reverse to their original shapes when the load force is removed from the contact system. The elastic deformation involves stretching of the bonds, but the atoms do not slip past each other.

The elastic deformation of a contact system is based on the Hertz theory [22, 103] on which the asperities deform elastically. According to this theory in Adams and Nosonovsky work [104], where the mechanical area of contact is assumed elliptical, each of the two bodies of the contact system is approximated by an elastic half-sphere loaded

over the plane elliptical contact area, the dimensions of the contact area must be smaller compared to the dimensions of each body and to the radii of curvature of the surfaces, the strains are sufficiently small for linear elasticity to be valid and the contact is frictionless, so that only a normal pressure is transmitted.

A contact system of the two elastic bodies are illustrated under elastic deformation in Figure 2.7. According to Johnson [22] on Hertz's [105] work, during compression by the contact normal load force  $F$ , distance points  $y_A$  and  $y_B$  displace distances of  $\delta_A$  and  $\delta_B$  respectively parallel to the  $y$ -axis. The deflection of contact bodies A and B ( $\delta_{AB}$ ) is equal with the sum of  $\delta_A$  and  $\delta_B$ . Moreover the deflection of contact bodies A and B is given by Eq. (2.5).  $R_{AB}$  represents the composite radius of curvature of contact bodies A and B and is given by Eq. (2.6).  $R_A$  and  $R_B$  are the radii of curvature contact bodies A and B respectively.  $E^*$  is given by Eq. (2.7) and represents the composite Young's modulus.  $E_A, E_B$  and  $\nu_A, \nu_B$  are the Young's moduli and Poisson's ratios for the contact bodies A and B respectively.

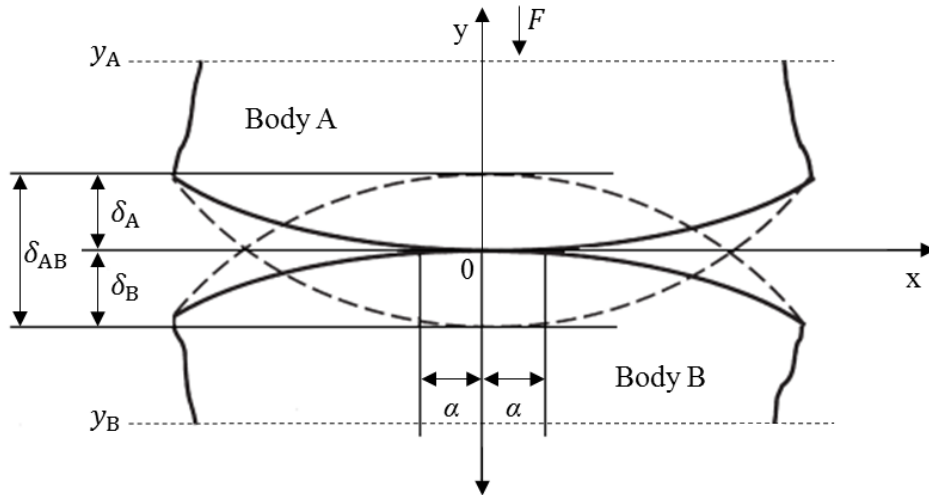


Figure 2.7. Hertz contact system of elastic bodies [104]

$$\delta_{AB} = \sqrt[3]{\frac{9F^2}{16R_{AB}E^{*2}}} \quad (2.5)$$

$$\frac{1}{R_{AB}} = \frac{1}{R_A} + \frac{1}{R_B} \quad (2.6)$$

$$\frac{1}{E^*} = \frac{1 - \nu_A^2}{E_A} + \frac{1 - \nu_B^2}{E_B} \quad (2.7)$$

For the case of bodies A and B of revolution [104], the contact area is circular and its radius is given by Eq. (2.8). The maximum contact pressure ( $p_0$ ) occurs at 0 (axis origin) and is given by Eq. (2.9).

$$a = \sqrt[3]{\frac{3FR_{AB}}{4E^*}} \quad (2.8)$$

$$p_0 = \sqrt[3]{\frac{6FE^{*2}}{\pi^3 R_{AB}^2}} \quad (2.9)$$

The elastic deformation of the contact system which is based on the Hertz theory [22] has been extended in different models by other researchers. For example, the contact of rough surfaces considering a distribution of the radii of the asperities [106], to the contact of rough curved surfaces [107], the contact of two nominally flat rough surfaces [108] and elliptic paraboloid surfaces [109]. All the above models correspond to the elastic deformation of contact system.

### 2.3.2 *Plastic deformation of contact system*

Plastic deformation results when the load force is sufficient to permanently deform the bodies within the contact system and begins to occur after elastic deformation. The level of the deformation depends on several parameters such as the level of the applied load and the hardness of the two bodies. The plastic deformation involves the breaking of a limited number of atomic bonds by movement and dislocations.

The plastic deformation model of a contact system is introduced by Abbott and Firestone [110] which is known as a profilometric model or a surface micro-geometry model. According to this model, the deformation of the rough surface of contact body

against a smooth rigid flat is assumed to be equivalent to the truncation of the initial rough surface at its intersection with the flat so that the contact area is simply the geometrical intersection of the original profile. The average contact pressure is equal to the indentation hardness of the softer body (or the flow pressure).

Moreover, Pullen and Williamson [111] introduced a volume conservation model for the plastic deformation of the contact system for high load forces based on the experimental results. This model is confirmed by Kucharski *et al.* [112], who used a finite element analysis.

### 2.3.3 *Elastic-plastic deformation of contact system*

The elastic-plastic deformation of contact system bridges the two extreme deformations, elastic and plastic. Chang *et al.* [113] in the 80's of the 20<sup>th</sup> century developed an elastic-plastic contact system model which is based on the volume conservation of the plastically deforming asperities. According to this elastic-plastic contact system model, Chang *et al.* [113] reported that the deformation mode changes from the elastic to plastic contact regime with no transition.

Johnson [22], in contrast to Chang *et al.* [113] focused on the analysis of the indentation of a sphere on a plane where there is a large transition regime from the elastic to plastic state. This transition is included in the contact system model of rough surfaces which is developed by Zhao *et al.* [114].

The elastic-plastic deformation of a contact system has been extended in different models by other researchers. For example, a finite element analysis on the elastic-plastic contact of a sphere and a rigid-flat [115], a finite element of elastic-plastic hemispherical contact against a rigid flat [116], an elliptic elastic-plastic asperity micro-contact model for rough surfaces [117], an elastic-plastic contact model of ellipsoid bodies [118] and an elliptical micro-contact model of elastic-plastic deformation [119].

### 2.3.4 *Contact interface models*

Various approaches have been used to identify the phenomena occurring in a contact interface. Initially, Holm [120] in the 1930's provided a fundamental theory to describe

contact mechanisms and contact resistance. Over time, this theory has been developed to include features such as asperity shape, contact spot number, contact spot distribution, material properties, surface profiles and operating conditions.

Greenwood-Williamson's model [63] in the 1950's assumes that asperities on a surface are hemispherical in shape with the same radius. According to this model, the peaks of a surface of asperities are considered to be located at different heights following a random Gaussian distribution. The asperities undergo elastic deformation (considering the plastic deformation under particular conditions) when a Greenwood-Williamson surface comes into contact with a flat plane. This model has been further developed by many researchers including Bhushan and Majumdar [69] who created a fractal surface profile with different asperity radii.

### 2.3.5 *Fractals in contact interface*

Bhushan [121], demonstrated the contact interface by using the fractal behaviour of natural phenomena of a surface. This approach illustrates that the measured asperity curvature and measured slope depend on the measurement resolution and the statistical sample size. For example, for a coarse measurement of resolution, only a few asperities of large curvature are observed while for smaller measurement of resolution more asperities of smaller curvature are observed [122]. To eliminate this scale dependency, the fractal approach is a possible technique to characterise realistically the surface using parameters such as the scaling parameter  $G$ , the fractal dimension  $D$ , and constant  $C$ . Eq. (2.10) showing the typical fractal surface exhibiting a spectral density with power law behaviour ( $P(\omega)$  describes the function of spectral density  $P$  with the spatial frequency  $\omega$ ). The roughness is modelled by the sum of multiple sinusoidal functions of angular spatial frequency  $\omega$ .

$$P(\omega) = C\omega^{-q} \quad (2.10)$$

Eq. (2.10) indicates some well-known behaviour for different values of  $q$  in the time domain. Considering that  $q = 0$ , the spectral density plot with angular spatial frequency  $\omega$ , gives a flat straight line which indicates an equal amount of each frequency component. This behaviour is known as white noise. Considering that  $q = 2$ , it is known

as brown noise which means that it consists of lower frequencies rather than higher frequencies [123]. The scaling parameter  $G$ , and the fractal dimension  $D$ , can be found from Eq. (2.11).

$$P(\omega) = \frac{C(G)}{\omega^{5-2D}} \quad (2.11)$$

According to Ciavarella *et al.* [124], the perfect fractal surface is the one that shows fractal behaviour at all scales, making an infinite number of contact spots of zero size with infinite pressure. The fractal approach to rough surfaces has problems which were aimed to be resolved by Gao *et al.* [125] by considering plastic flow at the surface. It was found that the total elastic-plastic contact area and the contact pressure could be easily defined but it was impossible to predict the number of contact spots and their sizes. They found out that the fractal behaviour at some lower limit cannot be exhibited, so it is necessary to conduct 3D profilometry at a resolution to define this limit.

### 2.3.6 Area of contact interface

An estimation of the mechanical area of contact can be calculated by using several different models. Under elastic deformation of the materials, Hertz's contact theory [126, 127] is used as shown in Eq. (2.12), where  $A_e$ , is the area of contact (under elastic deformation),  $F$  is the applied force,  $a$  is the radius of contacting spheres and  $E^*$  is a constant consisting of Young's modulus and Poisson's ratio of the materials involved.

$$A_e = \pi \left( \frac{3 Fa}{4 E^*} \right)^{2/3} \quad (2.12)$$

Bowden and Tabor [128] introduced the plastic deformation relationship. According to this relationship, it considers a surface as having a roughness where each asperity is plastically flowing when loaded with force ( $F$ ). Under plastic conditions the mechanical area of contact is given by Eq. (2.13). The hardness of the material symbolises with  $H$ . Bowden and Tabor [128] introduced this relationship as a rule of thumb in order to



estimate the mechanical area of contact under the domination of elastic and plastic deformation.

$$A_p = \frac{F}{H} \quad (2.13)$$

Archard [74] went further and modelled the surface as multiple levels of roughness so that the surface will have a protrusions upon a protrusions upon a protrusions. By using the Hertz theory [22] in which the asperities deform elastically, the elastic mechanical area of contact is found to converge to the Bowden and Tabor relationship (Eq. (2.13)).

Greenwood and Wu [129] identified three main aspects which are helpful to understand the contact interface. According to the first aspect the peaks on the surface have a high distribution that can be modelled by a simple exponential function. The second aspect identifies that each peak can be considered to have a hemispherical top. This aspect is essential to approximate the size of the area of contact that is based on the Bowden and Tabor [128] theory. According to the third aspect, the peaks on a surface profile correspond to asperities that make contact. Greenwood assumes that the number and radius of curvature of asperities is a false idea given by this aspect. This aspect was also opposed by Archard's [34] model of multiple levels of roughness.

Majumdar and Bhushan [28], developed a model which is valid for materials with a wide distribution of grain sizes. When an asperity of radius  $\alpha$  is deformed, it will initially deform elastically. However, beyond a critical point, the material will deform inelastically. For flexible materials, this causes plastic deformation and for inflexible materials fracturing takes place. Eq. (2.14) shows the derived model for the total mechanical area of contact.  $D$ , stands for the fractal dimension of the surface profile while  $A_L$ , is the area of the largest contact spot. Moreover, Eq. (2.14) focuses on the area of contact under plastic and deformation separately. The size distribution of contact spots can be calculated by this model which is very important for the theoretical estimation of contact resistance.

$$A_T = \frac{D}{2-D} A_L \quad (2.14)$$

### 2.3.7 Electrical contact interface

The electrical contact interface is the contact interface from which the electric current flows through the two conductive bodies. Figure 2.8(a) shows the contact system of two conductive bodies which are in mechanical contact at one point and the cross-section area is the same at any point across the length ( $l$ ) of the two bodies. The total resistance ( $R$ ) of a contact system with uniform cross-section with a uniform flow of electric current is given by Eq. (2.15). The electrical resistivity symbolises with  $\rho$  while  $A$  stands for the cross section area of the contact system.

$$R = \rho \frac{l}{A} \quad (2.15)$$

According to Myshkin *et al.* [130], the electrical resistivity is given from Eq. (2.16). Where  $m_e$ , is the mass of electron,  $V_F$  is the Fermi velocity,  $n_e$  is the number of electrons  $e$  is the charge of electron and  $l$  is the length of the conductive material. The mass ( $m_e$ ) and charge ( $e$ ) of electron are constant,  $9.109 \times 10^{-31}$  Kg and  $1.602 \times 10^{-19}$  C respectively. The Fermi velocity is given from Eq. (2.17). Where  $P_F$ , is the Fermi momentum and described from Eq. (2.18) [131]. Where  $T_F$  and  $k_B$  are the Fermi temperature and Boltzmann constant ( $1.380 \times 10^{-23}$  J/K) respectively [131].

$$\rho = \frac{m_e V_F}{n_e e^2 l} \quad (2.16)$$

$$V_F = \frac{P_F}{m_e} \quad (2.17)$$

$$P_F = \sqrt{2m_e T_F k_B} \quad (2.18)$$

Figure 2.8(b) shows the contact system of two conductive bodies which are in mechanical contact at one point and the cross-section area size has different values at any point across the length ( $l$ ) of two bodies. The total resistance ( $R$ ) of a contact system with non-uniform cross-sections (each cross-section has different size) with uniform flow of electric current (each cross-section has no more than one electrical contact spot, thus the amount of electric current flowing through each contact spot or cross-section area is equal) is given by Eq. (2.19). This equation can also be used and for the contact system of Figure 2.8(a) as well.

$$R = \rho \int_0^l \frac{1}{A(x)} dx \quad (2.19)$$

The total resistances of the contact systems in Figure 2.8(a) and Figure 2.8(b) can be characterised as the sum of the series resistances. Each series resistance corresponds to the resistance of the cross-section area. When the contact system is in mechanical contact in more than one point as presented in Figure 2.8(c), the calculation of the total resistance ( $R$ ) of the contact system becomes more complicated and nontrivial to calculate as the cross-section areas at contact interface have many contact spots. These contact spots are connected in parallel and their extensions across the two bodies have different length dimensions. This is a result of the rough surfaces of the conductive bodies which are in mechanical contact.

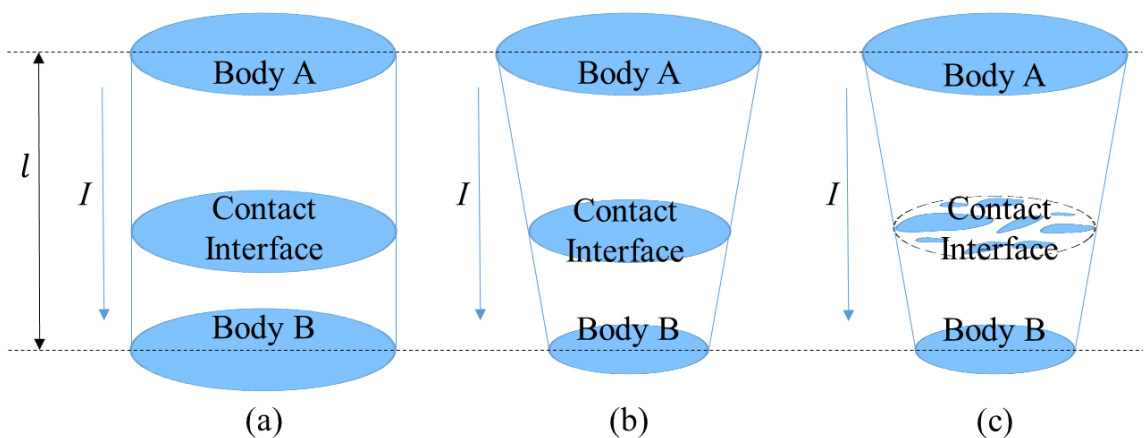


Figure 2.8. Electric current flowing through contact systems [132]

Figure 2.9 illustrates the schematic cross-section diagram of the contact system from Figure 2.8(c). This schematic diagram shows that the electric current lines become increasingly distorted as the electrical contact interface is approached and the flow lines bundle together to pass through the number of contact spots. According to Slade [21], the constriction of electric current by contact spots decreases the volume of material used for electrical conduction and thus increases the electrical resistance [21]. This increase in resistance is called the contact resistance (or constriction resistance) of the electrical interface.

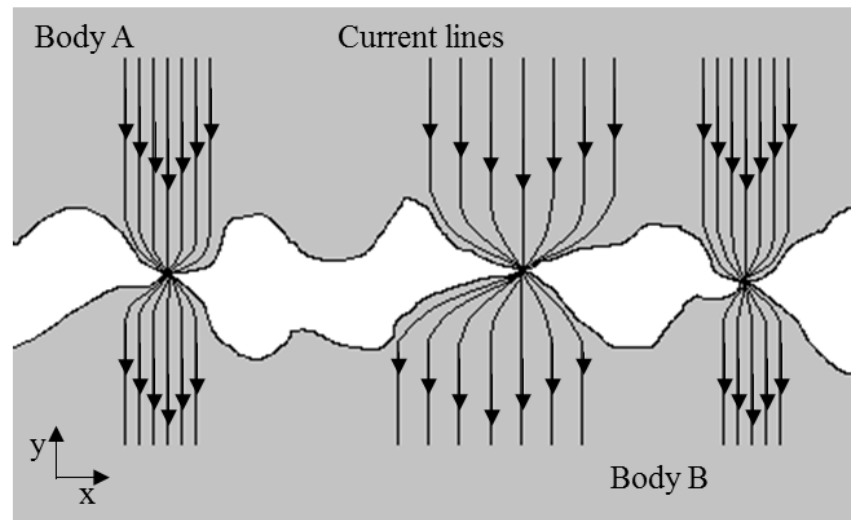


Figure 2.9. Schematic diagram of electric current flowing through contact interface

For a single circular contact spot of radius  $\alpha$ , Holm [20] reported that the contact resistance ( $R_c$ ) is given by Eq. (2.20). Where  $\rho$ , is the average value of the electrical resistivities for the two bodies in contact.

$$R_c = \frac{\rho}{2a} \quad (2.20)$$

For a larger number of contact spots, assuming the electrical resistivity of the two bodies is constant, Eq. (2.20) for a distribution of such radius  $\alpha_i$ ,  $i \in [1, n]$  (where  $i$  is the contact spot of interest and  $n$  is the total number of contact spots) can be written as illustrated in Eq. (2.21). Where  $\bar{\alpha}$ , is the average value of  $\alpha_i$ . According to Ciavarella *et al.* [122] commenting on the work of Jang and Barber [133], it is generally predicted by

fractal contact theories that  $n\bar{\alpha}$  is unbounded with progressive scale refinement which leads to the unlikely conclusion that for a fractal surface the contact resistances due to surface roughness is always zero.

$$R_c = \frac{\rho}{2 \sum_{i=1}^n a_i} = \frac{\rho}{2na} \quad (2.21)$$

Greenwood in [66], reported that if a two scale structure consists of a set of  $n$  actual contact areas of radius  $a_i$  (first scale structure) clustered within a circular ‘‘contour area’’ of radius  $b$  (second scale structure), the contact resistance is well approximated by Eq. (2.22).

$$R_c = \frac{\rho}{2na} + \frac{\rho}{2b} \quad (2.22)$$

Moreover, Greenwood [66] derived a formula for the contact resistance which depends on the distances between the set of circular contact spots. The Greenwood formula of the contact resistance is given by Eq. (2.23). Where  $a_i$ , is the radius of contact spot  $i$ ,  $a_j$  the radius of contact spot  $j$  and  $d_{ij}$  is the distance between the contact spots  $i$  and  $j$ .

$$R_c = \frac{\rho}{2 \sum a_i} + \frac{\rho}{\pi (\sum a_i)^2} \sum_{i \neq j} \frac{a_i a_j}{d_{ij}} \quad (2.23)$$

### 2.3.8 Reliability of electrical contact interface

The essential knowledge of the physics and mechanics of the electrical contact interface and properties of materials helps to achieve better performance and long-term reliability of the devices. MEMS such as switches becoming increasingly common in applications, require low contact resistance [1]. The value of the resistance depends on how good the electrical contact is between the two conductors of the switch. There are

many factors which play important role on how good the electrical contact is which are beneficial to connector users, their suppliers and equipment system design engineers. These factors are the normal-force (force perpendicular to the surface) and the general contact design, the wear and the environmental and electrical parameters [6].

The normal-force and the general contact design are fundamental issues for a good contact so that an acceptable level for the lifetime of the contact could be maintained. The larger the area of contact is, the better the electrical contact in terms of contact resistance is. This relationship is described from Eq. (2.12) and Eq. (2.13).

Wear is an essential factor for the reliability of contact systems as it can cause deterioration at contacting asperities. The wear can be caused by many different factors such as vibration, shock and difference in thermal expansion that can cause motion between the contacting asperities [6].

Environmental factors have an impact on the reliability of contacting asperities [134]. These factors are related to temperature and temperature changes in the application. Relevant to temperature are corrosion, diffusion relaxation and stress. Moreover, pollution in the atmosphere, the presence of pollutants and dust particles as well as the humidity and its alternations have an influence on the reliability of contacting asperities.

Undoubtedly, electrical parameters (voltage, current and frequency) can have a strong effect on the reliability of contacting asperities. According to Holm [20], a conduction through insulating films is caused by the fretting phenomenon at voltages higher than 50V resulting to create the contact less sensitive to insulating layers. Piet van Dijk [6] highlights that at voltages lower than 50V the reliability of contacting asperities is more critical.

Electrical current is very crucial for the reliability of contacting asperities. High currents cause heating at contacting asperities where the materials are softened and welded and the contact is improved [6]. According to Piet van Dijk [6], welding causes extreme wear and compromise the achievable number of mating cycles. Overheating at contacting asperities can be avoided if the constriction and contact resistances are low at high current values. Gagnon [135] showed that the contact resistance behaviour has no

important difference after investigating copper contacting asperities with fretting corrosion under AC and DC currents. If fretting occurs under AC current this leads to the formation of loose, flake-like debris spread at the area of contact, while fretting under DC current is more compacted and surface adhering.

High frequencies (>1GHz) is an issue of interest for the reliability of thermal contacting asperities in the electronics industry to cool the devices operating at these frequencies. Thermal management is essential for microscopic or larger devices [136].

## 2.4 Classification of Electrical Contacts

The electrical contact can be classified according to their surface geometry, nature, design and technology characteristics, application, current load and by other means [23, 137]. The classification of electrical contacts in general can be divided into two main categories: the stationary and moving. Figure 2.10 shows the most general classification of these contacts according to contact kinematics, design characteristics and functionality.

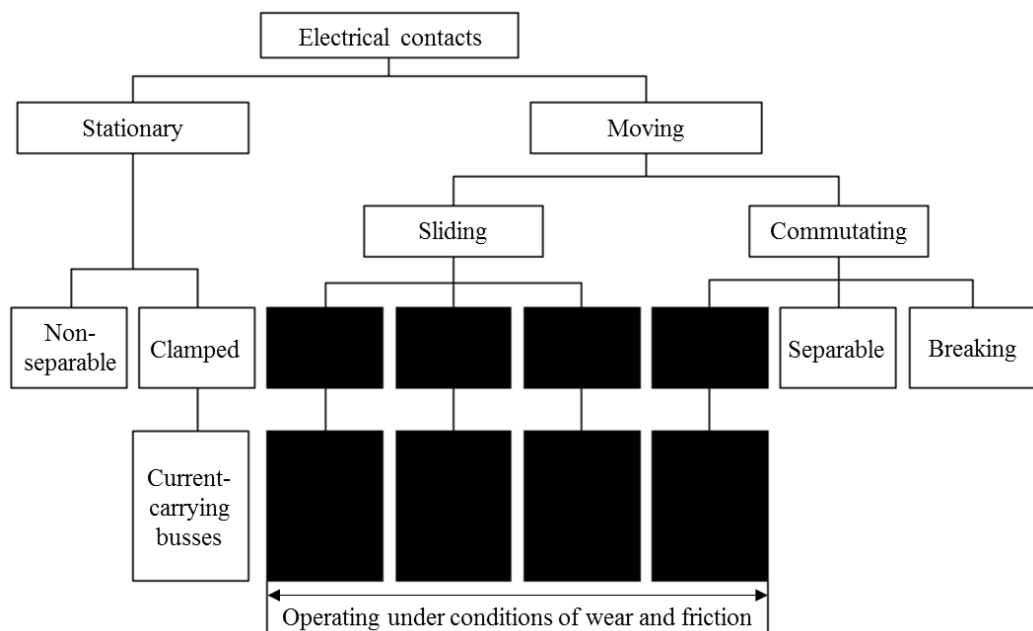


Figure 2.10. Classification of electrical contacts [23]

### 2.4.1 Stationary contacts

The stationary contacts are connected elastically or rigidly to the stationary part of the device in order to provide the permanent connection. The category of stationary

contacts is divided into two sub-categories: non-separable (glued, welded and soldered) and clamped (screwed, bolted and wrapped).

The non-separable contact connections have a high mechanical strength providing low contact transition resistance. Moreover, the connection of this sub-category is often formed within one contact member. For example, in commutating devices, only materials with a complex composition and arc-resistant coating, deposition, electro-spark alloying and mechanical methods of joining [23].

The clamped contacts consist of mechanically joining conductors which are connected directly with screws or bolts or using intermediate parts, like clamps. The contacts of this sub-category may be assembled or disassembled without degrading the connection integrity [23]. A simple way of a clamped contact is the connection of two conductors with a flat contact surface, like bus-bars.

#### 2.4.2 *Moving contacts*

Regarding the moving contacts, commonly one contact part is moving and the other one is static. Depending on their operating conditions the category of moving contacts is divided into two sub-categories: sliding and commutating.

At the sliding contact sub-category, the contact surfaces of the contact parts slide over each other without separation. The electric current flows through the contact region is accompanied by physical phenomena. These phenomena can be electrical and electromechanical and thermal and change the characteristics of the contacting surfaces of the contacting parts. The most important and widely used types of this sub-category of sliding contacts include contacts of electrical transportation machines which are intended to commute electric currents of moderate and high intensity, control systems and automotive systems.

The commutating contacts periodically control the electric circuit and are distinguished between separable and breaking. Separable contact parts are designed in such a way that they can be mated to other contact parts and be separated many times without degrading the connection integrity. The most important and widely used types of



separable contacts include USB sticks, mini-jacks (used for audio signal), kettle style power plugs and sockets.

Breaking contacts are used for intermittently opening and closing of an electrical circuit. The most important and widely used types of breaking contacts include relays, switches, contactors and similar devices.

## **2.5 Conclusion**

In this chapter a review of the origin of electrical contacts is given starting with surface and interface characterisation. In engineering, real surfaces are produced by a variety of material removal processes. According to Archard [74], the total geometry of these real surfaces resulting can be best divided into three categories: form, waviness and roughness. The form describes the macroscopic shape of surface, waviness describes the shape of the surface in microscopic scale and roughness describes the fine detail of the surface in microscopic scale. The most familiar surface roughness parameter is the surface mean roughness and is given by Eq. (2.9). Moreover, the surface mean roughness can be measured using different methods such as STM, small and large scan AFM, SEM, optical profilometry and stylus profilometry.

When two surfaces are brought together their roughness influences mechanical contact which occurs in a specific number of areas on the apparent area. These areas which are a result of mechanical contact are called contact spots and the aggregate of contact spots is called the contact interface. Various approaches have been used to understand the phenomena occurring in a contact interface such as Holm's [120] and Greenwood-Williamson's [63] contact interface models. The models include features such as asperity shape, contact spot number, contact spot distribution, material properties, surface profiles, operation conditions and fractal characteristics (spatial and size distributions).

The mechanical contact is a result of a load force which holds the two surfaces of the contact system in touch. When a load force is applied to a contact system, this results in the change of the shape of the two bodies consisting of the contact system. This result is called deformation and is categorized into elastic, plastic and elastic-plastic.

Electrical contacts provide electrical connection of two conductors. The main objective of an electrical connection is to allow the flow of electric current through the contact interface. The phenomena occurring at the contact interface are important factors in many fields of engineering and the sciences as they are an integral part of all electrical and micro-electronic devices. An understanding of these phenomena is crucial to achieve better performance and long-term reliability of devices constituting such contact interfaces. The most important processes which affect these phenomena include the normal force (force perpendicular to the surface) and general contact design, the wear and environmental (humidity and temperature) and electrical (voltage, current and frequency) parameters.

To sum up, the electrical contacts are classified according to their surface geometry, nature, design and technology characteristics, application, current load and by other means into two main categories: stationary and moving. The category of stationary electrical contacts is divided into non-separable and clamped sub-categories while the category of moving electrical contacts is divided into sliding and commutating sub-categories.

## **Chapter 3 – Visualisation Methods**

### **3.1 Introduction**

Visualisation methods are very important techniques for the contact interface characterisation examining the surfaces before and after they have been joined together. In this chapter the visualisation methods are categorised into destructive and non-destructive techniques.

Destructive techniques such as SEM [138] can be applied if one part of the interface is substituted to enable the viewing of the interface. If both parts of the original contact are to be investigated, then dismantling for analysis results in many of the features of investigation are being destroyed.

Recently, more studies have focused on non-destructive techniques involving Magnetic Resonance Imaging (MRI) and X-ray CT. These techniques offer the possibility to acquire 2D and 3D views of the samples without dismantling the component parts and thus not destroying any features of interest.

Due to the limitation of optical imaging, methods available for the contact interface measurement characteristics are only suitable for open or transparent systems. For most of the practical situations that require contact interface measurement characteristics at microscopic scale in non-transparent or enclosed systems, the traditional visualisation techniques are not effective. Based upon these requirements, a technique suitable for the electrical contact interface characteristics in non-transparent systems is developed by using X-ray CT. In this chapter the X-ray CT technique is analysed and explained in more details compared with the other visualisation techniques.

### **3.2 Destructive Visualisation Techniques**

Destructive visualisation techniques can only be applied if one part of the interface is substituted to enable the viewing of the interface or if both parts of the original contact are used. They are subsequently dismantled after testing for analysis. In the destructive visualisation method there are many techniques such as SEM [138], mass change [139], optical 3D profiler [140], and thermographic [141] that can be used to analyse the contact

interface. Some interesting examples of these destructive visualisation techniques are given below.

McBride [140] used an optical 3D profiler technique to perform an in-situ visualisation of the mechanical area of contact which is formed between a glass (microscope) slice and a metallic spherical component. Moreover, the use of this technique for low force (10 mN) enabled McBride to demonstrate a near linear relationship between contact force and mechanical area of contact showing predominantly plastic deformation at these force levels.

Myers *et al.* [141] visualised the contact area using a Thermographic Technique (TT) and calculated the current density distribution in the contact area. They used a hemispherical geometry metal which was in contact with a thin conductive film. The conductive film was set on a polished surface of Si material which is transparent in the infrared wavelength range (8 – 12  $\mu\text{m}$ ) used by the thermal camera. The thermal camera was used in combination with a 4x microscope lens. Since the TT cannot be used in contact metallic materials because of their low emissivity values, a carbon layer was used to coat the surface between the Si and conductive film.

### **3.3 Non-Destructive Visualisation Techniques**

Non-destructive visualisation techniques (such as MRI and X-ray CT) are of more interest in contrast with destructive visualisation techniques because they offer the opportunity to acquire 2D and 3D views of samples without dismantling the component parts and thus destroying any features of interest. Some interesting examples of these non-destructive visualisation techniques are given below.

Zhu *et al.* [142] used MRI to show the effectiveness of this technique for the visualization of transparent and non-transparent components measuring the internal contact angles between solids and liquids. A drawback of the MRI technique is that the sample shouldn't include ferrous materials (e.g. Fe and Ni) because of interaction with the applied high magnetic fields.

Johnson *et al.* [143] have also used the MRI technique to visualize the radio-lunate and radio-scaphoid joints within a human body. The acquired images of the technique

were used to create model geometry and kinematics for the calculation of peak contact pressures and average contact pressures, contact forces and contact areas.

The usefulness and importance of X-ray CT technique as a medical diagnostic tool is widely known but also it has been an important research tool for a wide variety of engineering subjects. Material research medical CT, micro CT, and since very recently nano CT are being used as evaluation techniques for engineering and geology purposes [144].

The X-ray CT technique has been used much more than the MRI technique in engineering and analysis of samples such as by Popovich *et al.* [145] and Green *et al.* [146]. Popovich *et al.* [145] used it to characterize the internal microstructure in multi-crystalline silicon solar cells. Green *et al.* [146] used the technique to calculate the contact area of gas/liquid and liquid “holdup” in structured packing.

Zschech *et al.* [37] reported that the function of the X-ray CT is to qualify and quantify any inner or outer dimension in a smooth, non-destructive process. Failure localization can be investigated in micro and nano electronic structures by the use of this technique. It has the capacity to visualise voids and residuals in on-chip metal interconnects without physical modification of the chip. The importance of synchrotron radiation experiments is essential to study procedures and materials implemented in the semiconductor industry. Moreover, Lalechos and Swingler [147] used the X-ray CT technique to identify the contact spots which are in mechanical contact without dismantling the specimens and produced a “2D Contact Map” of portion of areas of the electrical contact interface. From the contact maps much information can be extracted such as the area and the number of contact spots, the distance between them and the total contact resistance using appropriate models [147-149].

### **3.4 X-ray CT in Engineering and the Sciences**

#### *3.4.1 The use of the X-ray CT*

According to the International standards concerning X-ray CT [150], X-ray CT is a radiographic investigation method which is useful when the examination of a specimen aims to identify, locate and size planar and volumetric details in three dimensions. X-ray

CT permits the non-destructive physical and (in some limited cases) chemical characterisation of the internal structure of materials. Furthermore, unlike other investigation techniques (such as SEM and TT) X-ray CT can be used to investigate both, metallic and non-metallic specimens, solid and fibrous metals or smooth and irregularly surfaced objects. When used in conjunction with other non-destructive visualisation techniques such as ultrasound, X-ray CT can provide evaluations of material integrity that cannot currently be achieved non-destructively by any other means.

#### 3.4.2 *Historical use*

X-ray CT was initially used for medical diagnosis, now it has been used in gamma and X-radiation applications in order to identify some physical characteristics of wood, soils and other materials. These characteristic include density, mass attenuation coefficients, water content and soil particles sizes [151, 152].

The British engineer of Electrical and Musical Instruments (EMI) laboratories, Godfrey Hounsfield, developed the first X-ray CT system in 1972 [153]. In the same year, in Atkinson Morley hospital in Wimbledon, UK, the first X-ray CT system was installed, put in use and the first patient brain-scan was achieved. The invention of the X-ray CT technology attracted the interest of researchers. In the process, Jim Elliott developed the first micro X-ray CT system with higher resolutions at the beginning of the 1980s. The evaluation of the 3D micro-structure of trabecular bone was an issue of research which was achieved with the first micro X-ray CT invented by Feldkamp *et al.* [154-156]. A reconstructed slice of a small tropical snail, with pixel size about 50  $\mu\text{m}$ , were the first micro-tomographic (micro-cross-section slice) images published [157]. The invention of synchrotron radiation facilities, micro X-ray CT with resolutions of 1  $\mu\text{m}$  and the ongoing development of X-ray CT system, facilitated the investigation of different materials and objects.

#### 3.4.3 *X-radiation*

X-radiation (which consists of X-rays) is a form of electromagnetic radiation. Most X-rays have a wavelength between  $0.01 \times 10^{-9}$  m to  $10 \times 10^{-9}$  m corresponding to frequencies in the range of  $3 \times 10^{16}$  Hz to  $3 \times 10^{19}$  Hz and energies in the range of

$0.1 \times 10^3$  eV to  $100 \times 10^3$  eV. The wavelengths of the X-rays are shorter than those of ultraviolet rays and typically longer than those of gamma rays.

According to the Beer-Lambert law if a narrow beam of X-ray photons passes through some homogeneous material of a sample, the beam intensity is observed to decrease in accordance with Eq. (3.1). This effect is illustrated in Figure 3.1(a). Where  $I_0$ , is the incident intensity and  $I'$  is the final intensity. The intensity gives the number of photons per second per unit cross-section area. The attenuation coefficient vector  $\mu$  depends on both the density of the material of the sample and the nuclear composition characterized by the atomic number.

$$I' = I_0 \cdot e^{-\mu y} \quad (3.1)$$

If the X-ray beam passes through two different materials, distance  $y_1$  through medium 1 characterised by  $\mu_1$  and distance  $y_2$  through medium 2 characterised by  $\mu_2$ , the fractional decrease in intensity is given by Eq. (3.2). For several media the relation is given by Eq. (3.3) and described by Figure 3.1(b).

$$I' = I_0 \cdot e^{-\mu_1 y_1 - \mu_2 y_2} \quad (3.2)$$

$$I' = I_0 \cdot e^{-\sum_n \mu_n y_n} \quad (3.3)$$

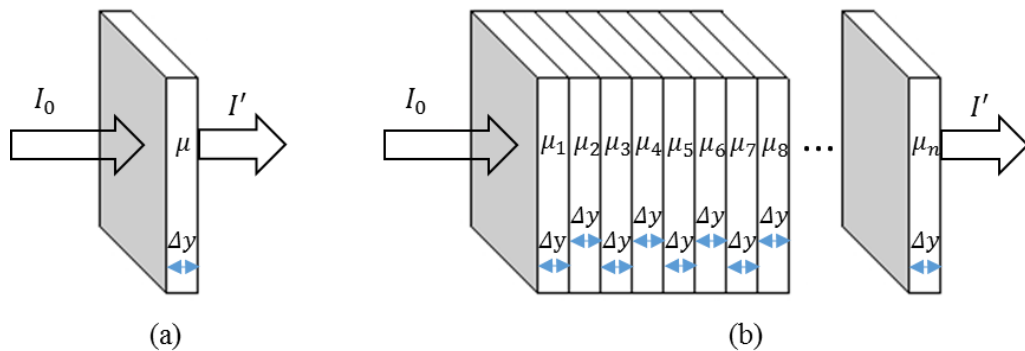


Figure 3.1. The effect of different absorption layers on the intensity of an X-ray beam

### 3.4.4 Basic operation of X-ray CT

X-ray CT has applications in both medical and industrial imaging. In general, there are two types of X-ray CT set-ups. Concerning the first set-up, much more like in an engineering X-ray CT, is based on the fact that the X-ray source and detector are typically stationary during the scan while the sample rotates. Regarding the second set-up, much more like in a clinical X-ray CT, is based on the fact that the sample is stationary in space while the X-ray source and detector rotate around.

A typical set-up of an engineering X-ray CT is illustrated in Figure 3.2. This technique requires X-rays to pass through an object in various different directions in order to obtain 2D tomography images (cross-section slice images). For each path of the X-ray transmission through the sample (see Figure 3.2(a), where a sample is rotated), there will be a particular level of interaction between the X-ray photons and atoms of the sample [158]. This results in an alteration of the X-ray intensity unique to that path.

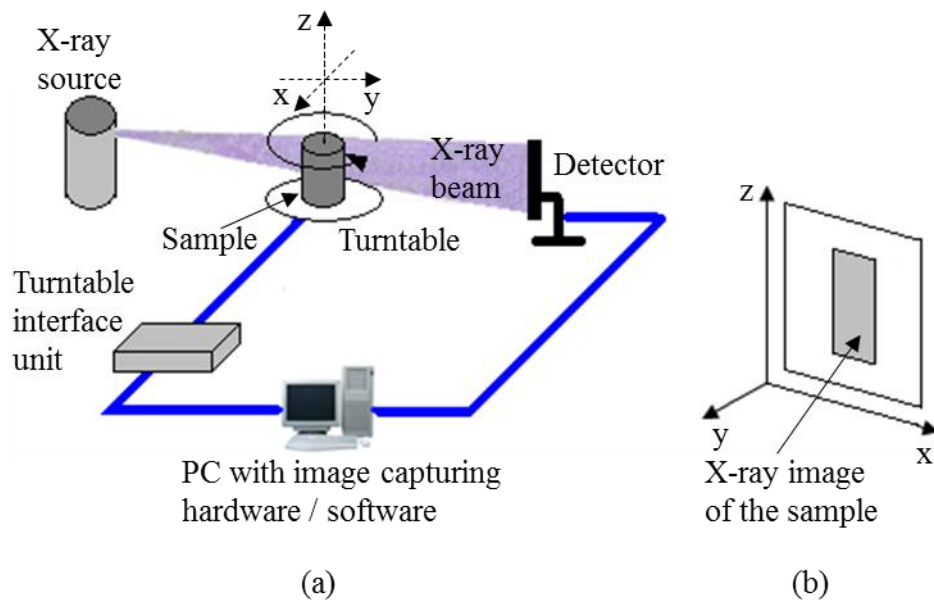


Figure 3.2. (a) Basic principle of X-ray CT, (b) Detector

X-ray absorption by matter has long been described by the famous Beer-Lambert law [159, 160]. According to this law, intensity data can be converted into an image which represents differences in X-ray attenuation in the specimen. The Beer-Lambert law relates the incident intensity  $I_0$  and the final intensity  $I'$  (at point  $(x, z)$  on the detector for a given



value of angle  $\theta$ ) through the sample's attenuation coefficient vector  $\mu$ , an intrinsic characteristic of the specimen, given by Eq. (3.4). Where  $y$ , is the distance coordinate along the X-ray path,  $ds$  is an element of length along the X-ray path and  $\mu(x, y)$ , are the values of the attenuation coefficient vector at the point  $(x, y)$ .

$$I'_{\theta}(x, z) = I_0 \cdot e^{-\int_0^y \mu(x, y) ds} \quad (3.4)$$

In Figure 3.2, the X-ray source emits the X-ray beam, which passes through the sample. During the rotation of the object at equally angularly spaced intervals, X-ray images are acquired. For example, Figure 3.3 illustrates the X-ray beam transmitting through a cross section of the sample. The X-ray photons which are transmitted in the direction shown by the arrow are considered to be a part of the beam. During the transmission of the beam, photons are constantly lost from the beam. This is due to the fact that they are either absorbed or scattered. A constant attenuation coefficient vector  $\mu$  accounts for both losses at each point.

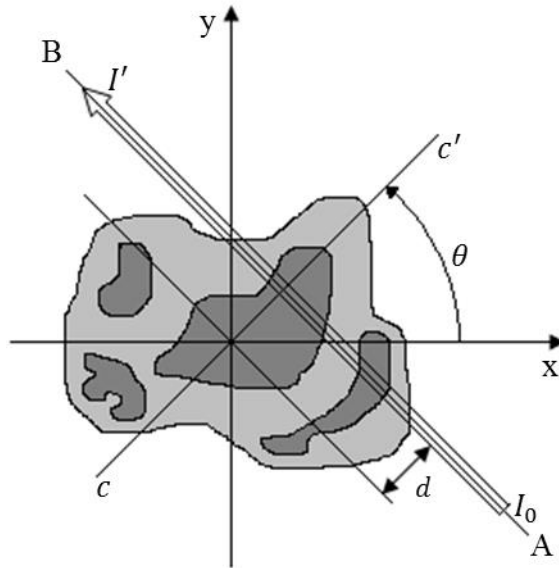


Figure 3.3. X-ray beam transmitting through a cross-section of the sample

A line AB, running through the sample in Figure 3.3 is called a ray while the integral along the sample is called a ray integral. A projection is formed by a set of ray integrals.

From Eq. (3.4),

$$\ln\left(\frac{I_0}{I_\theta(x, z)}\right) = \int_0^y \mu(x, y) ds \quad (3.5)$$

and the line integral AB in Figure 3.3 can be defined as

$$P_\theta(d) = \int_{rayAB} \mu(x, y) ds = \ln\left(\frac{I_0}{I_\theta(x, z)}\right) \quad (3.6)$$

The function  $P_\theta(d)$ , as a function of  $(d)$  (for a given value of angle  $\theta$ ) determines the projection of a sample for angle  $\theta$ .

X-ray CT records several hundreds or thousands of projections typically through  $180^\circ$  or  $360^\circ$  and consequently an even larger number of ray paths. This logged data are used during the reconstruction process as algorithms [161].

### 3.4.5 Image reconstruction

X-ray CT systems are supported with many different software packages which can load the 2D X-ray images of the sample and process them. This process consists of three main steps.

The first step of the process is the development of 3D (x-y-z) volume of X-ray images. The 3D volume of X-ray images is generated by “stacking” of each acquired 2D (x-z) X-ray image in the y-direction. The x-y cross-section slice images of the 3D volume of X-ray images are called projections (or sinograms). It is important to note that all 2D (x-z) X-ray images of the sample are acquired from the detector by rotating the turntable at equally spaced intervals.

The second step of the process is the development of 3D reconstructed volume. The software packages use different reconstruction algorithms in order to create the 3D

reconstructed volume of the sample. The reconstruction algorithms deal with the reconstruction of an image from its projections.

The final step of the process is to extract tomographic (cross-section slice) images from the 3D reconstructed volume. This whole process is described in Figure 3.4 and an analytical mathematical description is followed.

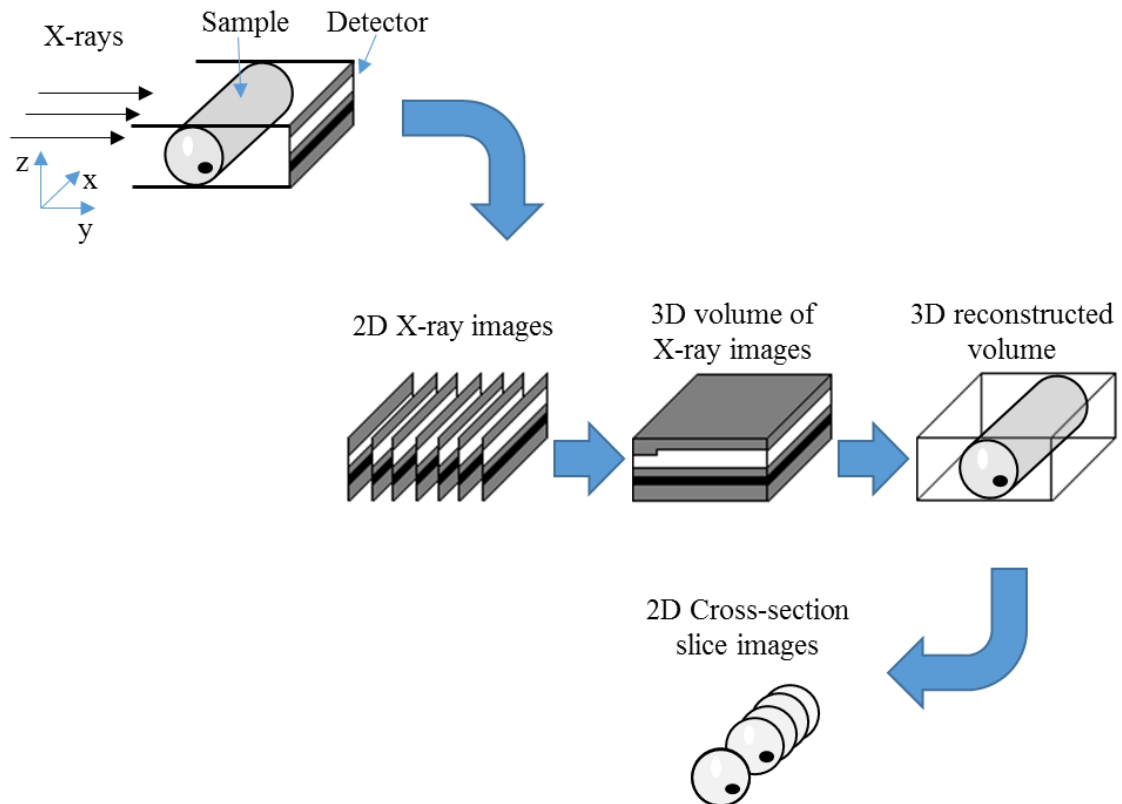


Figure 3.4. X-ray CT process

According to the definition, image reconstruction from projections is “the process of producing an image of a 2D distribution from estimates of its line integrals along a finite number of lines of known locations” [162]. A pre-processing is needed before the image reconstruction takes place as it makes use of the fact that X-rays attenuate as they propagate through the sample. According to this pre-processing, it is important to define ray integrals. Figure 3.5 shows the relationship between the measured projections of the sample for three different angles (each projection represents different angle). Each point of the projection is equal to the sum of sample along a ray (line integral) passing from that point. A projection is formed by combining the set of rays.

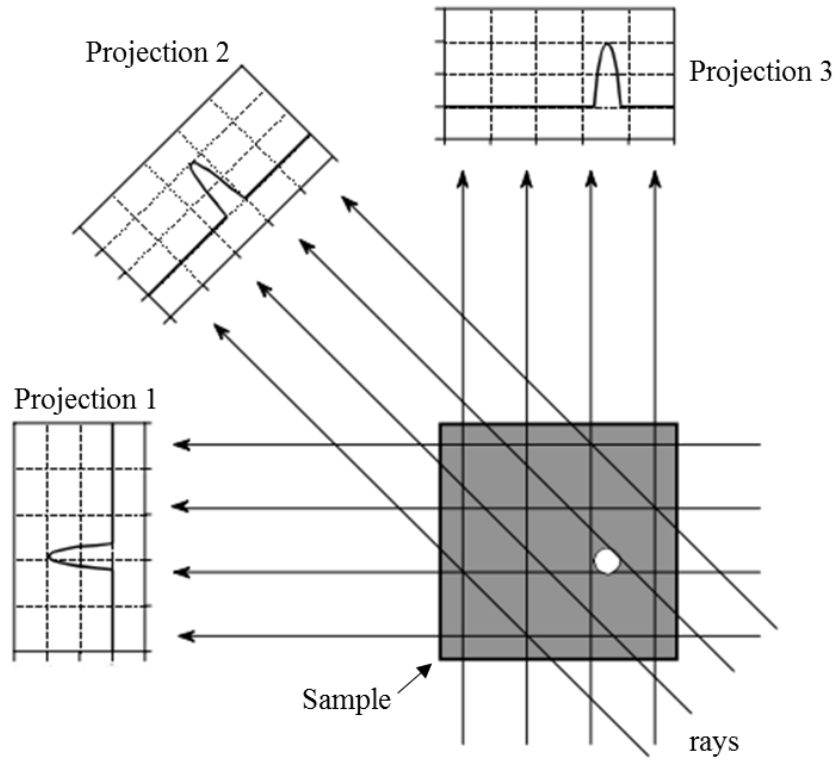


Figure 3.5. Projections are taken by measuring the rays of the sample for three different angles [163]

There are four main methods to calculate the tomographic (cross-section slice) image of the 3D reconstructed volume given the set of its projections. These methods are called reconstruction algorithms. The first method is based on solving many equations. This method is totally impractical, but gives a better understanding of the problem. According to Rosenfeld and Kak [164], mathematically the problem of reconstructing an image may be stated as following: The  $f(x,y)$  in Figure 3.6 represents a 2D function and a mathematical definition of a ray integral (line AB) can be found by using Eq. (3.7). Where  $d$ , is the perpendicular distance of the line AB from the origin of the axes.

$$d = x \cdot \cos(\theta) + y \cdot \sin(\theta) \quad (3.7)$$

Consequently, the ray integral of the function  $f(x,y)$  along the line AB may be define as described in Eq. (3.8). Where  $\delta$ , is Dirac's delta function [165, 166].

$$P_{\theta}(d) = \int_{rayAB} f(x,y) ds = \int_{-\infty}^{\infty} \int_{-\infty}^{\infty} f(x,y) \delta(x \cdot \cos(\theta) + y \cdot \sin(\theta) - d) dx dy \quad (3.8)$$

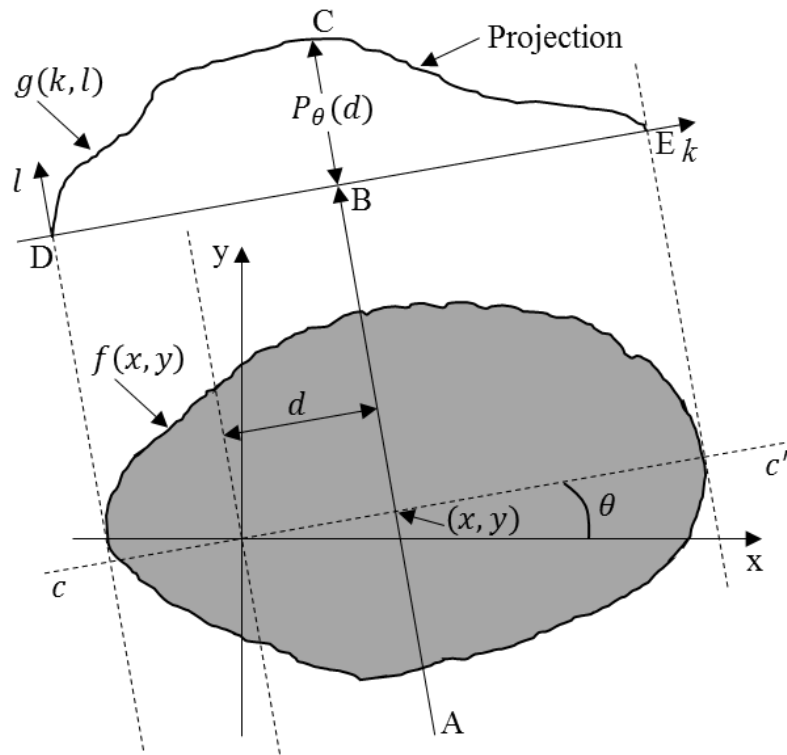


Figure 3.6. The function  $g(k, l)$  describes the projection of the function  $f(x, y)$  at angle  $\theta$

The function  $P_\theta(d)$  as a function of  $d$ , (for a given value of angle  $\theta$ ) determines the value of the projection of the function  $f(x, y)$  through the line AB for angle  $\theta$  at point C. The function  $g(k, l)$  is the projection of the function  $f(x, y)$  for angle  $\theta$  which is called the Radon transform. The projection is formed by combining the set of ray integrals between the points D and E.

One equation can be written for each ray integral. The number of ray integrals (or equations) is equal to the area of the detector in pixels. For example, if the detector size is  $512 \times 512$  pixels, the number of the ray integrals that should be calculated for each projection is 262144. Reconstructing an image, the detector takes some hundred projections so this number is multiplied with some hundred projections and the result gives a large number. The problem with this method of image reconstruction is computation time.

The second method is based on iterative techniques which calculates the cross-section slice image in small steps. According to Smith [163], there are several variations of this method: the algebraic reconstruction technique, simultaneous iterative

reconstruction technique and iterative least squares technique. The difference between these methods is how the successive corrections are made: ray by ray, pixel by pixel or simultaneously correcting the entire data set respectively.

The most simple method of iterative reconstruction is the algebraic reconstruction technique [167]. According to this [163], all the pixels in the image array are set to some arbitrary value. Subsequently, the iterative procedure is used gradually to change the image array in order to correspond to the profiles. The cycle of iteration consists of looping through each of the calculated data points. In the process, the calculated sample is compared with each value of the ray integrals. According to Smith [163], the comparison is stated as follows: If the value of the ray integral is higher than the calculated sample's value, all of the pixels values on the ray are decreased and if the value of the ray integral is lower than the calculated sample's value, all the pixels on the ray are increased in value. By the end of the first iteration cycle, there is an error between the values of ray integrals and the sample calculated value. The reason to this error is because the changes made for each calculation disrupts all the previous corrections made. A solution to decrease this error is to repeat the iterations until the image converges to the proper solution.

The third method for the calculation of the cross-section slice image of the 3D reconstructed model is the back-projection. This method reconstructs an image by taking each projection of the sample and "smearing" it along the path it was originally obtained [163]. The final back-projected image is taken as the sum of all the back-projected projections as illustrated in Figure 3.7(b). The resulting image (cross-section slice image) of the back-projection method is illustrated in Figure 3.7(b). Compared with the correct image of the sample (Figure 3.5) is blurry. The problem with the blurry image is solved using the filtered back-projection.

The filtered back-projection reconstructs an image by filtering each projection before back-projection. Using this, the blurring which is illustrated in simple back-projection (Figure 3.7) is removed resulting in a mathematically exact reconstruction of the image. The filtered back-projection is illustrated in Figure 3.8. Moreover, it is important to mention that the filtered back-projection is the most commonly used method for X-ray CT systems.

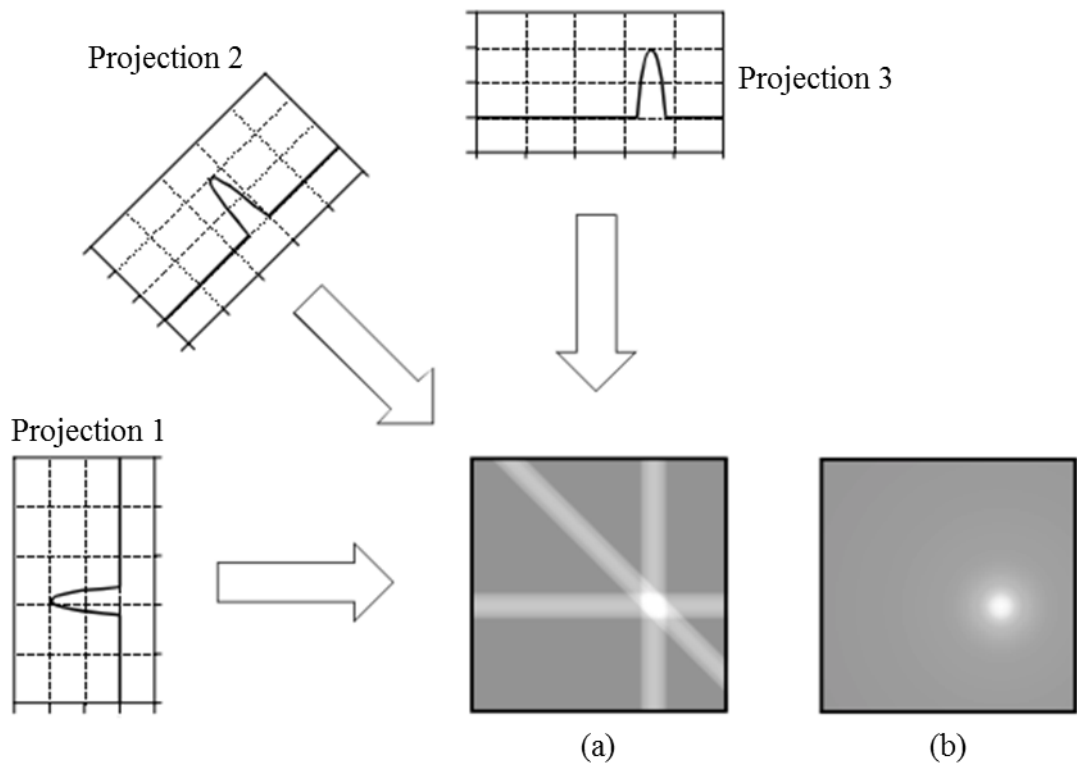


Figure 3.7. Back-projection. Sample cross-section slice image using (a) 3 projections and (b) many projections [163]

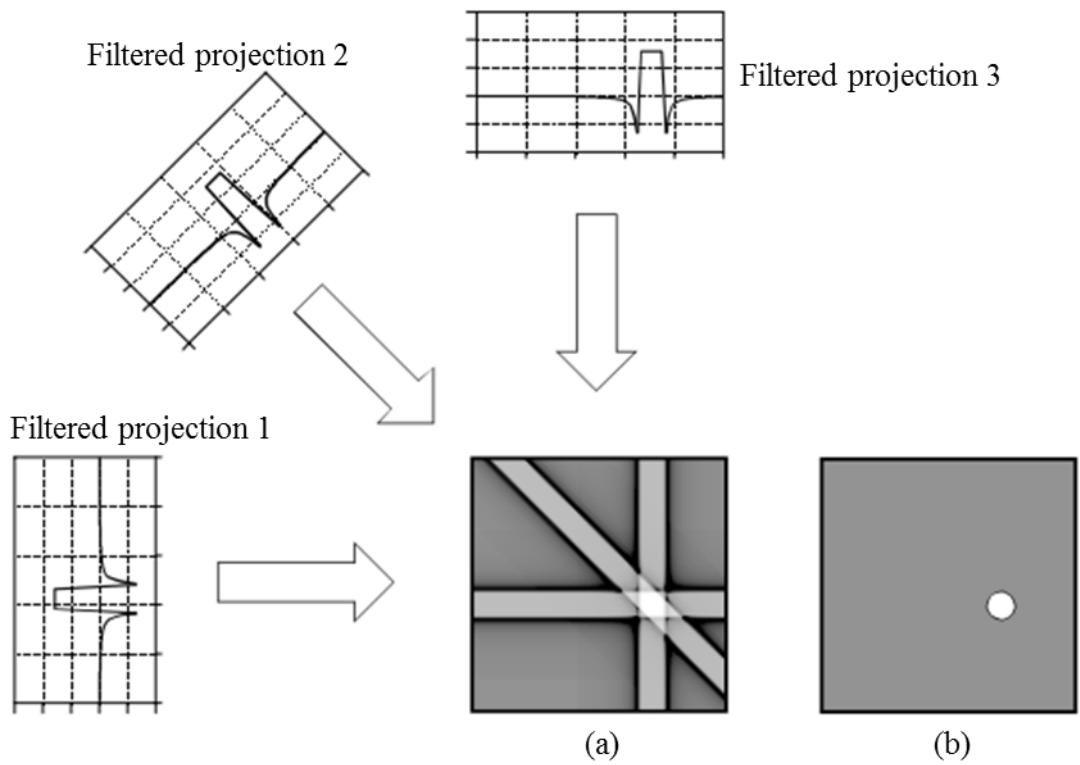


Figure 3.8. Filtered back-projection. Sample cross-section slice image using (a) 3 projections and (b) many projections [163]

The fourth method for the calculation of the cross-section slice image of the 3D reconstructed model is based on the Fourier slice theorem. According to Smith [163], this theorem describes the relationship between the sample and its projections in the frequency domain. In the spatial domain, each projection is found by calculating the ray integrals at a given angle. In the frequency domain, the spectrum of each projection is a 1D ‘‘slice’’ of the 2D image spectrum. Figure 3.9 shows the sample with its projections in the spatial domain and the image of the sample in the frequency domain.

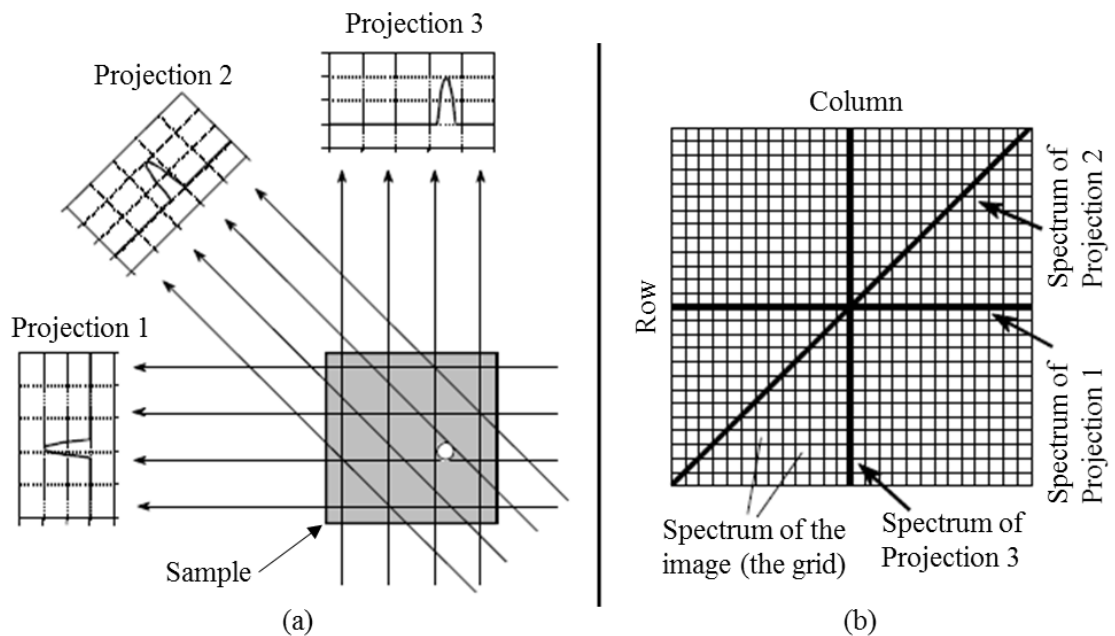


Figure 3.9. Fourier slice theorem in (a) spatial domain and (b) frequency domain [163]

The final step of the X-ray CT process is to extract tomographic (cross-section slice) images from the 3D reconstructed volume. There are many different 3D graphic software packages which can load the 3D reconstructed volume and extract from it 2D cross-section slice images from any direction (x-y, x-z or y-z). More details concerning the extraction of 2D cross-section slice images from the 3D reconstructed volume are given in Section 4.4.5.

### 3.4.6 Quality of the X-ray CT scan

The quality of the X-ray CT scan depends on the quality of the reconstructed cross-section slice images. The image quality is a characteristic of an image which measures



perceived image degradation (typically, compared to a perfect or ideal image) and depends on many factors. These include the image acquisition system, the amount of noise, the sharpness, the tone reproduction and colour.

The quality of the cross-section slice images in X-ray CT depends on five main factors: the resolution of the detector, the distance of the turntable from the X-ray source, the input power of the X-ray source (power of the X-ray beam) and the rotation angle steps of the turntable as well as the size and the material(s) of the sample. For example, the closer the sample is located against the X-ray source and the lowest the angle steps of the turntable, the higher resolution of the cross-section slice images of the X-ray scan.

According to the definition, image resolution is the capability to measure the smallest object with distinct boundaries in the image. The smallest object is called a pixel. The X-ray CT can typically achieve resolutions in the range of 1-20  $\mu\text{m}$  without processing or adding additional steps to the scan guide illustrated in Figure 3.10.

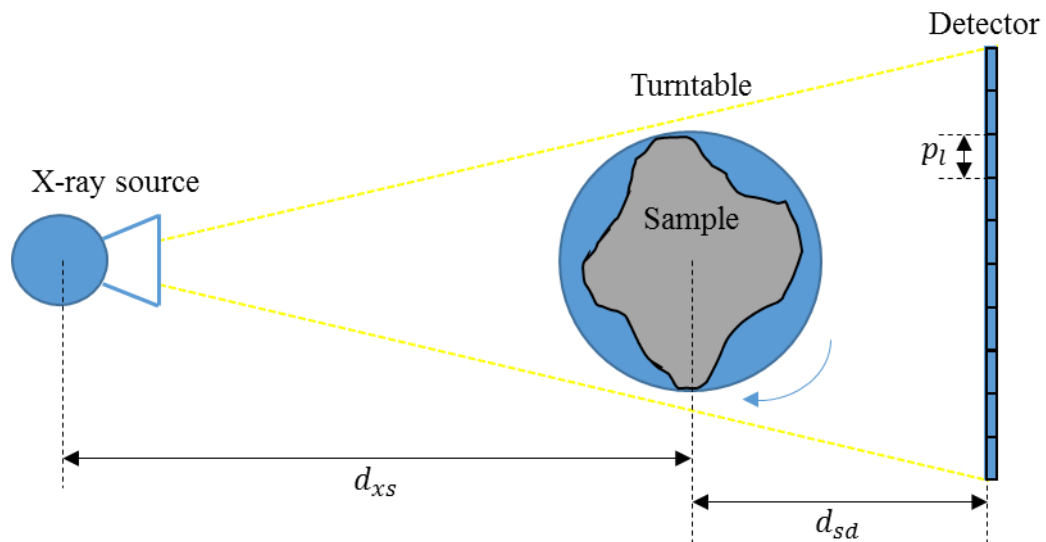


Figure 3.10. X-ray source, turntable and detector arrangement

The detector type defines the magnification and the detail level. Typically, there are three types of detectors:  $512 \times 512$  pixels,  $1024 \times 1024$  pixels and  $2048 \times 2048$  pixels. Figure 3.11 shows three images of the same size ( $d \times d$  pixels) and different resolution. The higher of a detector size in pixels and the smaller size of pixel, the higher the potential resolution of the image. However, larger detectors increase the size of the scan data

exponentially and the processing of such data could take from hours up to weeks for a simple scan [7]. Therefore, a larger detector should be used only when very high resolution is needed.

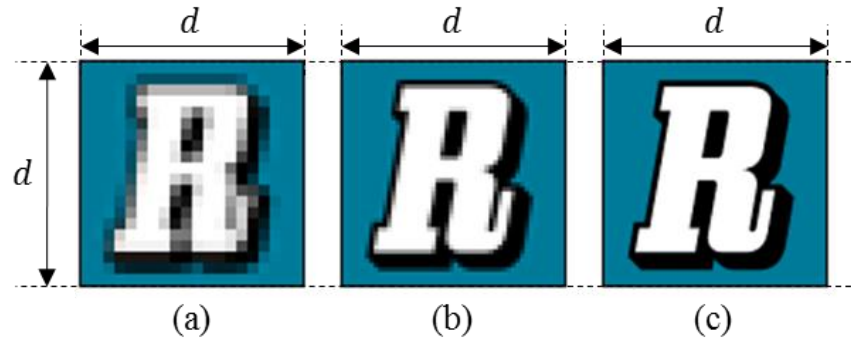


Figure 3.11. Image resolution in pixels. (a)  $20 \times 20$ , (b)  $50 \times 50$  and (c)  $100 \times 100$

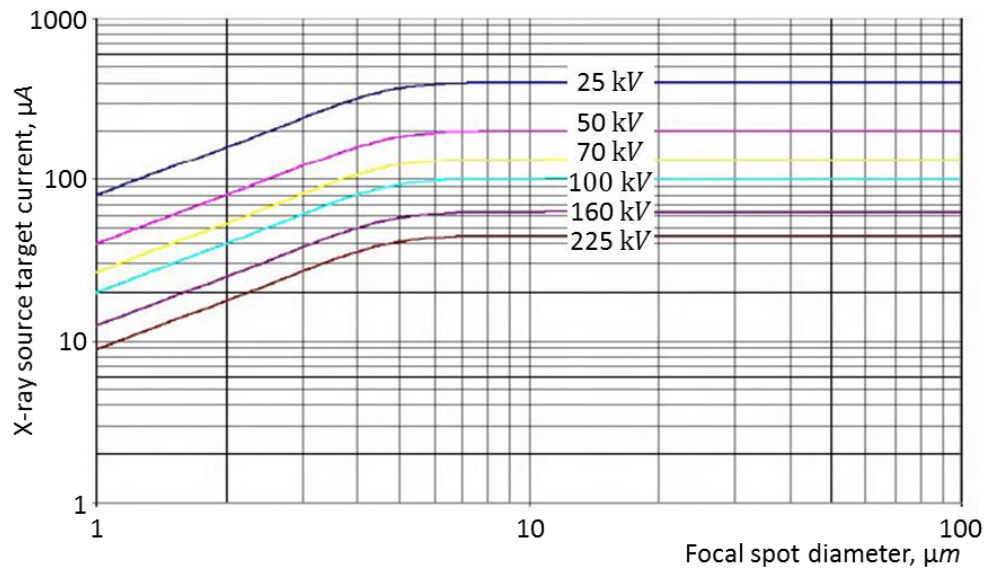
According to Paulus *et al.* [168], if the detector is limited by the pixel length  $p_l$ , the projection image blurring due to the finite pixel length may be described by a Gaussian function with standard deviation as given by Eq. (3.9). Where  $d_{xs}$ , is the distance between the X-ray source and the sample and  $d_{sd}$  is the distance between the sample and the detector (Figure 3.10). It is apparent from Eq. (3.9) that reducing the detector pixel length while also positioning the sample closer to the X-ray source improves the resulting resolution.

$$\sigma_d \approx \left( \frac{d_{xs}}{d_{xs} + d_{sd}} \right) \cdot \frac{1}{2p_l} \quad (3.9)$$

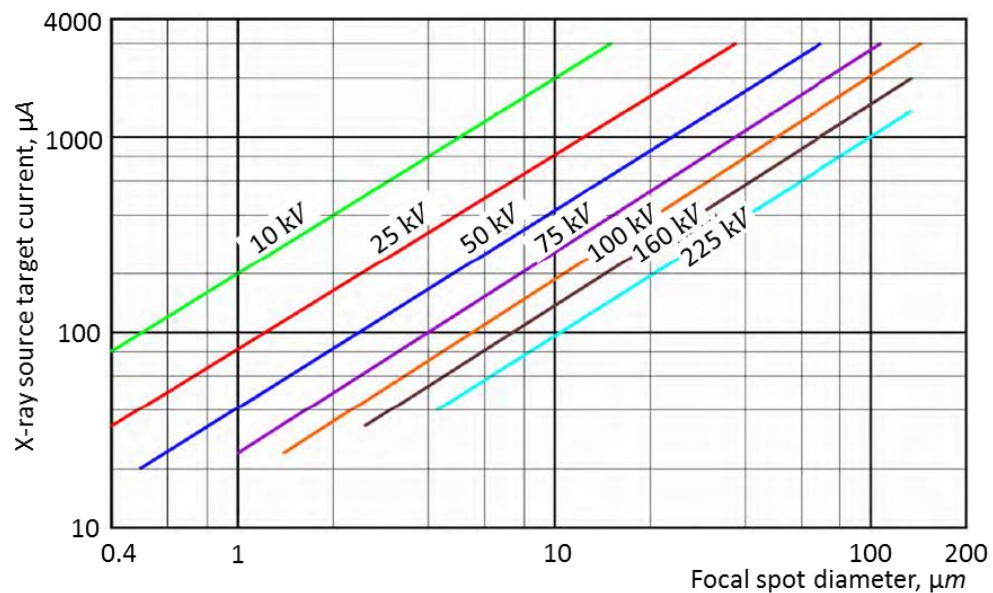
Moreover, the focal spot size also affects the resolution as depends on the input power (current and voltage) of the X-ray source. Figure 3.12 illustrates this result for two different X-ray sources. Most of the X-ray CT systems allow the target of the X-ray source to be changed easily to match the type of application and the sample scanned. An example of these X-ray sources are the multi-focus and micro-focus.

The multi-focus X-ray source unit [169] represents a basic tool for high definition X-ray CT systems suitable for detail recognition down to the nano and micro range as

well as for high power operation. Multi-focus X-ray source unit is being employed with considerable success for numerous applications in the field of non-destructive testing and components inspection. Some examples are: the inspection of solder joints in production of printed circuit boards, the inspection of micro-mechanical parts and electro-mechanical components and the testing of micro-porosity and micro-inclusions in ceramic components.



(a)



(b)

Figure 3.12. X-ray source power loadings. (a) Multi-focus [169], (b) Micro-focus [170]

The micro-focus X-ray source unit [170] represents a basic tool for micro X-ray CT systems suitable for detail recognition down to the micro range as well as for high power

operation. The micro-focus X-ray source unit is being employed with considerable success for numerous applications in the field of non-destructive testing and components inspection. Some examples are: the welding inspection, the inspection of micro-mechanical parts and electro-mechanical components and the improvement of casting methods for light metal casting.

The rotation angle steps of the turntable play an important role in the quality of the reconstructed cross-section slice images as they set the number of the acquired projections. The smaller angle step of the turntable for a full rotation ( $360^\circ$ ) is, the higher number of projections occur. Figure 3.13 shows as the number of projections are increased the quality of the image is increasing too as the sample is illustrated in more detail.

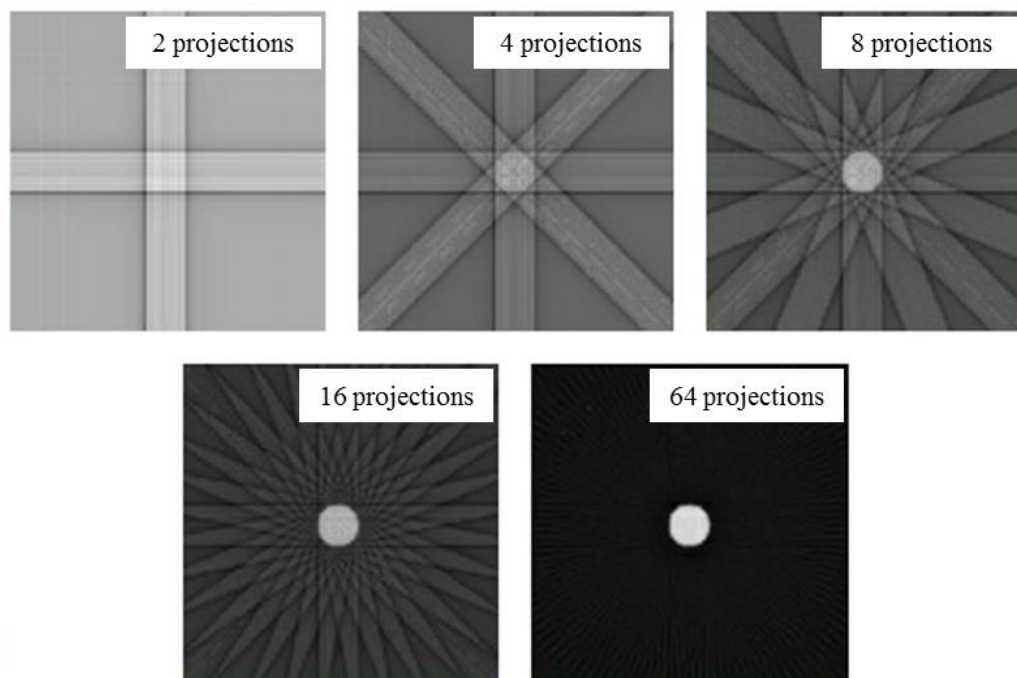


Figure 3.13. Cross-section slice image for different number of projections using back-projection method

The size and construction material of the sample is another main factor which plays an important role on the quality of the cross-section slice images. Different materials due to their density contrast and the long path length through them could cause some noise and shadowing in their cross-section slice images. This effect can be more clearly seen on the 3D model around the sample. For example, if comparing the cross-section slice

images and the 3D model of a metal sample with a rock sample, the amount of noise and shadowing of the rock sample is zero or negligible in contrast to the metal sample.

#### *3.4.7 Artifacts*

Artifacts are false information (voxel(s) or groups of voxels) which may appear on the 3D reconstructed volume. The existence of artifacts is not easy to detect. Frequently, they are integrated within the surface on the 3D reconstructed volume and the most common form of an artefact is beam hardening.

The attenuation coefficient vector  $\mu$ , is highly dependent on low energy X-rays. As the X-ray beam passes through the sample, the lower energy X-rays are absorbed at the surface of the sample causing the measured voxels numbers to be higher near the edges of the sample [7]. Various techniques have been developed in order to reduce the amount of artifacts [171-173]. However, great care must be taken before extracting 2D cross-section slice images from the 3D reconstructed volume, to ensure that no visible artifacts exist [174].

### **3.5 Conclusion**

Visualisation methods are very important techniques for the contact interface characterisation. In this chapter, the visualisation methods are categorised into destructive and non-destructive. Non-destructive visualisation methods are of more interest in contrast to the destructive visualisation methods as they offer the opportunity to acquire 2D and 3D views of the samples without dismantling the component parts and thus destroying any feature of interest.

Recent advantages in X-ray CT in hardware and software make it an indispensable high-resolution non-destructive visualisation technique. This research will attempt to introduce innovative techniques, which makes use of the capabilities of X-ray CT for the investigation of electrical contacts as well as their extensions to the two conductors which the contact system consists of.

## **Chapter 4 – Methodology**

### **4.1 Introduction**

The selection of the suitable contact system to be analysed with an X-ray CT and the use of the appropriate settings in X-ray CT scanning, and generally a strong experimental methodology, helps to achieve best results in experimental data for the visualisation and characterisation of the contact interface. This chapter refers to the factors that should be considered for the selection of the contact system, to the characteristics and structure of the selected contact system as well as to the X-ray CT system which is used for the collection of the experimental data. The post-processing and analysis of the experimental data is also included.

### **4.2 Selection of Contact System**

First of all, for the selection of the contact system the limitations of the X-ray CT system should be considered. These limitations include the dimensions and the weight of the contact system. The X-ray CT system used in this current project has a maximum scanning area of  $250 \times 330 \text{ mm}^2$  and allows samples with weight up to 50 kg.

Another factor that should be considered for the selection of the suitability of a contact system is the material of its conductors and the amount of the metalwork. Different materials due to their different density contrast and the long path length through them cause different amount of noise and shadowing in the experimental data. For example, conductors made of steel or copper cause more noise and shadowing in the experimental data compared with conductors made of aluminium. Moreover, the more amount of metalwork of the contact system exists, the more noise and shadowing in the experimental data appears.

According to the above considerations, in this research a single pole rocker switch is selected as a suitable contact system for investigation. More of interest of this selection is the fact that the area around the contact interface between the conductors of the single pole rocker switch is covered keeping it hidden from the human eye. This coverage around the area of contact interface shows the possibility of the X-ray CT technique to visualise the internal characteristics in non-transparent or enclosed contact systems

without the need to dismantle them. More information concerning the single pole rocker switch and its electrical, mechanical and material characteristics are given in Section 4.3.

### 4.3 The Selected Contact System

The term switch in electrical engineering is the electrical component that can break an electrical circuit, interrupt the current or divert it from one conductor to another. The electrical contacts which occur between the conductors of the single pole rocker switch are classified in the category of breaking contacts (see Figure 2.10).

The single pole rocker switch which is used in this current work is rated at 250 V, 16 A Alternative Current (AC) and its schematic diagram is illustrated in Figure 4.1. It consists of conductors and a contact force spring. The contact material is made of a silver alloy and other conductors are made from copper alloy. The geometry of the contact pair is a flat on flat with surface mean roughness,  $R_a = 0.42 \pm 0.11 \mu\text{m}$  for Conductor A and  $R_a = 0.25 \pm 0.04 \mu\text{m}$  for Conductor B. The surface roughness test was carried out using a contact profilometer Taylor-Hobson RTH Talysurf 5-120 with a lateral  $x$  resolution of  $0.1 \mu\text{m}$  and height  $y$  resolution of  $0.1 \text{ nm}$ . The contact force is found to be  $1.89 \pm 0.07 \text{ N}$  and the bulk resistance across the contact pair was found to be  $\sim 0.27 \text{ m}\Omega$  using the “four-wire” method. The dimensions of the single pole rocker switch are given in Figure 4.2.

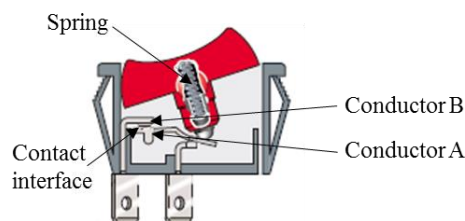


Figure 4.1. Schematic diagram of the single pole rocker switch [175]

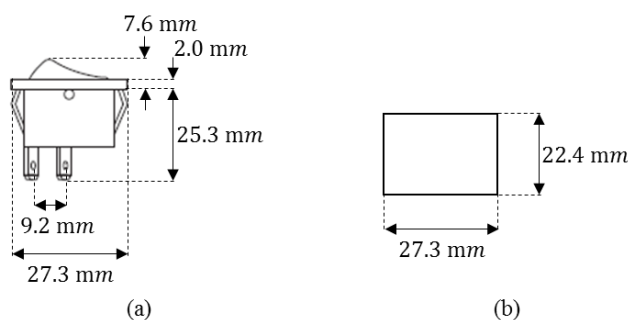


Figure 4.2. Dimensions of the single pole rocker. (a) Side-view [175], (b) Top-view

In this research, the same 250 V, 16 A rated AC single pole rocker switch is scanned four times under different AC current loading tests (accelerated testing at 0 A, 16 A, 32 A and 64 A). These current loading tests are selected in order to investigate the contact interface and its structures of the 250 V, 16 A rated AC single pole rocker switch at no-current (0 A) as well as at three multiples of the switch rated current (multiples of multiples 16 A: 16 A, 32 A and 64 A). These different current loading tests are categorised into normal operation and non-normal operation. The normal operation includes the current loading tests at 0 A and 16 A as the single pole rocker switch is rated at 16 A AC. The non-normal operation includes the 32 A and 64 A current loading test as these current values are out of the single pole rocker switch current limits.

The first scan (0 A) is conducted after non-current loading, the second is conducted after current loading at 16 A for 24 hours, the third is conducted after current loading at 32 A for 24 hours and the fourth is conducted after current loading at 64 A for 2 hours (the switch was not current loaded for more than 2 hours as the heat of the current would damage it). After each scan the switch is stored in the lab for approximately one month.

#### **4.4 Experimental Equipment – X-ray CT**

##### *4.4.1 Equipment characteristics*

An HMX 225 X-ray CT system scanner is used in this research which operates using an X-ray tomography designed by the X-Tek Systems Limited Group (Hertfordshire, UK). HMX 225 X-ray CT is a high performance real-time X-ray inspection system for general non-destructive testing. The X-ray CT system scanner which is used in this research is located at Abertay University, Dundee, UK and illustrated in the photo of Figure 4.3.

The equipment is capable of resolving details down to 3  $\mu\text{m}$  and with magnifications up to 160x. Defects can be rapidly located, zooming in for detailed analysis. As the sample is moved towards the x-ray source, the geometric magnification continuously increases from approximately 1x (close to the detector) to 160x (touching the x-ray source).

The source accelerator voltage ranges are up to a maximum of 160 kV or 225 kV. Concerning the voltage ranges up to a maximum of 160 kV is for general-purpose use,



ideal for plastics, PCB's, light alloys, small assemblies and organic or biological samples. At the maximum voltage of 160 kV it can penetrate 15 mm steel. The voltage ranges up to a maximum of 225 kV can perform all the above plus heavier castings, welds and high-density alloys [176].

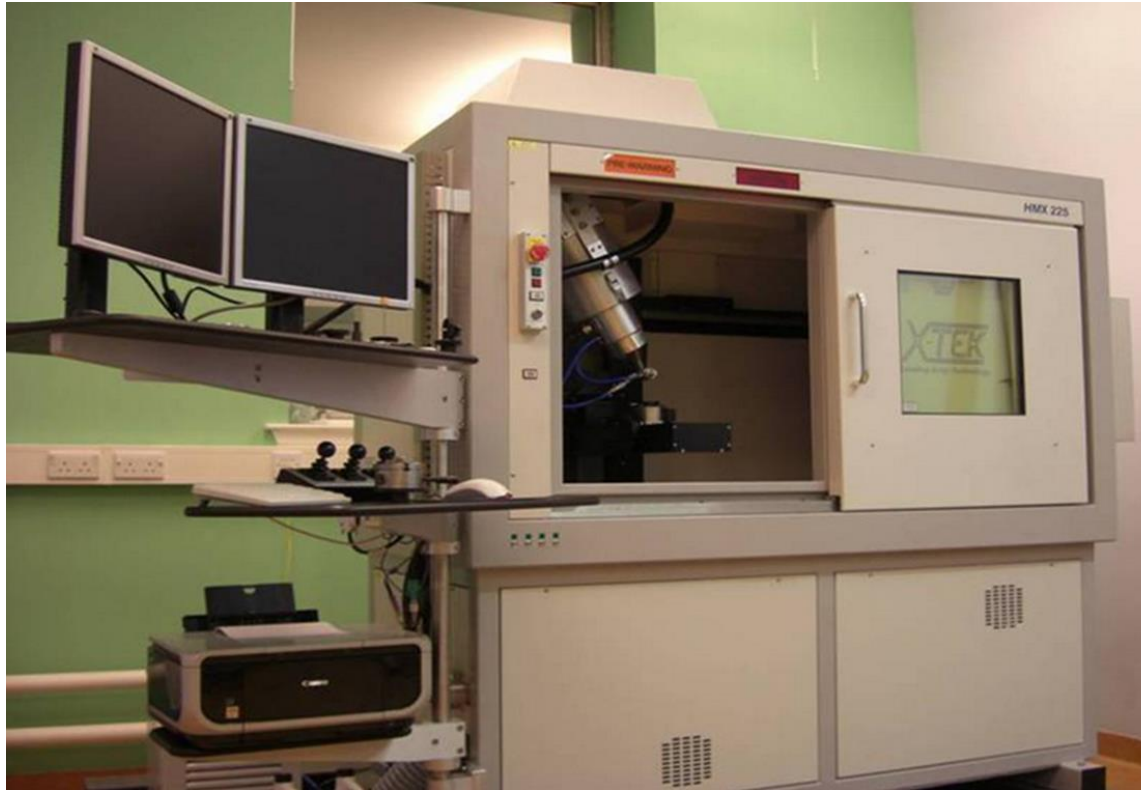


Figure 4.3. HMX 225 X-ray CT system scanner (Abertay University, Dundee, UK) [177]

Moreover, the sample can be manipulated on the turntable with four axes of freedom, whilst continuously viewing the image on a monitor. There are four turntables rated at 5 kg, 15 kg, 30 kg and 50 kg which are dependent on sample weight and required precision. All turntables provide three linear axes and two rotational axes, to view the sample at any angle. The turntable is normally controlled by variable speed joysticks. Additionally, it can also be program controlled via the rack-mounted industrial computer [176].

For each scan, the voltage and current were set to ensure that the X-rays were transmitted through the sample, making sure that the optimal contrast was achieved (no saturation of the image occurred and the dynamic range of the detector was fully utilized). Focusing on the X-ray beam for the specific voltage and current combination was

performed automatically, in addition to black, white and bad pixel reference imaging. For the acquisition of high resolution 2D X-ray images, the sample was rotated 360° with the optimal number of increments being dependent on the required resolution. The 2D X-ray images are acquired using a 1920 × 1536 pixels, 16-bit CCD camera (detector).

For the 3D reconstructed volume, the equipment uses the “CT-Pro” software which is using the 2D X-ray images as input. There are many different 3D graphic software packages which can load the 3D reconstructed volume and process it. The X-Tek Systems Limited Group, the manufacturer of the X-ray CT system scanner used, recommends and supplies with the X-ray CT system scanner the “VGStudioMax” software which can create 2D cross-section slice images from the 3D reconstructed volume.

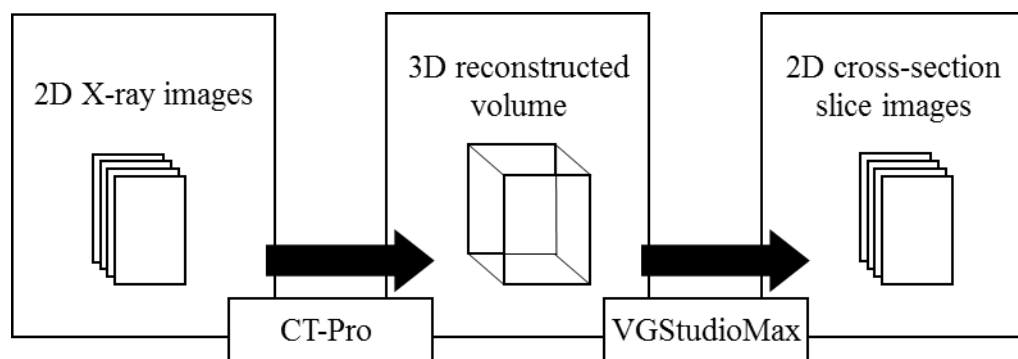


Figure 4.4. Installed softwares along with the equipment [75]

#### 4.4.2 Test environment

The X-ray CT system scanner used in this research is located in a room with a constant temperature of 20 °C in order to minimise any side effects caused by exogenous environmental factors. This eliminates any unwanted thermal expansion within the sample and therefore avoids changes at the surface of the scanned contact interface. Moreover, the X-ray CT system scanner is installed with precaution for vibration transmitted from the environment and it utilises a build vibration compensation system.

#### 4.4.3 X-ray CT system configuration to ensure a good quality of scan

The X-ray CT scanning procedure consists of several stages. For the best optimum results with the selected X-ray CT system scanner, before the scanning of the sample, the

factors which are analysed in Section 3.4.6 for the quality of the X-ray CT scan should be considered.

In order to maximize the resolution of the scanned images, the first factor that should be considered is to scan only the smallest area of interest. To achieve this, the turntable is moved closer to the X-ray source. The distance between the sample and the x-ray source  $d_{xs}$ , and the distance between the sample and the detector  $d_{sd}$ , are measured to be 41.08 mm and 958.92 mm respectively. These measurements are made automatically from the CT-Pro software and saved as a \*.xtekc file.

The selection of the correct input power (voltage and current) of the X-ray source is another factor that should be considered in order to achieve X-ray images with high quality images. The X-ray CT was used at high current and high voltage mode. The current level is responsible for the control of brightness of the 2D X-ray image because it is necessary to avoid very dark or saturated 2D X-ray images. The voltage level is used in order to configure the appropriate power of the X-ray beam. The required power is variable and depends on the type of material used [7].

All materials have the nature to absorb the X-ray beam; some highly X-ray beam absorbing and some other less X-ray beam absorbing. Typical examples of highly X-ray beam absorbing are copper and steel and of less X-ray beam absorbing are the silver and aluminium [7]. Therefore, before the scan, the appropriate voltage and current levels must be selected in order to avoid saturation and at the same time to ensure that enough power is used for the X-ray beam to penetrate the material(s) of the sample. If the power of the X-ray beam is lower than required, then, it will not be able to penetrate the material(s) of the sample. The 2D X-ray images will be darker and the full dynamic range of the detector will not be utilised. This would result in low quality 2D X-ray images [7].

The materials which are more X-ray beam absorbing require an X-ray beam of higher voltage level to be scanned properly. On the contrary, the materials which are less X-ray beam absorbing require an X-ray beam of lower voltage level to be scanned properly. It is apparent that in order to acquire images (both, 2D X-ray images and 2D cross-section slice images) with high quality resolution, it is crucial to use materials that tend not to absorb the X-ray beam (low-density materials) [7]. To optimise the X-ray CT scanning

process, the conductors of the selected contact system (sample in Section 4.3) are made of a small percentage of copper alloy and the rest percentage are made of silver alloy.

Generally, in order to achieve images with high quality and maximum resolution with a given X-ray CT system scanner, the following guidelines should be usually applied [7]: to scan only the smallest area of interest, select voltage level and current level carefully and select samples which consist of materials with low X-ray beam power absorbing. It is apparent that it is not always possible to take on-board all these requirements in the guidelines. However, it is crucial that the X-ray CT scanning process does not deviate significantly from these guidelines, otherwise the results of the scan (2D X-ray images and 2D cross-section slice images) will be of lower quality and possibly not usable.

#### *4.4.4 From 2D X-ray images acquisition to 3D reconstructed volume*

For each X-ray CT scan the X-ray source is set to 175 kV, 133  $\mu$ A which gives 23.28 W input power and offering the best results. Both voltage and current values are close to the maximum possible settings of the available equipment. The X-ray CT equipment rotates the sample (which is placed on the turntable) through 360°, taking a series of 2D X-ray images. The step-angle rotation of the turntable is set to 0.1476° resulting in acquiring 2439 2D X-ray images. All the acquired 2D X-ray images are 16-bit grayscale \*.tif files with dimensions of 1920  $\times$  1536 pixels (the 1920 pixels are in x-direction and the 1536 pixels are in z-direction). An example of these 2D X-ray images is illustrated in Figure 4.5 where the two conductors and the spring of the 16 A rated AC single pole rocker switch can be clearly seen.

The 16-bit grayscale images consist of 65536 different levels of greyscale (or colours) in the range between 0 and 65535. The colour with value 0 is 100% black and colour with value 65535 is 100% white. All the other colour values in the range between 0 and 65535 (0 and 65535 are not included) are shades of grey.

The 2D X-ray image of the 16 A rated AC single pole rocker switch in Figure 4.5 shows how the X-ray beam is absorbed at different points through the sample. The brighter areas are for lower X-ray beam absorption while the darker areas are for higher X-ray beam absorption. For example, the colour intensity variation can occur because

during the X-ray CT scanning several layers of different components/materials appear across the direction of the X-ray beam. On a 2D X-ray image, all the scanned components are shown on a single layer. This implies that no distinction can be made between the front, middle, rear or any of the in-between points of the sample across the direction of scanning [7].

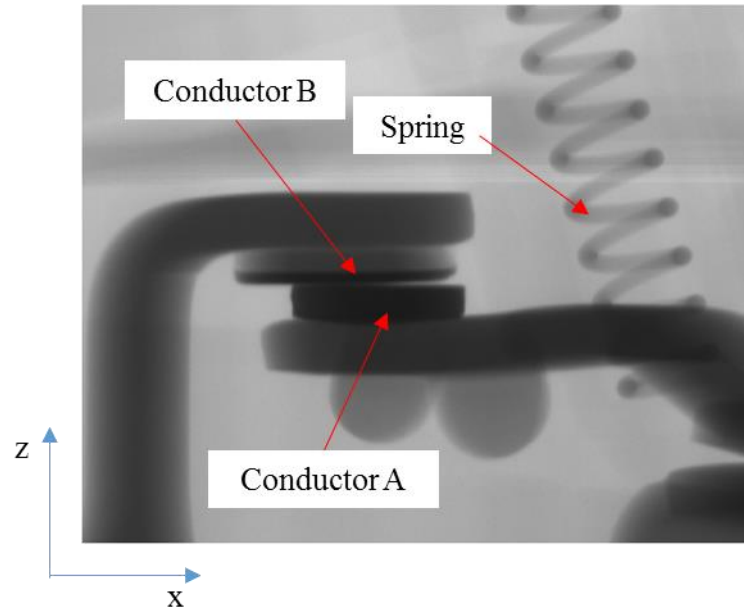


Figure 4.5. 2D X-ray image of the 16 A rated AC single pole rocker switch

As mentioned before, the detector of the X-ray CT scanner system acquires a 2D X-ray image for each step-angle rotation of the turntable until the turntable makes a full rotation of  $360^\circ$ . When the full rotation of the turntable is completed and the final 2D X-ray image is acquired from the detector the 3D volume of X-ray images and the 3D reconstructed volume of the sample can be created. The 3D reconstruction software (in this research the CT-Pro software) combines all the 2D (x-z) X-ray images by “stacking” them with the sequence which are acquired in the y-direction in order to develop the 3D volume of X-ray images.

As mentioned in Section 3.4, the x-y cross-section slices of the 3D volume of X-ray images are called projections (or sinograms). An example of these projections of the 3D volume of X-ray images is illustrated in Figure 4.6. All the projections are 16-bit grayscale \*.tif files with dimensions of  $1920 \times 2439$  pixels (the 1920 pixels are in x-direction and the 2439 pixels are in y-direction). The number of pixels in y-direction is equal with the total number of 2D X-ray images. The Figure 4.7 illustrates the position of

the 2D X-ray image of Figure 4.5 and the position of the projection of the Figure 4.6 in the 3D volume of X-ray images.

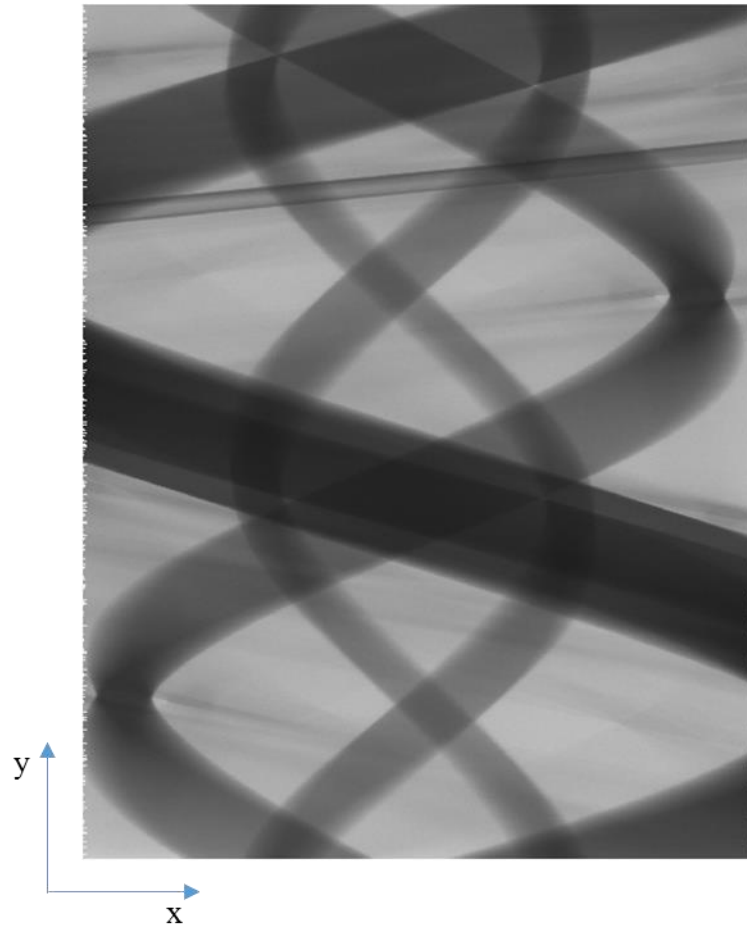


Figure 4.6. Projection of the 16 A rated AC single pole rocker switch

When the 3D volume of X-ray images is developed, the 3D reconstruction software uses the reconstruction algorithms in order to create the 3D reconstructed volume of the sample from the 3D volume of X-ray images. The 3D reconstructed volume is saved as 32-bit floating point \*.vgi file with dimensions of  $378 \times 407 \times 676$  voxels. The procedure of the 3D reconstructed volume development is fully automated for the user. The 3D reconstructed volume of the 16 A rated AC single pole rocker switch is illustrated in Figure 4.8 which the spring and the two conductors can be clearly seen.

CT-Pro software uses the 32-bit floating point because it is useful for certain arithmetic and filtering operations. Unlike all other image classes, a floating point image does not have a fixed intensity range [178]. The lowest value in the image is displayed as black, and the highest value in the image as white. The histogram of the Figure 4.9

illustrates the colour distribution of the voxels which consist of the 3D reconstructed volume of Figure 4.8. The colour of the voxels are in the range between the -1.19513 and 2.11417.

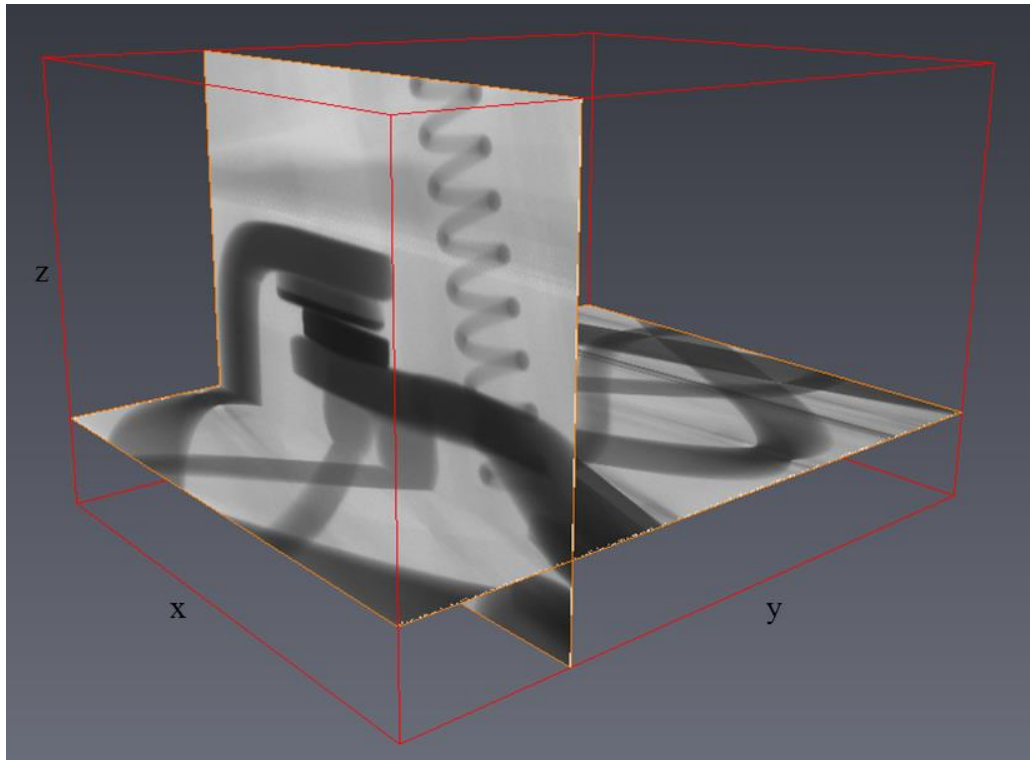


Figure 4.7. Positions of the X-ray image and the projection in the 3D volume of X-ray images

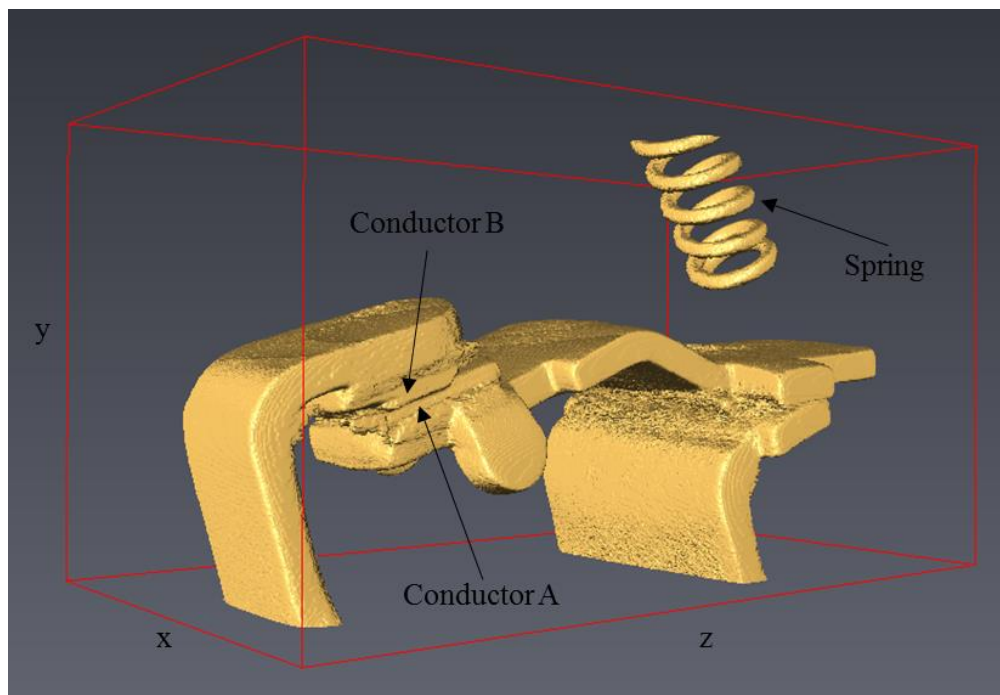


Figure 4.8. 3D reconstructed volume of the 16 A rated AC single pole rocker switch

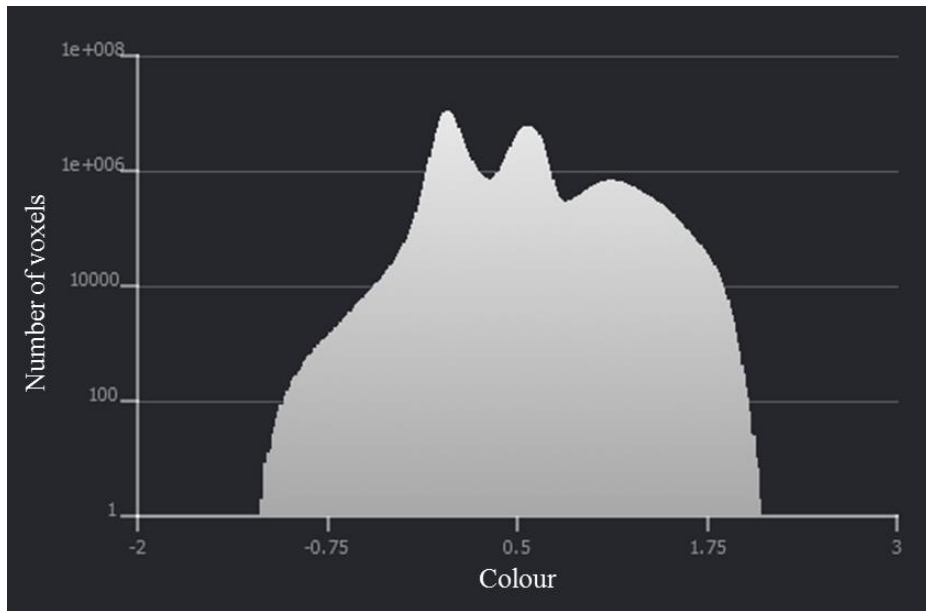


Figure 4.9. Colour histogram of the 3D reconstructed volume

#### 4.4.5 From 3D reconstructed volume to 2D cross-section slice images

There are many different 3D graphic software packages which can load the 3D reconstructed volume and process it. The X-Tek, the manufacturer of the X-ray CT system scanner used, recommends and supplies with the X-ray CT system scanner the VGStudioMax software.

The VGStudioMax software allows the 3D reconstructed volume to be processed using filters (if needed to improve the quality of 3D reconstructed volume). In this research the filters were not used as they might have affected the 3D reconstructed volume (filters add or remove voxels in order to enhance the resolution of 2D cross-section slice images). Moreover, the VGStudioMax software can be used to extract 2D cross-section slice images from the 3D reconstructed volume using the algebraic reconstruction technique (see Section 3.4.5) [176]. The extraction of the 2D cross-section slice images could be achieved from any direction (x-y, x-z or y-z).

For the extraction of 2D cross-section slice images from the 3D reconstructed volume, the user must specify the required number of images and the VGStudioMax software will save equally spaced 2D cross-section slice images on the hard drive of the computer. When extracting 2D cross-section slice images it is important to select the required number carefully. For simplicity and to avoid losing or processing too much



information, the total number of 2D cross-section slice images must be equal to the number of voxels of the volume across the horizontal axis of the selected direction.

When the automated function of the VGStudioMax software is used to extract the 2D cross-section slice images, all the names of the images include a sequential numbering. For example, if the 2D cross-section slice images are saved as with name “switch”, the 1<sup>st</sup> 2D cross-section slice image (image towards the front of the sample) would be saved as switch1, the 100<sup>th</sup> as switch100 and the last, N<sup>th</sup> as switchN. The sequential numbering of the 2D cross-section slice images is required in order to identify the part of the scanned sample that each 2D cross-section slice image represents.

Practically the 2D cross-section slice images are an “internal” conventional grayscale images of the scanned sample. When the automated function of the VGStudioMax software is used to extract 2D cross-section slice images, there is an option to select the bit-depth and the type for the candidate “stack” of the 2D cross-section slice images to save. Some of the bit-depths which included in the option are the 8-bit and 16-bit signed and unsigned grayscale images. Moreover some of the types which are included in the option are the \*.tif, \*.jpeg, \*.jpg and \*.bmp.

In this research, for each scan the extraction of 2D cross-section slice images from the 3D reconstructed volume was made by extracting 676 2D (x-y) cross-section slice from the z-direction. These 2D cross-section slice images are saved as 16-bit unsigned grayscale \*.tif files.

The Volume Graphics, the manufacturer of the VGStudioMax software used, recommends if the X-ray CT system scanner has 32-bit floating point as an output (3D reconstructed volume) and the X-ray CT system scanner is not capable of dealing with this amount of data to choose data of 16-bit unsigned bit-depth [176]. The X-ray CT system scanner used in this research is not capable of dealing with data of 32-bit floating point having as a result on 2D cross-section slice images to save as 16-bit unsigned grayscales. The 16-bit grayscale unsigned images consist of 65536 different colours in the range between 0 and 65535. The histogram of the Figure 4.10 illustrates the colour distribution of the pixels for all the 16-bit grayscale unsigned 2D cross-section slice images.

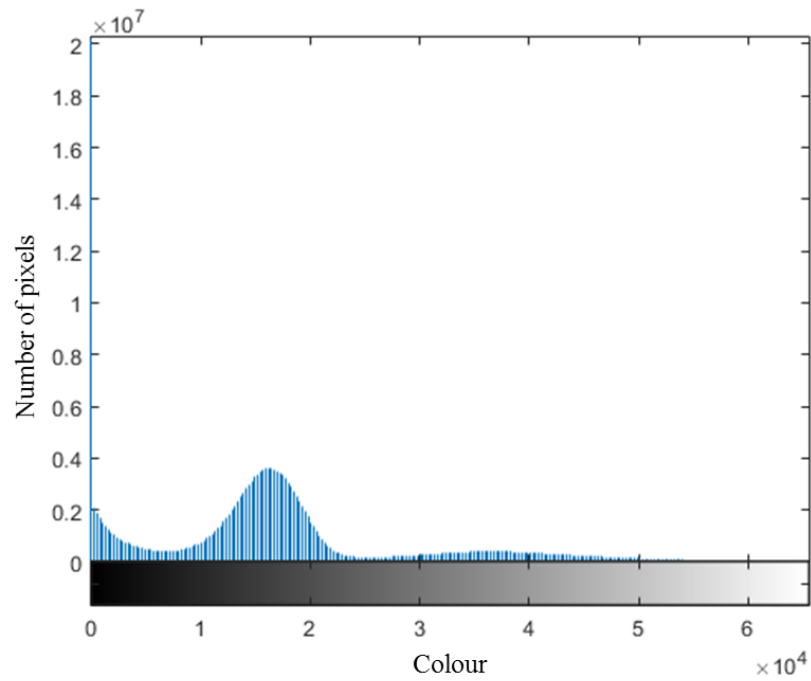


Figure 4.10. Colour histogram of the 2D cross-section slice images

An example of a 16-bit unsigned grayscale 2D (x-y) cross-section slice image is illustrated in Figure 4.11 (more analysis of this figure follows in Section 4.5). The dimensions of the 2D cross-section slice images are  $378 \times 407$  pixels (the 378 pixels are in x-direction and the 407 pixels are in y-direction). The position of the 2D cross-section slice image of Figure 4.11 in the 3D reconstructed volume is illustrated in Figure 4.12. The dimensions of the bounding box of 3D reconstructed volume of Figure 4.12 are  $407 \times 378 \times 676$  voxels.

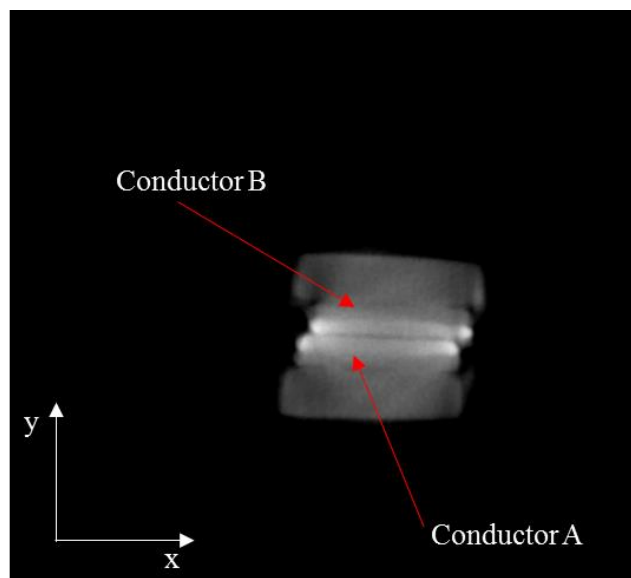


Figure 4.11. 2D cross-section slice image of the 16 A rated AC single pole rocker switch

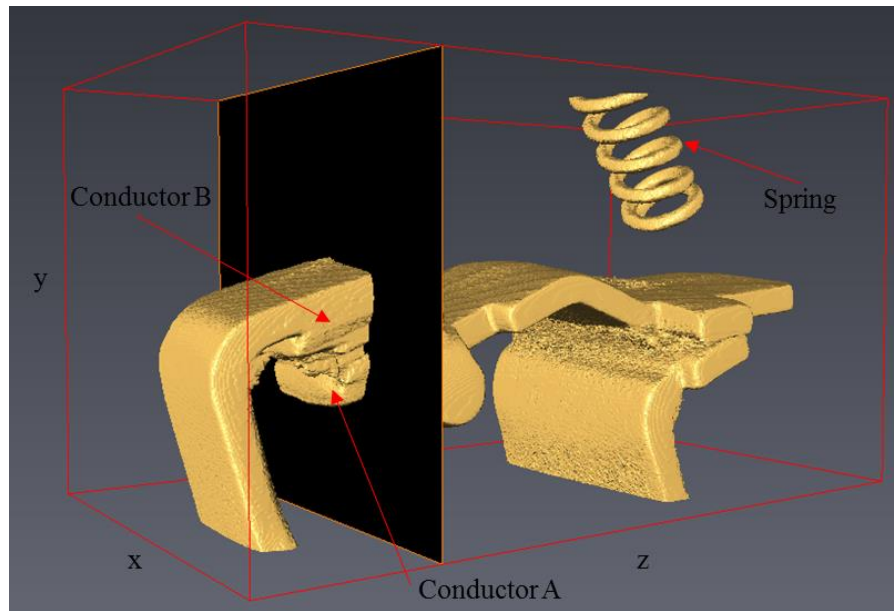


Figure 4.12. Position of the 2D cross-section slice image in the 3D reconstructed volume

#### 4.5 Post-Processing and Analysis of Experimental Data

Once the 2D cross-section slice images of the contact system are available, several post-processing and analyses can be conducted to extract information and features of interest to better understand the contact arrangement. The first step in this is to automate the process to distinguish between different metals (for example, a silver alloy contact and a copper alloy conductor) and to distinguish between a metal and air within the images. Figure 4.13(a) shows a cropped 16-bit grayscale 2D cross-section slice image of the sample across the area of interest with various intensities of pixel illuminations related to the level of X-ray absorption which indicate the different materials. The more highly absorbing silver alloy (lighter grayscale) is indicated with the less absorbing copper alloy metal, compared to minimally absorbing air (black on the grayscale). A darker region is seen between the two conductors indicating an air gap.

Figure 4.13(b) shows the levels of the grayscale colours over the section (pixels across the cyan line) indicated in Figure 4.13(a). According to the histogram of Figure 4.13(a) there is a reduction in the level of the grayscale colours over several pixels from the conductors to the air gap.

In the process, all the 16-bit grayscale 2D cross-section slice images are converted to 1-bit (binary) 2D cross-section slice images. The reason of the conversion is to separate

the contacting metal parts of the sample from the air-gaps. In this research, the air-gaps between the two conductors are also called voids.

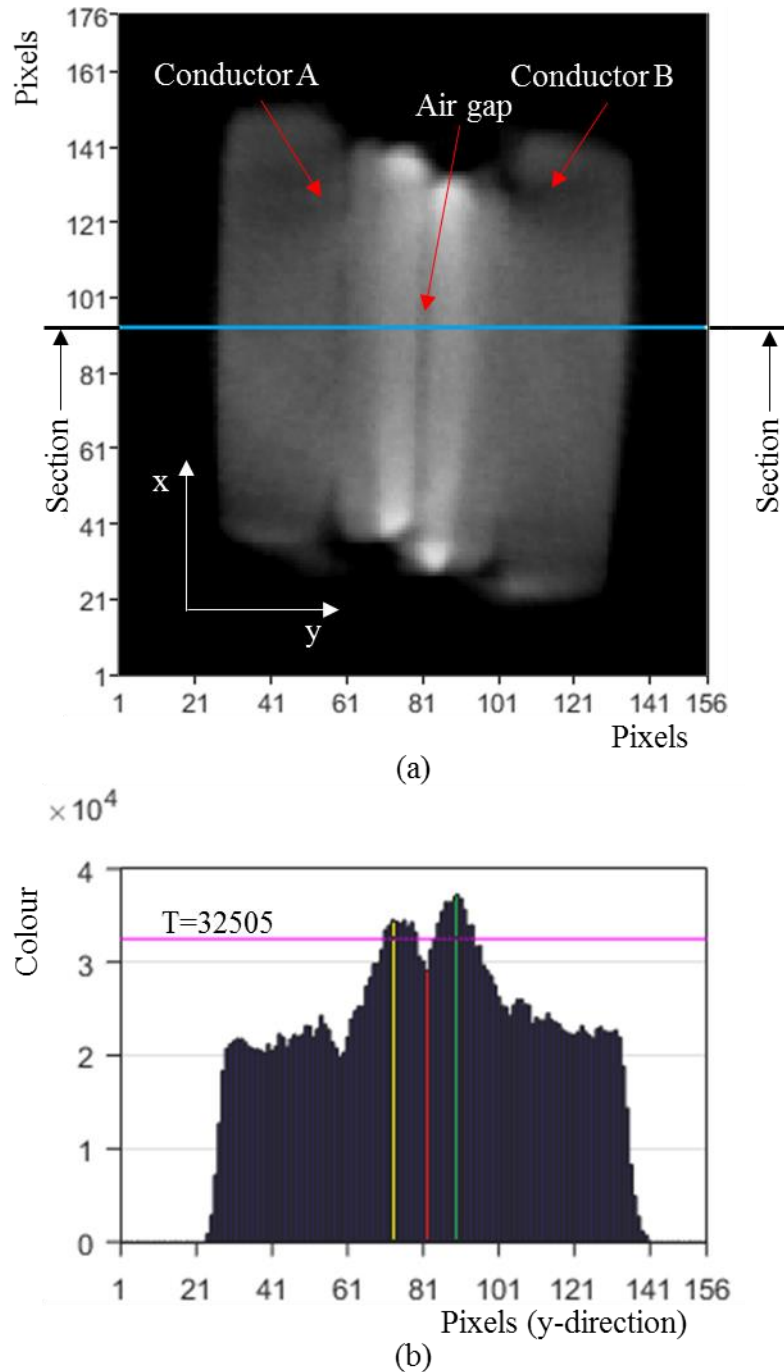


Figure 4.13. (a) 16-bit grayscale 2D cross-section slice image, (b) Colour values of the section

Figure 4.14 illustrates an example of 1-bit 2D cross-section slice image with dimensions  $176 \times 156$  pixels. The 2D cross-section slice image of the Figure 4.14 is the conversion of Figure 4.13(a) from 16-bit grayscale to 1-bit. More information concerning the selection of threshold value for the conversion from 16-bit grayscale to 1-bit is given

in Section 4.5.1. A 1-bit 2D cross-section slice image consists of only two colours in the range between 0 and 1. The colour with value 0 is 100% black and colour with value 1 is 100% white.

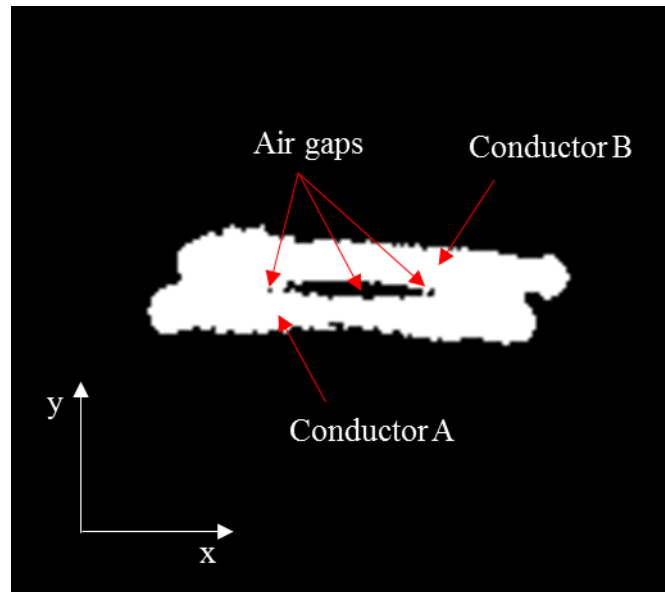


Figure 4.14. 1-bit 2D cross-section slice image of the 16 A rated AC single pole rocker switch

Once the 1-bit 2D cross-section slice images across the area of interest of the sample are available, the 3D volume of interest can be visualised. In this research, for the 3D volume of interest visualisation the “ImageVis3D” software is used [179]. This software creates the 3D volume by “stacking” the individual 1-bit 2D cross-section slice images on top of the other. The 3D volume of interest of the 16 A rated AC single pole rocker switch with bounding box dimensions of  $176 \times 156 \times 302$  voxels is illustrated in Figure 4.15.

#### 4.5.1 Threshold calculation

For the conversion of 16-bit grayscale 2D cross-section slice images to 1-bit the threshold ( $T$ ) value is required. All the pixels with colour value smaller than the threshold value are set to 0 while the pixels with colour value equal or bigger than the threshold value are set to 1.

The threshold value is calculated using the histogram of a section of a 16-bit grayscale 2D cross-section slice image of the sample. The section should consist of the

pixels which constitute a line which passes through the two conductors which have an air-gap between them. An example of section with its histogram is illustrated in Figure 4.13(a) and Figure 4.13(b) respectively.

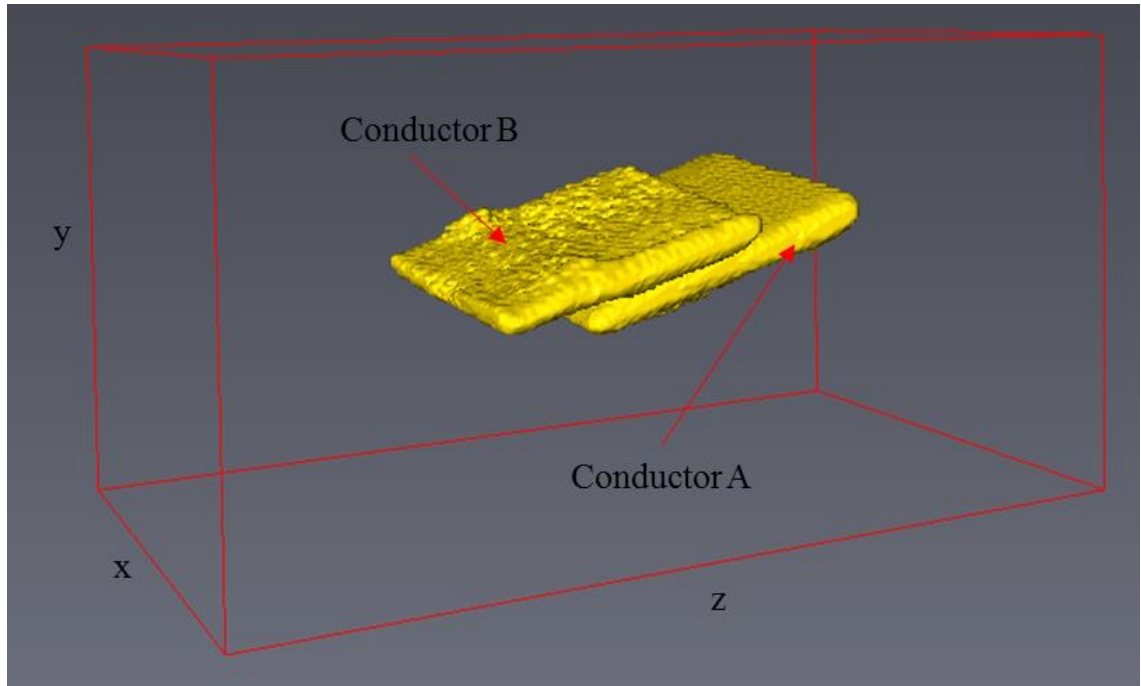


Figure 4.15. 3D volume of interest of the 16 A rated AC single pole rocker switch

In the process, the histogram is divided into two main regions in order to separate the pixels of two conductors across the section as illustrated in Figure 4.13(a). A reference point of the air-gap is defined as the minimum colour value between the two conductors ( $Gap_{min}$ ) which also shows the two main regions of the histogram (the pixels on the left of the reference point belong to Conductor A while the pixels on the right of the reference point belong to Conductor B). This reference point of the air-gap in Figure 4.13(b) is represented by the red bar colour value. Then, the maximum colour values of the two conductors are identified. These maximum colour values are the maximum values of the two conductors in each of the two main regions as illustrated in Figure 4.13(b). The maximum colour value of the Conductor A ( $ConA_{max}$ ) is represented by the yellow bar while the maximum colour value of Conductor B ( $ConB_{max}$ ) is represented by the green bar of the histogram of Figure 4.13(b). The threshold is given from the average value of the mean colour value of two conductors ( $ConA_{max}$  and  $ConB_{max}$ ) and the colour value of the reference point of air-gap ( $Gap_{min}$ ). This relationship is described by Eq. (4.1).

$$T = \frac{ConA_{\max} + ConB_{\max} + 2 \cdot Gap_{\min}}{4} \quad (4.1)$$

For more reliable results of the selected threshold value four different sections for four different x-z 16-bit grayscale 2D cross-section slice images are measured as presented in Table 4.1. According to the measured threshold values of Table 4.1, the 32954 with an error of  $\pm 1.363\%$  is selected as threshold value for the conversion of 16-bit grayscale 2D cross-section slice images to 1-bit.

Table 4.1. Threshold values for four different sections for four different x-y 16-bit grayscale 2D cross-section slice images

Number of 2D cross-section slice image	142 <sup>nd</sup>	145 <sup>th</sup>	149 <sup>th</sup>	152 <sup>nd</sup>
Threshold (16 – bit)	32505	32600	33403	33223

#### 4.5.2 Same sample X-ray CT scans

If the same sample is to be scanned more than once, it is important to select the same X-ray CT settings for all the X-ray CT scans (as described in Section 0) in order to have reliable results for comparison. Moreover, the selection of the appropriate threshold value is an important factor that should be considered carefully.

After the first scan of the sample, the selection of threshold value for the following scans is chosen by using a different method. This method compares the volume of 3D volume of interest in voxels of the first scan with the new scan in order to identify the appropriate threshold value of the new scan as the threshold value of the first scan is selected as described in Section 4.5.1. The reason for this comparison is based on the fact that each threshold value gives different volume in voxels. The threshold value which gives the closer value of the volume of the new scan with the value of volume of the first scan is selected.

The threshold at 0 A is calculated to be 32954 as explained in Section 4.5.1 and the volume is calculated by counting the voxels of the 3D volume of interest (27647617 voxels). The calculated volume value of the 3D volume of interest at 0 A is

selected as a reference volume for the calculation of the threshold values for the rest scans (at 16 A, 32 A and 64 A current loading tests) as it is assumed that it is kept unchanged. Each of the threshold values in Table 4.2 for the X-ray CT scans at 16 A, 32 A and 64 A gives the closer value of the volume of the 3D volume of interest to the reference volume (at 0 A).

Table 4.2. Threshold value at 16-bit greyscale and volume for each X-ray CT scan

Scan	0 A	16 A	32 A	64 A
Threshold (16 – bit)	32954	27379	40851	41173
Volume (voxels)	27647617	27647677	27646984	27647478

From Table 4.2, the volume of the 3D volume of interest of the 16 A rated AC single pole rocker switch is calculated to be 27647330.5 voxels with an error of  $\pm 0.003\%$ . The difference between the reference volume and the volume of the 3D volume of interest values in each scan is based on the position of the sample on the turntable. The position of the sample on the turntable in each scan has as a result to acquire 2D X-ray images with a different total number areas of interest and values of pixels within this area of interest. If the sample is scanned twice and the position of the sample at the first scan has an angle  $\theta_1$  and at the second scan has an angle  $\theta_2$  then the difference between the two angles is given by Eq. (4.2).

$$\varphi = |\theta_2 - \theta_1| \quad (4.2)$$

Figure 4.16(a) illustrates a schematic cross-section slice of a rectangular parallelepiped on the detector at  $0^\circ$ . The same rectangular parallelepiped is also illustrated on the detector at  $-90^\circ$  and  $30^\circ$  in Figure 4.17(a) and Figure 4.18(a) respectively. The rectangular parallelepiped for the following examples is assumed to consist of the same homogeneous material with dimensions of  $3 \times 2 \times 1$  voxels.

The position of the rectangular parallelepiped on the turntable at  $0^\circ$  and  $-90^\circ$  allows the detector to acquire equal number of rays with the actual number of pixels as the



rectangular parallelepiped fits exactly with the pixel dimensions of the detector. Figure 4.16(b) Figure 4.17(b) show the schematic 2D grayscale X-ray images of the rectangular parallelepiped at  $0^\circ$  and  $-90^\circ$  which are acquired from the detector. These schematic 2D grayscale X-ray images are consist of two colours, the black which represents the air and grey which represents the intensity of rays passing through the rectangular parallelepiped. All the rays passing through the rectangular parallelepiped have equal intensities (thus, each of the non-black pixels in the schematic 2D grayscale X-ray images have the same colour value) as it is assumed that the rectangular parallelepiped is made of the same homogeneous material.

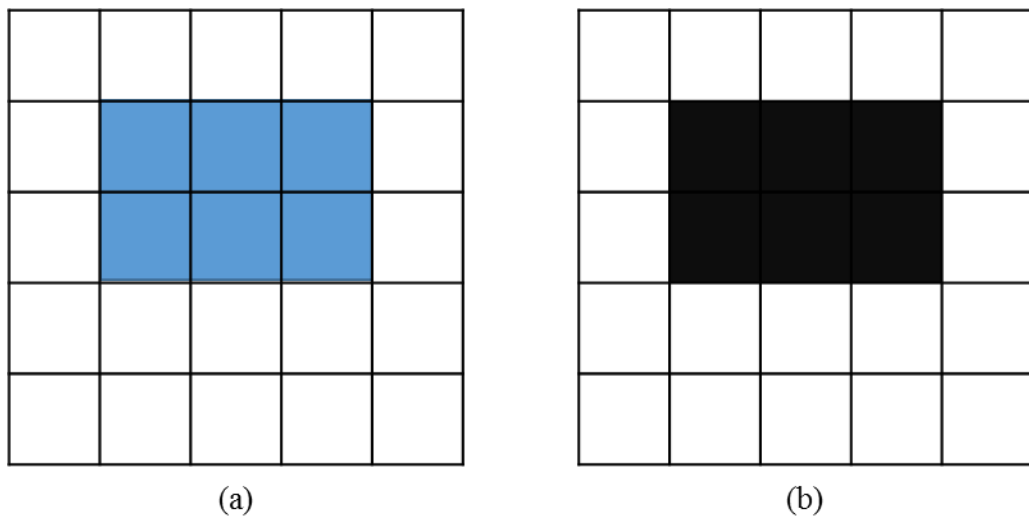


Figure 4.16. (a) Schematic cross-section slice of rectangular parallelepiped on the detector at  $\theta_1 = 0^\circ$ , (b) Schematic 2D grayscale X-ray images of rectangular parallelepiped at  $\theta_1 = 0^\circ$  with grid

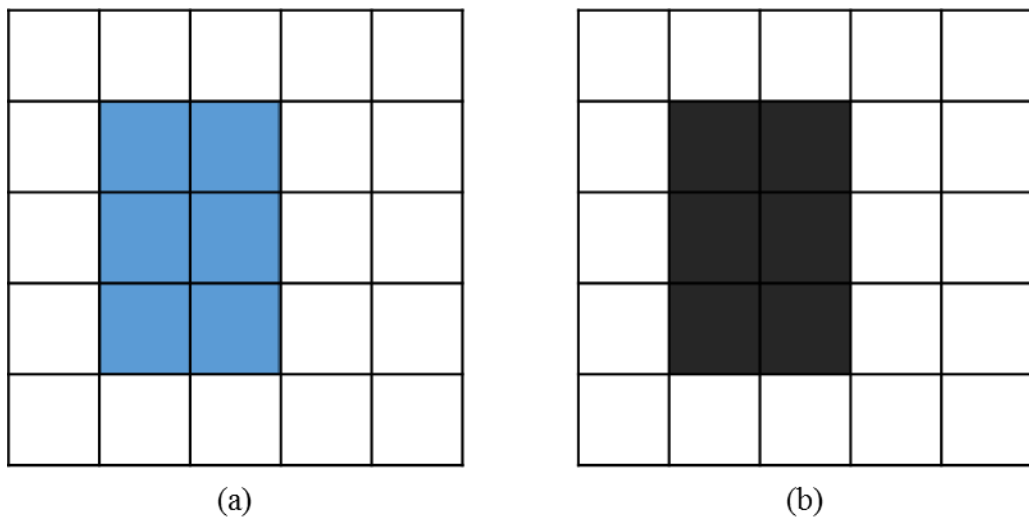


Figure 4.17. (a) Schematic cross-section slice of rectangular parallelepiped on the detector at  $\theta_2 = -90^\circ$ , (b) Schematic 2D grayscale X-ray images of rectangular parallelepiped at  $\theta_2 = -90^\circ$  with grid

If  $\sin(\varphi)$  equals 0 or 1, then the result of two areas of interest will be the same with same pixel colours (the area of the schematic 2D X-ray image at  $0^\circ$  equals with the schematic 2D X-ray image at  $-90^\circ$ , 6 pixels with same colours). The equal amount of pixels of the area of interest and the pixel values within the area of interest of the acquired 2D X-ray images of two X-ray CT scans with  $\sin(\varphi)$  equals to 0 or 1 gives equal values for the corresponding volumes of 3D volume of interest in each X-ray CT scan.

The error with the difference between the reference volume and the volume of the 3D volume of interest values appears if the result of  $\sin(\varphi)$  is not equal with 0 or 1. In this example the difference between the volumes values of the rectangular parallelepiped after two different scans with different positions of the rectangular parallelepiped on the turntable at  $0^\circ$  and  $30^\circ$  are compared and explained.

Figure 4.18(b) shows the schematic 2D grayscale X-ray image of the rectangular parallelepiped at the position of  $30^\circ$  which is acquired from the detector. It consists of more and different colour pixels (shades of black and white) compared with the schematic 2D grayscale X-ray image of Figure 4.16(b). The 2D grayscale X-ray image of Figure 4.18(b) consists of more pixels because the position of the rectangular parallelepiped at  $30^\circ$  covers more pixels on the detector than its position at  $0^\circ$  (see Figure 4.16(a) and Figure 4.18(a)).

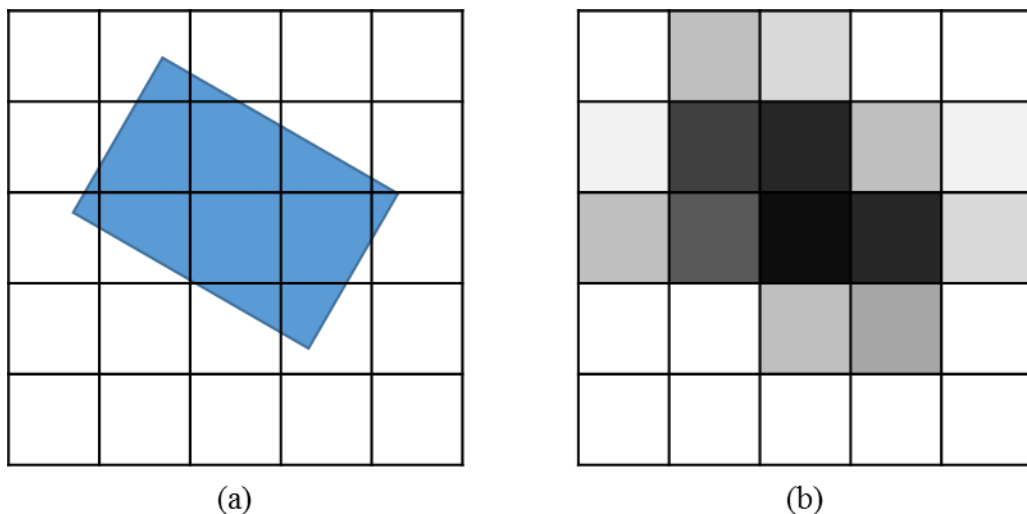


Figure 4.18. (a) Schematic cross-section slice of rectangular parallelepiped on the detector at  $\theta_2 = 30^\circ$ , (b) Schematic 2D grayscale X-ray images of rectangular parallelepiped at  $\theta_2 = 30^\circ$  with grid

In Section 3.4.4, each ray intensity value represents a pixel colour value on the detector. According to this, the rays passing through the rectangular parallelepiped have different intensity values because the material of the rectangular parallelepiped covers portion of areas (portion of pixels) on the detector. The rays with more diffraction on the rectangular parallelepiped are represented with darker colour pixels while rays with less diffraction on the rectangular parallelepiped are represented with lighter colour pixels.

If  $\sin(\varphi)$  is not equal to 0 or 1, then the result of two areas of interest will be different with different pixel colours (the area of the schematic 2D X-ray image at  $0^\circ$  equals with 6 pixels while the schematic 2D X-ray image at  $30^\circ$  equals with 13 pixels). The different amount of pixels in the area of interest and the pixel values within the area of interest of the acquired 2D X-ray images of two X-ray CT scans with the  $\sin(\varphi)$  different with 0 or 1 gives different values for the corresponding volumes of 3D volume of interest in each X-ray CT scan.

A different position of the sample on the turntable (different angle between the sample and turntable) for each X-ray CT scan produces different stack of 2D X-ray images. Different stacks of 2D X-ray images produces different 3D reconstructed volume of the sample. In this research, it was tried to place the sample on the same position on the turntable in each X-ray CT scan in order to acquire more reliable results. However, the 3D volume of interest in each X-ray CT scan show different results with an error of  $\pm 0.003\%$  and this is considered negligible.

At this point, it is important to note that the total error of the experimental data is given from the sum of the error of measured threshold values and the error of 3D volume of interest. This error is calculated to be  $\pm 1.366\%$ .

#### 4.5.3 3D reconstructed volume orientation

The 3D reconstructed volume orientation is an important parameter that should be considered for more reliable results when there is a comparison between different 3D volumes of interest. In this research, the direction of normal force ( $F$ ) is defined to be parallel with the force of the spring ( $F_{sp}$ ). Figure 4.19 illustrates the orientation of the 3D reconstructed volume (bounding box dimensions,  $417 \times 461 \times 782$  voxels) of the 16 A

rated AC single pole rocker switch where the direction of the normal force ( $F$ ) is set to be parallel with the y-axis.

The angles of the 3D reconstructed volume orientation are used in order to orientate the 3D volume of interest of the 16 A rated AC single pole rocker switch. Figure 4.20 shows the new position of the 3D volume of interest of the 16 A rated AC single pole rocker switch within the bounding box with dimensions  $223 \times 160 \times 224$  voxels.

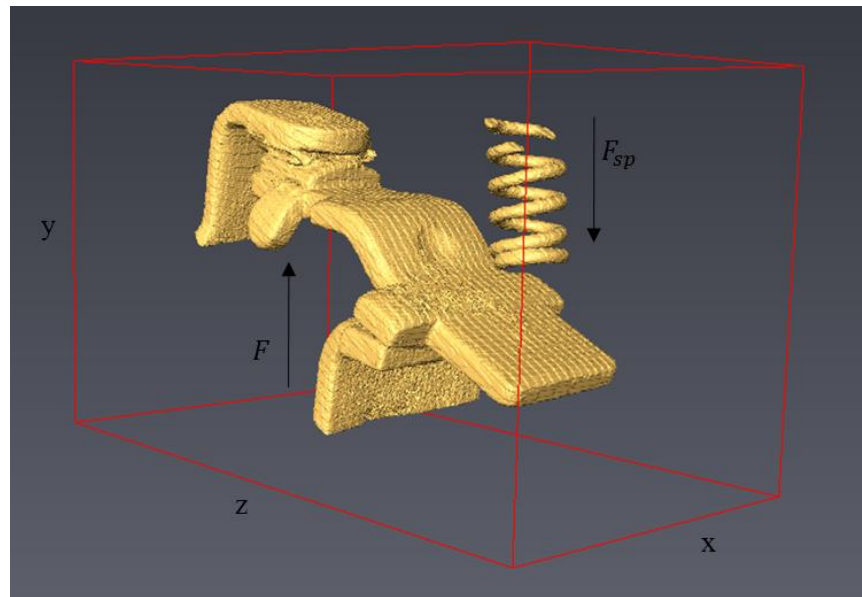


Figure 4.19. Orientation of the 3D reconstructed volume of the 16 A rated AC single pole rocker switch

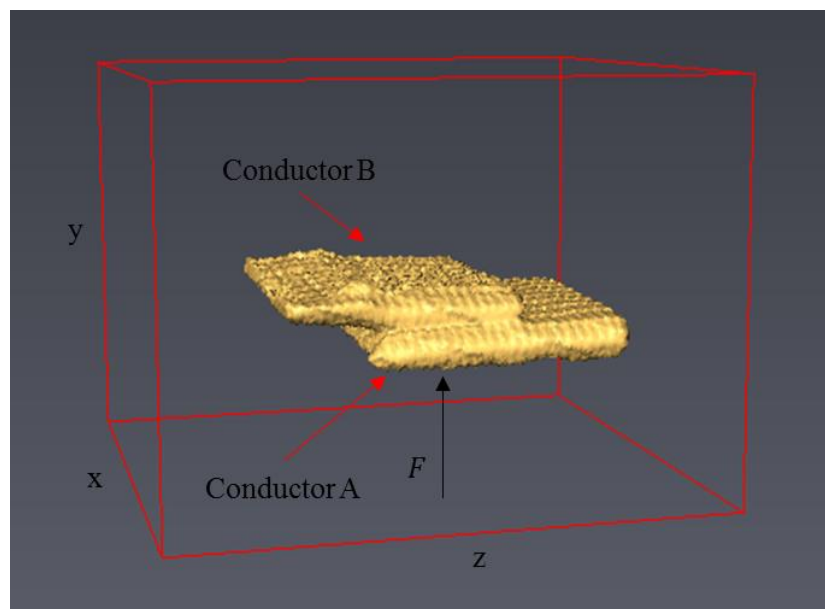


Figure 4.20. Orientation of the 3D volume of interest of the 16 A rated AC single pole rocker switch

#### 4.5.4 Validation method of pixel length

In order to ensure that the resolution of the 2D cross-section slice images of the 16 A rated AC single pole rocker switch is  $5\ \mu\text{m}$  for pixel length and presented correctly and accurately it is validated using an experimental method. According to this experimental method, the resolution is found to be  $5.005\pm 0.025\ \mu\text{m}$  for pixel length using the values of Table 4.3. These values (micro-meter measurement) are taken by measuring the length between particular characteristics of the Conductor B with a standard micro-meter as illustrated in Figure 4.21. Then, the values of micro-meter measurements are divided by 634 pixels in order to calculate the pixel length. The value of 634 pixels is the number of pixels between the first and last pixel across the x-direction as presented in Figure 4.22.

Table 4.3. Measured values for the validation of pixel length

Micro-meter measurement (mm)	3.16	3.17	3.18	3.19
Pixel length ( $\mu\text{m}$ )	4.98	5.00	5.02	5.03



Figure 4.21. Length measurement between particular characteristics of the Conductor B using a standard micro-meter

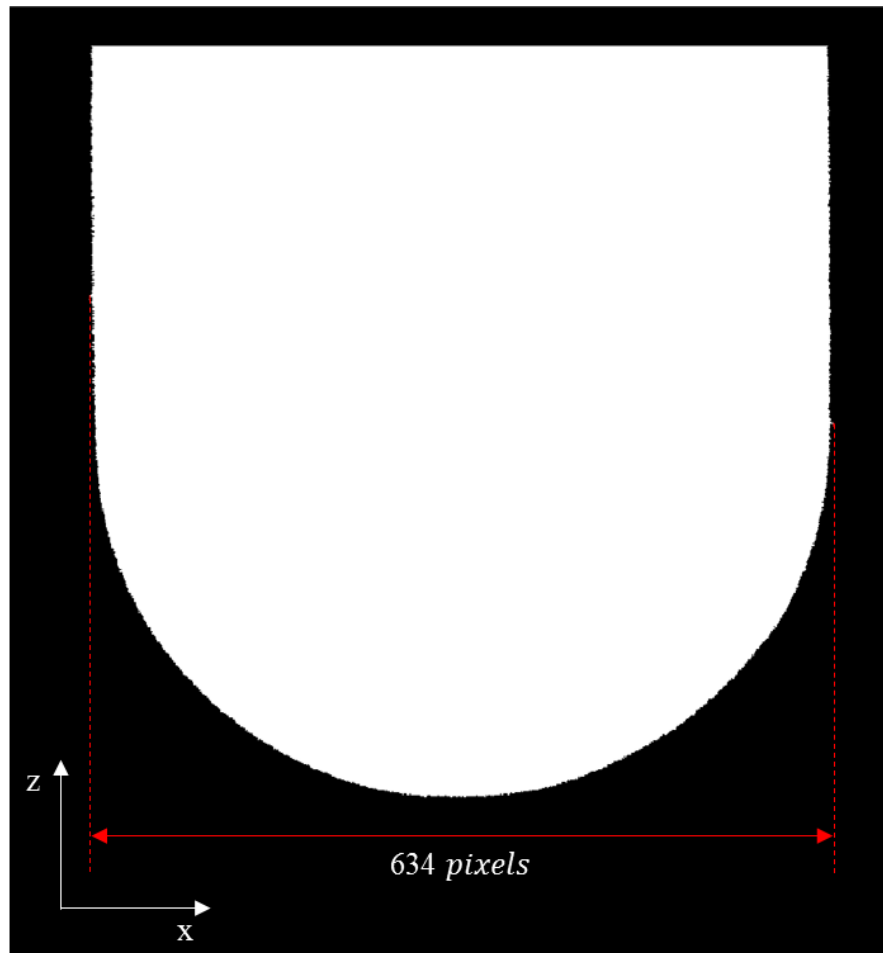


Figure 4.22. Top-view of the Conductor B

#### 4.6 Conclusion

In this chapter information concerning the selection of a suitable contact system for X-ray CT analysis and the use of the appropriate X-ray CT settings in order to achieve best results in experimental data for the visualisation and characterisation of contact interface are given. A 16 A rated AC single pole rocker switch is selected as a suitable contact system for investigation which is scanned using X-ray CT after four different current tests at 0 A, 16 A, 32 A and 64 A.

Moreover, a post-processing and analysis of the experimental (scanned) data is made in order to be used for the development of Contact Analysis Techniques (CAT\*). More information concerning the CAT\* development is given in the following chapters. It is important to note that the total error of the experimental data (the sum of the error of measured threshold values and the error of 3D volume of interest) was calculated to be  $\pm 1.366\%$ .

## **Chapter 5 – The 3D Nature of a Real Un-Dismantled Electrical Contact Interface**

### **5.1 Introduction**

A 3D contact analysis and modelling suite of tools are developed and introduced in this chapter. The “3D Contact Map” of an electrical contact interface is presented demonstrating the 3D nature of the contact. It gives information on where the electrical contact spots in a 3D surface profile are located. An X-ray CT technique is used to collect the 3D data to a resolution of 5  $\mu\text{m}$  of a real un-dismantled contact interface for analysis. Previous work by Lalechos and Swingler [7, 147-149, 180, 181] presented a “2D Contact Map” on a 2D contact profile from collected 3D data to a resolution of 8  $\mu\text{m}$ . The main advantages of both 2D and 3D mapping techniques focus on the fact that they are non-destructive and there is no need to dismantle the component of interest. This chapter, focuses on the 3D mapping technique showing its advantages over the 2D mapping technique. For test purposes, the experimental data of 250 V, 16 A rated AC single pole rocker switch after the four different current loading tests (0 A, 16 A, 32 A and 64 A) which were presented in Section 4.5 are used. A comparison for the total mechanical area of contact, the number of contact spots and the total contact resistance is conducted using both the 2D and 3D mapping techniques to a resolution of 5  $\mu\text{m}$ . Moreover, the angle for each contact spot is calculated using the 3D mapping technique. Some additional investigations concerning the fractal characteristics of the two contact conductors (A and B) of the 16 A rated AC single pole switch and the voids between them are also visualised and characterised.

### **5.2 A Suite of Contact Analysis Techniques Tools**

The Contact Analysis Techniques, or CAT\* developed in this chapter are incorporated in a software tool which is running in MATLAB. The different CAT\* developed in this chapter are show in the flowchart of Figure 5.1. The nomenclature of each CAT\* is given in Table 5.1.

The software tool uses as an input data the 2D cross-section slice images of the contact system which are post-processed and analysed as explained in Section 4.5. CAT2DCM and CAT3DCM analysis tools are used for the development of 2D and 3D contact maps respectively using the 2D post-processed and analysed cross-section slice

images of the contact system. For the visualization of both 2D and 3D contact maps the tool CATVis is used using the 2D processed cross-section slice images as illustrated in Figure 5.1.

The CATVis is also used for the visualisation of the contact spots of the 3D contact map in a 2D plane (using the 2D processed cross-section slice images of CAT3DCM) showing their contact angle with a different colour. In addition, the CATVis is used for the visualisation of the 3D voids (using the 2D processed cross-section slice images of CAT3DCM) which are located between the two bodies which consist of the contact system.

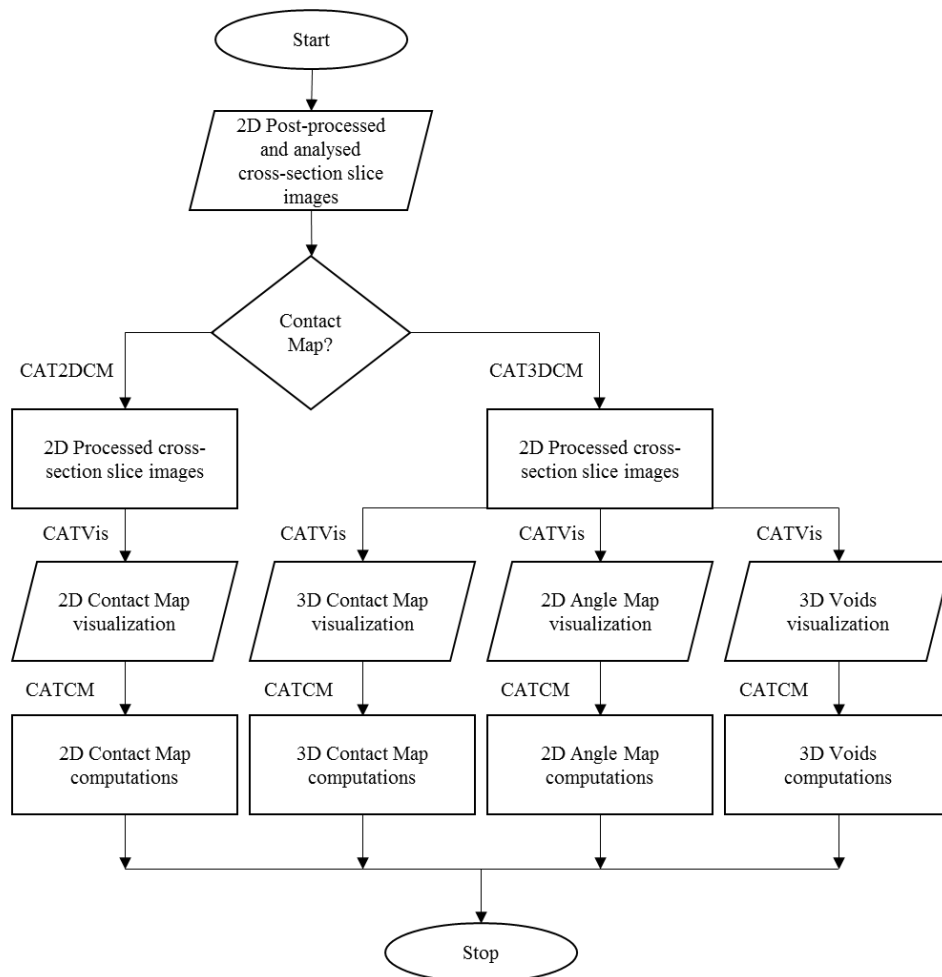


Figure 5.1. Flowchart of software tool

Moreover, for both 2D and 3D contact maps CATCM analysis tool is used for several computations. These computations include the calculation of the area of each contact spot and closed void (in 2D contact maps), the total mechanical area of contact, the number of contact spots and closed voids (in 3D contact maps), the volume of each closed void and



the total contact resistance. In addition, the CATCM is used for the calculation of the angle of each contact spot at 3D contact maps.

Table 5.1. Nomenclature of CAT\*

CAT2DCM	Contact Analysis Technique for 2D Contact Map
CAT3DCM	Contact Analysis Technique for 3D Contact Map
CATVis	Contact Analysis Technique for Visualization
CATCM	Contact Analysis Technique for Contact Map

### 5.3 Contact Analysis and Modelling Techniques

Cross-section slice images of the contact interface are used to produce 2D and 3D contact maps. 2D contact maps (as produced by Swingler and Lalechos [7, 147-149, 180, 181]) can be significantly different to 3D contact maps under particular conditions which will be discussed in Section 5.8. Figure 5.2 illustrates how both techniques work for a simple case. Figure 5.2(a) shows the schematic cross-section slice image of Body A and Body B which are in mechanical contact. The white areas of the schematic cross-section slice image between the two bodies are indicating closed voids and open voids.

Figure 5.2(b) shows the result of the 2D contact mapping technique of the schematic cross-section slice image of Figure 5.2(a), where the white areas (on the x-axis) in this case are illustrating the mechanical contact. The height of contact spots on the y-axis in the 2D contact maps is lost (y-direction is equal with zero). This type of technique was used by Lalechos and Swingler [7, 147, 148] and puts the contact interface onto a 2D plane when all cross-section slice images are joined together.

Figure 5.2(c) shows the result of the 3D contact mapping technique of the schematic cross-section slice image in Figure 5.2(a). This is a new technique for the visualization of the contact interface in the 3D plane developed in this research. The white areas of Figure 5.2(c) are indicating mechanical contact spots. In this technique, the contact spots are the line segments which are connecting the voids (closed and open). The contact interface forms a 3D profile when all cross-section slice images are joined together.

The 3D contact mapping technique uses a 3D reconstructed volume of the data taken from the cross-section slice images. A further technique is used to identify the contact spots and gives information on their 3D position. This technique consists of three steps. Firstly, it is required to divide the sample into equal cross-section slices across one of the three directions. Secondly, the direction of the normal force ( $F$ ) is identified and in this research is defined to be perpendicular to one of the other two directions (already introduced in Section 4.5.3). The direction of the normal force is used to define the orientation of the coordinate system used. The last step is the examination of each cross-section slice separately to generate the final result.

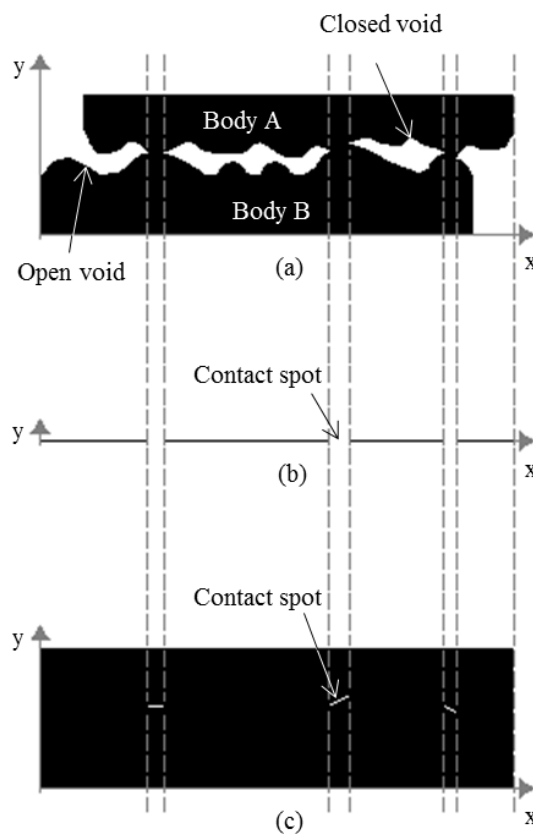


Figure 5.2. Schematic cross-section of (a) Bodies A and B, (b) 2D contact mapping technique and (c) 3D contact mapping technique [75]

For example, Figure 5.3 shows a schematic close-up of a cross-section slice of a sample which is divided in equal slices in the  $z$ -direction and the normal force is perpendicular to the  $x$ -direction (or parallel with  $y$ -direction). The sample consists of two bodies (Body A and Body B) which are in contact (at points across the line segment AB) having two voids where their circumferences are described by different functions ( $f_n(x, y)$  and  $f_{n+1}(x, y)$ ).

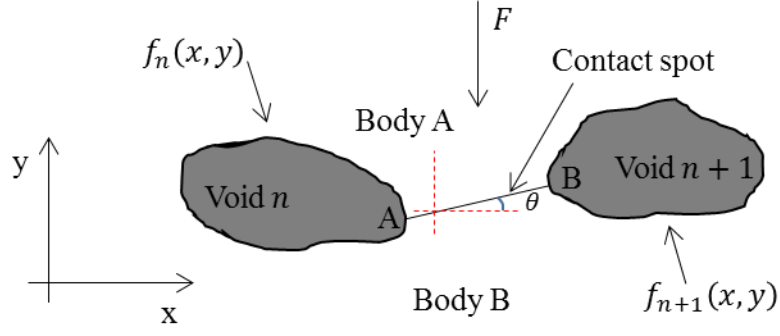


Figure 5.3. Schematic cross-section slice of a contact spot [75]

From Figure 5.2(a) it is obvious that the contact spots are presented between the voids which are the result of the roughness of the two bodies. Eq. (5.1) describes the line segment (contact spot) AB which is the connection of the maximum value  $x$  of void  $n$  ( $x_{max_n}$ ) with the minimum value of  $x$  of void  $n + 1$  ( $x_{min_{n+1}}$ ). Where  $\theta$ , is the angle of line segment (contact spot) AB.

$$f_{zl}(x) = \frac{f_{n+1}(x_{min_{n+1}}) - f_n(x_{max_n})}{x_{min_{n+1}} - x_{max_n}} (x - x_{max_n}) + f_n(x_{max_n}) \quad (5.1)$$

The coordinates of the points A and B are  $(x_{max_n}, f_n(x_{max_n}))$  and  $(x_{min_{n+1}}, f_{n+1}(x_{min_{n+1}}))$  respectively, because the  $x$  values of points A and B belong to the voids,  $x \in (x_{max_n}, x_{min_{n+1}})$ . The suffix  $z$  in Eq. (5.1) is the number of the cross-section slice,  $z \in [1, i]$  ( $i$  is the total number of cross-section slices). The suffix  $l$  is the number of the contact spot in each cross-section slice,  $l \in [n - 1, n]$  with  $n \in [2, \kappa]$ . Where  $n$ , is the number of void (open or closed) and  $\kappa$  is the total number of voids (open and closed) in each cross-section slice ( $\kappa \geq 2$  because each cross-section slice has 2 open voids). The 3D contact map consists of the plot of all line segments for all cross-section slices in 3D plane. In addition, from Eq. (5.1), the slope of the line segment (contact spot) can be extracted as described from Eq. (5.2). The angle of the line segment (contact spot) is given from Eq. (5.3).

$$Slope_{zl} = \frac{f_{n+1}(x_{min_{n+1}}) - f_n(x_{max_n})}{x_{min_{n+1}} - x_{max_n}} \quad (5.2)$$

$$\theta_{z,l} = \tan^{-1}(\text{Slope}_{z,l}) \quad (5.3)$$

In this chapter, a contact spot is defined as a collection of contacting pixels which are neighbouring with other contacting pixels by at least one point of their edges (pixels which are connected diagonally belong to the same contact spot, e.g. the contact spot 2 of Figure 5.4). Figure 5.4 shows a plan view of 3 contact spots. Contact spot 1 consists of 5 contacting pixels, contact spot 2 consists of 31 contacting pixels and contact spot 3 consists of only 1 contacting pixel. The mean-point pixel is the point with the mean values of  $x$  and  $z$  (and  $y$  in 3-axes) of each contact spot.

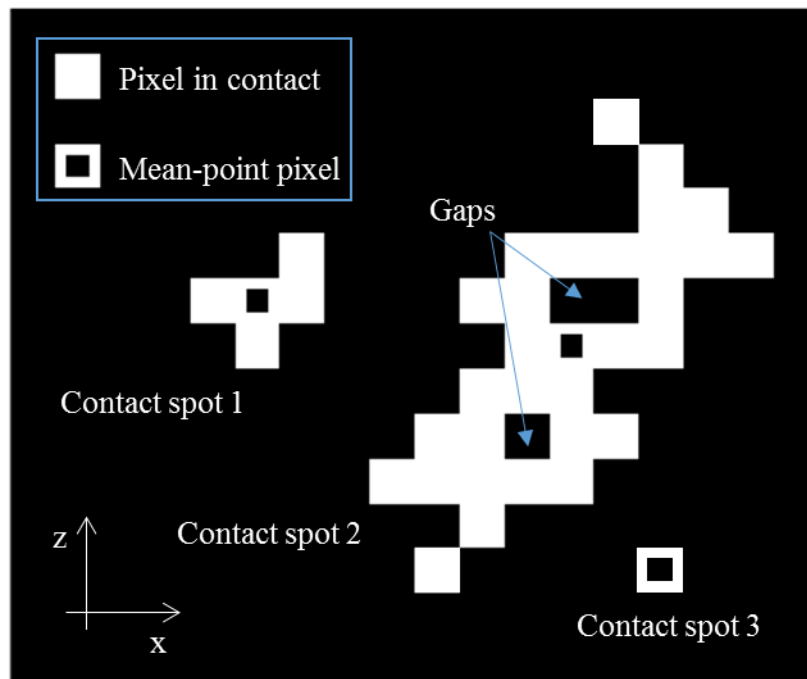


Figure 5.4. Schematic contact spots [75]

## 5.4 Results of 2D and 3D Mapping Techniques

### 5.4.1 Contact maps

Figure 5.5 shows the microscopic 2D contact maps of the contact interface of the two conductors (A and B) within the 16 A rated AC single pole rocker switch. Where the white areas on the 2D contact maps show mechanical contact consisting of “contacting pixels” while the black areas within the contacting pixels are showing “gaps” (non-contact). Each 2D contact map in Figure 5.5 is developed after each X-ray CT scan.

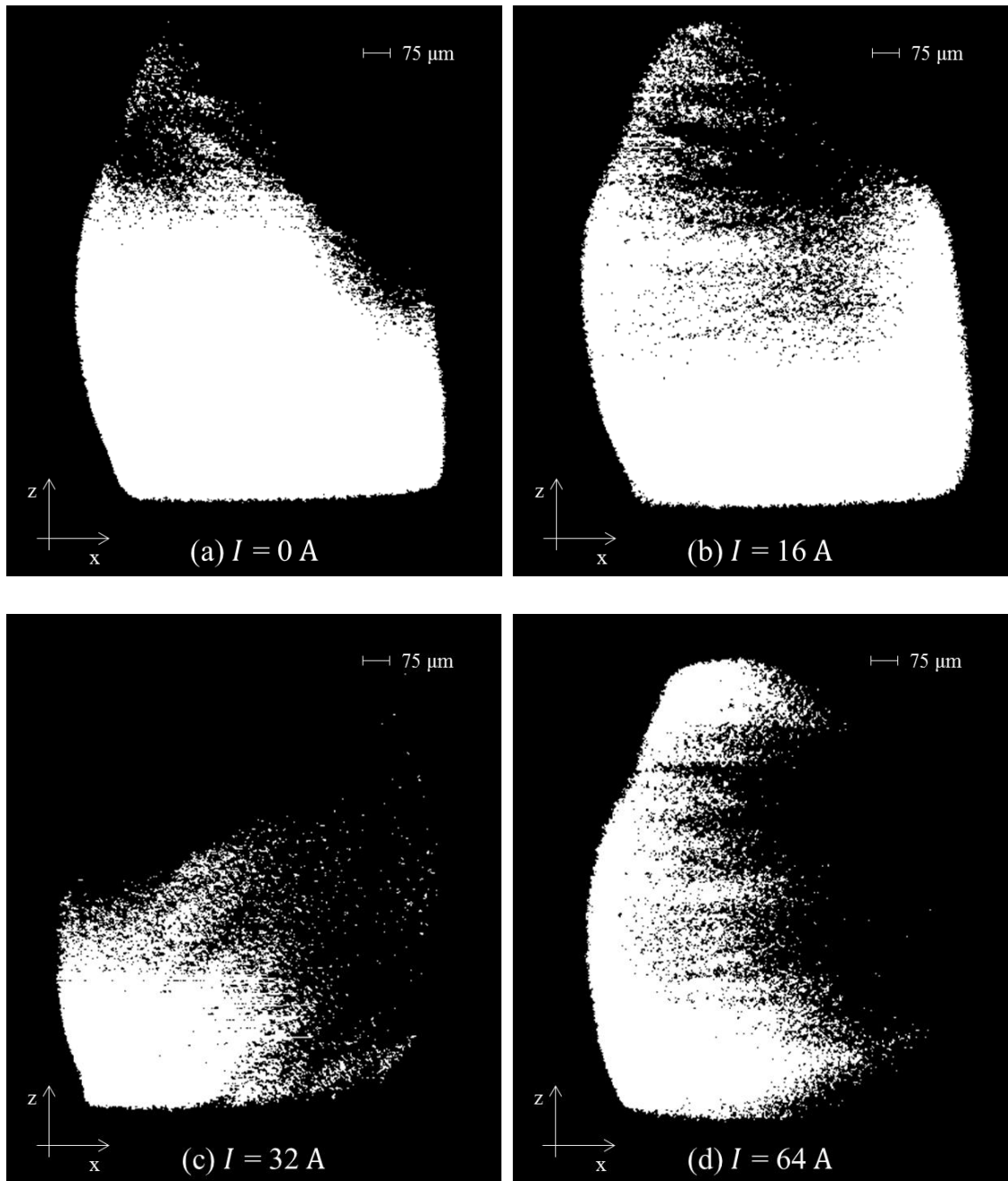


Figure 5.5. 2D contact maps of 16 A rated AC single pole rocker switch after four different current loading tests using CATVis

Figure 5.6 shows the microscopic 3D contact maps of the contact interface of the two conductors (A and B) within the 16 A rated AC single pole rocker switch. Where the black areas on the 3D contact maps show mechanical contact while the white areas within the black areas are showing gaps (non-contact). Each 3D contact map in Figure 5.6 is developed after each X-ray CT scan (after the four different current test). The visualisation of both 2D and 3D contact maps is made by using the CATVis while the analysis and computations of their characteristics (Section 5.2) are made by using the CATCM analysis tool as explained below.

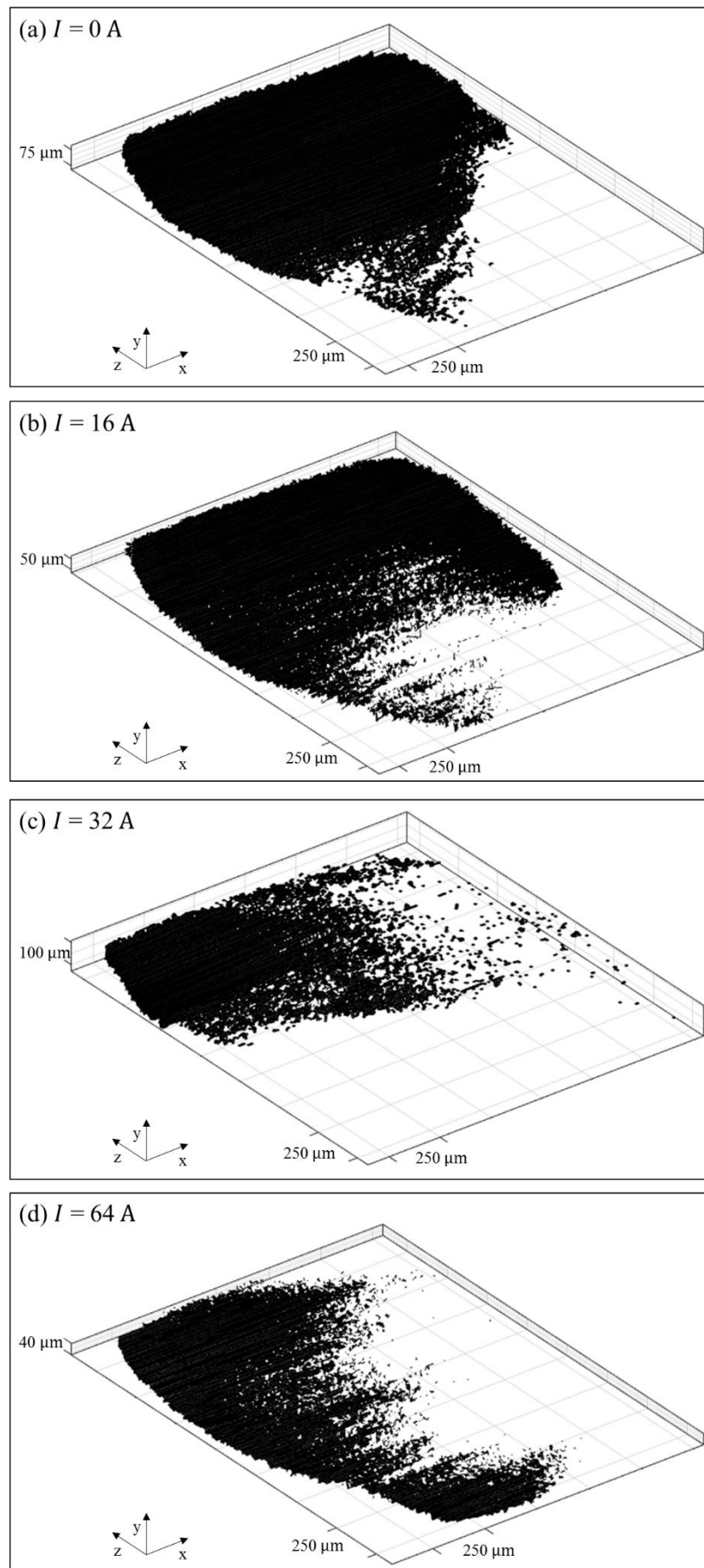


Figure 5.6. 3D contact maps of 16 A rated AC single pole rocker switch after the four different current loading tests using CATVis

#### 5.4.2 Total Mechanical area of contact

The total mechanical area of contact is calculated using the CATCM. According to CATCM, the area of each contact spot  $A_i$ , is defined as the sum of pixels within the contact spot and multiplied by  $25 \mu\text{m}^2$  (area of pixel). The sum of the contact areas of contact spots gives the total mechanical area of contact ( $A_T$ ) as described from Eq. (5.4) for  $i \in [1, n]$ . Where  $n$ , is the total number of contact spots. The smallest area of contact spot indicated on the 2D and 3D contact maps of Figure 5.5 and Figure 5.6 is  $25 \mu\text{m}^2$ , which is the resolution of the technique (1 pixel =  $25 \mu\text{m}^2$ ).

$$A_T = \sum_{i=1}^n A_i \quad (5.4)$$

The values of the total number of contact spots and the total mechanical area of contact for each 2D and 3D contact map of Figure 5.5 and Figure 5.6 are given in Table 5.2 and Table 5.3 respectively. The error of the calculated values presented in Table 5.2 and Table 5.3 is  $\pm 1.366\%$ . This error, represents the sum of the error of measured threshold values and the error of 3D volume of interest of the experimental data (already introduced in Section 4.5.2).

#### 5.4.3 Contact resistance calculation

For the total contact resistance calculation in both 2D and 3D contact maps two Contact Analysis Approaches (CAA\*) are developed, the Contact Analysis Approach for Cooper and Holm resistance (CAACHR) and the Contact Analysis Approach for Greenwood resistance (CAAGR). These CAA\* are included in CATCM. The CAACHR uses the Holm equation for a single contact spot and connects all contact spots in parallel following Cooper *et al.* [17] and CAAGR uses the Greenwood's formula as described in Eq. (2.23).

The CAACHR approach consists of two techniques, the Contact Analysis Technique for Holm Resistance (CATHR) and Contact Analysis Technique for Total Cooper Holm Resistance (CATTCHR). The CATHR is based on Holm's [20] work. According to Holm [20], the constriction resistance of a single contact spot in electric current path is given

by Eq. (2.20). In this research, it is considered an array of contact spots in the electric current path and the contact resistance of each contact spot is given from Eq. (5.5). Where  $\rho$ , is the electrical resistivity and  $a_j$  is the radius of contact spot  $j$  with  $j \in [1, n]$  ( $n$ , is the total number of contact spots). The CATTCHR is based on Cooper *et al.* [182] work. According to Cooper *et al.* [182] the total contact resistance can be calculated from the contact spots of which have constriction resistances being all in parallel. Thus, the CATTCHR is given from Eq. (5.6).

$$R_j = \frac{\rho}{2a_j} \quad (5.5)$$

$$R_c = \frac{1}{\sum_{j=1}^n R_j^{-1}} \quad (5.6)$$

Table 5.2. Characteristics of 2D contact maps

Test current (A)	0	16	32	64
Total number of contact spots	337 ± 5	419 ± 6	702 ± 10	511 ± 7
Total mechanical area of contact (mm <sup>2</sup> )	1.82 ± 0.02	2.01 ± 0.03	0.74 ± 0.01	1.17 ± 0.02
Greenwood contact resistance (μΩ)	3.34 ± 0.05	2.70 ± 0.04	2.15 ± 0.03	2.72 ± 0.04
Cooper Holm contact resistance (μΩ)	3.34 ± 0.05	2.70 ± 0.04	2.15 ± 0.03	2.72 ± 0.04

Table 5.3. Characteristics of 3D contact maps

Test current (A)	0	16	32	64
Total number of contact spots	407 ± 6	492 ± 7	743 ± 10	643 ± 9
Total mechanical area of contact (mm <sup>2</sup> )	1.83 ± 0.03	2.01 ± 0.03	0.74 ± 0.01	1.17 ± 0.02
Greenwood contact resistance (μΩ)	2.88 ± 0.04	2.48 ± 0.03	2.05 ± 0.03	2.32 ± 0.03
Cooper Holm contact resistance (μΩ)	2.88 ± 0.04	2.48 ± 0.03	2.05 ± 0.03	2.32 ± 0.03



The second approach, CAAGR is used to calculate the total contact resistance of the 3D contact interface using Greenwood's formula as described in Eq. (2.23). For both CAACHR and CAAGR calculations the electrical resistivity of silver ( $\rho = 15.87 \times 10^{-9} \Omega\text{m}$ ) is used. To achieve this, each contact spot is assumed to be a circle of radius  $\alpha$ . For example, the radius of contact spot  $i$  is calculated by Eq. (5.7). Where  $A_i$  is the total contact area of contact spot  $i$ . The distance  $d_{ij}$  between contact spot  $i$  and  $j$  is calculated from the mean-points of the contact spots  $i$  and  $j$ . The total contact resistance using both CAACHR and CAAGR approaches of each 2D and 3D contact map of Figure 5.5 and Figure 5.6 is given in Table 5.2 and Table 5.3 respectively.

$$\alpha_i = \sqrt{\frac{A_i}{\pi}} \quad (5.7)$$

## 5.5 Additional Investigations Using the Contact Spots of 3D Contact Maps

### 5.5.1 Contact spot area distribution

Figure 5.7 illustrates a set of graphs showing the number of contact spots which is inversely proportional to the contact area after four different current loading tests. The data are taken from the 3D contact maps represented in Figure 5.5 and are calculated using the CATCM. The smallest area of contact spot indicated on the graphs of Figure 5.7 is  $25 \mu\text{m}^2$ , which is the resolution of the technique (1 pixel =  $25 \mu\text{m}^2$ ) and the largest contact spots ( $A_L$ ) indicated are several  $\text{mm}^2$ . The number of contact spots,  $n$  with the smallest contact area ( $25 \mu\text{m}^2$ ) for each of the 3D contact maps of Figure 5.6 at 0 A, 16 A, 32 A and 64 A is calculated to be 154, 190, 357 and 283 respectively. Where  $A_L$  is the largest contact spot across the fit-line.

### 5.5.2 Contact spot angle distribution

Figure 5.8 illustrates a set of graphs showing the contact spot angle distribution for four different current values. The data are taken from the 3D contact maps represented in Figure 5.5 and are calculated using the CATCM. The angle of each contact spot is defined as the average angle calculated from the slope of neighbour pixels within the contact spots. All the angle values presented in Figure 5.8 are rounded towards an integer, resulting in an array of integers. An example of contact spot angle calculation is explained

below. The angle value of each contact spot is also presented with different colours as a ‘‘2D Angle Map’’. Figure 5.9 shows the 2D angle map at 64 A.

Figure 5.10 shows the top view of contact spot  $i$  of a schematic 3D contact map. The schematic 3D contact map is developed using the CAT3DCM tool as explained before in Section 5.3. This contact spot which is only in the 3D contact map consists of the contacting pixels of each x-y cross-section slice across the z-direction. For the angle calculation, the matrix  $[A]_{xz}$  is created which contains the height value (value of pixels in y-direction) of each pixel (in contact) of the 3D contact. Where the  $x$  suffix of the matrix represents the total number of cross-section slices in x-direction while the suffix  $z$  represents the total number of cross-section slices in z-direction. In the process, the slope of each group of neighbour pixels in contact in both directions (x and z) is calculated. The slope of each group of neighbour pixels in x-direction and y-direction is given from Eq. (5.8) and Eq. (5.9) respectively. Where the suffixes  $l$  and  $p$  represent the contact spot number and the group of pixels in contact in each cross-section slice respectively. For example, the cross-section slice  $z + 2$  of Figure 5.10 has only one contact spot ( $l = 1$ ) and two groups of pixels in contact ( $p = 2$ ). It is important to note that the slope in each contact spot  $l$  in z-direction can also be calculated using Eq. (5.2). After the calculation of slope of each group of neighbour pixels in contact within the contact spot  $i$ , the calculation of the average slope follows. The average slope of contact spot  $i$  is given from Eq. (5.10). Where  $P$ , is the total number of calculated slopes within the contact spot  $i$ . The average angle of contact spot  $i$  is given from Eq. (5.11).

$$Slope_{zlp} = y_{x+1} - y_x \quad (5.8)$$

$$Slope_{xlp} = y_{z+1} - y_z \quad (5.9)$$

$$Slope_i = \frac{\sum Slope_{zlp} + \sum Slope_{xlp}}{P} \quad (5.10)$$

$$\theta_i = \tan^{-1}(Slope_i) \quad (5.11)$$

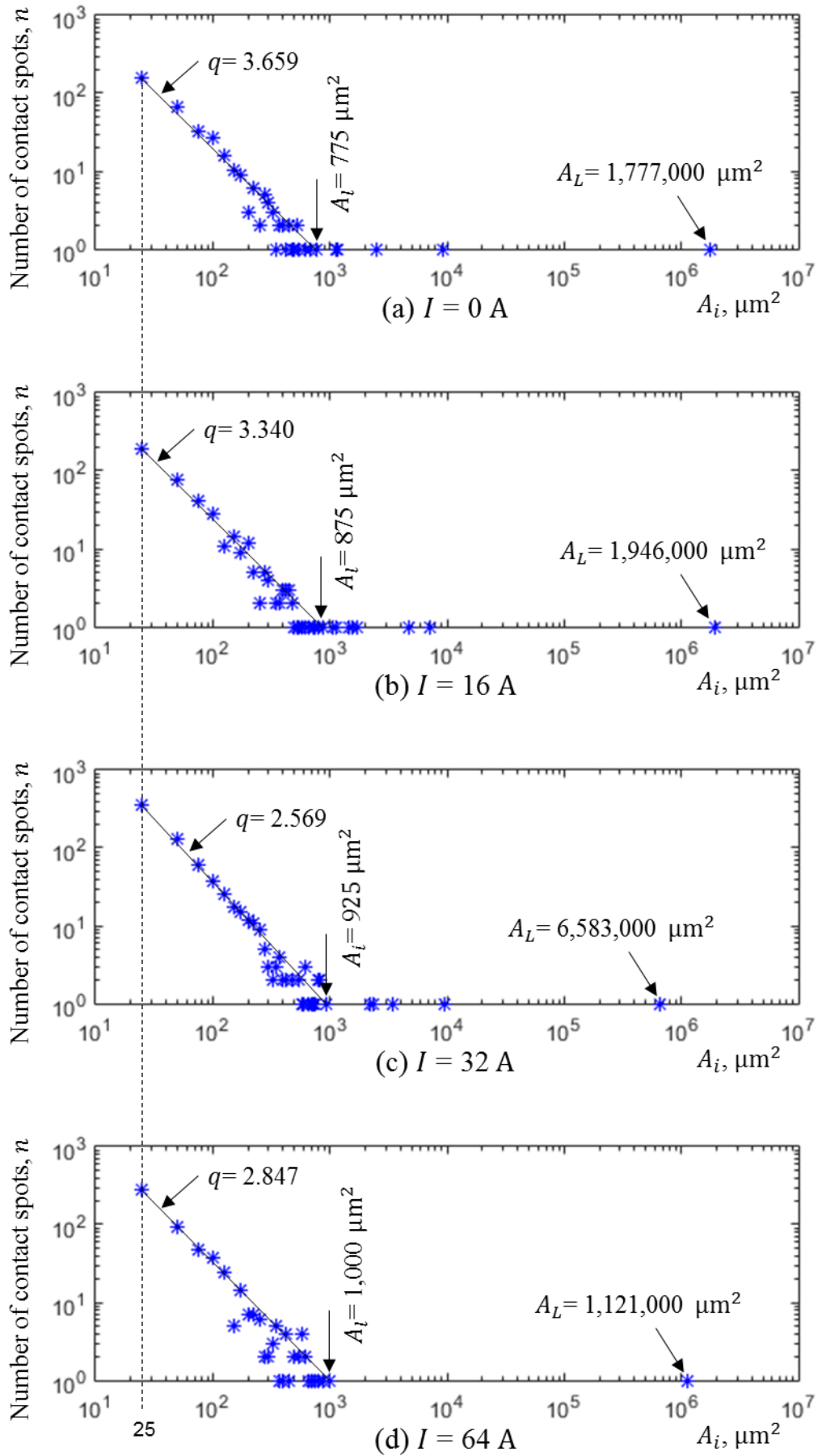


Figure 5.7. Contact spot area distribution after the four different current loading tests

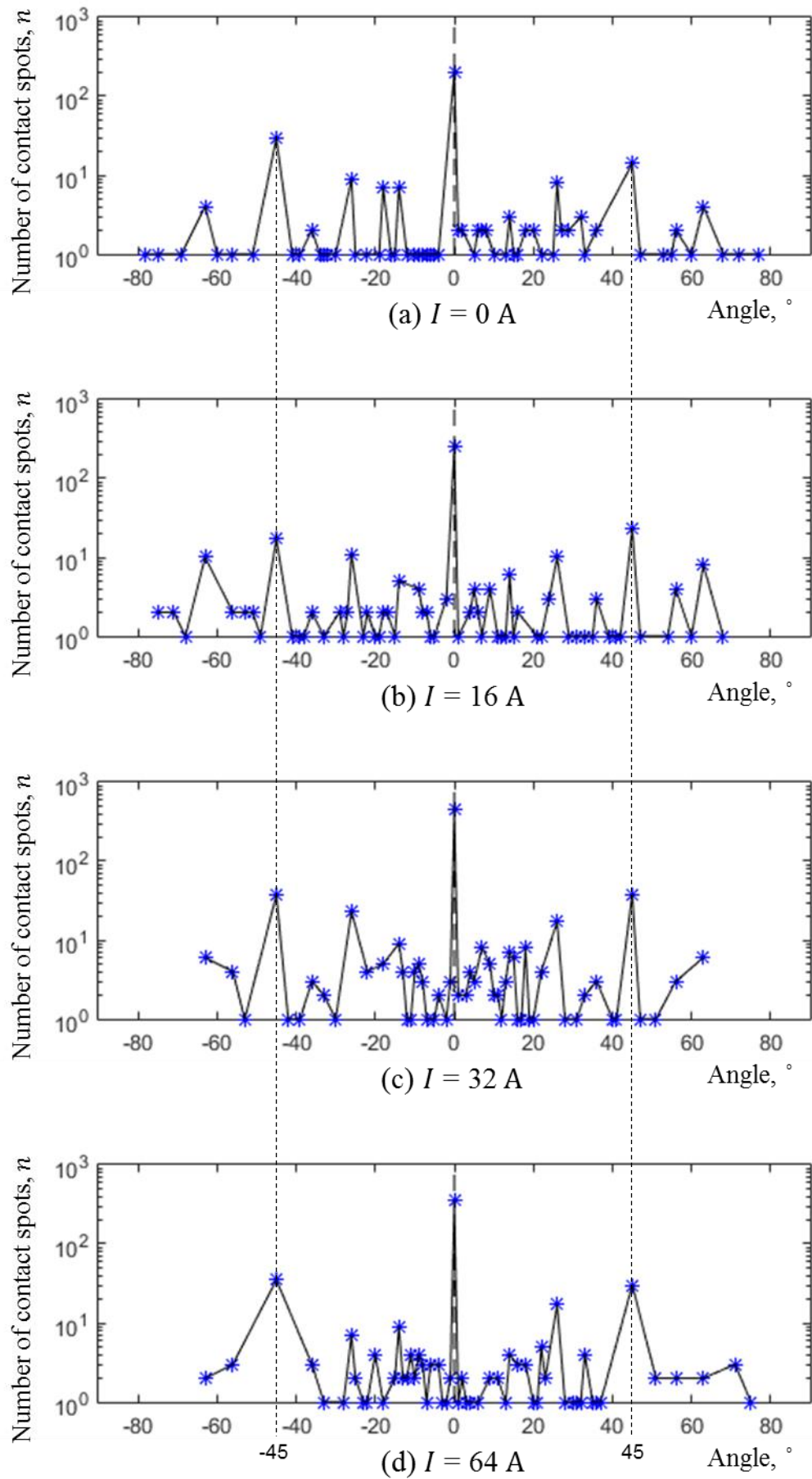


Figure 5.8. Contact spot angle distribution after the four different current loading tests

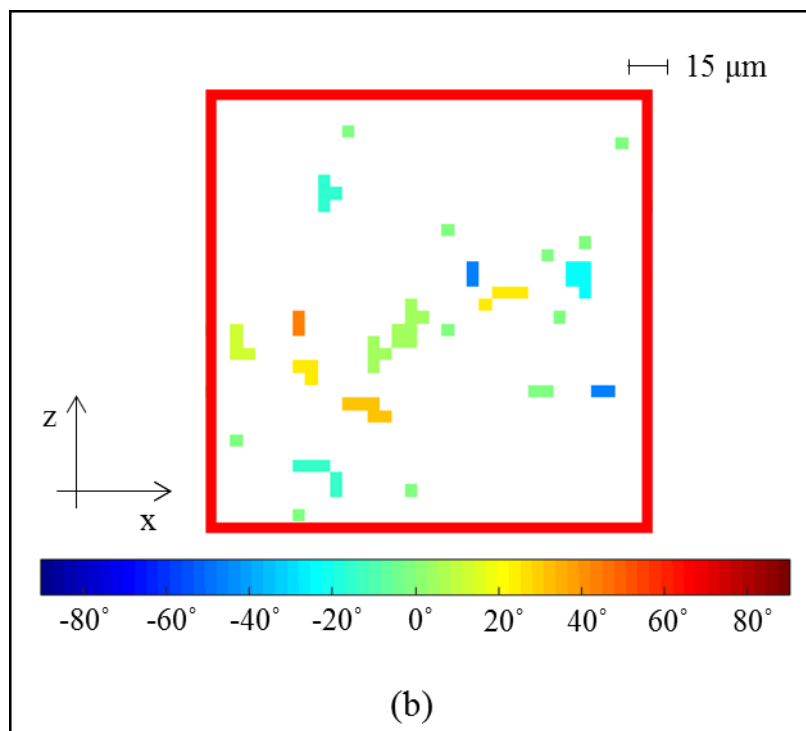
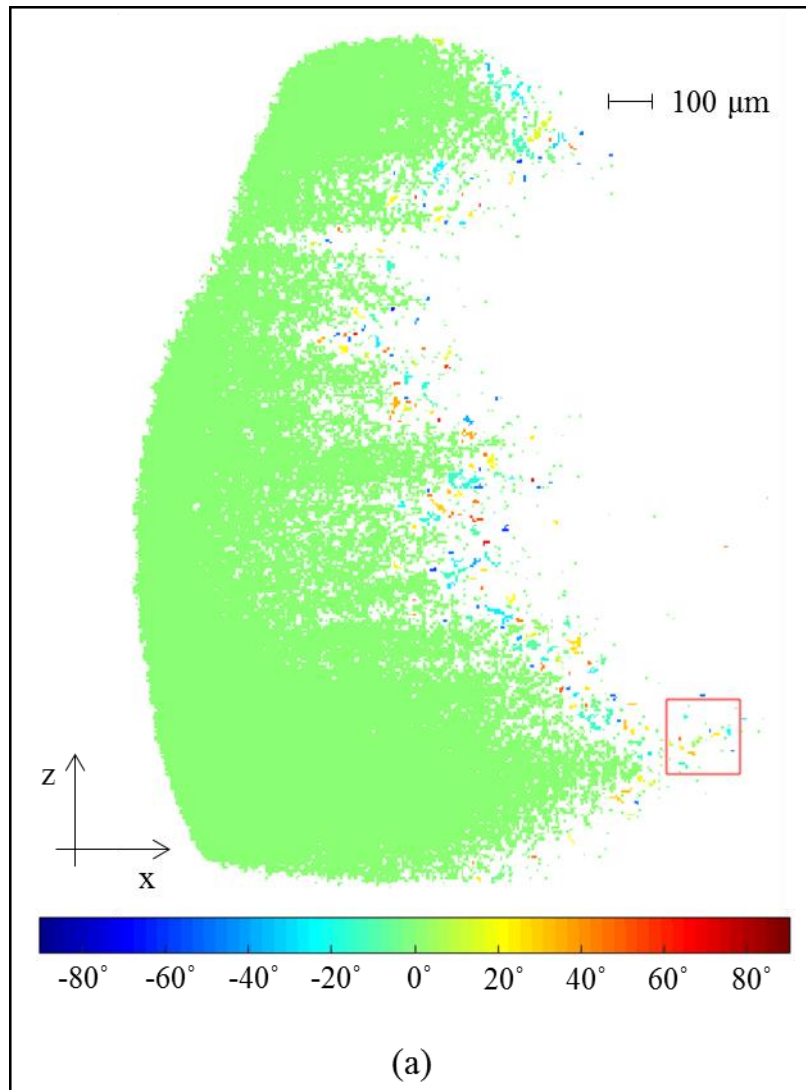


Figure 5.9. (a) 2D angle map of 16 A rated AC single pole rocker switch at 64 A, (b) Close-up view of the red box of 2D angle map

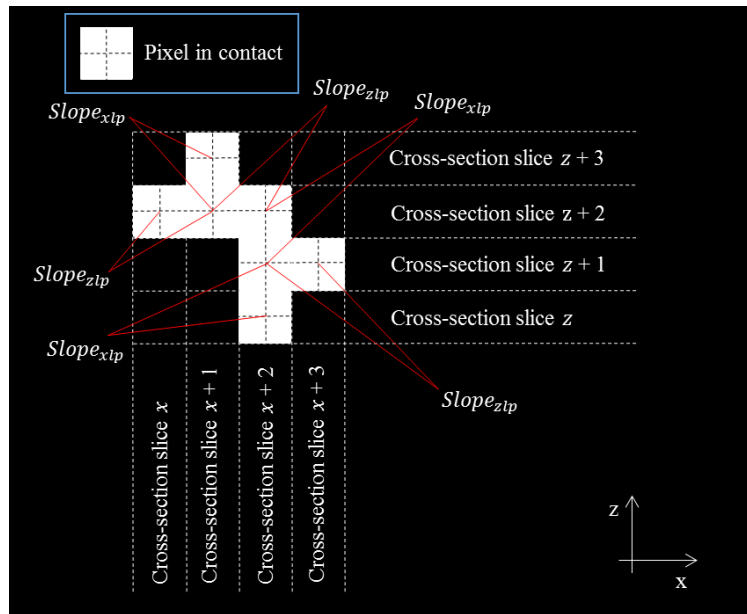


Figure 5.10. Schematic top view of contact spot  $i$ . Explanation of angle calculation

## 5.6 3D Voids Visualisation and Their Volume Distribution

### 5.6.1 Voids visualisation

3D volume analysis of the voids is also conducted using the oriented 3D volume of interest of the 16 A rated AC single pole rocker switch after the four different current loading tests which were presented in Section 4.5.3. Figure 5.11 illustrates the microscopic 3D voids between the two conductors (A and B) within the 16 A rated AC single pole rocker switch after the 64 A current loading test. The red void presented in Figure 5.11 is the largest in volume. A close-up view of this void is illustrated in Figure 5.12. The visualisation of 3D voids in both figures (Figure 5.11 and Figure 5.12) is made by using the CATVis.

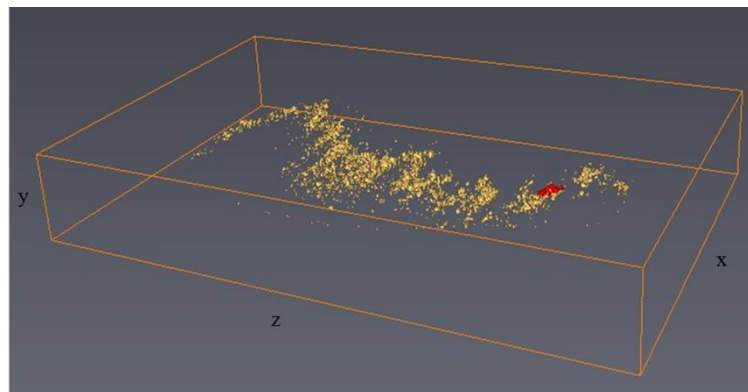


Figure 5.11. 3D voids of 16 A rated AC single pole rocker switch after the 64 A current loading test with bounding box dimensions of  $1.69 \times 0.42 \times 2.61$  mm

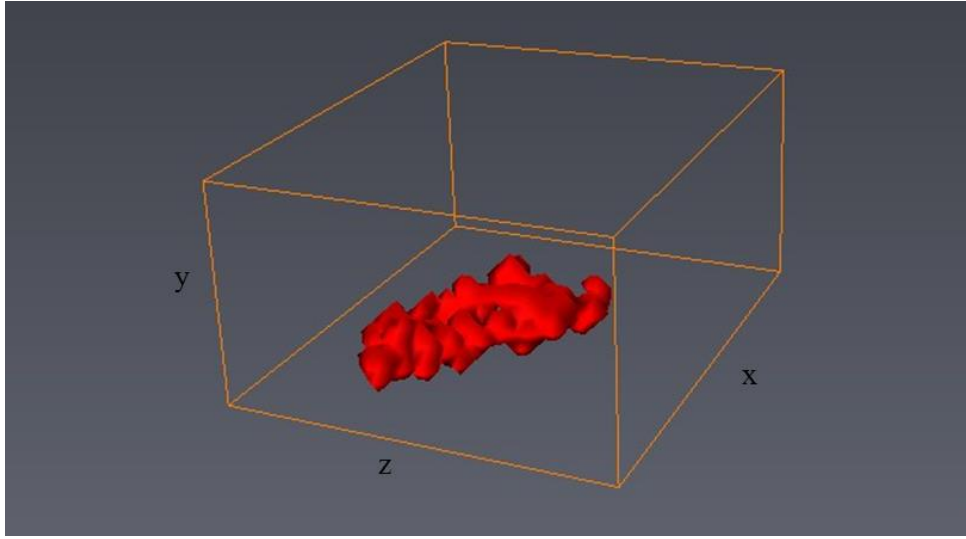


Figure 5.12. Close-up view of the largest void of the 16 A rated AC single pole rocker switch after the 64 A current loading test with bounding box dimensions of  $0.42 \times 0.20 \times 0.36$  mm

### 5.6.2 Void volume distribution

Figure 5.13 illustrates a set of graphs showing the 3D void volume distribution of the oriented 3D volume of interest (Section 4.5.3) of the 16 A rated AC single pole rocker switch after the four different current loading tests at 0 A, 16 A, 32 A and 64 A. The total volume of voids is calculated using the CATCM. According to CATCM, the volume of each void  $V'_i$ , is defined as the sum of the voxels within the 3D void and multiplied by  $125 \mu\text{m}^3$  (volume of voxel) with  $i \in [1, n_v]$  ( $n_v$ , is the total number of voids). The sum of the volume of 3D voids gives the total volume of voids ( $V'_T$ ) as described from Eq. (5.12).

$$V'_T = \sum_{i=1}^{n_v} V'_i \quad (5.12)$$

The smallest volume of 3D void indicated on the graphs of Figure 5.13 is  $125 \mu\text{m}^3$ , which is the resolution of the technique ( $1 \text{ voxel} = 125 \mu\text{m}^3$ ) and the largest spots ( $V'_L$ ) indicated are several  $\text{mm}^3$  in the volume. The number of 3D voids,  $n_v$  with the smallest volume for each of the oriented 3D volume of interest (at 0 A, 16 A, 32 A and 64 A) is calculated to be 302, 838, 474 and 691 respectively. The values of the total volume ( $V'_T$ ) and the total number of voids ( $n_v$ ) for each oriented 3D volume of interest after each current loading are given in Table 5.4. Where  $V'_L$ , is the largest void across the fit-line.

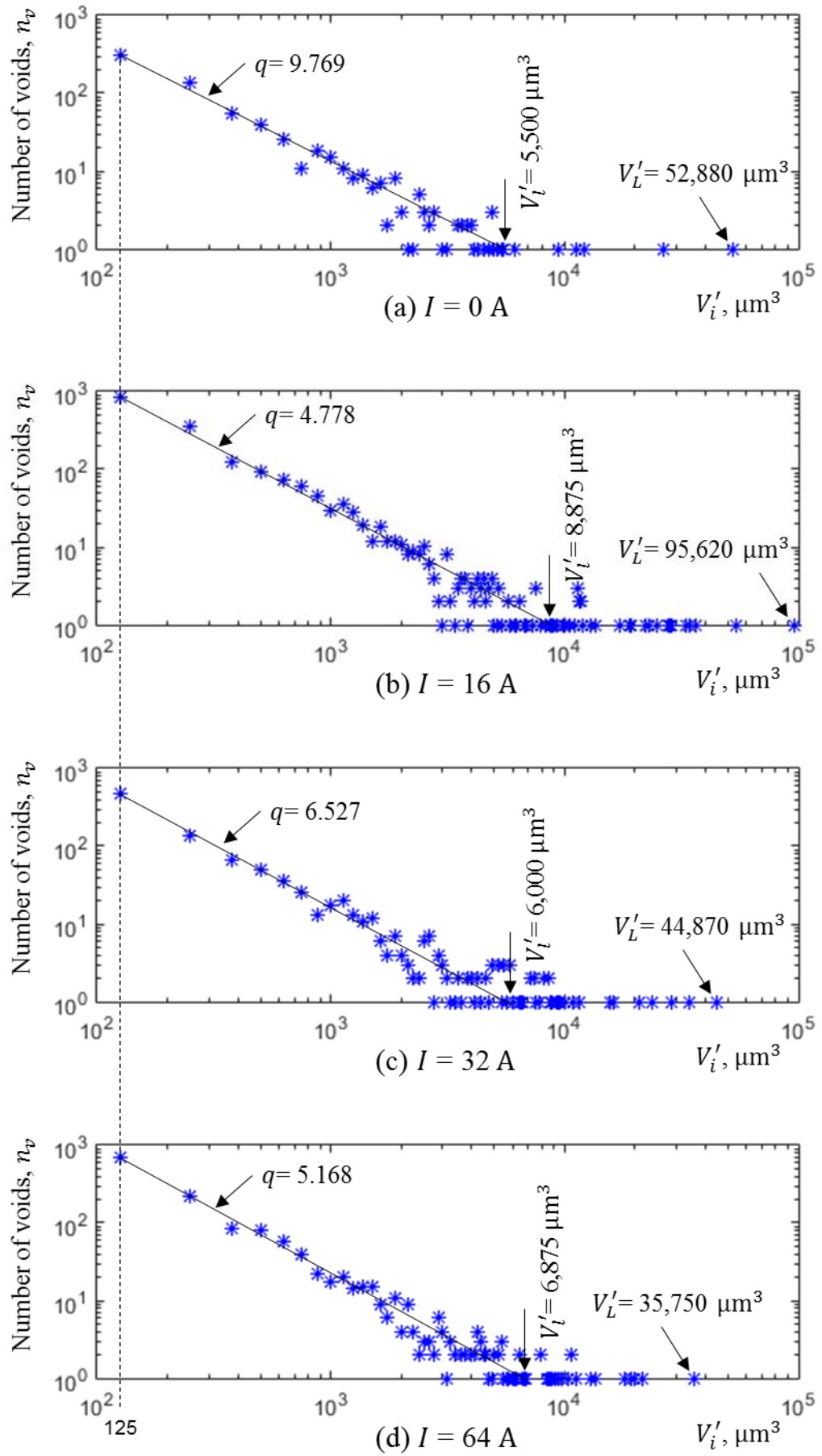


Figure 5.13. Void volume distribution after the four different current loading tests



Table 5.4. Characteristics of 3D voids

Test current (A)	0	16	32	64
Total number of voids	$700 \pm 10$	$1921 \pm 26$	$988 \pm 13$	$1411 \pm 19$
Total volume of voids ( $\times 10^{-12}\text{m}^3$ )	$0.49 \pm 0.01$	$1.82 \pm 0.02$	$0.91 \pm 0.01$	$1.03 \pm 0.01$

## 5.7 Conductors Visualisation and Their Fractal Characteristics

### 5.7.1 Conductors visualisation

The 3D contact map gives the opportunity to visualise each body of the contact system separately as it contains the spots which are the connections of the two bodies. The visualisation can be achieved by subtracting the 3D contact map from the contact system and adding it again back in each body separately. Figure 5.14 and Figure 5.15 show the conductors of the oriented 3D volume of interest (Section 4.5.3) of the 16 A rated AC single pole rocker switch after the 0 A current loading test. Where the red areas on the conductors illustrate the mechanical area of contact. The separation of the two conductors helps to calculate their fractal characteristics.

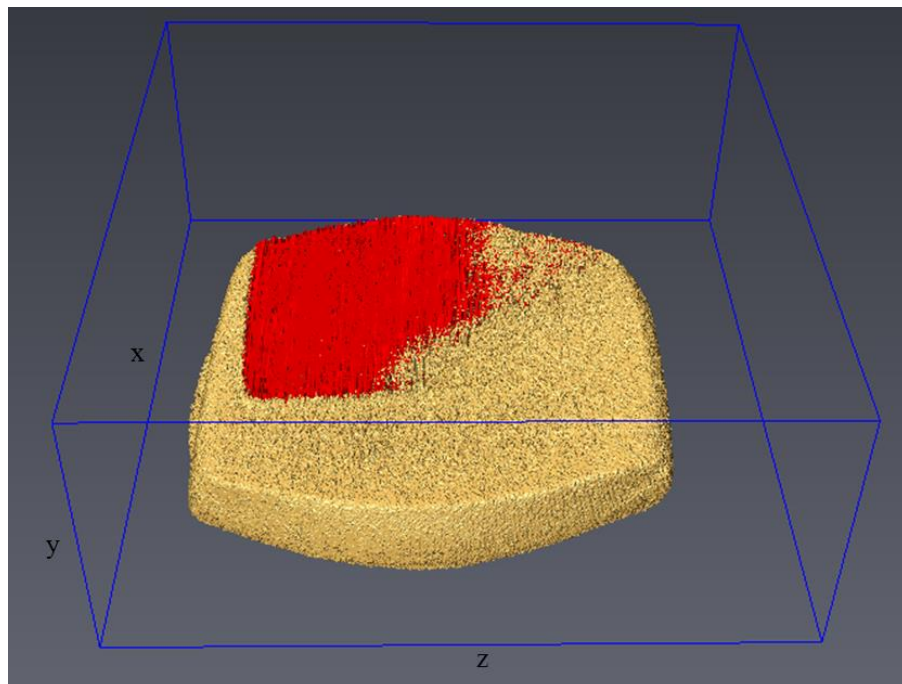


Figure 5.14. Conductor A of the 16 A rated AC single pole rocker switch after the first current loading test at 0 A with bounding box dimensions of  $3.95 \times 1.52 \times 3.62$  mm

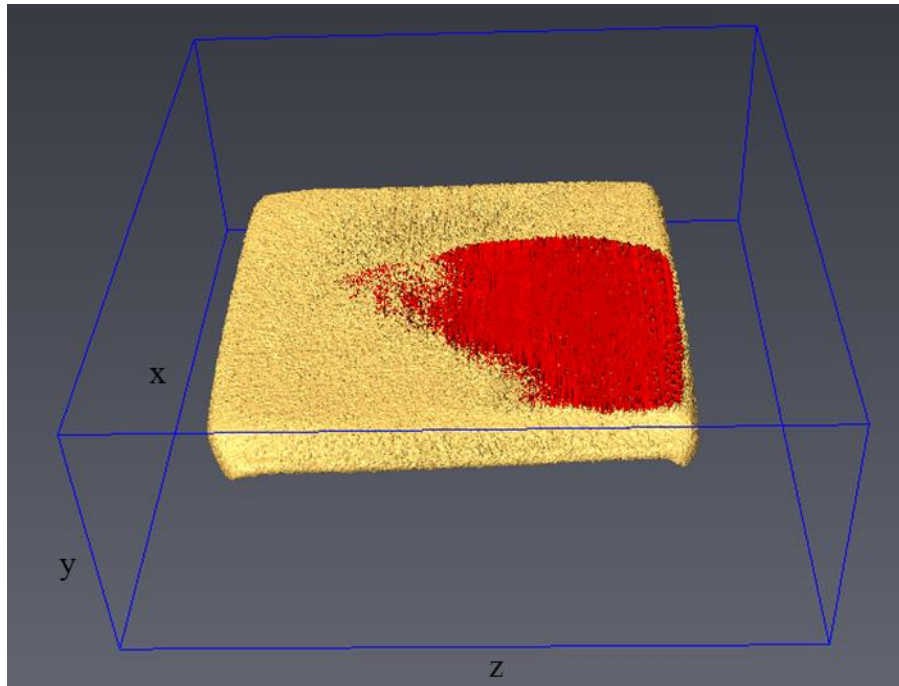


Figure 5.15. Conductor B of the 16 A rated AC single pole rocker switch after the first current loading test at 0 A with bounding box dimensions of  $3.95 \times 1.52 \times 3.62$  mm

### 5.7.2 Conductors fractal characteristics

For the fractal characteristics calculations three different height levels were used and examined for each conductor after each test current loadings at 0 A, 16 A, 32 A and 64 A. The selection of these height levels is based on a reference area point which gives the number of the x-z cross-section slice image with the smallest value of total mechanical area of contact ( $A_T$ ) between the two conductors. The histogram of Figure 5.16 illustrates the reference area point of the oriented 3D volume of interest after 0 A current loading test which is presented with the yellow bar. The bars before the yellow bar belong to Conductor A while the bars after the yellow bar belong to Conductor B. Then, the three x-z cross-section slice images before and the three after the reference area point are selected as different height levels for each conductor. The cyan bars on the histogram of Figure 5.16 represent the x-z cross-section slice images of the two conductors which are set to  $0 \mu\text{m}$  height level while the green and red bars represent the x-z cross-section slice images at  $5 \mu\text{m}$  and  $10 \mu\text{m}$  respectively. The x-z cross-section slice images of Conductor A and Conductor B for the three different height levels selection after the 0 A current loading test are presented in Figure 5.17 and Figure 5.18 respectively. The same procedure used for the selection of the three different height levels in each conductor after the 0 A current loading test is used for the rest current loading tests at 16 A, 32 A and 64 A.

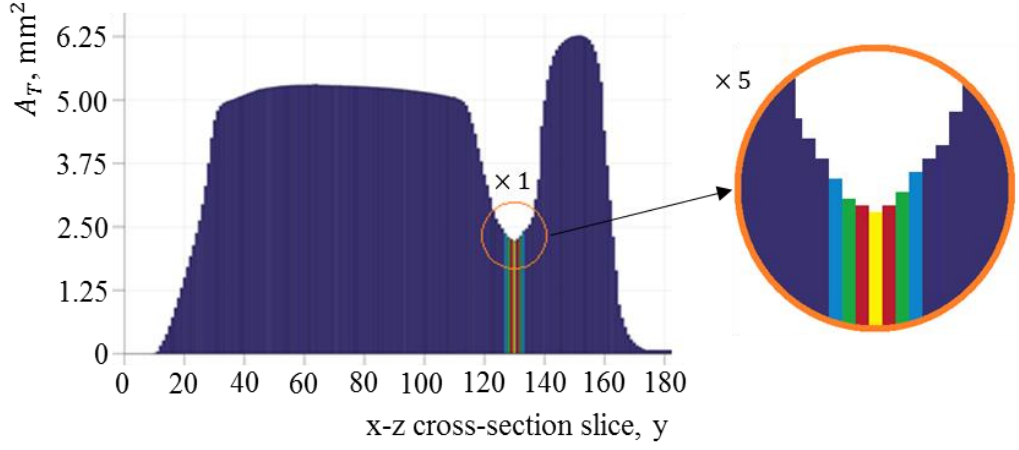


Figure 5.16. Total mechanical area of contact in each x-z cross-section slice image of the oriented 3D volume of interest after the 0 A current loading test

Figure 5.19 and Figure 5.20 are a set of graphs showing the contact spot area cumulative distributions of the two conductors at three different height levels after each current loading test at 0 A, 16 A, 32 A and 64 A. Eq. (5.13) describes the relationship as the contact spot area cumulative distribution function for the number of contact spots ( $N$ ) of a particular area ( $A_i$ ) which are equal or greater than a reference area ( $A_{ref}$ ) [183, 184]. Where  $m_a$ , is defined as the number of contact spots per unit area.

$$N(A_i \geq A_{ref}) = m_a \int_{A_{ref}}^{\infty} f(A_i) dA_i \quad (5.13)$$

Figure 5.21 and Figure 5.22 are a set of graphs showing the contact spot spatial cumulative distributions of the two conductors at three different height levels after each current loading test at 0 A, 16 A, 32 A and 64 A. The spatial difference between contact spots can be defined by several methods [180]. In this research, the spatial difference between contact spots  $i$  and  $j$  is defined as the distance  $d_{ij}$  between the mean-points of contact spots as explained in Section 5.4.3. Eq. (5.14) describes the relationship as the contact spot spatial cumulative distribution function for the number of contact spots ( $N_d$ ) less than or equal to a reference distance ( $d_{ref}$ ) [180, 183]. Where  $m_d$ , is defined as the number of contact spots per unit distance.

$$N_d(d_{ij} \leq d_{ref}) = m_d \int_{-\infty}^{d_{ref}} f(d_{ij}) dd_{ij} \quad (5.14)$$

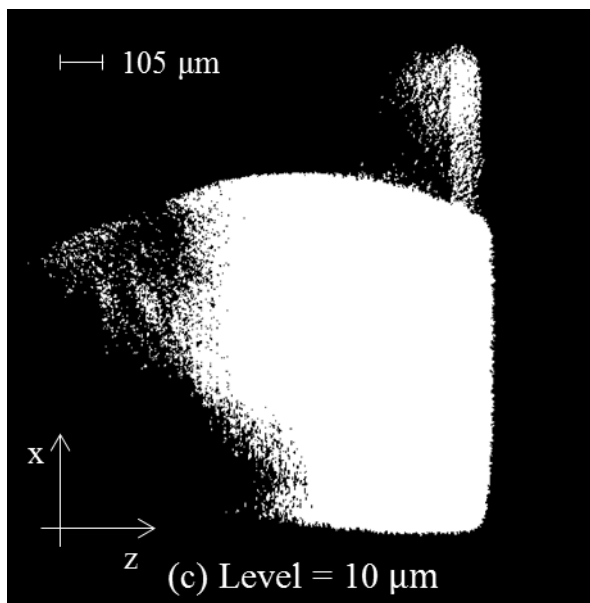
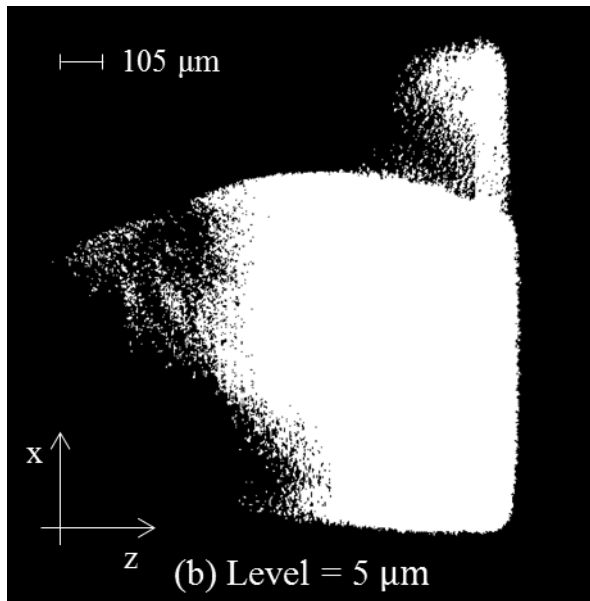
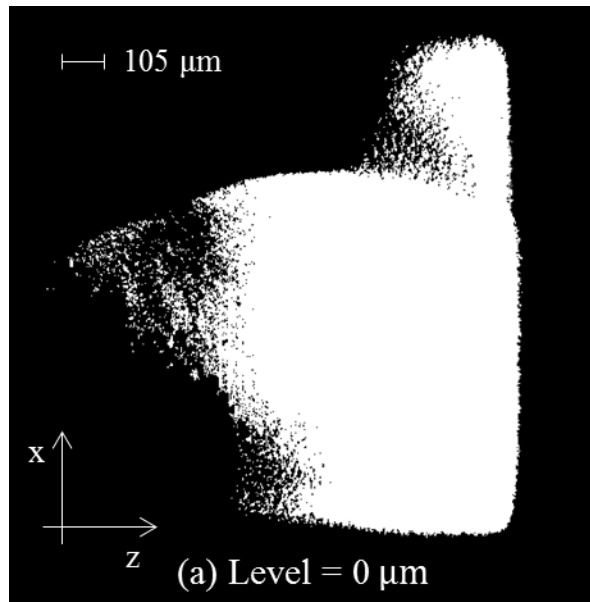


Figure 5.17. Cross-section slice images of Conductor A for the three different height levels selection after the 0 A current loading test

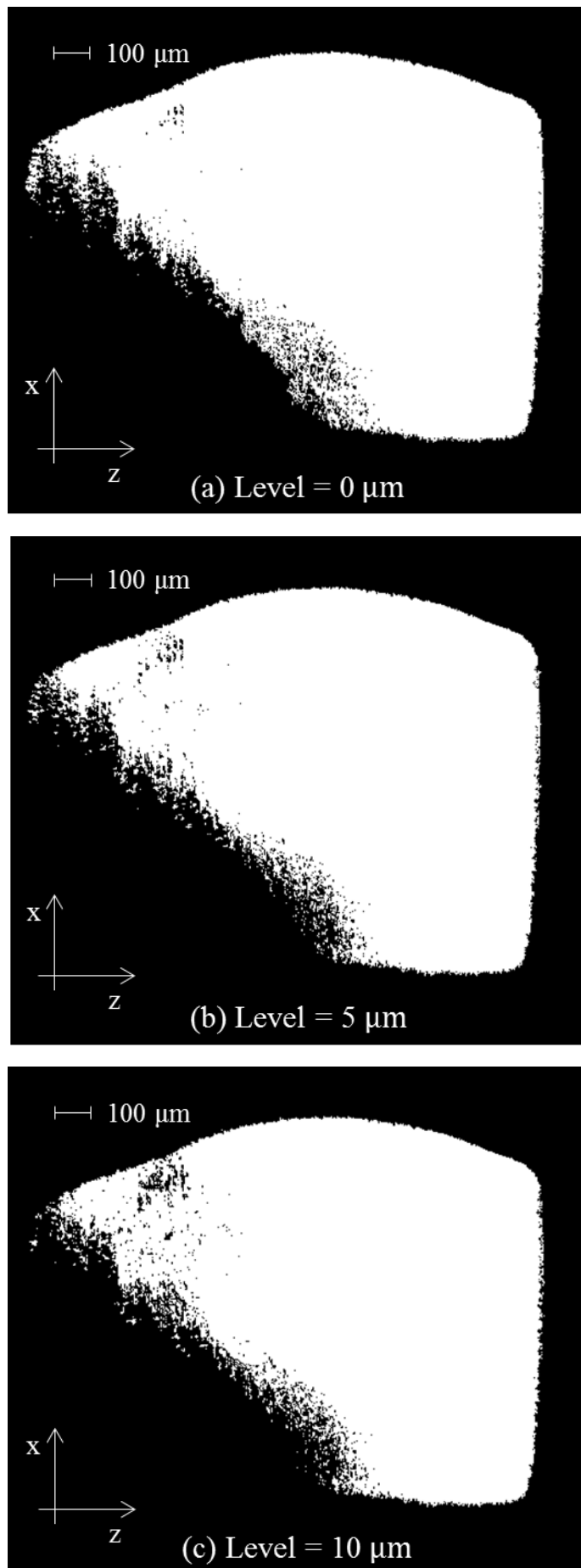


Figure 5.18. Cross-section slice images of Conductor B for the three different height levels selection after the 0 A current loading test

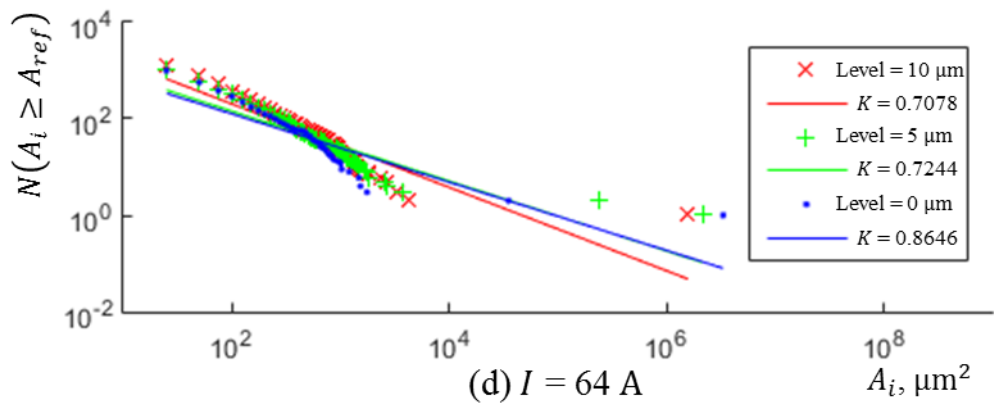
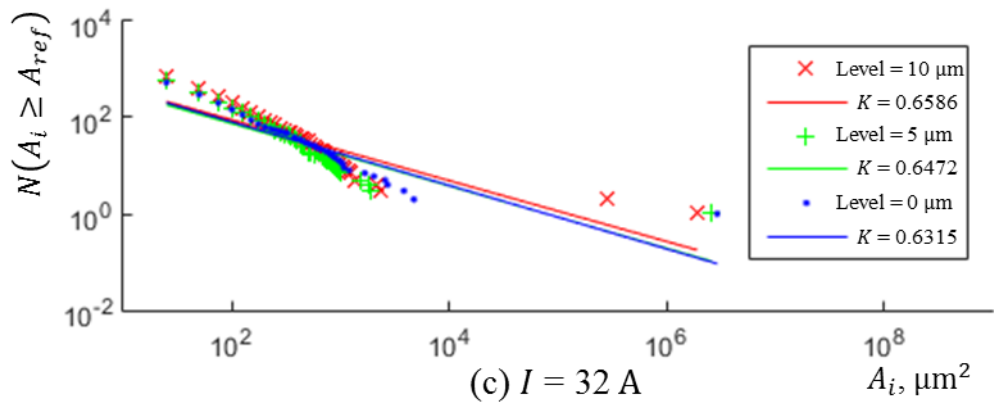
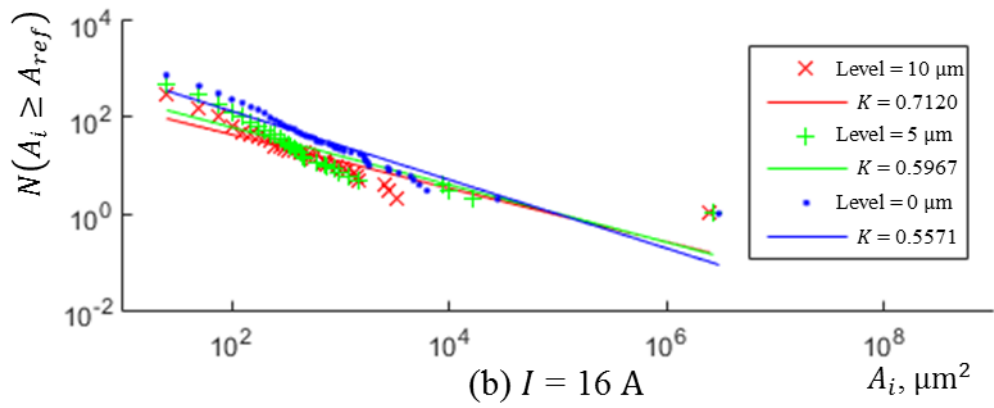
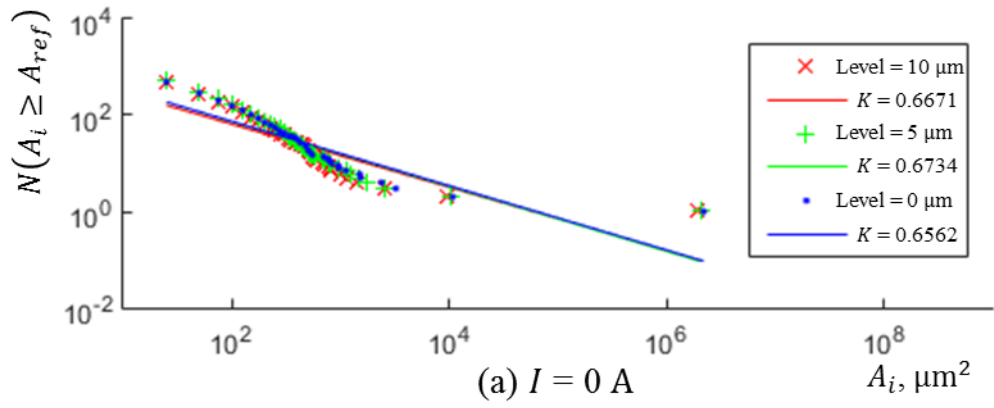


Figure 5.19. Contact spot area cumulative distributions according to different scales of Conductor A after the four different current loading tests. Where  $K$ , is the slope of the fitting line

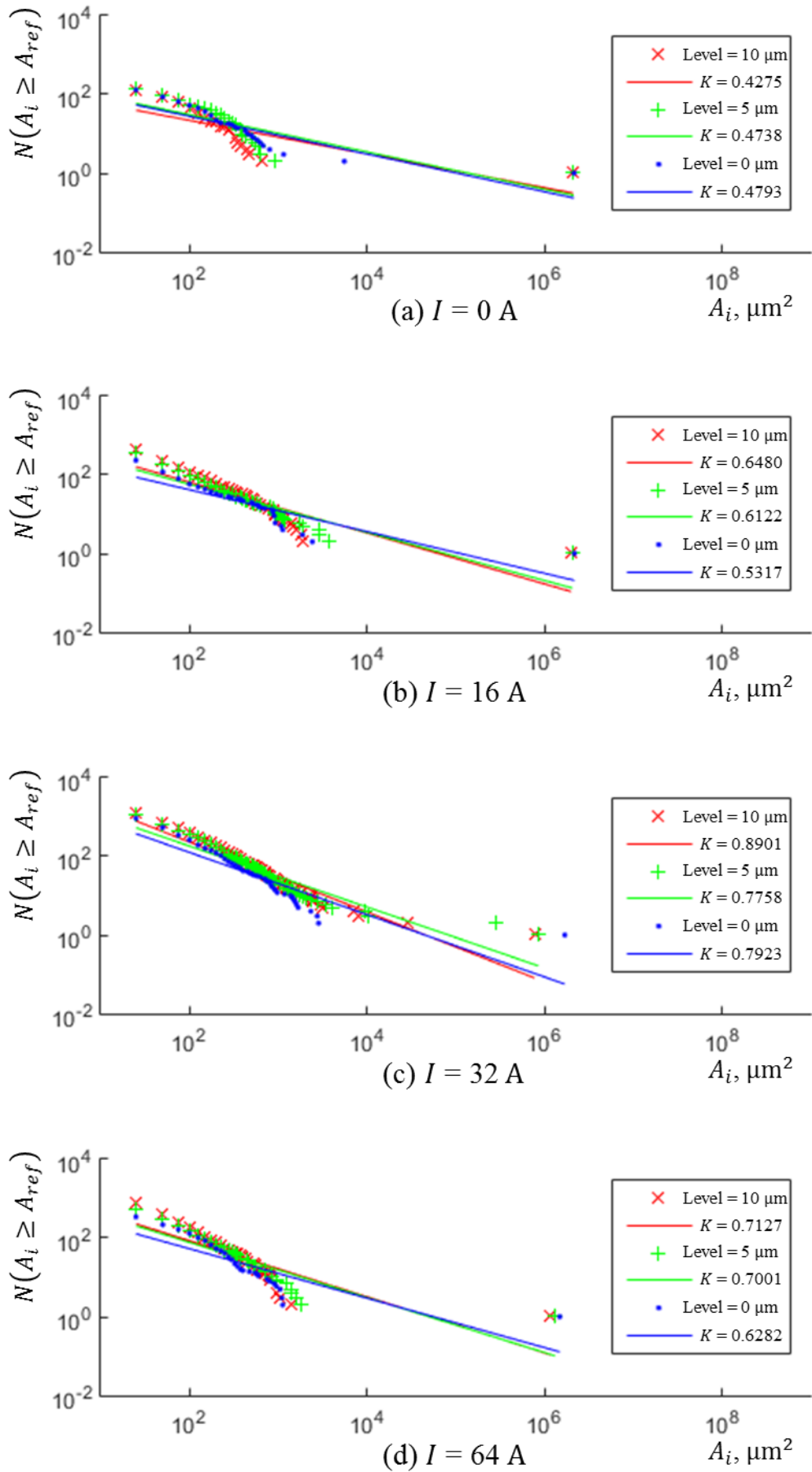


Figure 5.20. Contact spot area cumulative distributions according to different scales of Conductor B after the four different current loading tests. Where  $K$ , is the slope of the fitting line

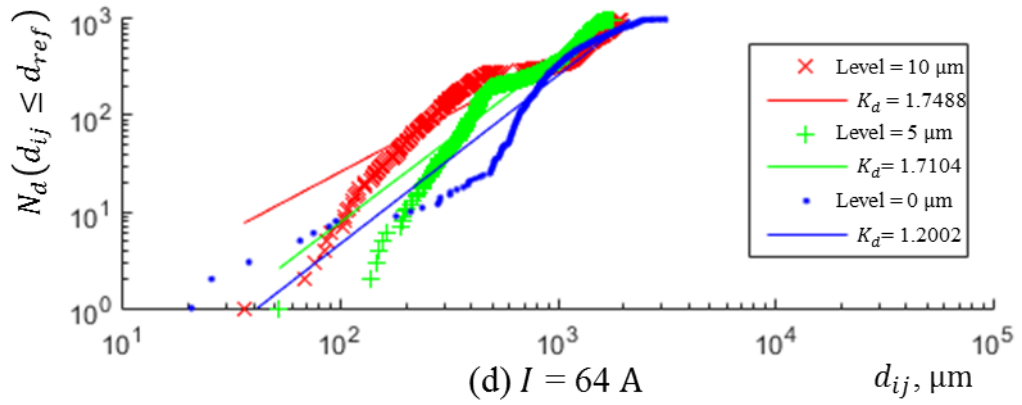
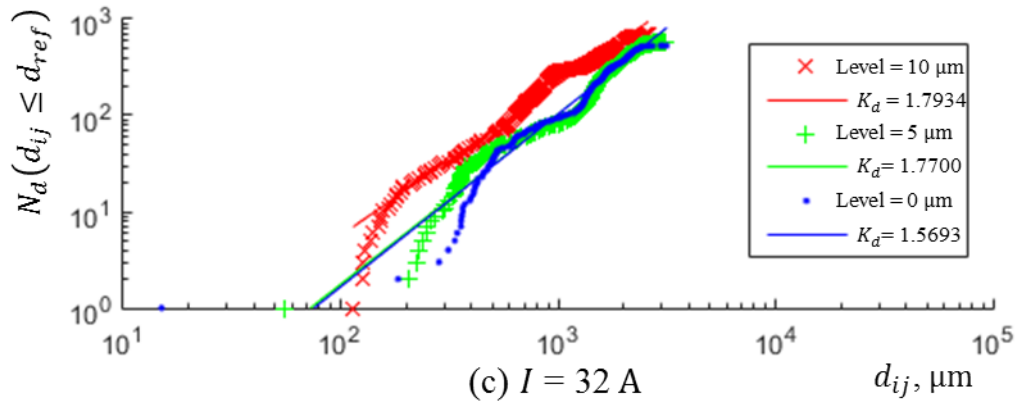
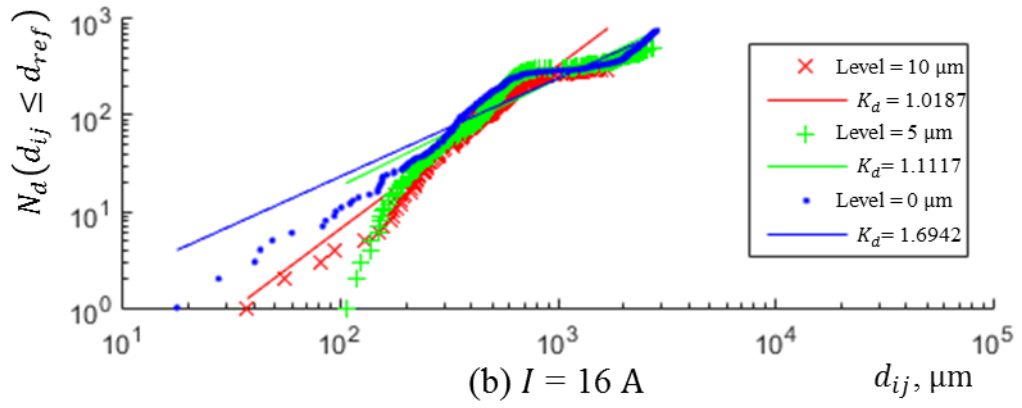
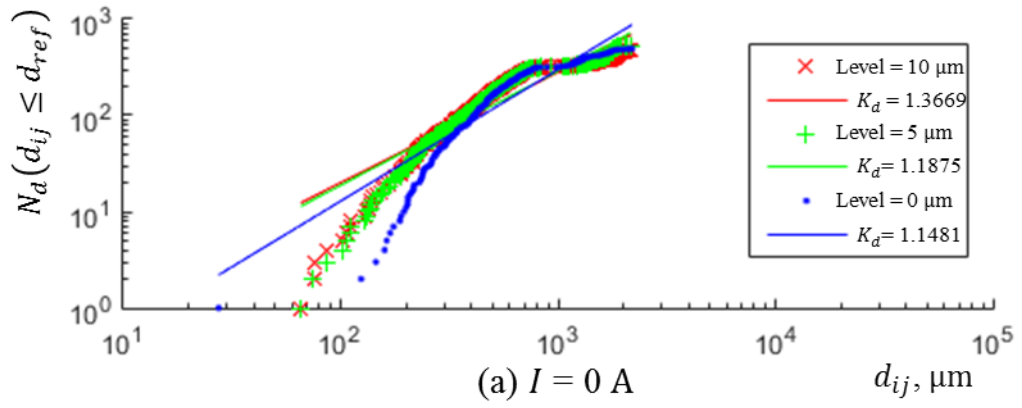


Figure 5.21. Contact spot spatial cumulative distributions according to different scales of Conductor A after the four different current loading tests. Where  $K_d$ , is the slope of the fitting line



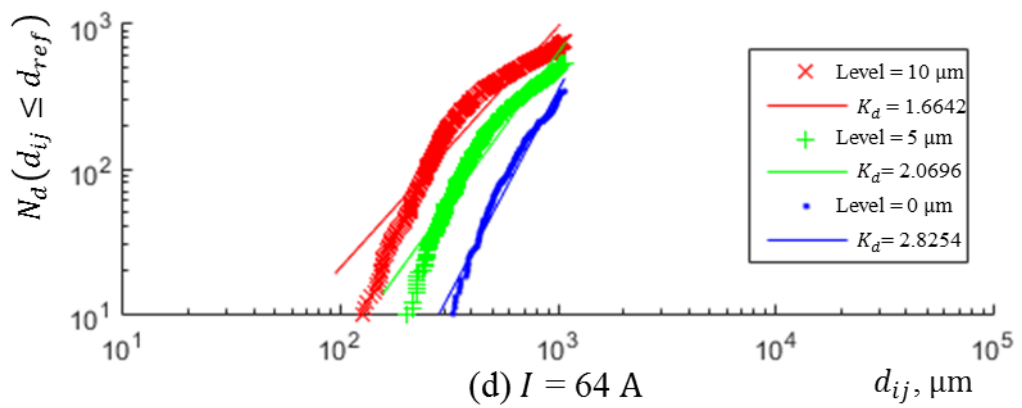
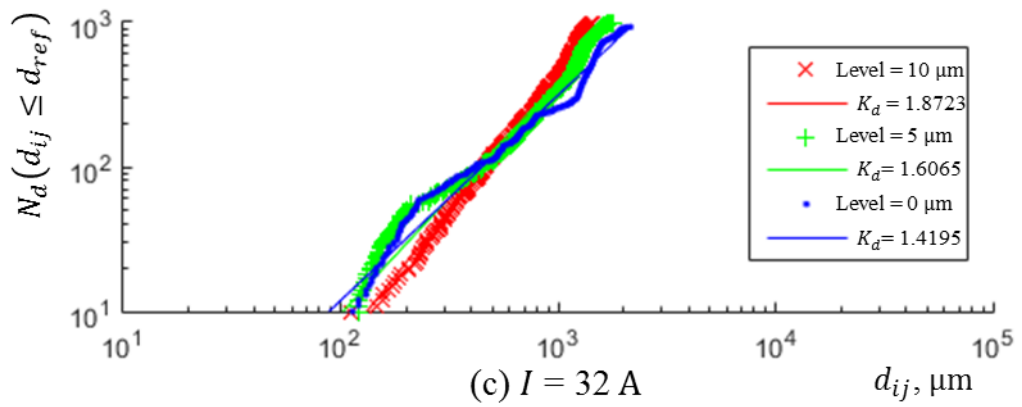
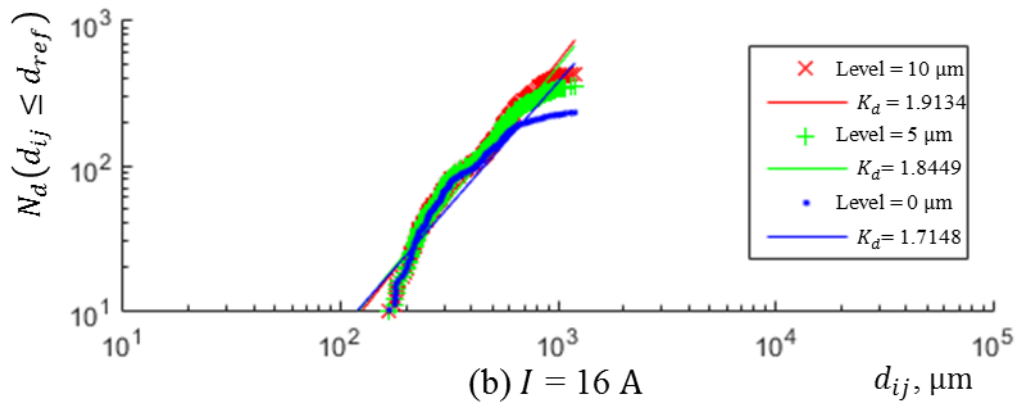
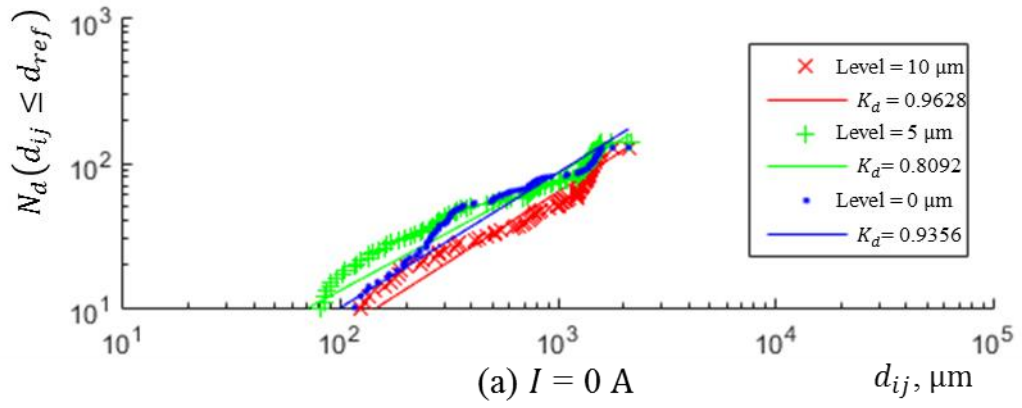


Figure 5.22. Contact spot spatial cumulative distributions according to different scales of Conductor B after the four different current loading tests. Where  $K_d$ , is the slope of the fitting line

## 5.8 Discussion

### 5.8.1 *The X-ray CT technique*

The results show that the X-ray CT technique is a useful tool for viewing the contact interface and the voids between the contact system without dismantling it and determining their characteristics. These characteristics include the total mechanical area of contact, the number of contact spots and the area of each contact spot, the total volume of voids, the number of voids and the volume of each void as well as the total contact resistance. In addition, the X-ray CT technique gives the possibility to determine and characterise the fractal characteristics of any cross-section slice image. The images (experimental data of a 16 A rated AC single pole rocker switch which was presented in Section 4.5) obtained with the current facility give a pixel resolution of  $5\ \mu\text{m} \times 5\ \mu\text{m}$  and an area resolution of  $25\ \mu\text{m}^2$  which is  $5\frac{1}{2}$  and  $1\frac{3}{5}$  times higher in resolution than previous work [185] and Swingler work [149, 181] on different facilities respectively.

Resolution is an important factor for the visualization and calculation techniques. For example, for a coarse measurement (e.g.  $100\ \mu\text{m}$ ) of resolution, only a few contact spots of large curvature are visualized while for smaller measurement (e.g.  $0.1\ \mu\text{m}$ ) of resolution, more contact spots of smaller curvature are visualized [122, 181]. The smallest resolution which can be obtained by the current facility is  $3\ \mu\text{m}$ . This depends on the sample dimensions and X-ray admittance of the sample materials. The resolution of  $5\ \mu\text{m}$  obtained in this research is the optimum that could be achieved with the sample configuration used. Ideally, a resolution in the order of  $0.1\ \mu\text{m}$  is needed to investigate a Greenwood-Williamson model of the asperities [63]. However, it should be noted that the Contact Analysis Techniques or CAT\* developed and implemented within a suite of tools in this chapter can be used with data of finer resolution. Nonetheless, some interesting features have been found with the data obtained which are discussed below.

### 5.8.2 *The 2D and 3D mapping techniques*

Analysis and modelling techniques are developed to produce 3D contact maps of an electrical contact interface which for the first time gives information as to where the electrical contacts in a 3D volume are located to a microscopic resolution. The mathematical modelling at the contact spots is described by Eq. (5.1). The equation

describes a line segment or a series of line segments through each contact spot and every contact spot at the interface.

Contact maps are visualized for different electric current values in 2D (Figure 5.5) and 3D (Figure 5.6) after four different current loading tests at 0 A, 16 A, 32 A and 64 A. In this research the results of these different loading tests are categorised into normal operation and non-normal operation. The normal operation includes the current loading tests at 0 A and 16 A as the single pole rocker switch is rated at 16 A AC. The non-normal operation includes the 32 A and 64 A current loading test as these current values are out of the single pole rocker switch current limits.

The analysis of the contact map data (Table 5.2 from 2D mapping technique and Table 5.3 from 3D mapping technique) at normal operation (from 0 A to 16 A) shows that the number of contact spots and the total mechanical area of contact are bigger at the higher current (16 A) irrespective of whether the 2D mapping technique or the 3D mapping technique is used. The contact resistance, thus, is smaller after the sample has been stressed with the 16 A current loading. This is indicating that current stressing a contact system increases the number of smaller spots and the dispersion of those spots. This may be due to local heating and melting at the contact spots causing them to come together. These are only initial results as more samples need to be investigated.

The analysis of the contact map data (Table 5.2 from 2D mapping technique and Table 5.3 from 3D mapping technique) from normal operation to non-normal operation (from 16 A to 32 A) shows that the number of contact spots is bigger and the total mechanical area of contact is smaller at the higher current (32 A) irrespective of whether using the 2D mapping technique or the 3D mapping technique. The contact resistance is smaller after the sample has been stressed with the 32 A current loading. This is indicating that current stressing a contact system increases the number of smaller spots and the dispersion of those spots. This may be due to local heating and melting at the plastic which holds the spring on the Conductor A (see Figure 4.1) causing it to move.

The analysis of the contact map data (Table 5.2 from 2D mapping technique and Table 5.3 from 3D mapping technique) at non-normal operation (from 32 A to 64 A) shows that the number of contact spots is smaller and the total mechanical area of contact

is bigger at the higher current (64 A) irrespective of whether using the 2D mapping technique or the 3D mapping technique. The contact resistance is bigger after the sample has been stressed with the 64 A current loading. This is indicating that current stressing a contact system decreases the number of smaller spots and the dispersion of those spots. This is probably due to local heating and melting at the plastic which hold the two conductors causing them to move and come together. It is important to note that the fourth scan is conducted after current loading at 64 A for 2 hours comparing with the other scans which are conducted after current loading at 0 A, 16 A and 32 A for 24 hours. This is because the switch was not current loaded for more than 2 hours as the heat of the current would damage it.

### 5.8.3 *Loss of information with 2D contact maps*

Comparing the 2D mapping technique with the 3D mapping technique shows some points that need to be noted since the data in Table 5.2 and data in Table 5.3 are different. The number of contact spots after each current loading test at 0 A, 16 A, 32 A and 64 A A produced by the 2D mapping technique is smaller comparing with the 3D mapping technique. This difference is a result of an issue which the 2D contact mapping technique presents.

This issue, given the label of Overlapping Void Disaggregation Error (OVDE), is where overlapping voids in the y-direction (and associated multiple contact spots visualized in 3D) mask contact spots when seen in 2D visualizations. This is a result of the contact interface in reality being a 3D surface and when analysed with the 2D mapping technique the height (y-direction) information of that x-z surface is omitted from the data. The explanation of this issue is illustrated in Figure 5.23. Figure 5.23(a) shows the schematic cross-section slice image of Body A and Body B which are coming in mechanical contact. The white areas of the schematic cross-section slice image between the two bodies are indicating open voids and closed voids. Where contact spot 1 is the mechanical contact created by the top surfaces at the peaks of the two bodies and contact spot 2 is the mechanical contact created by portions of side surfaces of the peaks of two bodies. Figure 5.23(b) shows the 2D contact mapping technique which illustrates only the contact spot 1. The 3D contact mapping technique in Figure 5.23(c) in contrast to Figure 5.23(b) illustrates all the contact spots which are presented in Figure 5.23(a) (contact spot 1 and contact spot 2). Due to the OVDE of the 2D mapping technique, this results in less

contact spots and also smaller total mechanical area of contact compared to the 3D mapping technique.

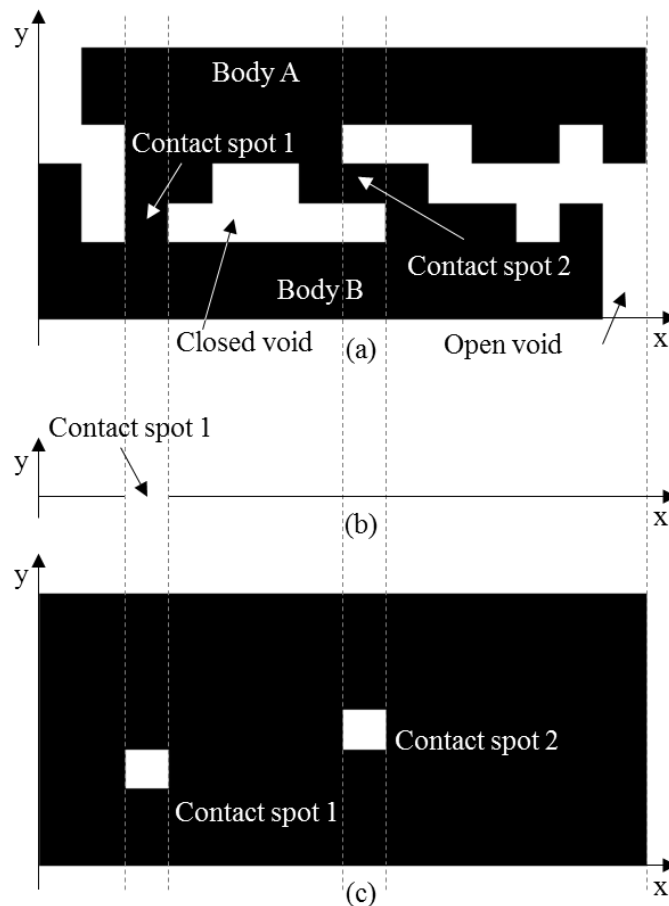
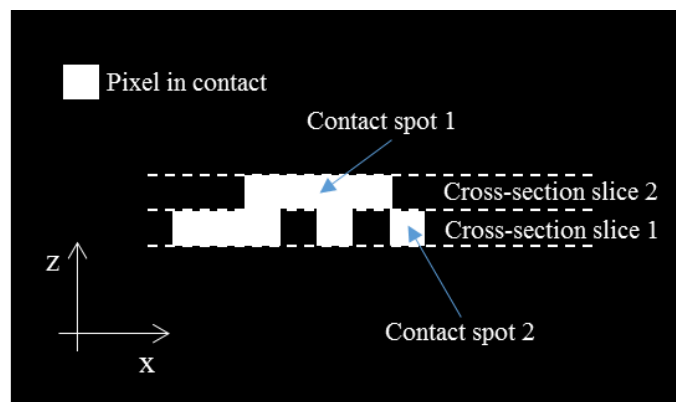


Figure 5.23. Peak and side contact spots. Schematic cross-section slice of (a) Bodies A and B, (b) 2D contact mapping technique and (c) 3D contact mapping technique [75]

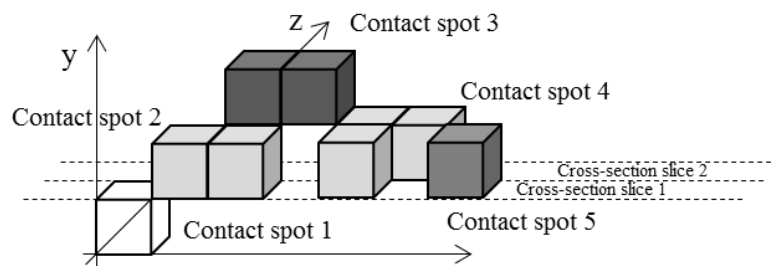
In previous work [75], it is reported that the 2D contact mapping technique presents another issue, the Neighbouring Contact Spot Aggregation Error (NCSAE). This issue is presented when the method of Lalechos [7] for grouping pixels to contact spots is used. According to this method, a contact spot is defined as the collection of contacting pixels which are neighbouring with other pixels by at least one of their sides. It is important to mention that a contacting pixel which is only diagonal with a neighbour contacting pixel belonging to a contact spot and is not considered to be a part of that spot (see the contact spots in Figure 5.24(a)).

NCSAE is where multiple neighbouring contact spots as visualized in 3D are seen as one contact spot in 2D visualizations. This is a result of the contact interface in reality being a 3D surface and when analysed with the 2D mapping technique the height (y-

direction) information of that x-z surface is omitted from the data. The explanation of this issue is illustrated in Figure 5.24. Figure 5.24(a) shows the 2D contact mapping technique of two contact spots which are developed by two cross-section slice images and consist of 8 and 1 contacting pixels respectively. The contact spots shown in Figure 5.24(a) are presented in Figure 5.24(b) in the 3D contact mapping technique as 5 contact spots. For the definition of contact spot in 3D contact maps, a technique used in 2D contact maps is used as well. A contact spot in the 3D contact map is defined as a collection of contacting voxels which are neighbouring other contacting voxels with at least one of their sides. Contact spot 1 in Figure 5.24(b) consists of only 1 contacting voxel, contact spot 2 consists of 2 contacting voxels, contact spot 3 consists of 2 contacting voxels, contact spot 4 consists of 3 contacting voxels and contact spot 5 consists of only 1 contacting voxel. Due to the NCSAE of the 2D mapping technique, this results in less small contact spots but same total mechanical area of contact compared to the 3D mapping technique.



(a)



(b)

Figure 5.24. Schematic contact spots in (a) 2D contact map and (b) 3D contact map [75]

It is important to note that the NCSAE is not affected in this research as the contacting pixels (or voxels) are grouped to contact spots using a different method, as explained in Section 5.4.2. Moreover, it is reported that the method used in this research

shows that the pixels or voxels which are connected diagonally are part of the same contact spot as they belong to the same contact asperity [132, 186].

#### 5.8.4 Total mechanical area of contact findings

The total mechanical area of contact after each current loading test at 0 A, 16 A, 32 A and 64 A using the 2D contact mapping technique is found to be 1.8210 mm<sup>2</sup>, 2.0052 mm<sup>2</sup>, 0.7359 mm<sup>2</sup> and 1.1692 mm<sup>2</sup> with an error of  $\pm 1.366$  % (the error is calculated in Section 4.5.2) respectively. The total mechanical area of contact after each current loading test at 0 A, 16 A, 32 A and 64 A using the 3D contact mapping technique is found to be 1.8277 mm<sup>2</sup>, 2.0135 mm<sup>2</sup>, 0.7359 mm<sup>2</sup> and 1.1741 mm<sup>2</sup> with an error of  $\pm 1.366$  % respectively. The total mechanical area of contact after each current loading test at 0 A, 16 A, 32 A and 64 A using the 2D contact mapping technique is smaller but within the error limits after each corresponding current loading test when using the 3D contact mapping technique. Comparing the corresponding values of the total mechanical area of contact in Table 5.2 and Table 5.3 it is obvious that they are very close with very small difference. At this point, it is important to mention that Lalechos *et al.* [148] reported that the result of the calculation of the total mechanical area of contact using 2D contact mapping technique gives values close to experimental findings using Bowden and Tabor [128] formula (Eq. (2.13)).

#### 5.8.5 Contact resistance findings

The contact resistance is calculated using two different approaches, the CAAGR and CAACHR for both, 2D and 3D contact mapping techniques. The results of the two approaches in each contact mapping technique in Table 5.2 and Table 5.3 show that they give the same value after each current test 0 A, 16 A, 32 A and 64 A. However, these results after the sixth decimal digit are different and the difference between them is very small. This small difference may be the result of the technique used to calculate the distances between the contact spots. For practical reasons the calculation of the distance  $d_{ij}$  between the contact spot  $i$  and contact spot  $j$  is calculated from the mean-points of the contact spots  $i$  and  $j$  as described in [75]. Greenwood [66], reported that  $d_{ij}$  is the distance between contact spots  $i$  and  $j$ . Investigating this it's clear that Greenwood means  $d_{ij}$  is the minimum distance between the contact spots  $i$  and  $j$ . However, the difference is very small and the CATGR could be used as it is.

The contact resistance after each current loading test at 0 A, 16 A, 32 A and 64 A using the 2D contact mapping technique is calculated to be bigger when using the 3D contact mapping technique. The difference in corresponding values in 2D and 3D contact maps is a result of the OVDE issue analysed beforehand in Section 5.8.3. According to Greenwood [66], the contact resistance when using Eq. (2.23), depends on the number of contact spots, the radius of each contact spot and the distances between them.

#### 5.8.6 Contact spot area distribution findings

The graphs of contact spot area distribution in Figure 5.7 show that the contact spots follow the same distribution after each current test 0 A, 16 A, 32 A and 64 A. These graphs can be compared with the corresponding graphs in Swingler and Lalechos work [149] which visualised the contact area in 2D contact maps under different contact forces. The results show that the area of contact spots follow the same distribution in both situations. The smallest contact spot indicated on the graphs of Figure 5.7 is  $25 \mu\text{m}^2$ , which is the resolution of the technique (when a pixel length is  $5 \mu\text{m}$ ) and the largest contact spots indicated are several  $\text{mm}^2$ .

Moreover, it can be seen that each graph of Figure 5.7 consists of two regimes. The first where the contact spot area distribution follows a power relationship with a slope between  $2.569 \leq q \leq 3.659$  and the second is for a small number of particularly large contact spots in area with a slope approximately equal to zero. The slope is given by Eq. (5.15).

Table 5.5 presents the slope ( $q$ ) and constant ( $C$ ) of Eq. (5.15) after each current loading test at 0 A, 16 A, 32 A and 64 A for the first regime of graphs of Figure 5.7. The constant ( $C$ ) value in log-log graphs of Figure 5.7 after each current loading test represents the number of contact spots ( $n$ ) who have area equal with  $1 \mu\text{m}^2$ . In this research, the area of  $1 \mu\text{m}^2$  does not exist as the smallest area of a contact spot is  $25 \mu\text{m}^2$  (area of pixel). In addition, the graphs of Figure 5.7 show that the transition between the two regimes in each current loading test at 0 A, 16 A, 32 A and 64 A occurs at  $775 \mu\text{m}^2$ ,  $875 \mu\text{m}^2$ ,  $925 \mu\text{m}^2$  and  $1,000 \mu\text{m}^2$  respectively.

$$n(A_i) = CA_i^{-q} \quad (5.15)$$



Table 5.5. Characteristics of the first regime of the contact spot area distribution after each current loading test at 0 A, 16 A, 32 A and 64 A

Test current (A)	0	16	32	64
Slope ( $q$ )	3.659	3.340	2.569	2.847
Constant ( $C$ )	$100 \times 10^6$	$40 \times 10^6$	$4 \times 10^6$	$10 \times 10^6$

### 5.8.7 Contact spot angle distribution findings

The graphs of contact spot angle distribution in Figure 5.8 show that the contact spots follow same the distribution after each current test 0 A, 16 A, 32 A and 64 A. These distributions which their points (points in graphs) are connected with lines present peaks and valleys like spectral density plot with angular frequency [121, 187]. The distribution in negative axis can be characterised as a reflection in positive axis and vice versa.

In addition, the graphs in Figure 5.8 show that the maximum number of contact spots have an angle equal with  $0^\circ$  and the angles with values equal to  $-45^\circ$  and  $45^\circ$  are follow in number of contact spots. The reason for the maximum number of contact spots who have an angle equal with  $0^\circ$  is based on the fact that contact spots with area 1 pixel (or  $25 \mu\text{m}^2$ ) are set to have this angle ( $0^\circ$ ). This is because for the calculation of the slope two pixels are required. The graphs of contact spot area distribution in Figure 5.7 show that the majority of contact spots have an area equal to  $25 \mu\text{m}^2$ , so this number of contact spots is set to have an angle equal to  $0^\circ$ .

Concerning the contact spots with angle values equal to  $-45^\circ$  and  $45^\circ$  they also depend on the area of the contact spots. The majority of these spots (with values equal to  $-45^\circ$  or  $45^\circ$ ) is found to have an area equal to 2 pixels (or  $50 \mu\text{m}^2$ ) and are connected diagonal. An example of these cases is illustrated in Figure 5.25 which presents two contact spots and each of them consists of two pixels. The contact spots of Figure 5.25(a) has an angle equal to  $-45^\circ$  while the contact spot of Figure 5.25(b) has an angle equal to  $45^\circ$ .

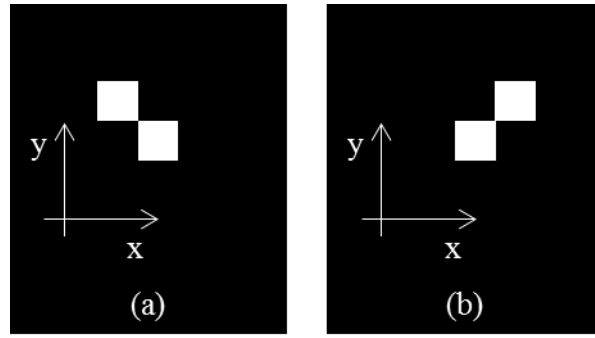


Figure 5.25. Contact spots with angle values equal with (a)  $-45^\circ$  and (b)  $45^\circ$

### 5.8.8 Void volume distribution findings

The graphs of voids volume distribution in Figure 5.13 show that the voids follow the same distribution after each current test 0 A, 16 A, 32 A and 64 A. These graphs can be compared with the corresponding graphs of contact spot area distribution which were presented in Figure 5.7. The results show that the volume of voids follow a similar distribution with the area of contact spots. The smallest void indicated on the graphs of Figure 5.13 is  $125 \mu\text{m}^2$ , which is the resolution of the technique (when a pixel length is  $5 \mu\text{m}$ ) and the largest void indicated are several  $\text{mm}^3$  in volume.

Moreover, it can be seen that each graph of Figure 5.13 consists of two regimes. The first where the voids volume distribution follows a power relationship with a slope between  $2.569 \leq q \leq 3.659$  and the second is for a small number of particular large voids in volume with a slope approximately equal to zero. The slope is given by Eq. (5.16).

$$n_v(V_i') = C(V_i')^{-q} \quad (5.16)$$

Table 5.6 presents the slope ( $q$ ) and constant ( $C$ ) of Eq. (5.16) after each current loading test at 0 A, 16 A, 32 A and 64 A for the first regime of graphs of Figure 5.13. The constant ( $C$ ) value in log-log graphs of Figure 5.13 after each current loading test represents the number of voids who have volume equal to  $1 \mu\text{m}^3$ . In this research, the volume of  $1 \mu\text{m}^3$  does not exist as the smallest volume of a void is  $125 \mu\text{m}^3$  (volume of voxel). In addition, the graphs of Figure 5.13 show that the transition between the two

regimes in each current loading test at 0 A, 16 A, 32 A and 64 A occurs at  $5,500 \mu\text{m}^3$ ,  $8,875 \mu\text{m}^3$ ,  $6,000 \mu\text{m}^3$  and  $6,875 \mu\text{m}^3$  respectively.

Table 5.6. Characteristics of the first regime of the voids volume distribution after each current loading tests

Test current (A)	0	16	32	64
Slope ( $q$ )	9.769	4.778	6.527	5.168
Constant ( $C$ )	$2 \times 10^{24}$	$9 \times 10^{13}$	$3 \times 10^{17}$	$5 \times 10^{14}$

### 5.8.9 Conductors fractal characteristics findings

Bhushan [121] picks out and emphasizes the importance of area and distance distributions of contact spots in elaborating theories in contact physics and tribology. The contact spot distance distribution is significant in working at the stress and dynamic interactions between contact spots. In an electrical contact, the contact spot area and distance distributions are significant as they have been used by many researchers [20, 66, 127] to develop expressions to model the contact resistance.

Swingler and Lalechos in [188] and Swingler in [189] show that the area cumulative distribution of the contact spots in 2D plane followed a Korcak-type distribution similar to the spatial cumulative distribution neglecting the effects of differences in scale. The contact spot area cumulative distribution shows the number of contact spots with the area equal or greater than a reference area,  $A_{ref}$  as described in Eq. (5.17). Where  $A_L$ , is the area of the largest contact spot and  $K$  is the Korcak exponent.

$$N(A_i \geq A_{ref}) = \left( \frac{A_L}{A_{ref}} \right)^{-K} \quad (5.17)$$

The cumulative spatial distribution shows the number of contact spots with the distance  $d_{ij}$  equal or greater than a reference contact spot distance  $d_{ref}$  as described in Eq. (5.18). Where  $n_{res, i}$  is the number of contact spots  $i$ , separated from contact spots  $j$

by the resolution of the technique,  $d_{res}$  (pixel length). Where  $K_s$ , is the slope of contact spot spatial distribution [180, 183, 190].

$$N_d(d_{ij} \leq d_{ref}) = n_{res} \left( \frac{d_{ref}}{d_{res}} \right)^{K_s} \quad (5.18)$$

Jang and Jang [183] reported that the scale dependency of contact distributions should be considered; because contact spots are formulated by rough surfaces at different scales having different morphologies. They worked on area and spatial distributions of contacts in random fractal surfaces and natural contacts (real islands). The distribution of the contact spots is investigated when the surface is cut at any given height. Jang and Jang [183] used the same procedure as Swingler in [189] to investigate the multi-scale area and spatial distributions of contact spots. Using this procedure, they analysed the area and distance distribution of natural contact spots for different scales and demonstrated that the area and spatial distribution of random and natural contact spots follow the Korcak-type empirical relationship [190].

In this research, the fractal characteristics of the conductors of a 16 A rated AC single pole rocker switch are examined considering their scale dependency of contact distributions after four different current loading tests at 0 A, 16 A, 32 A and 64 A. The fractal surfaces are generated by ‘‘cutting’’ each conductor at three different height levels as explained in Section 5.7.2. These fractal surfaces are presented as 2D x-z cross-section slice images in Figure 5.17 and Figure 5.18. These 2D x-z cross-section slice images show that smaller contact spots tended to occur near larger contact spots and tended to cluster with the next height level contact spots into groups. In addition, the 2D x-z cross-section slice images of the Conductor A (Figure 5.17) present more contact spots compared with the 2D x-z cross-section slice images of the Conductor B (Figure 5.18). This was expected as the measured mean roughness ( $R_\alpha$ ) value of Conductor A is bigger than the measured mean roughness ( $R_\alpha$ ) value of Conductor B (see Section 4.3).

From the different height levels contact spots, the number of contact spots ( $N$ ) of a particular area ( $A_i$ ) which are equal or greater than a reference area ( $A_{ref}$ ) is determined as described in Eq. (5.13). Figure 5.19 and Figure 5.20 show the graphs of contact spot

area cumulative distribution of the two conductors (A and B respectively) for the three different height levels after each current loading test at 0 A, 16 A, 32 A and 64 A with their fitting lines. It is evident that the number of contact spots equal or greater than a particular value area (the reference value of  $A_{ref}$ ) have a linear relation in the log-log graphs indicating that this distribution is a Korcak-type distribution. If  $N(A_i \geq A_{ref})$  is obtained from each fitting line of Figure 5.19 and Figure 5.20, Eq. (5.19) can be obtained. Where  $C$  and  $K$  are the constant and Korcak exponent respectively [191].

$$N(A_i \geq A_{ref}) = CA_i^{-K} \quad (5.19)$$

Jang and Jang [183], on Seuront [192] work reported that the Korcak exponent ( $K$ ) is related to the Korcak dimension ( $D_K$ ) which is given by Eq. (5.20). Where  $D_E$ , is the dimension of the embedding Euclidian space ( $D_E = 2$  in the case of this research). Concerning the calculation of contact spots area fractal dimension ( $D$ ), Jang and Jang [183] reported that it is related to the Korcak dimension ( $D_K$ ) and is given from Eq. (5.21).

$$K = \frac{D_K}{D_E} \quad (5.20)$$

$$D = D_K + 1 \quad (5.21)$$

The characteristics of each fitting line of the contact spot area cumulative distribution graphs (Figure 5.19 and Figure 5.20) of the two conductors (A and B respectively) which are described form Eq. (5.19) are given in Table 5.7 and Table 5.9 respectively. Table 5.8 and Table 5.10 illustrate the average Korcak exponent value of the three different height levels at 0  $\mu\text{m}$ , 5  $\mu\text{m}$  and 10  $\mu\text{m}$  for each conductor (A and B respectively) after each current loading test at 0 A, 16 A, 32 A and 64 A. The average contact spots area fractal dimension ( $D$ ) is also included in each current loading test which is calculated using the average Korcak exponent values of Table 5.8 and Table 5.10 and Eq. (5.20) and Eq. (5.21).

Table 5.7. Korcak exponent and constant values for each contact spot area cumulative distribution graph of Conductor A

Test current (A)		0	16	32	64
Korcak exponent ( $K$ )	Height level = 0 $\mu\text{m}$	0.6562	0.5571	0.6315	0.8646
	Height level = 5 $\mu\text{m}$	0.6734	0.5967	0.6472	0.7244
	Height level = 10 $\mu\text{m}$	0.6671	0.7120	0.6586	0.7078
Constant ( $C$ )	Height level = 0 $\mu\text{m}$	1,339.5	569.8	1,640.6	10,842
	Height level = 5 $\mu\text{m}$	1,634.4	969.6	1,470.6	10,332
	Height level = 10 $\mu\text{m}$	1,629.1	3,562	1,673.5	3,284

Table 5.8. Average Korcak exponent and average contact spots area fractal dimension of Conductor A

Test current (A)	0	16	32	64
Average Korcak exponent ( $K$ )	0.6656	0.6219	0.6458	0.7656
Average area fractal dimension ( $D$ )	2.3312	2.2438	2.2916	2.5312

The values of average contact spots area fractal dimension of Conductor A in Table 5.8 for each current loading test show that the maximum value (2.5312) presented at 64 A and the minimum (2.2438) at 16 A. Concerning the Conductor B, the maximum value (2.6388) is presented at 32 A and the minimum (1.9204) at 0 A.

The results of contact spot area cumulative distributions can be compared with area distributions of real data. Swingler and Lalechos [149] reported that Africa is found to have a Korcak exponent  $K = 0.5$  resulting from one very large predominant and rapidly decreasing area distribution of associated islands. Moreover, the North America is found to have a Korcak exponent  $K = 0.75$  with less of rapid decrease in the area distribution. According to Jang and Jang [183], the Korcak exponent of islands of French Polynesian is found to be from  $K = 0.79$  to  $K = 0.82$  according to different sea height levels. In addition, an examination of data from the whole world yields a Korcak exponent  $K = 0.65$ .

Table 5.9. Korcak exponent and constant values for each contact spot area cumulative distribution graph of Conductor B

Test current (A)		0	16	32	64
Korcak exponent ( $K$ )	Height level = 0 $\mu\text{m}$	0.4275	0.6480	0.8901	0.7127
	Height level = 5 $\mu\text{m}$	0.4738	0.6122	0.7758	0.7001
	Height level = 10 $\mu\text{m}$	0.4793	0.5317	0.7923	0.6282
Constant ( $C$ )	Height level = 0 $\mu\text{m}$	156.9	4,297	13,964	2,279
	Height level = 5 $\mu\text{m}$	272.2	966.7	6,510	1,948
	Height level = 10 $\mu\text{m}$	252.6	484.1	4,842	964.9

Table 5.10. Average Korcak exponent and average contact spots area fractal dimension of Conductor B after each current loading test

Test current (A)	0	16	32	64
Average Korcak exponent ( $K$ )	0.4602	0.5973	0.8194	0.6803
Average area fractal dimension ( $D$ )	1.9204	2.1946	2.6388	2.3606

From the different height levels contact spots, the number of contact spots ( $N_d$ ) of a particular distance ( $d_{ij}$ ) which are less than or equal to a reference area ( $d_{ref}$ ) is determined as described in Eq. (5.14). Figure 5.21 and Figure 5.22 show the graphs of contact spot spatial cumulative distribution of the two conductors (A and B respectively) for the three different height levels after each current loading test at 0 A, 16 A, 32 A and 64 A with their fitting lines. It is evident that the number of contact spots less than or equal to a particular value of a reference distance ( $d_{ref}$ ) have a linear relation in the log-log graphs indicating that this distribution is a Korcak-type distribution. The linear behaviour of the log-log graphs become more evident as the scale becomes finer. If  $N_d(d_{ij} \leq d_{ref})$  is obtained from each fitting line of Figure 5.21 and Figure 5.22, Eq. (5.22) can be obtained. Where  $C$ , is a constant and  $K_s$  is the slope of contact spot spatial distribution [191].

$$N_d(d_{ij} \leq d_{ref}) = Cd_{ij}^{K_s} \quad (5.22)$$

The characteristics of each fitting line of the contact spot spatial cumulative distribution graphs (Figure 5.21 and Figure 5.22) of the two conductors (A and B respectively) which are described from Eq. (5.22) are given in Table 5.11 and Table 5.13 respectively.

Table 5.11. Slope of contact spot spatial distribution and constant values for each contact spot spatial cumulative distribution graph of Conductor A

Test current (A)		0	16	32	64
Slope ( $K_s$ )	Height level = 0 $\mu\text{m}$	1.1481	1.6942	1.5693	1.2002
	Height level = 5 $\mu\text{m}$	1.1875	1.1117	1.7700	1.7104
	Height level = 10 $\mu\text{m}$	1.3669	1.0187	1.7934	1.7488
Constant ( $C$ )	Height level = 0 $\mu\text{m}$	0.1012	0.0027	0.0041	0.1034
	Height level = 5 $\mu\text{m}$	0.0792	0.1104	0.0005	0.0030
	Height level = 10 $\mu\text{m}$	0.0238	0.2124	0.0004	0.0015

The Table 5.12 and Table 5.14 illustrate the average slope value of contact spot spatial distribution of the three different height levels at 0  $\mu\text{m}$ , 5  $\mu\text{m}$  and 10  $\mu\text{m}$  for each conductor (A and B respectively) after each current loading test at 0 A, 16 A, 32 A and 64 A. The average slope values of the contact spot spatial cumulative distributions for the two conductors vary for each current loading test. The average slope values of Conductor A in Table 5.11 show that the maximum value (1.7109) is presented at 32 A and the minimum (1.2342) at 0 A. Concerning the Conductor B, the maximum value (2.1864) is presented at 64 A and the minimum (0.9025) at 0 A.

The results of average slope values of contact spot spatial cumulative distributions can be compared with Swingler's [180] and Jang and Jang's [183] results. Swingler [180] investigated the spatial cumulative distribution of the contact spots of a bolted connector for different contact forces at 0.8 kN, 1.6 kN and 3.2 kN. The slope values of the contact



spot spatial cumulative distributions are found to be  $K_s = 1.48$  for 0.8 kN,  $K_s = 1.70$  for 1.6 kN and  $K_s = 1.10$  for 3.2 kN. Jang and Jang's [183] investigated the spatial cumulative distribution of the French Polynesian islands for different sea height levels and reported that the slope values of island spatial cumulative distributions are  $K_s = 0.9282$  and  $K_s = 0.9930$  for 0 m and 6 m sea height levels respectively.

Table 5.12. Average slope of contact spots spatial distribution of Conductor A

Test current (A)	0	16	32	64
Average slope ( $K_s$ )	1.2342	1.2749	1.7109	1.5531

Table 5.13. Slope of contact spot spatial distribution and constant values for each contact spot spatial cumulative distribution graph of Conductor B

Test current (A)		0	16	32	64
Slope ( $K_s$ )	Height level = 0 $\mu\text{m}$	0.9628	1.9134	1.8723	1.6642
	Height level = 5 $\mu\text{m}$	0.8092	1.8449	1.6065	2.0696
	Height level = 10 $\mu\text{m}$	0.9356	1.7148	1.4195	2.8254
Constant ( $C$ )	Height level = 0 $\mu\text{m}$	0.0818	0.0009	0.001	0.0098
	Height level = 5 $\mu\text{m}$	0.3177	0.0014	0.0059	0.0003
	Height level = 10 $\mu\text{m}$	0.1344	0.0027	0.0172	$1 \times 10^{-6}$

Table 5.14. Average slope of contact spots spatial distribution of Conductor B

Test current (A)	0	16	32	64
Average slope ( $K_s$ )	0.9025	1.8244	1.6328	2.1864

Comparing the average slope values of contact spot spatial cumulative distributions of 16 A rated AC single pole rocker switch after each current loading test (at 0 A, 16 A, 32 A and 64 A) with Swingler's [180] and Jang and Jang's [183] results it is obvious that

there is a similarity in some cases. For example, the contact spots of Conductor A at 32 A current loading test follow similar spatial distribution with the contact spots of bolted connector at 1.6 kN. Concerning the contact spots of Conductor B at 0 A it is clear that they follow similar spatial distribution with the islands of French Polynesian at 6 m sea height level.

## 5.9 Conclusion

The X-ray CT technique has been used to produce 2D and 3D contact maps of a 16 A rated AC single pole rocker switch interfaces without the need to dismantle the contact system after four different current loading tests at 0 A, 16 A, 32 A and 64 A. For the 2D and 3D contact maps, Contact Analysis Techniques, CAT\*, are developed and implemented with a suite of tools developed in MATLAB and Image Processing Toolbox which can be used for any value of resolution. These CAT\* consist of a variety of tools which are divided into visualisation tools and calculation tools.

The visualisation tools can visualise the 2D and 3D contact maps of the contact interface, the 2D angle map, the 3D voids and the conductors (and each conductor separately) of the contact system. The calculation tools can calculate the contact resistance using two different approaches (Greenwood and Holm), the number of contact spots, the area of each contact spot and the total mechanical area of contact in both 2D and 3D contact maps. Moreover, the calculation tools can calculate the angle of each contact spot in 3D contact maps and the number of voids which are located between the two bodies of the contact system. In addition, the calculation of the volume of each void and the total volume of voids are conducted to the calculation tools. The tools of CAT\* give the possibility to examine and characterise the contact system under different conditions and operations.

Comparing the different techniques (2D or 3D contact maps) it is found that they produced different results. The 3D mapping technique demonstrates that the contact interface is not a 2D plane but has a 3D nature. This is important when analysing contact interfaces. The 2D mapping technique is shown to have an issue with the “Overlapping Void Disaggregation” as information in the third dimension can be lost due to the 3D nature of a contacting surface interface. Thus, a 3D analysis technique should be used when investigating contact interfaces.

The area and spatial cumulative distributions of the conductors of the 16 A rated AC single pole rocker switch were investigated after four different current loading test at 0 A, 16 A, 32 A and 64 A. The area and spatial distributions of the contact spots of the conductors are analysed from three different fractal surfaces (x-z cross-section slice images) which are cut from three different height levels. It is confirmed that the area distribution of contact spots, such as the number of contact spots equal or greater than a particular area, exhibits a Korcak-type empirical relationship with fractal behaviour. In the same analysis, it was observed that the spatial distribution of contact spots, which is the number of contact spots less than or equal to a particular distance, followed a power law relationship as the scale of the surface became finer.

## **Chapter 6 – Towards a 3D Technique to Determine the Geometric Path of Electric Current Flow through a Contact System**

### **6.1 Introduction**

The effective conductivity of a contact system is an important characteristic used to link the microstructure of the contact system to its performance. A resistor network model has been developed from the cross-sectional slices of a given electrical contact system. This allows the total resistance across the model and hence the total conductance of the contact system to be calculated. The resistor network model can be used on any conductive contact system with non-uniform cross-section areas (perpendicular to the electric current direction) and each cross-section area can include more than one contact spot/asperity (spot in a 2D plane and asperity in a 3D plane). Moreover, the simulated electric current in the model can flow in a non-uniform path through a contact system (each cross-section across the contact interface has more than one contact spot, thus the amount of electric current flowing through each contact spot may be different). An example is given in Figure 2.8 (explained in Section 2.3.7) which describes three cases of an electric current flowing through a contact system. In this example, it is assumed that the electric current flows through the whole cross-section area of Body B and passes to Body A through the contact interface. The concept of the resistor network model development is based on this example.

In this chapter, the resistor network model is developed from data of a real contact system. For the development and test purposes, the experimental data of a 250 V, 16 A rated AC single pole rocker switch after the four different current loading tests (0 A, 16 A, 32 A and 64 A) which were presented in Section 4.5 are used. The resistor network model is constructed from a 3D contact map which identifies contact asperities across the conjoined two bodies of the contact system. Furthermore, in this chapter the resistor network model is used in order to show the geometric path of electric current flowing through a contact system exhibiting multiple contact spots/asperities. Additionally, the total cross-section area of each cross-sectional slice (perpendicular on the electric current direction) is calculated and presented in comparison with the corresponding total cross-section area of each cross-section slice of electric current pathway. The number of asperities in each of these cross-sectional slices is also calculated and compared with the number of asperities which the electric current flows through.

## 6.2 Contact Analysis and Modelling Techniques

### 6.2.1 *The concept and characteristics of a resistor network model system*

The calculation of the electric current pathways through a contact system requires knowledge of the distribution of the contact material constituents and their conductivities, as well as the size distribution of the contact asperities at the interface. In this chapter, it is assumed that the contact system is made of the same material to simplify the resistor network model. 2D cross-section slice images in the x-y and x-z directions are extracted from the oriented 3D volume of interest of the contact system. It is this resistor network model which is used to determine the current pathways. The method consists of different techniques (Contact Analysis Techniques or CAT\*) which are given in Section 6.2.2. For the resistor network model development, a similar method used to calculate the electrical resistance of a contact system (Eq. (2.19)) is used. Figure 6.1(a) illustrates a schematic oriented 3D volume of interest of a contact system which is used in order to explain this method. The chosen dimensions of the schematic contact system are selected for the practical presentation as well as for an easier understanding of the CAT\* which are developed in this chapter. The schematic contact system of Figure 6.1(a) consists of two rough bodies, A and B which are in mechanical contact. The mechanical contact occurs at the two constriction asperities (grey voxels in Figure 6.2(a)). In this research, the extensions of these constriction asperities above and below the two bodies of the schematic oriented 3D volume of interest of a contact system are called contact asperities while the roughness of two bodies which their “peaks” are not in contact are called non-contact asperities. The schematic oriented 3D volume of interest of a contact system of Figure 6.2(a) consists of 2 contact asperities and 5 non-contact asperities. These asperities (contact asperities and non-contact asperities) are illustrated in Figure 6.1(b) and Figure 6.1(c) respectively. More information concerning the development and characterisation of contact and non-contact asperities is explained in more detail in Chapter 7.

### 6.2.2 *Development of Open/Closed and Closed resistor network models*

First of all, the contact system is required to be divided into equal x-z cross-section slices across the electric current ( $I$ ) direction (y-direction). The electric current direction is defined to be parallel with the normal force ( $F$ ) and it is assumed that it flows through the whole cross-section area of the first and last x-z cross-section slices (already shown in Section 4.5.3). The direction of the normal force is used to define the orientation of the

coordinate system used. The schematic 3D model of contact system of Figure 6.1(a) consists of six x-z cross-section slices and the 2<sup>nd</sup> is illustrated in Figure 6.1(c).

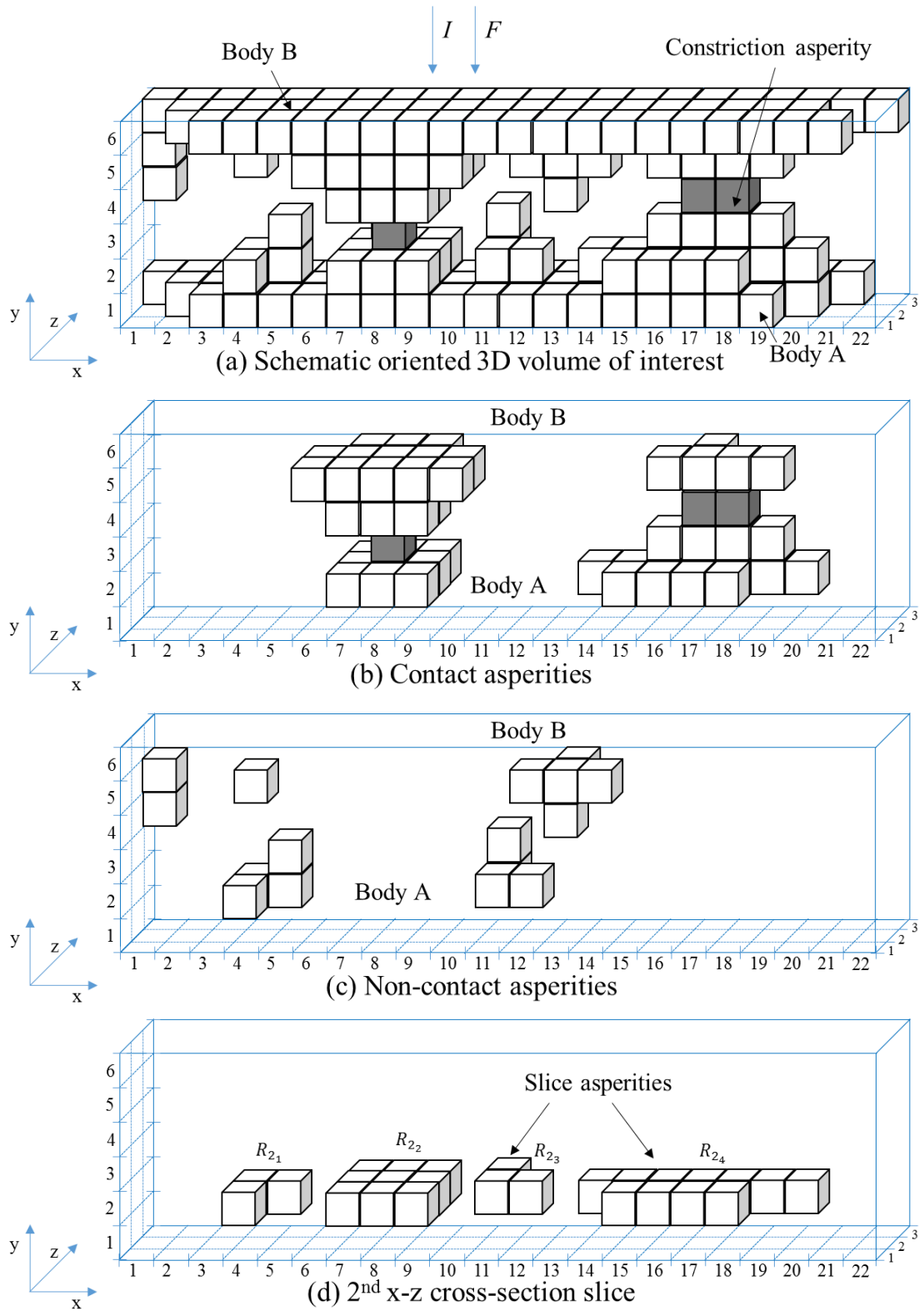


Figure 6.1. Schematic contact system with its characteristics

Figure 6.2(b) shows the resistor network of the schematic oriented 3D volume of interest of the contact system of Figure 6.2(a) (same with Figure 6.1(a)). Each resistor  $R_{ij}$  (where the suffixes  $i$  and  $j$  represent the cross-section slice and the resistor numbers respectively), corresponds to a slice asperity on each x-z cross-section slice. A slice asperity is defined as a collection of voxels which are neighbouring other voxels by at least one edge. For example, the x-z cross section slice of Figure 6.1(d) has 4 slice asperities, or resistors where their values are given by Eq. (2.15) (where the length  $l$  in y-direction equals with the resolution of the X-ray CT technique,  $5\ \mu\text{m}$  in this research). The blue slice asperities (groups of blue voxels) are connected to open circuits while the red slice asperities (groups of red voxels) are connected to closed circuits.

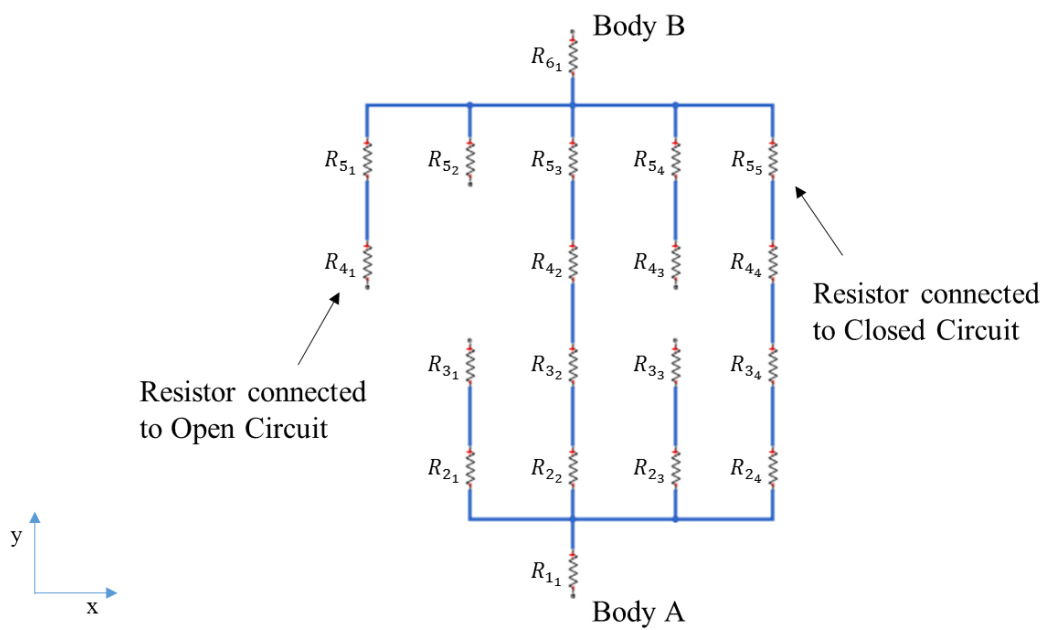
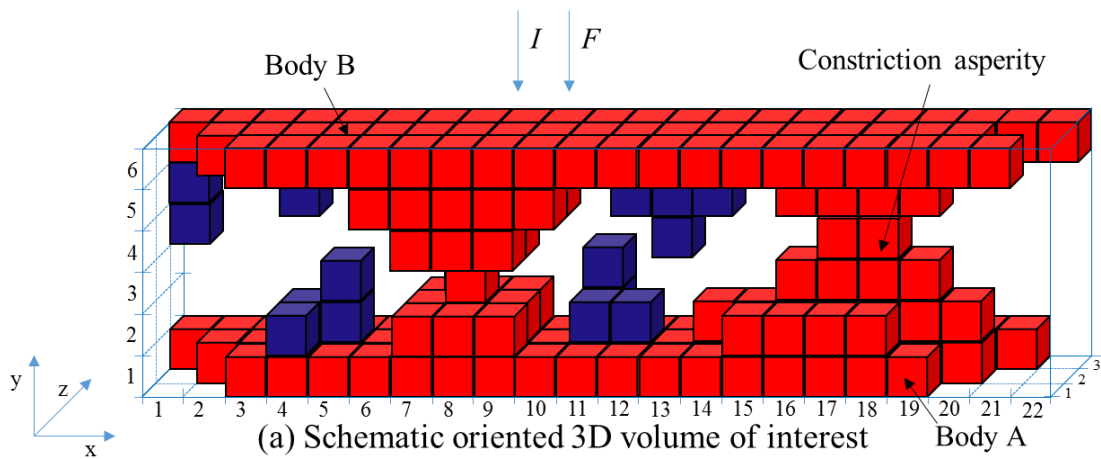


Figure 6.2. Schematic oriented 3D volume of interest of contact system with its resistor network

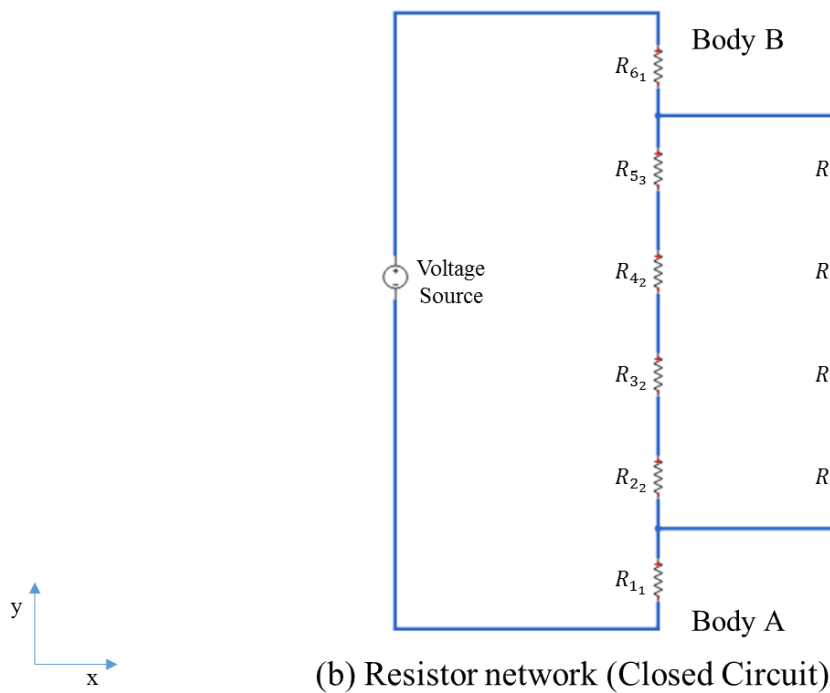
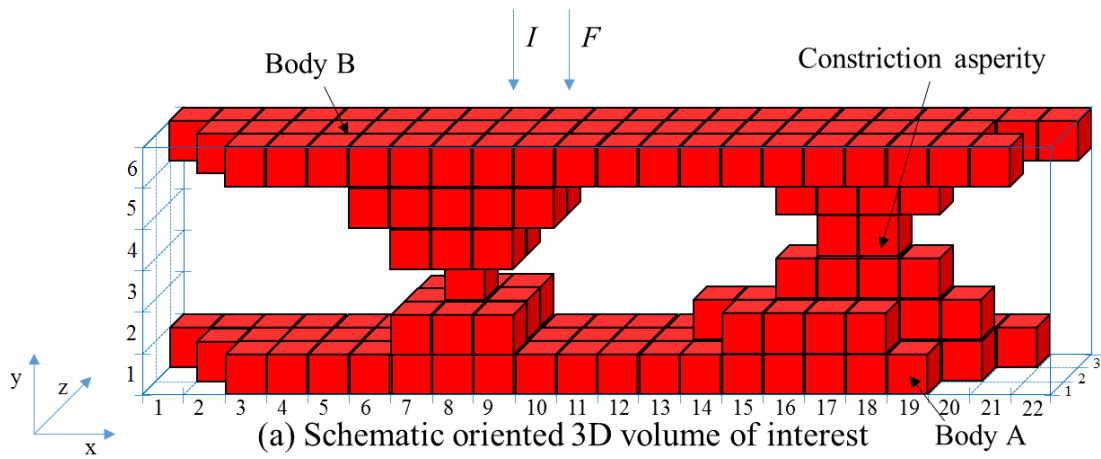


Figure 6.3. Schematic 3D contact source model of the schematic oriented 3D volume of interest of contact system with its resistor network

To show the geometric pathway of electric current flow through the contact system of Figure 6.2(a) (and Figure 6.2(b)), a potential difference across the two bodies is applied. It is obvious that the current flows only through the slice asperities (resistors) which are connected to the network as a closed circuit as illustrated in Figure 6.3(a) (and Figure 6.3(b)). To show the geometric pathways of electric current flow through the contact system of Figure 6.2(a), it is required to modify the x-z cross-section slices of it in order to present only the slice asperities (resistors) which the current flows through like the contact system of Figure 6.3(a) and the resistor network of Figure 6.3(b). For these modifications, three Contact Analysis Techniques (CAT\*) are used.



The first technique is to develop the 3D constriction asperities map using the Contact Analysis Technique for Asperities (CATA) which gives information on where the electrical constriction asperities in a 3D volume profile are located. CATA shows that the electric current flows through the 3D constriction asperities [193]. This technique is a continuation of the 3D contact maps developed in Section 5.3 and extended by one voxel in electric current direction as presented in [193] as 3D constriction asperities maps. Figure 6.4(a) illustrates the 3D constriction asperities map of the schematic oriented 3D volume of interest of the contact system of Figure 6.2(a).

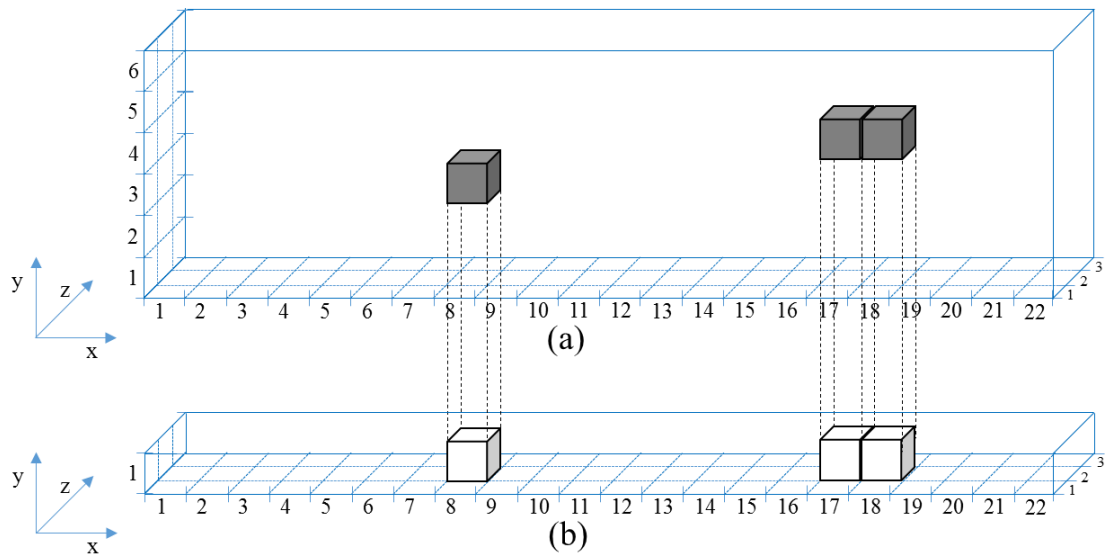


Figure 6.4. (a) 3D constriction asperities map. (b) x-z contact slice [132]

The second technique is the Contact Analysis Technique for Contact Voxels (CATV). This technique is used to create an x-z contact slice with all the constriction asperities at the same height (y-direction) as illustrated in Figure 6.4(b). As mentioned before, the electric current flows through the 3D constriction asperities, consequently, it flows through the x-z contact slice.

The third technique, Contact Analysis Technique for Comparison (CATC) is developed in order to compare each x-z cross-section slice with the x-z contact slice. The reason for making a comparison is to identify which of the slice asperities of x-z cross-section slice are connected with any of the constriction asperities of x-z contact slice. If there is a connection between the slice asperity  $j$  of x-z cross-section slice with any of the constriction asperities in x-z contact slice, then, the electric current flows through the slice asperity  $j$  of x-z cross-section slice.

If there is no connection between the slice asperity  $j$  of x-z cross-section slice with any of the constriction asperities in x-z contact slice, then, the electric current does not flow through the slice asperity  $j$  and this slice asperity is removed from x-z cross-section slice. A mathematical example of this technique is given below describing the geometric path of electric current flows through the schematic oriented 3D volume of interest of contact system of Figure 6.2(a).

The matrix  $[A]$  of Eq. (6.1) represents the x-z contact slice of Figure 6.4(b), where zeros and  $\alpha$  elements of matrix  $[A]$  represent voxels with air and solids of the schematic oriented 3D volume of interest of contact system respectively (note that the matrix dimensions are equal with x-z contact slice dimensions). A constriction asperity is defined as a collection of solid voxels which are neighbouring other solid voxels by at least one of point of their edges. The matrix  $[A]$ , or the x-z contact slice consists of two constriction asperities.

$$[A] = \begin{bmatrix} 0 & 0 & 0 & 0 & 0 & 0 & 0 & 0 & 0 & 0 & 0 & 0 & 0 & 0 & 0 & 0 & 0 & 0 & 0 & 0 \\ 0 & 0 & 0 & 0 & 0 & 0 & 0 & \alpha & 0 & 0 & 0 & 0 & 0 & 0 & 0 & \alpha & \alpha & 0 & 0 & 0 \\ 0 & 0 & 0 & 0 & 0 & 0 & 0 & 0 & 0 & 0 & 0 & 0 & 0 & 0 & 0 & 0 & 0 & 0 & 0 & 0 \end{bmatrix} \quad (6.1)$$

Matrix  $[B_{ij}]$ , represents the x-z cross-section slice for  $i \in [1, N]$  and  $j \in [1, S]$ . Where  $i$  is the number of x-z cross-section slice,  $N$  is the total number of x-z cross-section slices,  $j$  is the number of the slice asperity and  $S$  is the total number of the slice asperities within the x-z cross-section slice. Zeros and  $\beta$  elements of matrix  $[B_{ij}]$  represent voxels with air and solids of the schematic oriented 3D volume of interest of the contact system respectively. The matrix  $[B_2]$ , or the 2<sup>nd</sup> x-z cross-section slice of Figure 6.2(a) consists of 4 slice asperities. The matrices of Eq. (6.2), Eq. (6.3), Eq. (6.4) and Eq. (6.5) represent the 1<sup>st</sup>, 2<sup>nd</sup>, 3<sup>rd</sup> and 4<sup>th</sup> slice asperity of the 2<sup>nd</sup> x-z cross-section slice respectively.

$$[B_2] = \begin{bmatrix} 0 & 0 & 0 & 0 & 0 & 0 & 0 & 0 & 0 & 0 & 0 & 0 & 0 & 0 & 0 & 0 & 0 & 0 & 0 & 0 \\ 0 & 0 & 0 & \beta & \beta & 0 & 0 & 0 & 0 & 0 & 0 & 0 & 0 & 0 & 0 & 0 & 0 & 0 & 0 & 0 \\ 0 & 0 & 0 & \beta & 0 & 0 & 0 & 0 & 0 & 0 & 0 & 0 & 0 & 0 & 0 & 0 & 0 & 0 & 0 & 0 \end{bmatrix} \quad (6.2)$$

$$[B_{2_2}] = \begin{bmatrix} 0 & 0 & 0 & 0 & 0 & 0 & \beta & \beta & \beta & 0 & 0 & 0 & 0 & 0 & 0 & 0 & 0 & 0 & 0 & 0 & 0 \\ 0 & 0 & 0 & 0 & 0 & 0 & \beta & \beta & \beta & 0 & 0 & 0 & 0 & 0 & 0 & 0 & 0 & 0 & 0 & 0 & 0 \\ 0 & 0 & 0 & 0 & 0 & 0 & \beta & \beta & \beta & 0 & 0 & 0 & 0 & 0 & 0 & 0 & 0 & 0 & 0 & 0 & 0 \end{bmatrix} \quad (6.3)$$

$$[B_{2_3}] = \begin{bmatrix} 0 & 0 & 0 & 0 & 0 & 0 & 0 & 0 & 0 & 0 & \beta & 0 & 0 & 0 & 0 & 0 & 0 & 0 & 0 & 0 & 0 \\ 0 & 0 & 0 & 0 & 0 & 0 & 0 & 0 & 0 & 0 & \beta & \beta & 0 & 0 & 0 & 0 & 0 & 0 & 0 & 0 & 0 \\ 0 & 0 \end{bmatrix} \quad (6.4)$$

$$[B_{2_4}] = \begin{bmatrix} 0 & 0 \\ 0 & 0 & 0 & 0 & 0 & 0 & 0 & 0 & 0 & 0 & 0 & 0 & \beta & \beta & \beta & \beta & \beta & \beta & \beta & 0 & 0 \\ 0 & 0 & 0 & 0 & 0 & 0 & 0 & 0 & 0 & 0 & 0 & 0 & \beta & \beta & \beta & \beta & 0 & 0 & 0 & 0 \end{bmatrix} \quad (6.5)$$

To compare if there is a connection between the 1<sup>st</sup> ( $j = 1$ ) slice asperity of the 2<sup>nd</sup> ( $i = 2$ ) x-z cross-section slice with any of the constriction asperities in x-z contact slice, Eq. (6.1) and Eq. (6.2) are added as presented in Eq. (6.6). To compare if there is a connection between the 2<sup>nd</sup> ( $j = 2$ ) slice asperity of the 2<sup>nd</sup> ( $i = 2$ ) x-z cross-section slice with any of the constriction asperities in x-z contact slice, Eq. (6.1) and Eq. (6.3) are added as presented in Eq. (6.7). The same procedure is used for the 3<sup>rd</sup> ( $j = 3$ ) and 4<sup>th</sup> ( $j = 4$ ) slice asperities of the 2<sup>nd</sup> x-z cross-section slice as presented in Eq. (6.8) and Eq. (6.9) respectively. The matrix  $[C_{ij}]$  is the sum of matrix  $[A]$  with matrix  $[B_{ij}]$ . The  $\gamma$  element represents the summation of  $\alpha$  and  $\beta$  elements showing if there is a connection between the slice asperity  $j$  of  $i$  x-z cross-section slice with any of the constriction asperities in x-z contact slice.

Each of the slice asperities presented in the matrix  $[C_{ij}]$  is examined separately in order to identify if the electric current flows through it or not. If the electric current flows through a slice asperity, the  $\gamma$  element is included within the slice asperity and a new matrix  $[D_{ij}]$  is created which contains only this slice asperity which is renamed with the  $\delta$  elements. This condition is described by the matrices of Eq. (6.11) and Eq. (6.19). A

slice asperity without the  $\gamma$  element is replaced with zeros as described by the matrices of Eq. (6.10) and Eq. (6.18).

$$[C_{2_1}] = \begin{bmatrix} 0 & 0 & 0 & 0 & 0 & 0 & 0 & 0 & 0 & 0 & 0 & 0 & 0 & 0 & 0 & 0 & 0 & 0 & 0 & 0 \\ 0 & 0 & 0 & \beta & \beta & 0 & 0 & \alpha & 0 & 0 & 0 & 0 & 0 & 0 & 0 & \alpha & \alpha & 0 & 0 & 0 \\ 0 & 0 & 0 & \beta & 0 & 0 & 0 & 0 & 0 & 0 & 0 & 0 & 0 & 0 & 0 & 0 & 0 & 0 & 0 & 0 \end{bmatrix} \quad (6.6)$$

$$[C_{2_2}] = \begin{bmatrix} 0 & 0 & 0 & 0 & 0 & 0 & \beta & \beta & \beta & 0 & 0 & 0 & 0 & 0 & 0 & 0 & 0 & 0 & 0 & 0 \\ 0 & 0 & 0 & 0 & 0 & 0 & \beta & \gamma & \beta & 0 & 0 & 0 & 0 & 0 & 0 & \alpha & \alpha & 0 & 0 & 0 \\ 0 & 0 & 0 & 0 & 0 & 0 & \beta & \beta & \beta & 0 & 0 & 0 & 0 & 0 & 0 & 0 & 0 & 0 & 0 & 0 \end{bmatrix} \quad (6.7)$$

$$[C_{2_3}] = \begin{bmatrix} 0 & 0 & 0 & 0 & 0 & 0 & 0 & 0 & 0 & 0 & \beta & 0 & 0 & 0 & 0 & 0 & 0 & 0 & 0 & 0 \\ 0 & 0 & 0 & 0 & 0 & 0 & 0 & \alpha & 0 & 0 & \beta & \beta & 0 & 0 & 0 & \alpha & \alpha & 0 & 0 & 0 \\ 0 & 0 & 0 & 0 & 0 & 0 & 0 & 0 & 0 & 0 & 0 & 0 & 0 & 0 & 0 & 0 & 0 & 0 & 0 & 0 \end{bmatrix} \quad (6.8)$$

$$[C_{2_4}] = \begin{bmatrix} 0 & 0 & 0 & 0 & 0 & 0 & 0 & 0 & 0 & 0 & 0 & 0 & 0 & 0 & 0 & 0 & 0 & 0 & 0 & 0 \\ 0 & 0 & 0 & 0 & 0 & 0 & 0 & \alpha & 0 & 0 & 0 & 0 & 0 & \beta & \beta & \beta & \gamma & \gamma & \beta & \beta \\ 0 & 0 & 0 & 0 & 0 & 0 & 0 & 0 & 0 & 0 & 0 & 0 & 0 & \beta & \beta & \beta & \beta & 0 & 0 & 0 \end{bmatrix} \quad (6.9)$$

$$[D_{2_1}] = \begin{bmatrix} 0 & 0 & 0 & 0 & 0 & 0 & 0 & 0 & 0 & 0 & 0 & 0 & 0 & 0 & 0 & 0 & 0 & 0 & 0 & 0 \\ 0 & 0 & 0 & 0 & 0 & 0 & 0 & 0 & 0 & 0 & 0 & 0 & 0 & 0 & 0 & 0 & 0 & 0 & 0 & 0 \\ 0 & 0 & 0 & 0 & 0 & 0 & 0 & 0 & 0 & 0 & 0 & 0 & 0 & 0 & 0 & 0 & 0 & 0 & 0 & 0 \end{bmatrix} \quad (6.10)$$

$$[D_{2_2}] = \begin{bmatrix} 0 & 0 & 0 & 0 & 0 & 0 & \delta & \delta & \delta & 0 & 0 & 0 & 0 & 0 & 0 & 0 & 0 & 0 & 0 & 0 \\ 0 & 0 & 0 & 0 & 0 & 0 & \delta & \delta & \delta & 0 & 0 & 0 & 0 & 0 & 0 & 0 & 0 & 0 & 0 & 0 \\ 0 & 0 & 0 & 0 & 0 & 0 & \delta & \delta & \delta & 0 & 0 & 0 & 0 & 0 & 0 & 0 & 0 & 0 & 0 & 0 \end{bmatrix} \quad (6.11)$$

$$[D_{2_3}] = \begin{bmatrix} 0 & 0 \\ 0 & 0 \\ 0 & 0 \end{bmatrix} \quad (6.12)$$

$$[D_{2_4}] = \begin{bmatrix} 0 & 0 \\ 0 & 0 & 0 & 0 & 0 & 0 & 0 & 0 & 0 & 0 & 0 & 0 & \delta & \delta & \delta & \delta & \delta & \delta & 0 & 0 & 0 \\ 0 & 0 & 0 & 0 & 0 & 0 & 0 & 0 & 0 & 0 & 0 & 0 & 0 & \delta & \delta & \delta & \delta & 0 & 0 & 0 & 0 \end{bmatrix} \quad (6.13)$$

The last matrix is created in order to include all the slice asperities of the slice where the electric current flows through them and is described by Eq. (6.14). The final matrix of the 2<sup>nd</sup> x-z cross-section slice of the schematic oriented 3D volume of interest of contact system of Figure 6.2(a) is given by Eq. (6.15). The same procedure used in 2<sup>nd</sup> x-z cross-section slice, is used for the rest of x-z cross-section slices of the contact system.

$$[E_i] = \sum_{j=1}^S [D_{i_j}] \quad (6.14)$$

$$[E_2] = \begin{bmatrix} 0 & 0 & 0 & 0 & 0 & 0 & \delta & \delta & \delta & 0 & 0 & 0 & 0 & 0 & 0 & 0 & 0 & 0 & 0 & 0 & 0 \\ 0 & 0 & 0 & 0 & 0 & 0 & \delta & \delta & \delta & 0 & 0 & 0 & \delta & \delta & \delta & \delta & \delta & \delta & 0 & 0 & 0 \\ 0 & 0 & 0 & 0 & 0 & 0 & \delta & \delta & \delta & 0 & 0 & 0 & 0 & \delta & \delta & \delta & \delta & 0 & 0 & 0 & 0 \end{bmatrix} \quad (6.15)$$

The geometric path of electric current flowing through a contact system consists of all the processed x-z cross-section slices in a 3D plane. The result of this procedure is called 3D contact source model. For example, the schematic oriented 3D volume of interest of Figure 6.2(a) is illustrated in Figure 6.3(a) which consists of the red voxels only. The non-contact asperities (groups of blue voxels) are removed from the oriented 3D volume of interest because they are connected to open circuits (the electric current is not flowing through the open circuits when a voltage is applied). In addition, the 3D contact source model of Figure 6.3(a) consists of two contact asperities (more information about the visualisation and characterisation of these asperities is given in Chapter 7).

## 6.3 Results and Analysis

### 6.3.1 Contact system

Figure 6.5 shows a part of the oriented 3D volume of interest of the contact system of the 16 A rated AC single pole rocker switch after the first current loading test at 0 A which is labelled as the 3D source model. This part of volume is selected from the oriented 3D volume of interest (the whole oriented 3D volume of interest is presented in Section 4.5.3, Figure 4.20). The reason for this selection is explained in detail in Section 6.4.2. The same procedure used for the development of the 3D source model of the 16 A rated AC single pole rocker switch after the 0 A current loading test is used for the rest 3D source models development at 16 A, 32 A and 64 A current loading tests.

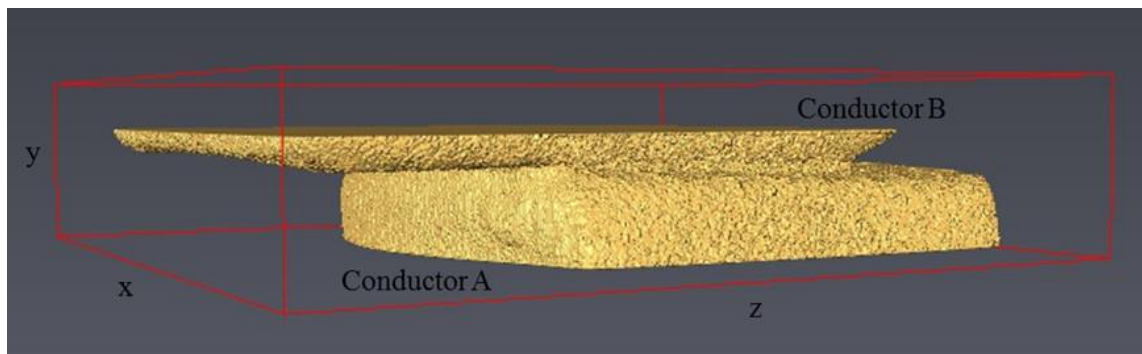


Figure 6.5. 3D source model of the 16 A rated AC single pole rocker switch after the first current loading test at 0 A with bounding box dimensions of  $3.22 \times 0.71 \times 3.31$  mm

### 6.3.2 2D and 3D contact maps

Figure 5.6 illustrates the 3D contact maps of the contacting interface between the conductors of the 3D source model after each current loading test at 0 A, 16 A, 32 A and 64 A. The 3D contact maps are visualized using the 2D cross-section slice images which are processed and implemented using CAT\* with a suite of tools developed in MATLAB as described in Section 5.3. These 3D contact maps, consist of contact spots (surfaces) which are the cross-section areas of the constriction asperities (volumes). Figure 6.6 illustrates the 2D cross-sections of x-z contact slices of the 3D source model after each current loading test at 0 A 16 A, 32 A and 64 A. The x-z contact slices are developed using CATV in order to set all the contact spots of the 3D contact maps of Figure 5.6 to the same height.

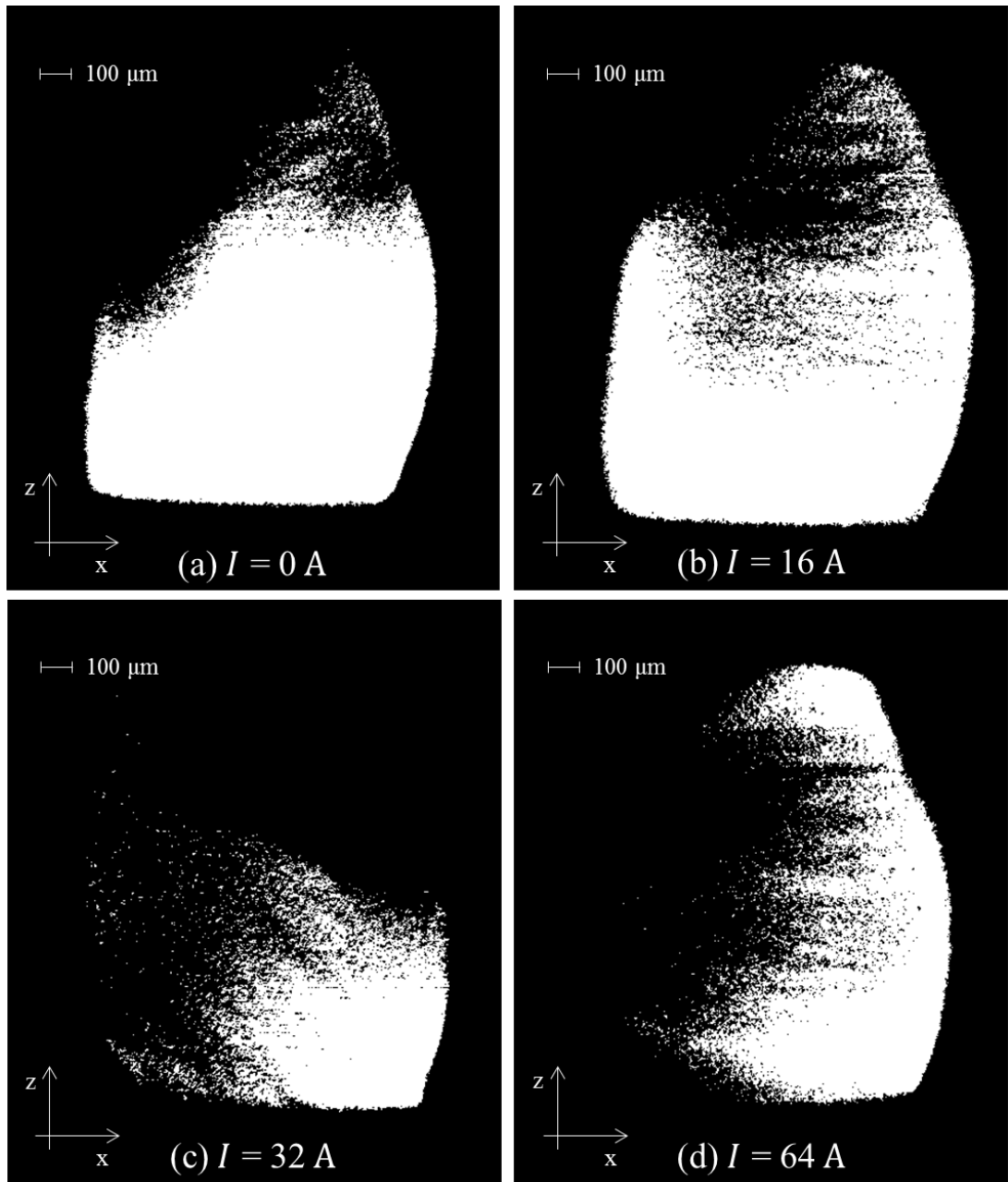


Figure 6.6. 2D cross-sections of x-z contact slices of the 3D source model after each current loading test using CATVis

### 6.3.3 Resistor network model of the contact system

Figure 6.7 shows a set of graphs of the number of resistors in each x-z cross-section slice of the 3D source model (as explained in Section 6.3.1) and the 3D contact source model (the processed x-z cross-section slice images of the 3D source model as explained in Section 6.2) after the four different current loading tests. Each resistor represents a slice asperity in the x-z cross-section slice. The graphs are separated as Open/Closed Circuit (the x-z cross-section slice images of the 3D source model) and Closed Circuit (the x-z

cross-section slice images of the 3D contact source model) which present the number of resistors which make up the Open/Closed Circuit or Closed Circuit as illustrated in Figure 6.2(c) or Figure 6.3(b) respectively. Each of the graphs presented in Figure 6.7 is divided into regions and zones. The reason of this division is explained in detail in Section 6.4.3. If voltage is applied the current will flow through the Closed Circuit. This 3D contact source model shows exactly where the current will flow and its magnitude.

#### 6.3.4 *Electric current path maps*

Figure 6.8, Figure 6.9, Figure 6.10 and Figure 6.11 illustrate the electric current path maps (or electric current maps) of the contact system of the 16 A rated AC single pole rocker switch after each current loading test at 0 A, 16 A, 32 A and 64 A respectively. In this research, an electric current map is defined by the x-z cross-section slice of the 3D source model (Open/Closed Circuit) with the largest number of resistors which are connected to closed circuits. For example, the electric current map of the 3D source model (Open/Closed Circuit) at 0 A which is illustrated in Figure 6.8 is the 33<sup>rd</sup> x-z cross-section slice. This 33<sup>rd</sup> x-z cross-section slice has the largest number of resistors in the Closed Circuit. When a simulated potential difference is applied across the 3D source model, an electric current will flow through it. The red areas of electric current map present the areas which are affected by electric current. The geometric path of electric current which flows through these red areas of the electric map of the 3D source model is presented with the red colour. The blue areas present the areas which the electric current is not flowing through them while white areas indicate voids.

#### 6.3.5 *Total cross-sectional area of slice asperities*

The cross-sectional area of a slice asperity is defined as the sum of pixels within the slice asperity. The sum of the cross-sectional area of slice asperities in each x-z cross-section slice gives the total cross-section area of the x-z cross-section slice. Figure 6.12 shows a set of graphs of the total cross-section area in each x-z cross-section slice of the 3D source model and the 3D contact source model after the four different current loading tests at 0 A, 16 A, 32 A and 64 A. The graphs are separated as Closed Circuit (3D contact source model) and Open/Closed Circuit (3D source model) which present the areas which are affected (electric current flows through them) when a simulated potential difference is applied, or not, across the two conductors of the 3D source model.



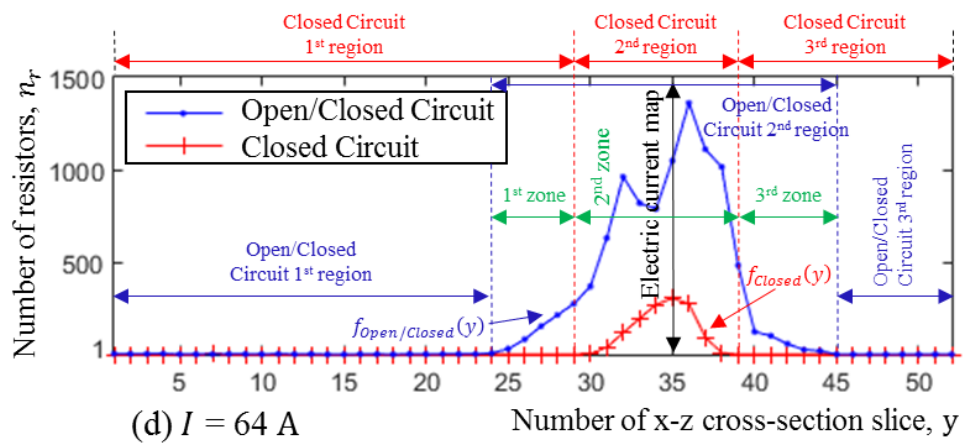
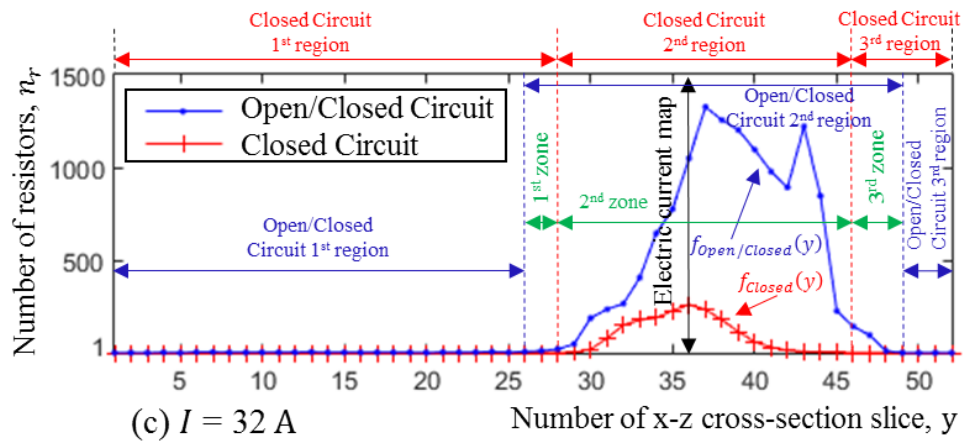
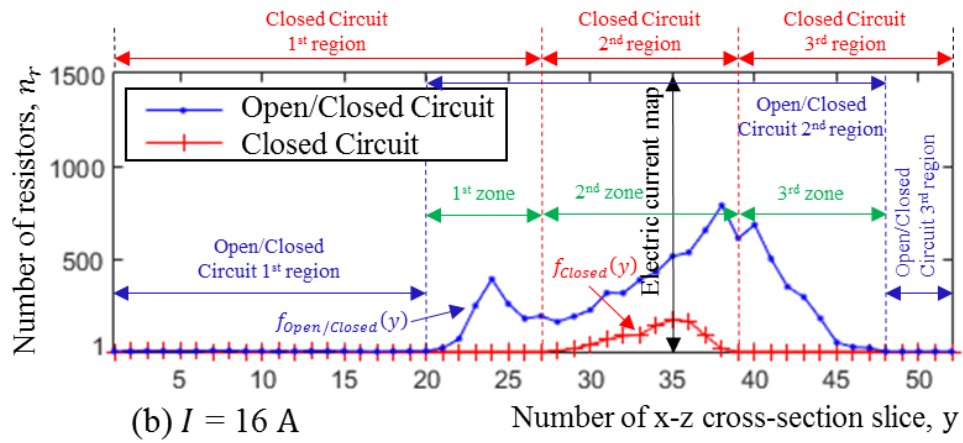
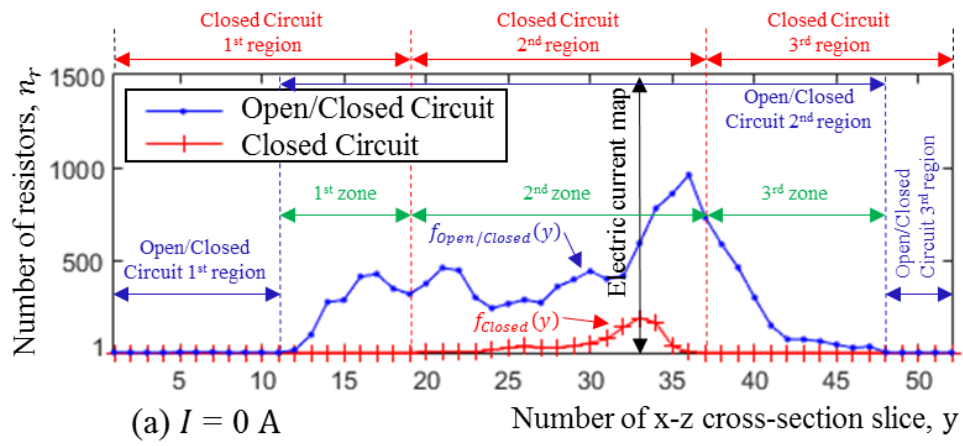


Figure 6.7. Number of resistors in each x-z cross-section slice image of the 3D source model for Open/Closed and Closed Circuits after the four different current loading tests

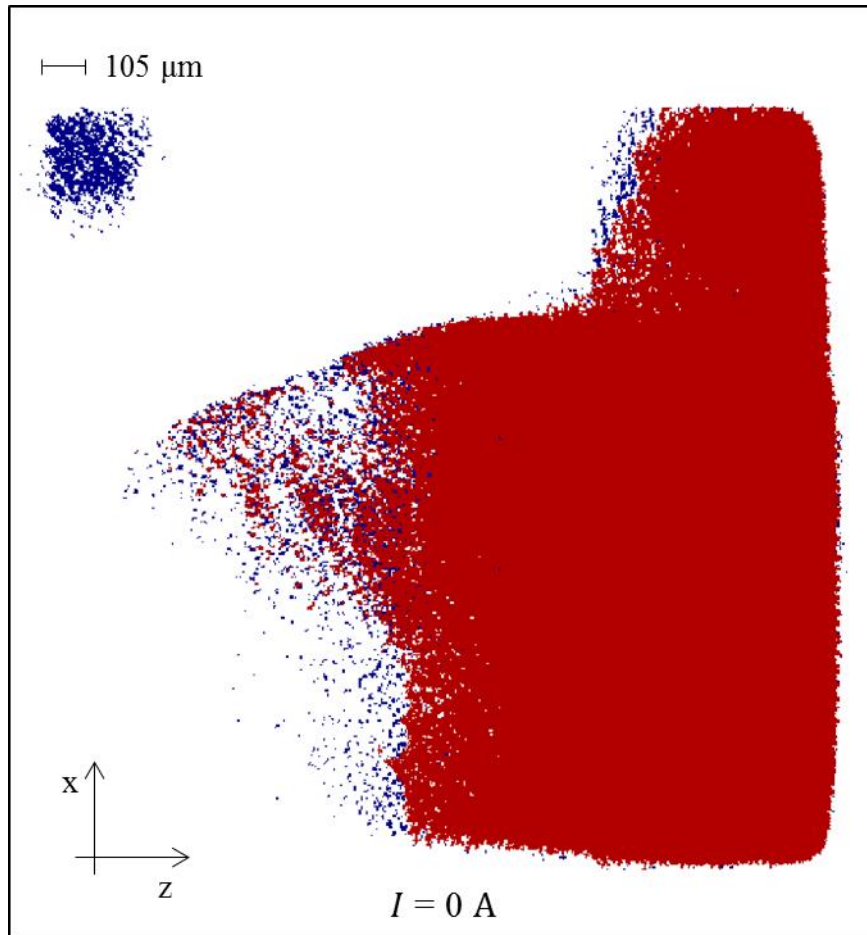


Figure 6.8. Cross-section area of the 33<sup>rd</sup> x-z cross-section slice of the 3D source model at 0 A

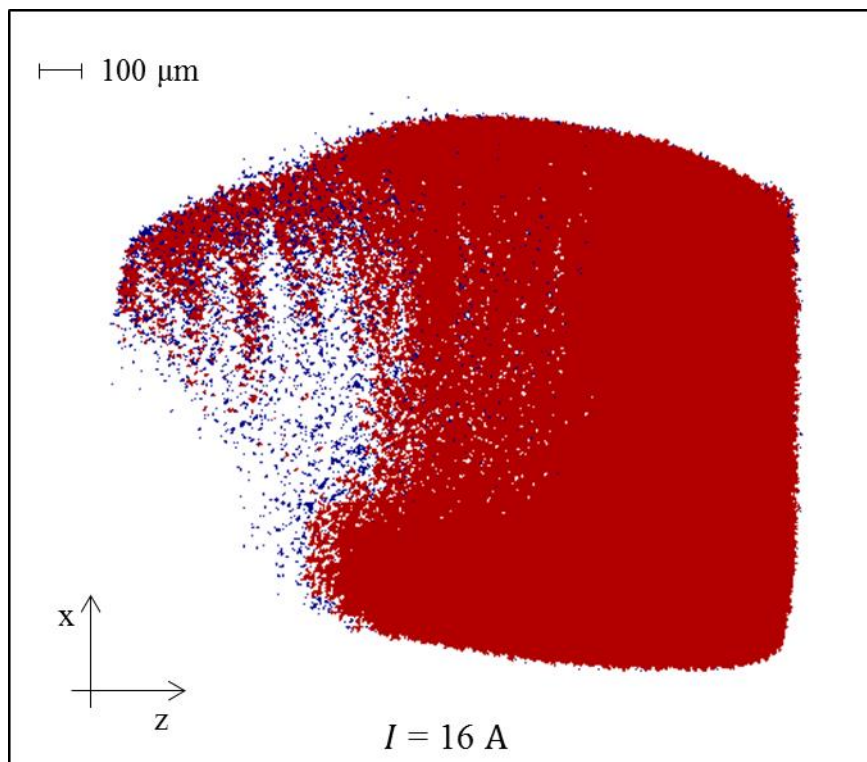


Figure 6.9. Cross-section area of the 35<sup>th</sup> x-z cross-section slice of the 3D source model at 16 A

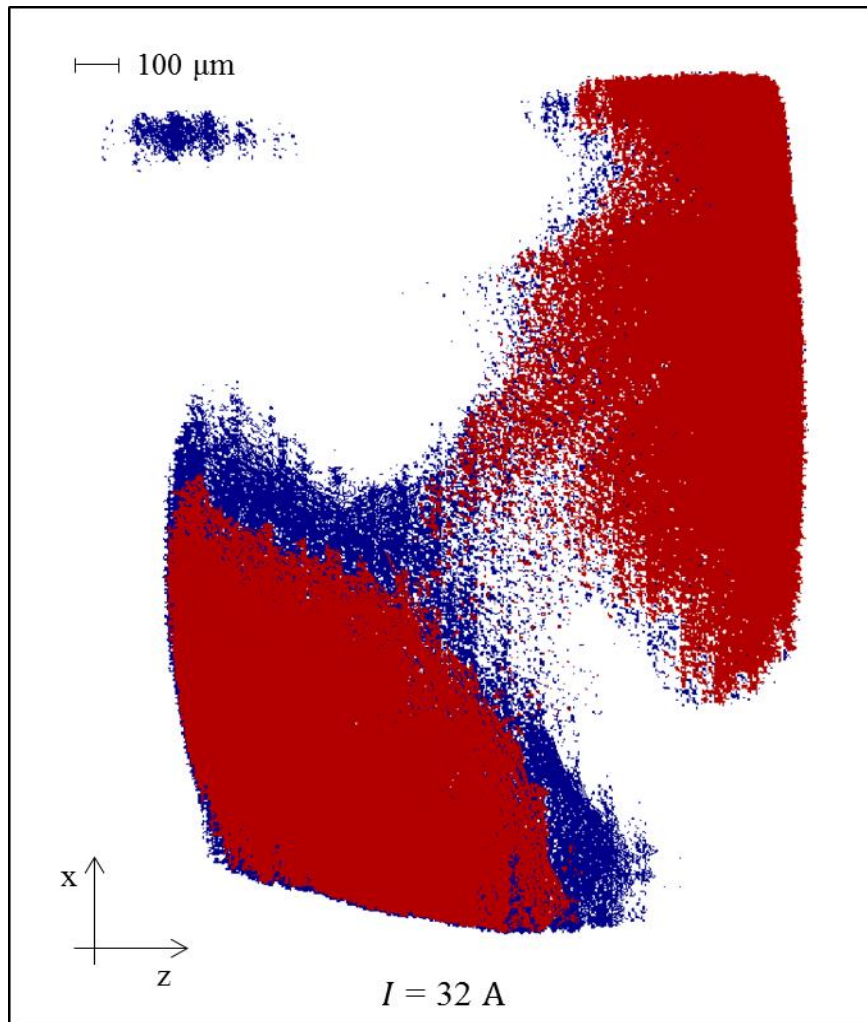


Figure 6.10. Cross-section area of the 36<sup>th</sup> x-z cross-section slice of the 3D source model at 32 A

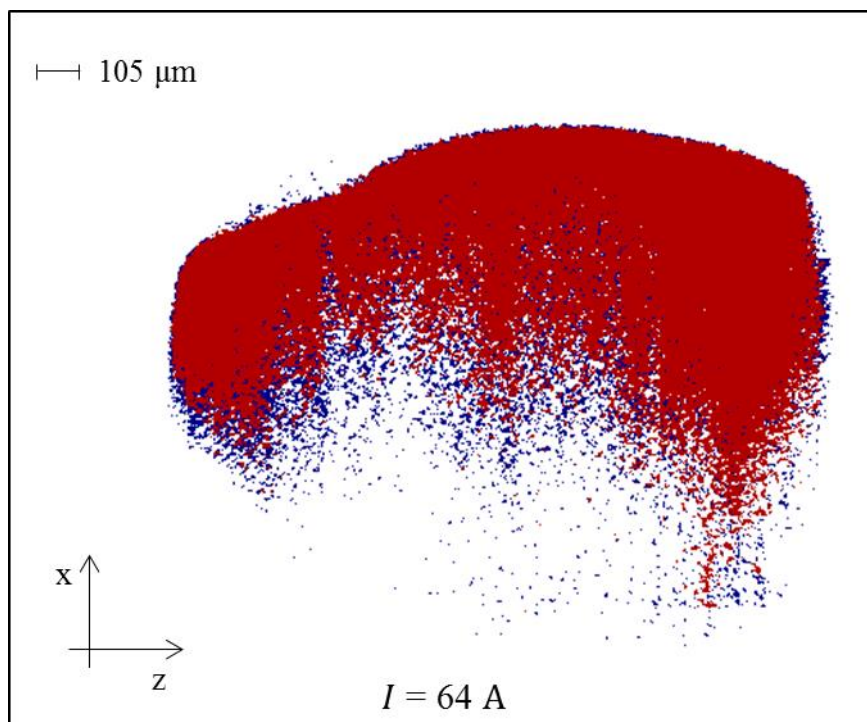


Figure 6.11. Cross-section area of the 35<sup>th</sup> x-z cross-section slice of the 3D source model at 64 A

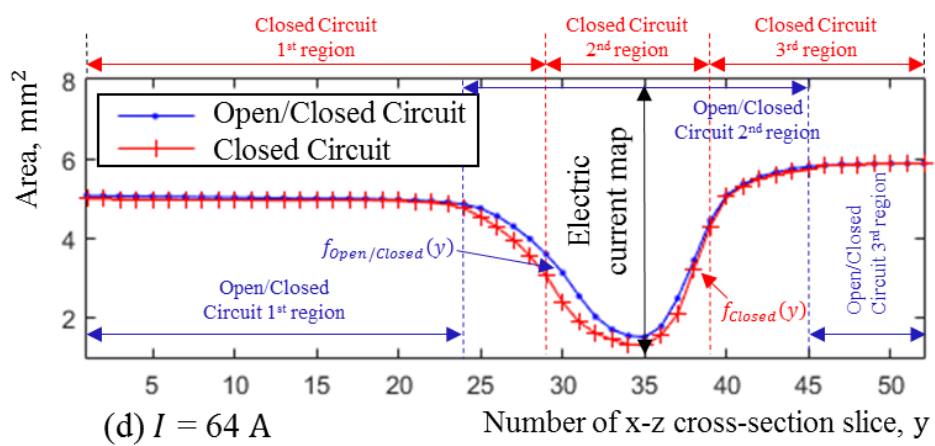
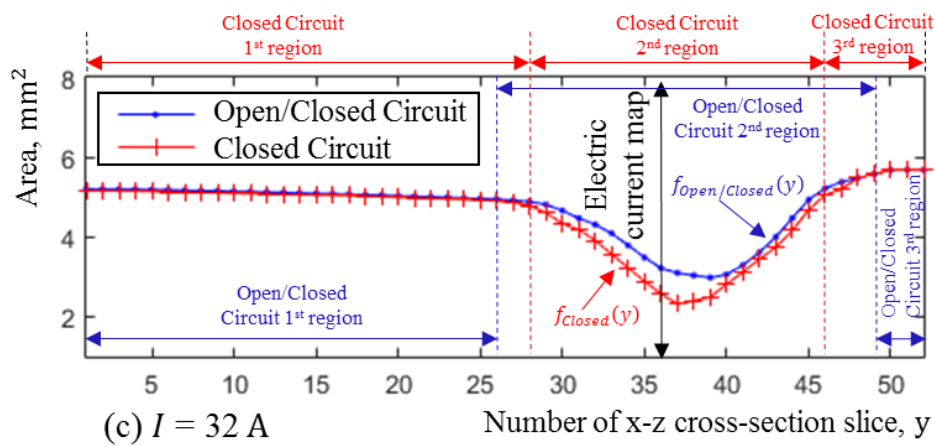
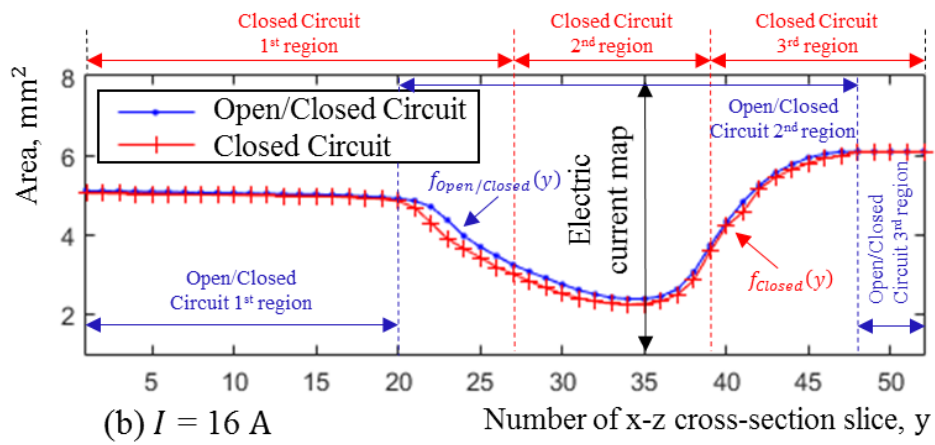
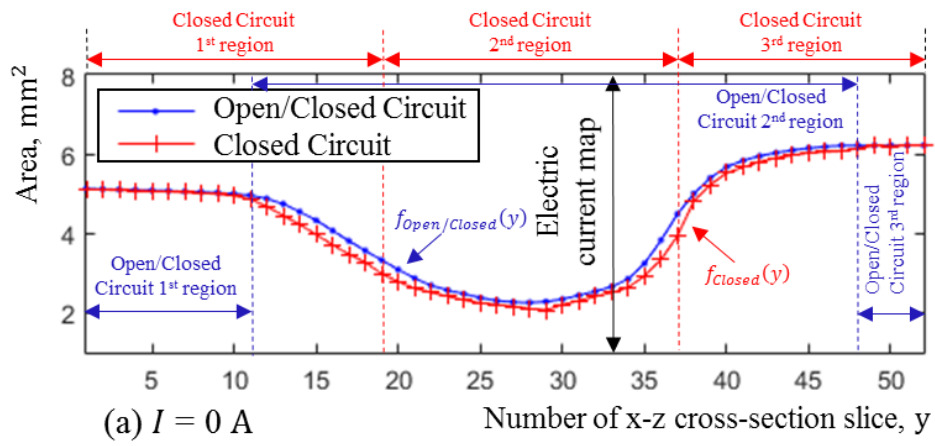


Figure 6.12. Total cross-section area in each x-z cross-section slice image of the 3D source model for Open/Closed and Closed Circuits after the four different current loading tests

## 6.4 Discussion

### 6.4.1 X-ray CT technique

The results show that the X-ray CT technique is a powerful and useful tool for viewing the contact interface of a contact system without needing to dismantle it. The experimental data acquired using this technique with voxel resolution of  $5\ \mu\text{m} \times 5\ \mu\text{m} \times 5\ \mu\text{m}$  gives the ability of examination and processing in order to investigate different characteristics which occur in contact interface and its extension to the two conductors of the contact system. The additional characteristics presented in this chapter include the development of resistor network model of a given contact system. The resistor network model which is introduced in this chapter is developed in order to determine its effective resistance or conductance showing the geometric path of electric current which flows through any perpendicular cross-section slice in the electric current direction.

As mentioned in Section 5.8.1, the resolution is a very important factor for the calculation and visualization techniques. For example, for a coarse measurement (e.g.  $100\ \mu\text{m}$ ) of resolution, only a few asperities of large curvature are visualized while for smaller measurement (e.g.  $0.1\ \mu\text{m}$ ) of resolution, more asperities of smaller curvature are visualized [124, 181]. The smallest resolution which can be obtained by the current facility is  $3\ \mu\text{m}$ . This depends on the sample dimensions and X-ray admittance of the sample materials. The resolution of  $5\ \mu\text{m}$  obtained in this research is the optimum that could be achieved with the sample configuration used. However, it should be noted that the CAT\* developed and implemented within a suite of tools in this chapter can be used with data of smaller resolution.

### 6.4.2 Contact analysis techniques

Analysis and modelling techniques are developed to build the resistor network model of a given contact system in order to determine its effective resistance or conductance showing the geometrical path of electric current which flows through any cross-section slice. These techniques (CATA, CATV and CATC) are developed in MATLAB using Image Processing Toolbox and their general method is based on Eq. (2.19).

The selection of the number of x-z cross-section slice images which produce the 3D source model after each current loading test at 0 A, 16 A, 32 A and 64 A is based on two

factors. The first factor is based on their 16-bit grayscale values. As mentioned in Section 4.4.3 and Section 4.5, the various intensities of pixel illuminations related to the level of X-ray absorption indicate different materials of the voxel, thus different resistivities. These x-z cross-section slices are from the lighter area of the 16-bit x-y cross-section slice images (see Figure 4.11) which are then converted to 1-bit x-y cross-section slice images (see Figure 4.14) as it is assumed that the slice asperities have the same resistivity in order to simplify the resistance calculations (the resistance of each slice asperity is given by Eq. (2.15)). From these x-y cross-section slice images, the oriented 3D volume of interest is developed as explained in Section 4.5.3.

The second factor which is related with the selection of the number of x-z cross-section slice images which consist the 3D source model after each current loading test at 0 A, 16 A, 32 A and 64 A is to identify its limits in the y-direction. The identification of the limits of the 3D source model in the y-direction is based on a reference area point which gives the number of the x-z cross-section slice image with the smallest value of total mechanical area of contact ( $A_T$ ) between the two conductors of the contact system. The histogram of Figure 6.13 illustrates the reference area point of the oriented 3D volume of interest after 0 A current loading test which is presented with the yellow bar. The bars before the yellow bar belong to Conductor A while the bars after the yellow bar belong to Conductor B. Then, in each conductor, the number of bar with the largest value of total mechanical area of contact is selected as a limit number of the x-z cross-section-slices in y-direction. The limit numbers of the x-z cross-section-slices in y-direction in Figure 6.13 are presented with the red bars. All the x-z cross-section-slices between the red bars (the red bars are included) consist of the 3D source model of Figure 6.5.

The same procedure used for the development of the 3D source model of the 16 A rated AC single pole rocker switch after the 0 A current loading test is used for the rest of the 3D source models development at 16 A, 32 A and 64 A current loading tests. The number x-z cross-section slice images of the 3D source model after each current loading test is given in Table 6.1. Each asperity in the x-z cross-section slice corresponds with a spot in 2D x-z cross-section slice image and with a resistor in resistor network model.

In the process, the smallest value of Table 6.1, (52) is used as a reference value in order to create a new sequence (new numbering) of the x-z cross-section slice images of

the 3D source model after each current loading test. The new sequence for each 3D source model is used for the graphs of Figure 6.7 and Figure 6.12. With the new sequence, the axes of x-z cross-section slice (y-direction) on the graphs are presented more evenly matched. The new sequence of x-z cross-section slice images of the 3D source model contains only the last 52 (reference value) x-z cross-section slice images of the 3D source model for each current loading test. For example, the 1<sup>st</sup> x-z cross-section slice image of the new sequence at 0 A current loading test is 51 bars before the second red bar (Conductor B) of the histogram of Figure 6.13 and the 52<sup>nd</sup> x-z cross-section slice image of the new sequence is the second red bar (Conductor B).

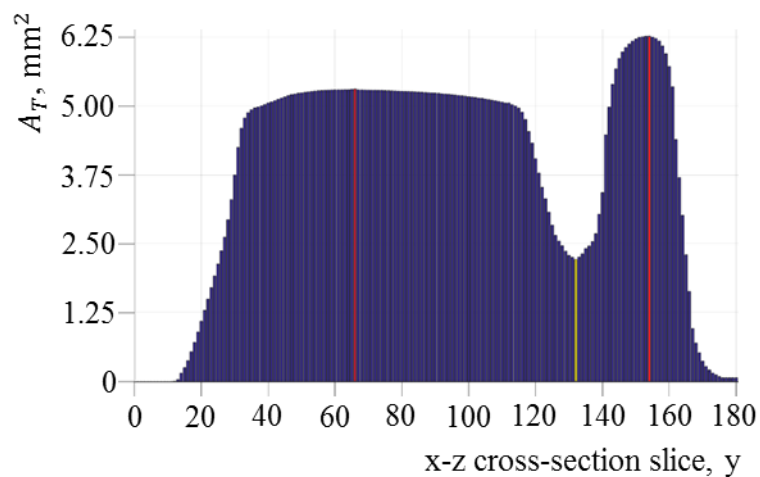


Figure 6.13. Total mechanical area of contact in each x-z cross-section slice image of the oriented 3D volume of interest after the first current loading test at 0 A

Table 6.1. Number of x-z cross-section slice images in y-direction of 3D source model after the four different current loading tests

Test current (A)	0	16	32	64
Number of x-z cross-section slice images	85	68	52	70

In Section 2.3.7, it is mentioned that the electric current flows through the contact interface. This contact interface is visualized as a 3D contact map as described in Section 5.3. According to this, the 3D contact map of the conductors of the 16 A rated AC single pole rocker switch after each current loading test at 0 A, 16 A, 32 A and 64 A as presented in Figure 5.6 of the contact system is converted into a 2D contact map (or 2D cross-section of x-z contact slice) as illustrated in Figure 6.6. The 2D contact map is used as the

reference x-z contact slice to make a comparison with each x-z cross-section slice of the contact system as described in Section 6.2 in order to investigate from which of the spots of the x-z cross-section slice the electric current flows. It is important to note that 2D contact maps are also developed by Lalechos and Swingler [147, 149] using a different method. The differences of these methods are given in Section 5.8.3.

#### 6.4.3 Resistor network model of the contact system findings

The resistor network model is developed based on the separation of voxels into slice asperities according to which a slice asperity of a contact systems corresponds with a resistor in the resistor network model. For the calculations the resistor network model is separated as Open/Closed Circuit (when No Voltage applied) and Closed Circuit (when Voltage applied). The Open/Closed Circuit resistor network model is referred when a potential difference does not apply to it and its resistors correspond to the slice asperities of non-processed x-z cross-section slices. The Closed Circuit resistor network model is referred when a potential difference applies to it and its resistors correspond to the slice asperities of processed x-z cross-section slices.

The graphs of Closed Circuit and Open/Closed Circuit of the resistor network model for each current loading test at 0 A, 16 A, 32 A and 64 A in Figure 6.7 show that the resistors follow different distribution. The graphs of the Open/Closed Circuit resistor network model consist of minimums and maximums at many points across the region of contact. Table 6.2 shows the number of x-z cross-section slice images on the Open/Closed Circuit graph (Figure 6.7) which contains the largest number of resistors after each current loading test at 0 A, 16 A, 32 A and 64 A. The total number of resistors within these x-z cross-section slice images is also included. The error of the calculated values presented in Table 6.2 is  $\pm 1.366\%$ . This error, represents the sum of the error of measured threshold values and the error of 3D volume of interest of the experimental data (already introduced in Section 4.5.2).

According to the graphs of the Open/Closed Circuit resistor network model after each current loading test at 0 A, 16 A, 32 A and 64 A in Figure 6.7, the resistor network model can be divided into three main regions. The limits of each of these three main regions are given in Table 6.3. Each x-z cross-section slice image of the first and third region consists of only one slice asperity (resistor). According to Eq. (2.19), the resistors



of the first and third regions are connected in series as each x-z cross-section slice image has only one resistor. The resistors at the second region are connected intricate in closed and open circuits (see the example of Figure 6.2(b)) making the calculation of the total resistance in the region difficult and complicated. This region is the result of the roughness of two conductors of the contact system in the contact section.

Table 6.2. The total number of resistors for a x-z cross-section slice image with the maximum number of resistors for the Open/Closed Circuit resistor network model after the four different current loading tests

Test current (A)	0	16	32	64
Number of x-z cross-section slice image	36	38	37	36
Total number of resistors	$960 \pm 13$	$788 \pm 11$	$1,326 \pm 18$	$1,360 \pm 19$

Table 6.3. Limits of each main region of the Open/Closed Circuit resistor network model after the four different current loading tests

Test current (A)		0	16	32	64
1 <sup>st</sup> region	Number of first x-z cross-section slice image	1	1	1	1
	Number of last x-z cross-section slice image	11	20	26	24
2 <sup>nd</sup> region	Number of first x-z cross-section slice image	12	21	27	25
	Number of last x-z cross-section slice image	48	48	49	45
3 <sup>rd</sup> region	Number of first x-z cross-section slice image	49	49	50	46
	Number of last x-z cross-section slice image	52	52	52	52

Open/Closed Circuit resistor network models are developed for different electric current values after four different current loading tests at 0 A, 16 A, 32 A and 64 A. In this research, the results of these different current loading tests are categorised into normal operation and non-normal operation. The normal operation includes the current loading tests at 0 A and 16 A as the single pole rocker switch is rated at 16 A AC. The non-normal operation includes the 32 A and 64 A current loading tests as these current values are out of the single pole rocker switch current limits.

The graphs of second region of Open/Closed Circuit resistor network model of Figure 6.7 illustrate that there is a trend after each current loading test in both operations (normal and non-normal). This means that the height between the two conductors of the 3D source model of the contact system decreases and the two conductors are coming closer when the current loading increases. The height between the two conductors of the 3D source model after each current loading test is given in Table 6.4. The height between the two conductors of the source model is defined as the distance from the first to the last x-z cross-section slices of the second region of Open/Closed Circuit resistor network model and multiplied with 5  $\mu\text{m}$  (width of voxel). The error ( $\pm 1.366\%$ ) of the calculated values presented in Table 6.4 is already introduced in Section 4.5.2.

Table 6.4. Second region characteristics of the Open/Closed Circuit resistor network model after the four different current loading tests

Test current (A)	0	16	32	64
Height ( $\mu\text{m}$ )	$180 \pm 2$	$135 \pm 2$	$110 \pm 2$	$100 \pm 1$
Total number of resistors	$12,533 \pm 171$	$8,584 \pm 117$	$12,953 \pm 177$	$9,663 \pm 132$

Table 6.4 illustrates the total number of resistors at the second region of Open/Closed Circuit resistor network model after the four different current loading tests. The total number of resistors at the second region is given from Eq. (6.16). Where  $f_{Open/Closed}(y)$ , is the function which describes the graph of Open/Closed Circuit in Figure 6.7.

$$N_r = \int_{2^{nd} \text{ region}} f_{Open/Closed}(y) dy \quad (6.16)$$

The analysis of the graphs of the Open/Closed Circuit resistor network model in Figure 6.7 for both, normal operation (from 0 A and 16 A) and non-normal operation (from 32 A and 64 A) shows that the total number of resistors at the second region decreases at high currents (16 A and 64 A). This is indicating that current loading stressing the 3D source model of the contact system decreases the number of small slice asperities (resistors) and the dispersion of those slice asperities. This may be due to the local heating and melting at the slice asperities causing them to come together.

The analysis of the graphs of the Open/Closed Circuit resistor network model in Figure 6.7 from normal operation to non-normal operation (from 16 A and 32 A) shows that the total number of resistors at the second region is bigger at the higher current (32 A). This is indicating that current loading stressing the 3D source model of the contact system increases the number of small slice asperities (resistors) and the dispersion of those slice asperities. This may be due to the local heating and melting at the plastic which holds the Conductor A (see Figure 4.1) causing it to move. These are only initial results as more samples and current loading tests are need to be investigated.

More interest is focused on the Closed Circuit resistor network model as this includes only the resistors where the electric current flows through them. Compared with the Open/Closed Circuit resistor network model the Closed Circuit resistor network includes only the resistors which are connected to closed circuits (see the example of Figure 6.3(b)). Each graph of the Closed Circuit resistor network model of Figure 6.7 consists of a maximum in the contact section (second region). Table 6.5 shows the number of x-z cross-section slice image on the Closed Circuit graph (Figure 6.7) which contains the largest number of resistors after each current loading test at 0 A, 16 A, 32 A and 64 A. The x-z cross-section slice image with the largest number of resistors in Closed Circuit resistor network model is labelled as the electric current map. The total number of resistors within these x-z cross-section slice images (or electric current maps) is also included for both resistor network models (Open/Closed Circuit and Closed Circuit). More details concerning the electric current maps are given in Section 6.4.5.

Table 6.5. Electric current map characteristics in Open/Closed and Closed Circuit resistor network models after the four different current loading tests

Test current (A)	0	16	32	64
Number of x-z cross-section slice image	33	35	36	35
Number of resistors in Closed Circuit	188 ± 3	171 ± 2	261 ± 4	304 ± 4
Number of resistors in Open/Closed Circuit	592 ± 8	514 ± 7	1,047 ± 14	1,049 ± 14

According to the graph of the Closed Circuit resistor network model after each current loading test at 0 A, 16 A, 32 A and 64 A in Figure 6.7, the resistor network model

can be divided into three main regions as illustrated in Table 6.6. Each x-z cross-section slice image of the first and third region consists of only one slice asperity (resistor). According to Eq. (2.19), the resistors of the first and third regions are connected in series as each x-z cross-section slice image has only one resistor. The resistors at the second region are connected intricate making the calculation of the total resistance in the region difficult and complicated (but easier compared to the second region of Open/Closed Circuit resistor network). This region corresponds to the roughness of two conductors of the contact system.

Table 6.6. Limits of each main region of the Closed Circuit resistor network model after the four different current loading tests

Test current (A)		0	16	32	64
1 <sup>st</sup> region	Number of first x-z cross-section slice image	1	1	1	1
	Number of last x-z cross-section slice image	19	27	28	29
2 <sup>nd</sup> region	Number of first x-z cross-section slice image	20	28	29	30
	Number of last x-z cross-section slice image	37	39	46	39
3 <sup>rd</sup> region	Number of first x-z cross-section slice image	38	40	47	40
	Number of last x-z cross-section slice image	52	52	52	52

Closed Circuit resistor network models are developed for different electric current values after four different current loading tests at 0 A, 16 A, 32 A and 64 A. In this research, the results of these different current loading tests are categorised into normal operation and non-normal operation. The normal operation includes the current loading tests at 0 A and 16 A as the single pole rocker switch is rated at 16 A AC. The non-normal operation includes the 32 A and 64 A current loading test as these current values are out of the single pole rocker switch current limits.

The graphs of second region of Closed Circuit resistor network model of Figure 6.7 illustrate that there is a trend after each current loading test in both operations (normal and non-normal). This means that the height between the two conductors of 3D source model of the contact system decreases and the two conductors are coming closer when

the current loading increases. The height between the two conductors of the 3D source model after each current loading test is given in Table 6.4. The height between the two conductors of the source model is defined as the distance between the first and last x-z cross-section slices of the second region of Open/Closed Circuit resistor network model and multiplied with 5  $\mu\text{m}$  (width of voxel).

The analysis of the graphs of the Closed Circuit resistor network model in Figure 6.7 for both, normal operation (from 0 A to 16 A) and non-normal operation (from 32 A to 64 A) shows that the height between the two conductors of the 3D contact source model of the contact system at the second region decreases at high currents (16 A and 64 A). The height between the two conductors of the 3D contact source model after each current loading test is given in Table 6.7. The height between the two conductors of the source model is defined as the distance between the first and last x-z cross-section slices of the second region of the Closed Circuit resistor network model and multiplied by 5  $\mu\text{m}$  (width of voxel). The analysis of the graphs of the Closed Circuit resistor network model in Figure 6.7 from normal operation to non-normal operation (from 16 A to 32 A) shows that the height between the two conductors of the 3D contact source model of the contact system at the second region is bigger at the higher current (32 A). This is indicating that current loading stressing the 3D source model of the contact system increases the number of small slice asperities (resistors) and the dispersion of those slice asperities. This may be due to the local heating and melting at the plastic which holds the Conductor A (see Figure 4.1) causing it to move. The error of the calculated values of height at the second region as well as the total number of resistors presented in Table 6.7 is calculated to be  $\pm 1.366\%$  (already introduced in Section 4.5.2).

Table 6.7. Second region characteristics of the Closed Circuit resistor network model after the four different current loading tests

Test current (A)	0	16	32	64
Height ( $\mu\text{m}$ )	$90 \pm 1$	$60 \pm 1$	$90 \pm 1$	$50 \pm 1$
Total number of resistors	$839 \pm 11$	$881 \pm 12$	$1,757 \pm 24$	$1,309 \pm 18$

Table 6.7 illustrates the total number of resistors at the second region of Closed Circuit resistor network model after the four different current loading tests. The total

number of resistors at the second region is given from Eq. (6.17). Where  $f_{closed}(y)$ , is the function which describes the graph of Closed Circuit in Figure 6.7.

$$N_r = \int_{2^{nd} \text{ region}} f_{Closed}(y) dy \quad (6.17)$$

The analysis of the graphs of the Closed Circuit resistor network model in Figure 6.7 for normal operation (from 0 A to 16 A) and from normal operation to non-normal operation (from 16 A to 32 A) shows that the total number of resistors at the second region increases when the current increases (see Table 6.7). This is indicating that current loading stressing the 3D contact source model of the contact system increases the number of small slice asperities (resistors) and the dispersion of those slice asperities. Concerning the analysis of the graphs of the Closed Circuit resistor network model in Figure 6.7 for non-normal operation (32 A and 64 A) shows that the total number of resistors at the second region decreases when the current loading increases. These are only initial results as more samples and current loading tests are needed to be studied for any conclusions.

#### 6.4.4 Total resistance and total conductance of the contact system

The total resistance across the contact system is given from the sum of total resistance in each region. The Closed Circuit resistor network model which is introduced in this research will be used in order to calculate the total resistance across conductors of the 16 A rated AC single pole rocker switch and hence the total conductance of it. The Open/Closed Circuit resistor network model is excluded as the open circuits do not affect the total values of the resistance and conductance.

Table 6.8 illustrates the total resistance of the first zone, second zone (or second region as they have the same limits) and third zone as well as the total resistance across the first and third zone of the 3D contact source model (Closed Circuit resistor network model) of the 16 A rated AC single pole rocker switch after the four different current loading tests. The limits of the 2<sup>nd</sup> region of Open/Closed Circuit resistor network model are the same with the limits between the first and third zone of the contact system (see Figure 6.7). Where the first zone on the graphs of Figure 6.7 is defined by the common x-z cross-section slices between the first region of the Closed Circuit and the second

region of the Open/Closed Circuit. The third zone on the graphs of Figure 6.7 is defined as the common x-z cross-section slices between the third region of the Closed Circuit and the second region of the Open/Closed Circuit. These zones (first and third) are defined in order to set limits for the resistance measurement as the measurement from the first x-z cross-section slice to the last gives arbitrary value for the resistance of the 3D source model of the contact system (this is because the graphs of Figure 6.7 at 0 A, 16 A and 64 A consist of a part of the whole 3D source model, see Section 6.4.2 and Table 6.1).

The total resistance of the first and third zone after each current loading test presented in Table 6.8 is calculated by adding the resistance of each x-z cross-section slice image of the 3D contact source model (Closed Circuit) using Eq. (2.15). The resistance of each x-z cross-section slice (of first and third zone) is calculated by using the total mechanical area of contact in each x-z cross-section slice image. The total mechanical area of contact of each x-z cross-section slice image is given in Figure 6.12 (the Closed Circuit values). Where the length  $l$  in y-direction and electrical resistivity (of silver)  $\rho$  of Eq. (2.15) are equal to  $5 \mu\text{m}$  and  $15.87 \times 10^{-9} \Omega\text{m}$  respectively. The error of the calculated values presented in Table 6.8 is  $\pm 1.366\%$ . This error, represents the sum of the error of measured threshold values and the error of 3D volume of interest of the experimental data (see Section 4.5.2).

Table 6.8. Resistance values in each zone and the total resistance across the 1<sup>st</sup> and 3<sup>rd</sup> zone of the 3D contact source model after the four different current loading tests

Test current (A)		0	16	32	64
Resistance (nΩ)	1 <sup>st</sup> zone	168.67 ± 2.30	151.89 ± 2.07	32.879 ± 0.45	104.43 ± 1.43
	2 <sup>nd</sup> region	617.67 ± 8.44	336.02 ± 4.59	402.17 ± 5.49	348.80 ± 4.76
	3 <sup>rd</sup> zone	172.79 ± 2.36	155.58 ± 2.13	59.669 ± 0.82	105.64 ± 1.44
	Total	959.13 ± 13.1	643.49 ± 8.79	494.72 ± 6.76	558.87 ± 7.63

The resistance across the second region is difficult to calculate due to the intricate connections of the resistors at the region. However, an approach is introduced in this research by modifying Greenwood's formula which is given from Eq. (2.23). This gives the total contact resistance which depends on the distances between the set of circular

contact spots (the formula is based on electrostatics [194]). According to this, Eq. (2.23) applies in surfaces (contact spots). The modification on Eq. (2.23) which is given from Eq. (6.18) is made in order to apply in volumes (slice asperities). It is important to note that the potential difference across each slice asperity (each resistor) in the x-z cross-section slice is assumed to be equal with the other slice asperities (resistors) in the x-z cross-section slice of the 3D contact source model (Closed Circuit resistor network).

$$R = \frac{\rho \cdot l}{\sum A_i} + \frac{\rho}{\pi(\sum a_i)^2} \sum_{i \neq j} \frac{a_i a_j}{d_{ij}} \quad (6.18)$$

Eq. (6.18) gives the total resistance for each x-z slice on the second region of Closed Circuit (see Figure 6.7) resistor network model of the 3D contact source model. To achieve this, the cross-section area of each slice asperity in the y-direction is assumed to be a circle of radius  $\alpha$ . For example, the radius of contact spot  $i$  is calculated by Eq. (5.7). Where  $A_i$  is the total cross-section area of slice asperity  $i$ . The distance  $d_{ij}$  between slice asperity  $i$  and  $j$  is calculated from the mean-points of slice asperities  $i$  and  $j$  (see Figure 5.4). Where the length  $l$  in y-direction and electrical resistivity (of silver)  $\rho$  of Eq. (6.18) are equal to  $5 \mu\text{m}$  and  $15.87 \times 10^{-9} \Omega\text{m}$  respectively. The total resistance of the second region after each current loading test presented in Table 6.8 is calculated by adding the total resistance of each x-z slice of the Closed Circuit (see Figure 6.7) resistor network model of the 3D contact source model.

The total resistance value after each current loading test is presented in Table 6.8. This value is calculated by adding the total resistance of three zones. It is important to note that the bulk resistance is measured across the two conductors of the 16 A rated AC single pole rocker switch after the 0 A current loading test using the ‘‘four-wire’’ method and is found to be approximately equal to  $0.27 \text{ m}\Omega$  (Section 4.3). Comparing this value with the value of total resistance in Table 6.8 after the 0 A current loading test it is obvious that it is larger. This was expected because the value of the resistance is increasing when the length of the material is increasing (see Eq. (2.15)).

The conductance in each zone and the total conductance across the 1<sup>st</sup> and 3<sup>rd</sup> zone of the 3D contact source model of the 16 A rated AC single pole rocker switch after the



four different current loading tests at 0 A, 16 A, 32 A and 64 A are given in Table 6.9. The conductance values presented in Table 6.9 are calculated using the corresponding resistance values presented in Table 6.8. The conductance is given from the inverse value of resistance.

Table 6.9. Conductance values in each zone and the total conductance across the 1<sup>st</sup> and 3<sup>rd</sup> zone of the 3D contact source model after the four different current loading tests

Test current (A)		0	16	32	64
Conductance (MS)	1 <sup>st</sup> zone	5.929 ± 0.08	6.584 ± 0.09	30.415 ± 0.42	9.576 ± 0.13
	2 <sup>nd</sup> region	1.619 ± 0.02	2.976 ± 0.04	2.487 ± 0.03	2.867 ± 0.04
	3 <sup>rd</sup> zone	5.787 ± 0.08	6.428 ± 0.09	16.759 ± 0.23	9.466 ± 0.13
	Total	1.043 ± 0.01	1.554 ± 0.02	2.021 ± 0.03	1.789 ± 0.02

#### 6.4.5 Electric current maps findings

The cross-section area of the x-z cross-section slice images for the current loading tests at 0 A, 16 A, 32 A and 64 A which was presented in Table 6.5 are illustrated in Figure 6.8, Figure 6.9, Figure 6.10 and Figure 6.11 respectively. These x-z cross-section slice images show their resistors in red and blue spots and are labelled as electric current maps. The red and blue spots show the resistors of the Open/Closed Circuit resistor network model. The red spots show the resistors of the Closed Circuit resistor network model and the geometric path of electric current which flows through the voxels (or pixels in 2D) of these x-z cross-section slice images. The total number of spots (or resistors) for both resistor network models (Open/Closed Circuit and Closed Circuit) of Figure 6.8, Figure 6.9, Figure 6.10 and Figure 6.11 is given from the corresponding current test value of Table 6.5.

The analysis of electric current maps of both circuit resistor network models (Open/Closed Circuit and Closed Circuit) in Figure 6.8 and Figure 6.9 for normal operation (0 A and 16 A) shows that their total number of resistors decreases when the loading current increases (Table 6.5). The analysis of electric current maps of both Circuit resistor network models (Open/Closed Circuit and Closed Circuit) in Figure 6.10 and

Figure 6.11 for non-normal operation (32 A and 64 A) shows that their total number of resistors increases when the loading current increases (Table 6.5). Concerning the analysis of electric current maps of both Circuit resistor network models (Open/Closed Circuit and Closed Circuit) in Figure 6.9 and Figure 6.10 from normal operation to non-normal operation (from 16 A to 32 A) shows that their total number of resistors increases when the loading current increases (Table 6.5). These are only initial results as more samples and current loading tests are needed for each operation (normal and non-normal) to be investigated for any conclusions.

#### 6.4.6 Total cross-sectional area of slice asperities findings

The cross-section area of each x-z cross-section slice of the 3D source model (Open/Closed Circuit) and 3D contact source model (Closed Circuit) is calculated by counting the number of voxels in each slice and multiplied with the pixel size ( $5 \mu\text{m} \times 5 \mu\text{m}$ ). The cross-section area of each x-z cross-section slice for both (Open/Closed Circuit and Closed Circuit) resistor network models after each current loading test is illustrated in Figure 6.12. The graphs of Figure 6.12 show that the cross-section areas of both (Open/Closed Circuit and Closed Circuit) resistor network models follow similar distributions after each current loading test at 0 A, 16 A, 32 A and 64 A. It is important to mention that the graphs of the Figure 6.12 show that as the resistors (slice asperities) tend to the contact region their cross-sectional area decreases.

Table 6.10 shows the number of x-z cross-section slice image on the Open/Closed Circuit graph (Figure 6.12) which have the smallest cross-section area after each current loading test at 0 A, 16 A, 32 A and 64 A. The total cross-section area of these x-z cross-section slice images is also included.

Table 6.10. Number of x-z cross-section slice image with the smallest total cross-section area and its total cross-section area for the Open/Closed Circuit resistor network model after the four different current loading tests

Test current (A)	0	16	32	64
Number of x-z cross-section slice image	28	34	39	34
Total cross-section area ( $\text{mm}^2$ )	$2.26 \pm 0.03$	$2.39 \pm 0.03$	$2.98 \pm 0.04$	$1.51 \pm 0.02$

Table 6.11 shows the number of x-z cross-section slice image on the Closed Circuit graph (Figure 6.12) which have the smallest cross-section area after each current loading test at 0 A, 16 A, 32 A and 64 A. The total cross-section area of these x-z cross-section slice images is also included. The error of the calculated values presented in Table 6.10 and Table 6.11 is  $\pm 1.366\%$  (see Section 4.5.2).

Table 6.11. Number of x-z cross-section slice image with the smallest total cross-section area and its total cross-section area for the Closed Circuit resistor network model after the four different current loading tests

Test current (A)	0	16	32	64
Number of x-z cross-section slice image	29	34	37	34
Total cross-section area (mm <sup>2</sup> )	$2.07 \pm 0.02$	$2.25 \pm 0.03$	$2.32 \pm 0.03$	$1.31 \pm 0.02$

Table 6.12 illustrates the total volume of resistors at the second region of Open/Closed Circuit resistor network model after the four different current loading tests. The total volume of resistors at the second region is given from Eq. (6.19). Where  $f_{open/closed}(y)$ , is the function which describes the graph of Open/Closed Circuit in Figure 6.12 and  $p_l$  is the pixel length (5  $\mu\text{m}$  in this research).

Table 6.12. Total volume of resistors at the second region of the Open/Closed Circuit resistor network model after the four different current loading tests

Test current (A)	0	16	32	64
Total volume of resistors (mm <sup>3</sup> )	$0.707 \pm 0.009$	$0.525 \pm 0.007$	$0.456 \pm 0.006$	$0.366 \pm 0.005$

$$V_R = p_l \cdot \int_{2^{nd} \text{ region}} f_{Open/Closed}(y) dy \quad (6.19)$$

The graphs of second region of Open/Closed Circuit resistor network model of Figure 6.12 illustrate that there is a trend of the total volume of resistors after each current loading test in both operations, normal and non-normal. This means that the total volume of resistors between the two conductors of 3D source model of the contact system

increases and the two conductors are coming closer when the current loading increases. The total volume of resistors at the second region of the 3D source model (Open/Closed Circuit) after each current loading test is given in Table 6.12. The error of the calculated values presented in Table 6.12 is  $\pm 1.366\%$ . This error, represents the sum of the error of measured threshold values and the error of 3D volume of interest of the experimental data (see Section 4.5.2).

Table 6.13 illustrates the total volume of resistors at the second region of Closed Circuit resistor network model after the four different current loading tests. The total volume of resistors at the second region is given from Eq. (6.20). Where  $f_{closed}(y)$ , is the function which describes the graph of Closed Circuit in Figure 6.12 and  $p_l$  is the pixel length (5  $\mu\text{m}$  in this research).

Table 6.13. Total volume of resistors at the second region of the Closed Circuit resistor network model after the four different current loading tests

Test current (A)	0	16	32	64
Total volume of resistors ( $\text{mm}^3$ )	$0.209 \pm 0.003$	$0.136 \pm 0.002$	$0.292 \pm 0.004$	$0.084 \pm 0.001$

$$V_R = p_l \cdot \int_{2^{nd} \text{ region}} f_{closed}(y) dy \quad (6.20)$$

The analysis of the graphs of the Closed Circuit resistor network model in Figure 6.12 for both normal operation (0 A and 16 A) and non-normal operation (32 A and 64 A) shows that the total volume of resistors at the second region decreases at high currents (16 A and 64 A). The total volume of resistors at the second region of Closed Circuit resistor network model is given in Table 6.13 with error of  $\pm 1.366\%$  (see Section 4.5.2).

The analysis of the graphs of the Closed Circuit resistor network model in Figure 6.7 from normal operation to non-normal operation (from 16 A to 32 A) shows that the total number of resistors at the second region (see Table 6.13) is bigger at the higher current (32 A). These are only initial results as more samples and current loading tests are need to be investigated for any conclusions.

### 6.4.7 Electric current constriction

The resistor network model which is developed in this research is found to demonstrate that the contact system consists of open and closed circuits. In the modelling process, the open circuits are then removed from the resistor network model and picture any cross-section area of the contact system and show from which voxels the electric current flows. Figure 6.14(a) illustrates the schematic diagram of a contact system with the limits of each region of resistor network model (Open/Closed and Closed Circuits).

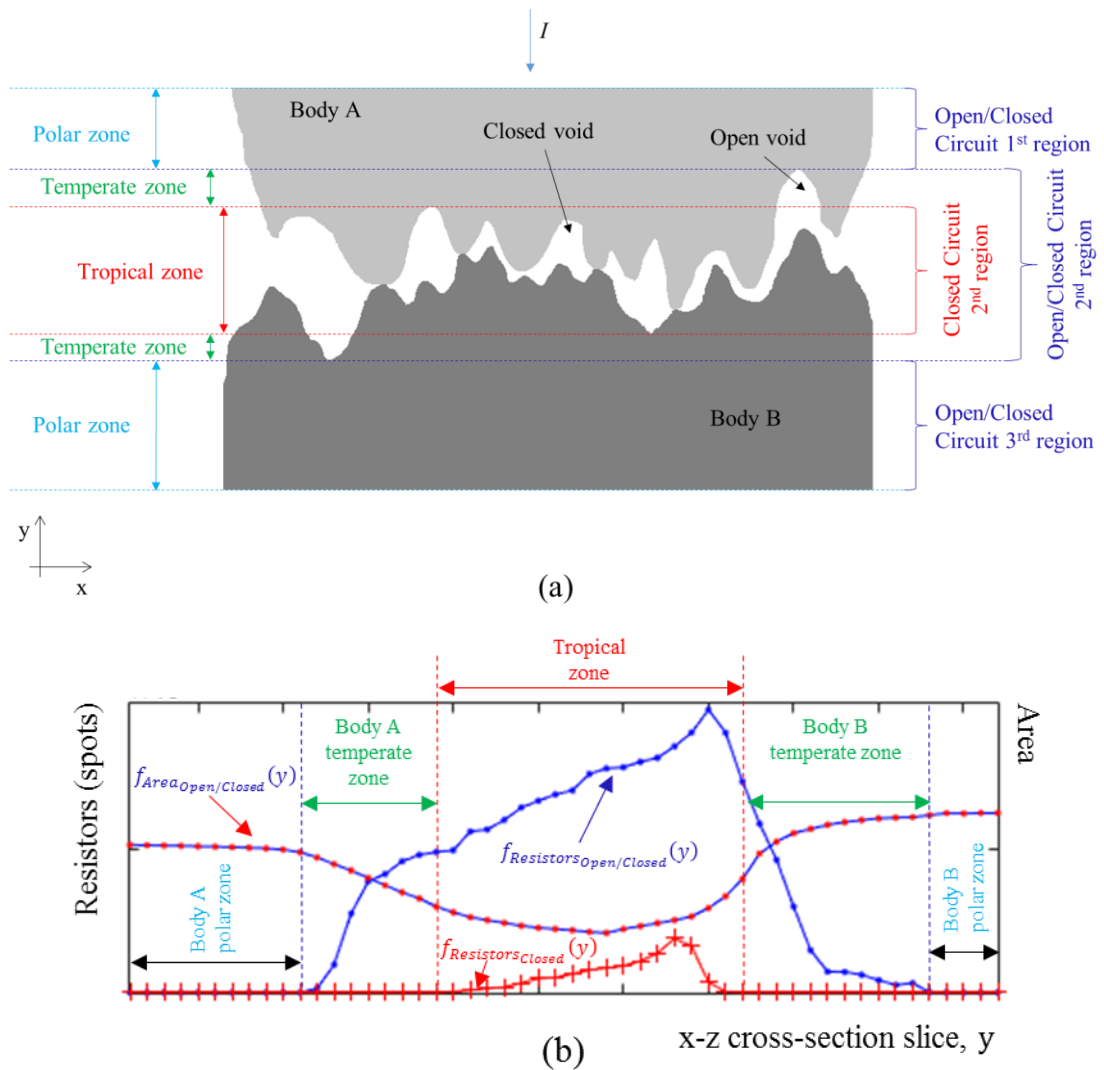


Figure 6.14. (a) Schematic diagram of a contact system. (b) Schematic diagram of resistors of a contact system in each x-z cross-section slice

When a simulated potential difference is applied across the contact system, an electric current will flow through it. From Figure 6.14(a) it is obvious when the electric current tends to contact region is constricted. According to this, the contact system can

be divided into constriction zones. These constriction zones are labelled as polar, temperate and tropical. For example, as the electric current flows from polar zone to the tropical zone the constriction increases and when flows (the electric current) from tropical zone to the polar zone the constriction decreases. This constriction of electric current through a contact system shows behaviour analogous to the climate zones of earth.

The limits of constriction zones in bodies A and B can be identify from the Open/Closed Circuit and Closed Circuit resistor network models. Where the polar zones in Body A and Body B are given from the limits of the 1<sup>st</sup> region and 3<sup>rd</sup> region of Open/Closed Circuit resistor network model respectively. Where the temperate zone in Body A is defined the district between the 1<sup>st</sup> region of Open/Closed Circuit and 2<sup>nd</sup> region of Closed Circuit. Where the temperate zone in Body B is defined the district between the 2<sup>nd</sup> region of Closed Circuit and the 3<sup>rd</sup> region of Open/Closed Circuit. Where the tropical zone of contact system is given from the limits of the 2<sup>nd</sup> region of Closed Circuit. The limits of each zone of Figure 6.14(a) are also presented in Figure 6.14(b). It is important to note that the limits of polar zones (the repel direction of temperate zone of each body) are arbitrary as they could be from any cross-section slice of the bulk of contact bodies. On the other hand, the limits of temperate and tropical zone are given exactly from the 2<sup>nd</sup> region of Open/Closed and Closed Circuits resistor network models of contact system.

## **6.5 Conclusion**

The X-ray CT technique is used in order to visualize the contact system of a 16 A rated AC single pole rocker switch without the need to dismantle the sample. A resistor network model of a contact system is developed and introduced based on the slice asperities of the cross-section slice images. These slice asperities consist of voxel or voxels which represent the 3D microstructures of the contact system. The cross-section slice images of the contact system which are acquired from the X-ray CT are processed using Contact Analysis Techniques, CAT\* which are developed and implemented with a suite of tools developed in MATLAB and Image Processing Toolbox. These techniques can be used for any contact system for any value of resolution.

The resistor network model is found to demonstrate that the contact system consists of open and closed circuits. In the modelling process, the open circuits are then removed from the resistor network model with a technique presented in this chapter which pictures

any cross-section area of the contact system and shows from which voxels the electric current flows.

The resistor network model is divided into three main regions where two regions have resistors connected in series. The third region is located between the other two regions and its resistors are connected in a nontrivial fashion of parallel and series components. For the resistance across this region an approach has been introduced by modifying the Greenwood's formula of total contact resistance. The sum of the total resistance in each region gives the total resistance across the resistor network model of the contact system.

Moreover, it is found that as a cross-section slice of the resistor network model (for Closed Circuit) tends to the contact region the total number of its resistors (slice asperities) increases. Furthermore, it is important to note that as a cross-section slice of the resistor network model (for both circuits, Open/Closed and Closed) tends to the contact region the total cross-section area of the cross-section slice decreases. This indicates that as the cross-section slice tends to the contact region the total volume of its resistors (slice asperities) decreases.

The resistor network model which is developed in this chapter illustrates that the constriction of electric current through the contact system shows behaviour analogous to the climate zones of earth.

In addition, in this chapter it is found that the electric current causes changes in the three main regions the resistor network model. These changes includes the limits of each region, the number of resistors in each slice of the region as well as the total number and the total volume of resistors. These changes have an impact on the total resistance across the resistor network model. The results presented in this chapter are limited as more samples and current loading tests need to be investigated for any conclusions concerning the effect of electric current across the resistor network model of the contact system.

## **Chapter 7 – The 3D Contact Analysis Approach for the Visualisation and Characterisation of the Electrical Contact Asperities**

### **7.1 Introduction**

The contact spots are found to be very important by many researchers which are visualised using different destructive and non-destructive visualisation techniques (as described in Section 3.2 and Section 3.3 respectively). Many recent contact spots visualization techniques do not recognize the effects of scale dependent properties [7, 141, 147, 148]; in fact, many classical and widely used contact spots area visualization techniques completely ignore the effect of scale and the 3D nature of contact spots and picture the contact area in a 2D plane. The work presented in this chapter aims to build on the visualisation technique developed in a previous chapter (Chapter 5) where the contact spots are pictured in a 3D plane as a “3D Contact Map” in order to visualise the contact asperities.

The contact asperities have been considered for decades due to their significant importance in several branches of science and engineering such as surface science [40-42], tribology [43-45], heat transfer [46-49] and recently in Micro-Electro-Mechanical Systems (MEMS) [50-56]. Due to this significant importance, several models [57-62] are developed in order to provide information about their features such as contact asperity dimensions, number, distribution material properties, surface profiles and operating conditions. One of the most popular models has been developed by Greenwood-Williamson [63]. According to this model, it assumes the two bodies of the contact asperities on a surface are hemispherical in shape with the same radius. The peak of each contact asperity is assumed to be located at different heights following a random Gaussian distribution. When a flat plane is brought into contact with the Greenwood-Williamson surface, the contact asperities deform elastically with consideration of plastic deformation under particular limits.

The contact asperities describe the structures above and below of the contact interface (the contact spots of the 3D contact map) to the two conductors which make the contact system. The contact asperities require the discretization of the 3D microstructures of the contact system into voxels. A contact analysis approach has been developed and introduced in this chapter which shows the way to 3D visualise the contact asperities of



a given contact system. For the discretization of a 3D microstructure of contact system into voxels, the X-ray CT technique is used in order to collect the data of a 16 A rated AC single pole rocker switch which is used as a contact system for investigation.

In this chapter, a contact analysis approach has been developed and introduced which shows the structures of the contact spots of the conductors of a 16 A rated AC single pole rocker switch as 3D contact asperities. For the development and test purposes of this approach, the experimental data of the 250 V, 16 A rated AC single pole rocker switch after the four different current loading tests (0 A, 16 A, 32 A and 64 A) which are presented in Section 4.5 are used. Moreover, the total number, the volume and the height of the 3D contact asperities are calculated and presented with their distribution. In addition, the surface area of the 3D contact asperities which is exposed to the air is also calculated and presented with their distribution.

## 7.2 Contact Analysis and Modelling Techniques

For the 3D visualization of contact asperities, a similar approach used in the previous chapter (Chapter 6) in order to picture any cross-section slice of the contact system showing from which voxels the electric current flows is used. Figure 7.1(a) shows a schematic oriented 3D volume of interest of the contact system which is used in order to explain this contact analysis approach. The oriented 3D volume of interest of the contact system consists of two rough bodies, A and B which are in mechanical contact. The mechanical contact takes place at three contacting regions which are presented with red voxels in Figure 7.1(a).

The contact analysis approach consists of further stages starting with the division of the contact system into equal x-z cross-section slices across the electric current ( $I$ ) direction (y-direction). The electric current direction is defined to be parallel with the normal force ( $F$ ) and it is assumed that it flows through the whole cross-section area of the first and last x-z cross-section slices. The direction of the normal force is used to define the orientation of the coordinate system used. The schematic oriented 3D volume of interest of the contact system of Figure 7.1(a) (and Figure 7.1(b)) consists of six x-z cross-section slices and the 2<sup>nd</sup> x-z cross-section slice of Figure 7.1(b) is illustrated in Figure 7.1(c). The schematic oriented 3D volume of interest of the contact system of Figure 7.1(a) consists of contact asperities and non-contact asperities. The definition of

contact asperity (see Figure 6.1(b)) and non-contact asperity (see Figure 6.1(c)) was already introduced in Section 6.2. For example, the Body B of Figure 7.1(a) has 2 non-contact asperities and 3 contact asperities while Body A has 3 non-contact asperities and 3 contact asperities. It is important to note that the number of contact asperities for both bodies (A and B) of any contact system is equal. Moreover, the voxels of each x-z cross-section slice are labelled as slice asperities. A slice asperity is defined as a collection of voxels which are neighbouring other voxels by at least one edge. For example, the 2<sup>nd</sup> x-z cross-section slice of Figure 7.1(a) consists of four slice asperities and the 2<sup>nd</sup> x-z cross-section slice of Figure 7.1(b) consists of two slice asperities. The 2<sup>nd</sup> x-z cross-section slice of Figure 7.1(b) is illustrated in Figure 7.1(c).

The second stage of the contact analysis approach is the development of the oriented 3D contact volume of interest of the contact system which is illustrated in Figure 7.1(b). This 3D contact volume of interest includes only the contact asperities from which the electric current flows when a potential difference is applied across the two bodies (A and B). For example, Figure 7.1(b) includes only the contact asperities of Figure 7.1(a) with their extensions. More details about the development of the 3D contact volume of interest of the contact system are given in the previous chapter (Chapter 6) where the 3D contact volume of interest consists of resistors which are connected to closed circuits.

To visualize only the contact asperities of the 3D contact volume of interest of the contact system of Figure 7.1(b), three Contact Analysis Techniques (CAT\*) are developed. The first technique is to develop the 3D constriction asperities map using the Contact Analysis Technique for Asperities (CATA) which gives information on where the electrical constriction asperities in a 3D volume profile are located. CATA shows that the electric current flows through the 3D constriction asperities [193]. This technique is a continuation of the 3D contact maps developed in Section 5.3 and extended by one voxel in electric current direction as presented in [193] as 3D constriction asperities maps. Figure 7.2(a) illustrates the 3D constriction asperities map of the schematic oriented 3D volume of interest of the contact system of Figure 7.1(b). It is important to note that the 3D constriction asperities map is the same in both, oriented 3D volume of interest and oriented 3D contact volume of interest of the contact system.

The second technique is the Contact Analysis Technique for Contact Voxels (CATV). This technique is used to create an x-z contact slice with all the voxels of the

3D constriction asperities map of Figure 7.2(a) at the same height (y-direction) as illustrated in Figure 7.2(b). As mentioned before, the electric current flows through the 3D constriction asperities map, consequently, it flows through the x-z contact slice. The collection of solid voxels in this x-z contact slice which are neighbouring other solid voxels by at least one point of their edges are defined as slice asperities (same definition as in x-z cross-section slices). The x-z contact slice of Figure 7.2(b) consists of 3 slice asperities.

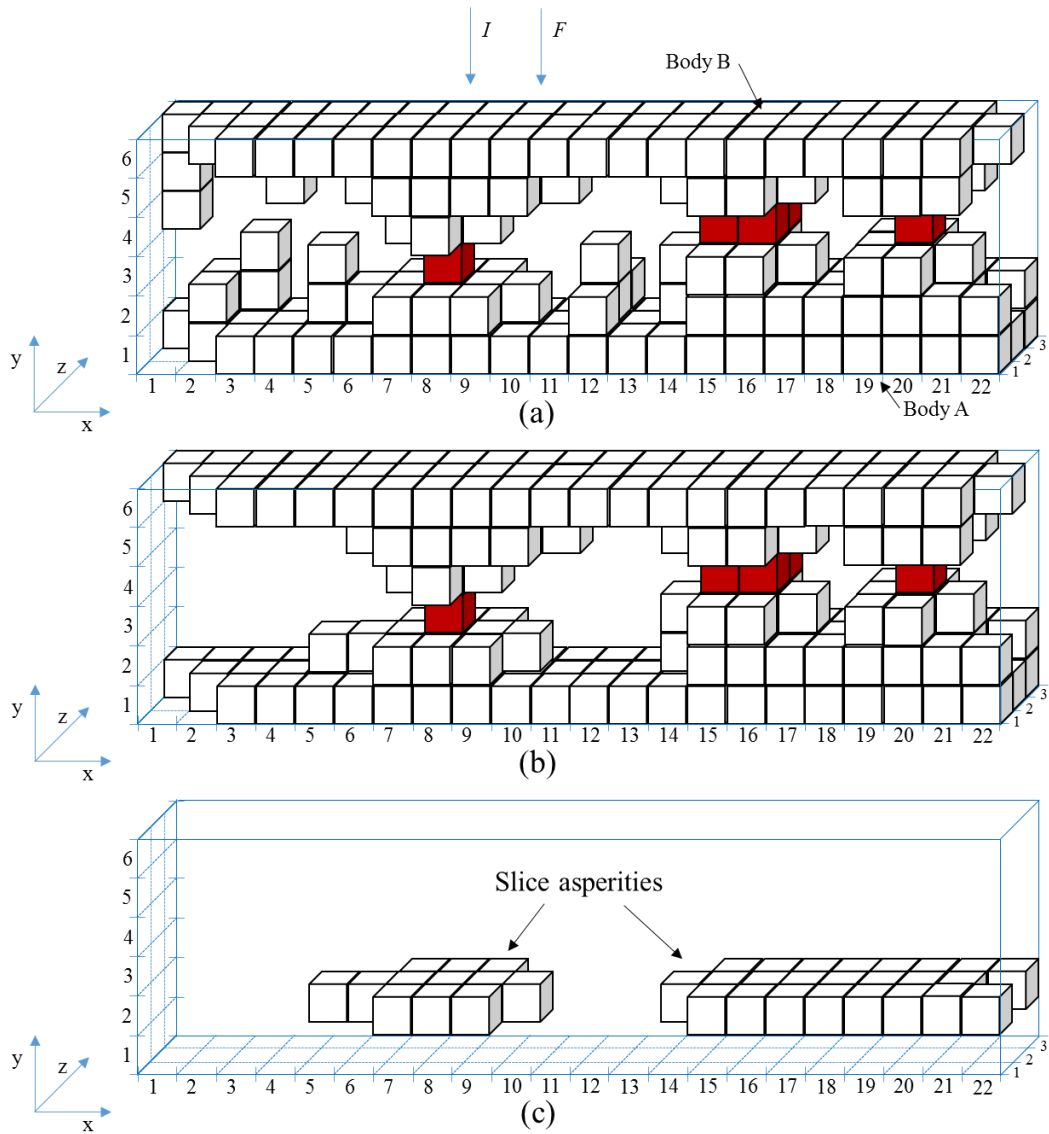


Figure 7.1. (a) Schematic oriented 3D volume of interest. (b) Schematic oriented 3D contact volume of interest. (c) 2<sup>nd</sup> x-z cross-section slice of the schematic oriented 3D contact volume of interest [186]

The third technique, Contact Analysis Technique for Asperities Comparison (CATAC) which consists of several stages starts with the visualization of each slice

asperity separately with its extensions to the two bodies A and B. To achieve this, a comparison of each slice asperity of the x-z contact slice with the slice asperities of each x-z cross-section slice is made. The reason of making a comparison is to identify which of the slice asperities of the x-z cross-section slice are connected with the slice asperity  $k$  of the x-z contact slice. Where  $k$ , is the number of slice asperity of the x-z contact slice (it is also the number of contact asperity, as the slice asperity belongs to the constriction asperity). If there is a connection between the slice asperity  $k$  of x-z contact slice with any of the slice asperities in the x-z cross-section slice, then, the connected slice asperity in x-z cross-section slice belongs to the contact asperity  $k$ . If there is no connection between the slice asperity  $k$  of the x-z contact slice with the slice asperities in the x-z cross-section slice, then, the disconnected slice asperities are removed from the x-z cross-section slice. A mathematical example of this technique is given below describing the 3D visualization of contact asperities of the schematic oriented 3D volume of interest of the contact system of Figure 7.1(b) where each x-z cross-section slice is described by different matrix.

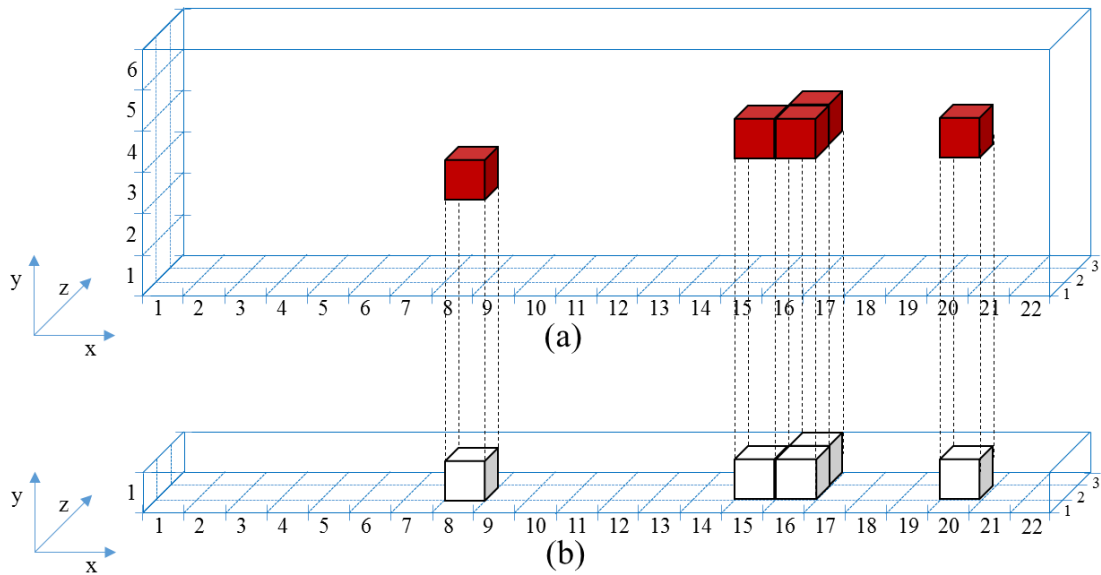


Figure 7.2. (a) 3D constriction asperities map. (b) x-z contact slice [186]

The matrix  $[A]$  of Eq. (7.1) represents the x-z contact slice of Figure 7.2(b), where zeros and  $a$  elements of matrix  $[A]$  represent voxels with air and solids of the schematic oriented 3D volume of interest of the contact system respectively. A slice asperity in matrix  $[A]$  is defined as a collection of solid voxels which are neighbouring other solid voxels by at least one point of their edges. The matrix  $[A]$  consists of three slice asperities.

$$[A]=\begin{bmatrix} 0 & 0 & 0 & 0 & 0 & 0 & 0 & 0 & 0 & 0 & 0 & 0 & 0 & 0 & 0 & \alpha & 0 & 0 & 0 & 0 & 0 & 0 \\ 0 & 0 & 0 & 0 & 0 & 0 & 0 & \alpha & 0 & 0 & 0 & 0 & 0 & 0 & \alpha & \alpha & 0 & 0 & 0 & \alpha & 0 & 0 \\ 0 & 0 \end{bmatrix} \quad (7.1)$$

Matrix  $[A_k]$ , represents the  $k$  slice asperity of the x-z contact slice for  $k \in [1, S]$ . Where  $S$ , is the total number of slice asperities of the x-z contact slice (or the total number of slice asperities of matrix  $[A]$ ). The matrix  $[A_1]$  in Eq. (7.2) represents the 1st slice asperity of the x-z contact slice.

$$[A_1]=\begin{bmatrix} 0 & 0 \\ 0 & 0 & 0 & 0 & 0 & 0 & 0 & \alpha & 0 & 0 & 0 & 0 & 0 & 0 & 0 & 0 & 0 & 0 & 0 & 0 & 0 \\ 0 & 0 \end{bmatrix} \quad (7.2)$$

Matrix  $[B_i]$ , represents the  $i^{th}$  x-z cross-section slice for  $i \in [1, N]$ , where  $i$  is the number of x-z cross-section slice and  $N$  is the total number of x-z cross-section slices. Zeros and  $\beta$  elements of matrix  $[B_i]$  represent voxels of air and solid material of the oriented 3D volume of interest of the contact system respectively. The collection of solid voxels in matrix  $[B_i]$  which are neighbouring to other solid voxels by at least one point of their edges are called slice asperities. The matrix  $[B_2]$ , or the 2<sup>nd</sup> x-z cross-section slice of Figure 7.1(b) consists of 2 slice asperities and is described by Eq. (7.3).

$$[B_2]=\begin{bmatrix} 0 & 0 & 0 & 0 & 0 & 0 & \beta & \beta & \beta & 0 & 0 & 0 & 0 & \beta & \beta & \beta & \beta & \beta & \beta & \beta \\ 0 & 0 & 0 & 0 & \beta & \beta & \beta & \beta & \beta & \beta & 0 & 0 & 0 & \beta & \beta & \beta & \beta & \beta & \beta & \beta & 0 \\ 0 & 0 & 0 & 0 & 0 & 0 & \beta & \beta & \beta & 0 & 0 & 0 & 0 & \beta & \beta & \beta & \beta & \beta & \beta & \beta & \beta \end{bmatrix} \quad (7.3)$$

To identify if there is a connection between the 1<sup>st</sup> ( $k = 1$ ) slice asperity of x-z contact slice with any of the slice asperities in the 2<sup>nd</sup> ( $i = 2$ ) x-z cross-section slice, Eq. (7.2) and Eq. (7.3) are added as presented in Eq. (7.4). The matrix  $[C_{k_i}]$  is the sum of matrix  $[A_k]$  with matrix  $[B_i]$ . The  $\gamma$  element represents the summation of  $a$  and  $\beta$  elements and shows if there is a connection between the slice asperity  $k$  of the x-z contact

slice with any of the slice asperities in the  $i^{th}$  x-z cross-section slice. The same procedure is used for the rest of the x-z cross-sectional slices.

$$[C_{1_2}] = \begin{bmatrix} 0 & 0 & 0 & 0 & 0 & 0 & \beta & \beta & \beta & 0 & 0 & 0 & 0 & 0 & \beta & \beta & \beta & \beta & \beta & \beta & \beta \\ 0 & 0 & 0 & 0 & \beta & \beta & \beta & \gamma & \beta & \beta & 0 & 0 & 0 & \beta & \beta & \beta & \beta & \beta & \beta & \beta & 0 \\ 0 & 0 & 0 & 0 & 0 & 0 & \beta & \beta & \beta & 0 & 0 & 0 & 0 & 0 & \beta & \beta & \beta & \beta & \beta & \beta & \beta \end{bmatrix} \quad (7.4)$$

Each of the slice asperities presented in the matrix  $[C_{k_i}]$  is examined separately in order to identify if it belongs to the  $k$  3D contact asperity with its extensions to bodies A and B. If a slice asperity belongs to this  $k$  3D contact asperity with its extensions to bodies A and B, the  $\gamma$  element is included within the slice asperity and a new matrix is created which contains only this slice asperity which is renamed with the  $\delta$  elements. A slice asperity without the  $\gamma$  element is replaced with zeros. These conditions are described by matrix  $[D_{k_i}]$ . The matrix  $[D_{1_2}]$  of Eq. (7.5) shows that the slice asperity ( $\delta$  elements) of the 2<sup>nd</sup> ( $i = 2$ ) x-z cross-section slice of matrix  $[D]$  belongs to the 1<sup>st</sup> ( $k = 1$ ) 3D contact asperity with its extensions to bodies A and B. The same procedure is used for the rest of the x-z cross-sectional slices of the oriented 3D volume of interest of the contact system.

$$[D_{1_2}] = \begin{bmatrix} 0 & 0 & 0 & 0 & 0 & 0 & \delta & \delta & \delta & 0 & 0 & 0 & 0 & 0 & 0 & 0 & 0 & 0 & 0 & 0 & 0 \\ 0 & 0 & 0 & 0 & \delta & \delta & \delta & \delta & \delta & \delta & 0 & 0 & 0 & 0 & 0 & 0 & 0 & 0 & 0 & 0 & 0 \\ 0 & 0 & 0 & 0 & 0 & 0 & \delta & \delta & \delta & 0 & 0 & 0 & 0 & 0 & 0 & 0 & 0 & 0 & 0 & 0 & 0 \end{bmatrix} \quad (7.5)$$

Figure 7.3(a) shows the 1<sup>st</sup> ( $k = 1$ ) 3D contact asperity with its extensions to bodies A and B which is developed with the stack of matrices  $[D_{1_i}]$  in the y-direction for  $i \in [1, N]$ . The same procedure used for the visualization of 1<sup>st</sup> ( $k = 1$ ) 3D contact asperity with its extensions to bodies A and B is used for the rest of  $k$  3D contact asperities with their extensions to bodies A and B. The results of this procedure for the 2<sup>nd</sup> and 3<sup>rd</sup> ( $k = 2$  and  $k = 3$ ) 3D contact asperities with their extensions to bodies A and B are illustrated in Figure 7.3(b) and Figure 7.3(c) respectively.

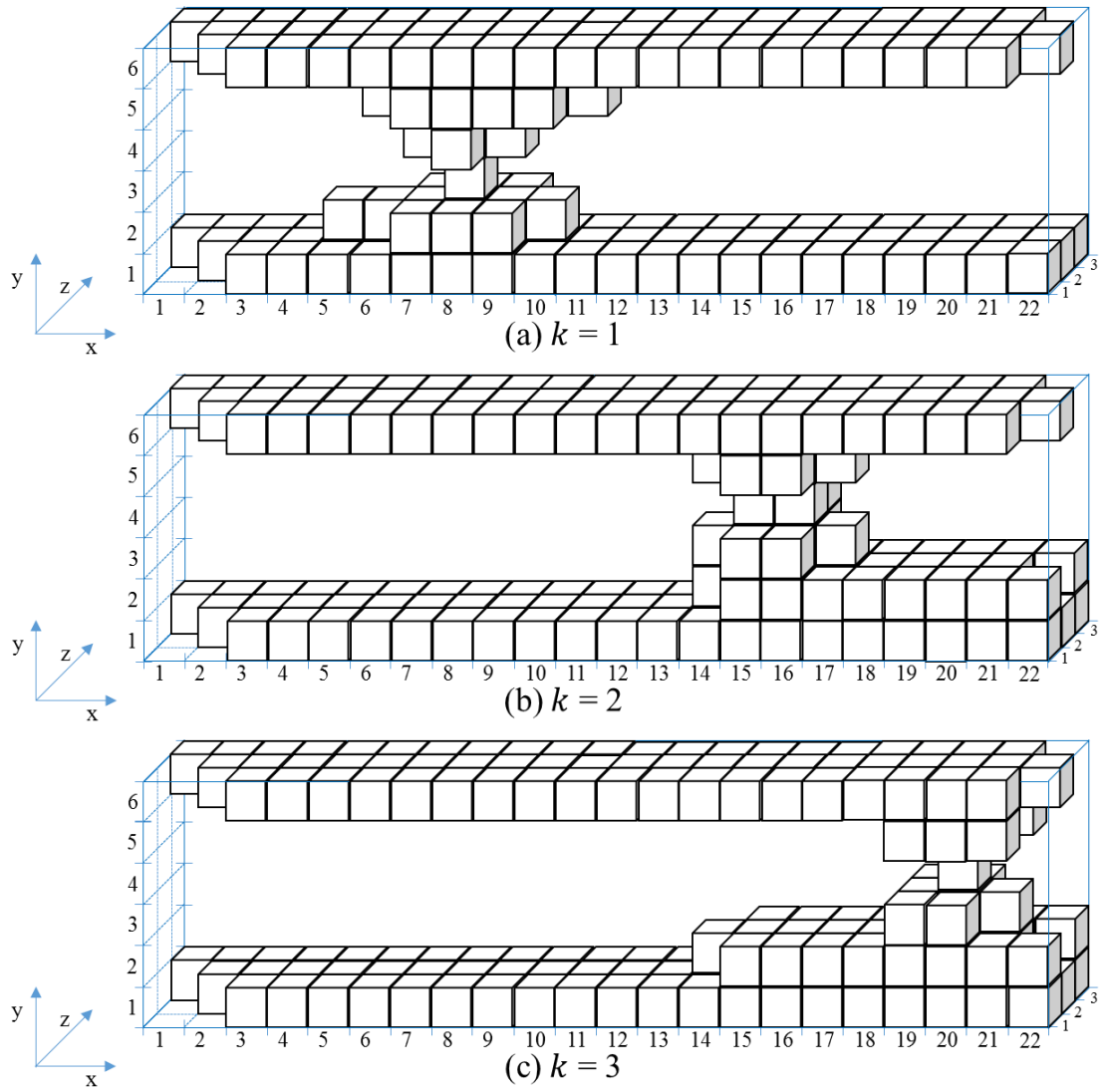


Figure 7.3. Three different 3D contact asperities with their full extensions to the two bodies A and B [186]

For the visualization of 3D contact asperities (without their full extensions to bodies A and B) the 3D contact asperities with their extensions to bodies A and B presented in Figure 7.3 are used to create 3D matrices for examination. Each 3D matrix  $[E_k]$  represents the  $k$  3D contact asperity with its extensions to bodies A and B of Figure 7.3. Each voxel of the solid of Figure 7.3 represented with  $\varepsilon$  element in the  $[E_k]$  3D matrix while the air is represented with zero elements. For the separation of 3D contact asperities from their full extensions to bodies A and B, all the 3D matrices,  $[E_k]$  are added as described in Eq. (7.6).

$$[F] = \sum_{k=1}^S [E_k] \quad (7.6)$$

The summation of Eq. (7.6) is illustrated in Figure 7.4(a) with voxels in different colours. The colour of each voxel depends on the value of each element  $\varphi_{x,y,z}$  (where the suffixes  $x, y, z$  represent the position of the  $\varphi$  element in the 3D matrix  $[F]$ ) of the 3D matrix  $[F]$ . The  $\varphi_{x,y,z}$  element takes three types of values as described from Eq. (7.7). The elements with zero value represent the air while the elements with  $\varepsilon$  and  $m \cdot \varepsilon$  values represent white and gray voxels respectively. The zero values of the 3D matrix  $[F]$  are not illustrated in the figures as they represent air.

$$\varphi_{x,y,z} = \begin{cases} 0 \\ \varepsilon \\ m \cdot \varepsilon, \quad (m \in \mathbb{R}) \end{cases} \quad (7.7)$$

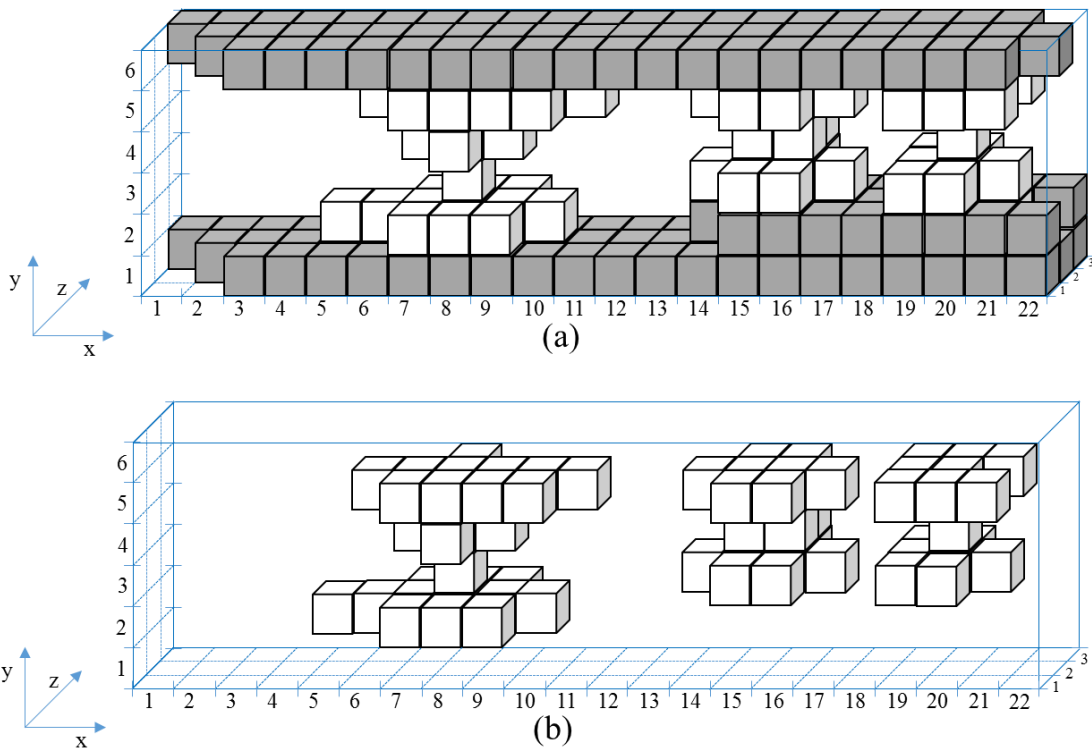


Figure 7.4. (a) Summation of the voxels of 3D contact asperities with their extensions to bodies A and B. (b) 3D contact asperities [186]

The final stage of the CATAC technique is to visualize only the 3D contact asperities (white voxels in Figure 7.4(a)). At this stage each element  $\varphi_{x,y,z}$  in the 3D matrix  $[F]$  of Eq. (7.6) is examined separately as described from Eq. (7.8). If  $\varphi_{x,y,z} = \varepsilon$  then the  $g_{x,y,z}$  element in the 3D matrix  $[G]$  equals to  $g$  and if  $\varphi_{x,y,z} \neq \varepsilon$  then the  $g_{x,y,z}$  element equals to zero. The zero and  $g$  values in 3D matrix  $[G]$  represent air and solid respectively. The



result of the 3D matrix  $[G]$  in voxels is illustrated in Figure 7.4(b). The collection of solid voxels which are neighbouring to other solid voxels by at least one point of their edges are called 3D contact asperities.

$$g_{x,y,z} = \begin{cases} g, & \text{if } \varphi_{x,y,z} = \varepsilon \\ 0, & \text{if } \varphi_{x,y,z} \neq \varepsilon \end{cases} \quad (7.8)$$

## 7.3 Results and Analysis

### 7.3.1 Contact system

Figure 7.5 illustrates the 3D source model of the 16 A rated AC single pole rocker switch after the second current loading test at 16 A. More details concerning the development of the 3D source model and the use of it are already explained in detail in Section 6.3.1.

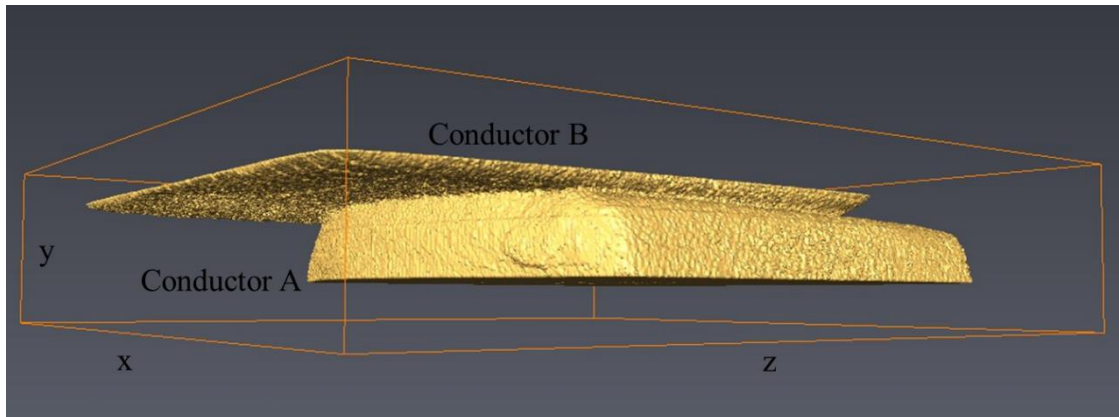


Figure 7.5. 3D source model of the 16 A rated AC single pole rocker switch after the second current loading test at 16 A with bounding box dimensions of  $3.22 \times 0.69 \times 3.40$  mm

Figure 7.6 illustrates a part of 3D contact source model of the 16 A rated AC single pole rocker switch after the second current loading test at 16 A. This model is developed and visualised using some selected 2D cross-section slice images of the 3D source model of Figure 7.5 which have been processed as described in Section 6.2 (the 2D cross-section slice images of the Closed Circuit resistor network model). The reason for this selection, of these 2D cross-section slice images from the 3D source model is explained in detail in Section 7.4.2. In this chapter, the part of 3D contact source model is used as the oriented 3D contact volume of interest of the contact system.

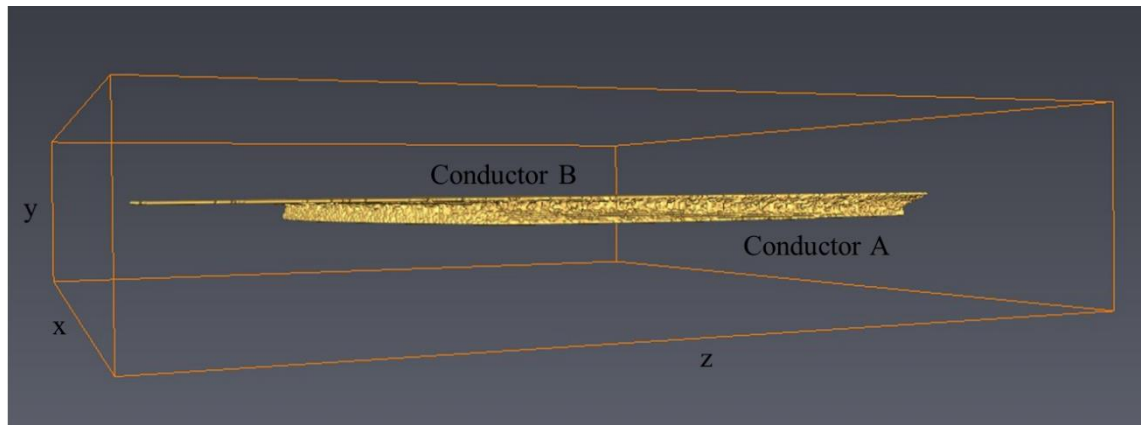


Figure 7.6. Part from 3D contact source model of the 16 A rated AC single pole rocker switch after the second current loading test at 16 A with bounding box dimensions of  $2.78 \times 0.58 \times 2.62$  mm

### 7.3.2 2D and 3D contact maps

Figure 5.6 (in Chapter 5) illustrates the 3D contact maps of the contacting interface between the conductors of the 3D source model (or the 3D contact source model as the 3D contact map is the same in both models) after each current loading test at 0 A, 16 A, 32 A and 64 A. The 3D contact maps are visualized using the 2D cross-section slice images which are processed and implemented using CAT\* with a suite of tools developed in MATLAB as described in Section 5.3. These 3D contact maps consist of contact spots (pixels, surfaces) which are the cross-section areas of the slice asperities (CATA: voxels, volumes) of the 3D constriction asperities map.

Figure 6.6 (in Chapter 6) illustrates the 2D cross-sections of the x-z contact slices (or 2D contact maps) of the 3D source model (or the 3D contact source model as the 2D contact map is the same in both models) after each current loading test at 0 A 16 A, 32 A and 64 A. The x-z contact slices are developed using CATV in order to set all the contact spots of the 3D contact maps of Figure 5.6 to the same height.

Figure 7.7(a) shows the 2D cross-section of the x-z contact slice (or 2D contact map) of the 3D source model (or the 3D contact source model) after the 16 A current loading test (the same 2D cross-section is also presented in Figure 6.6(b)). Figure 7.7(b) shows the close-up view of the red box of the x-z contact slice of Figure 7.7(a) which includes contact spots (cross-sections of constriction asperities). The contact spots *ii*, *jj*, *kk* and *ll* of Figure 7.7 are selected randomly in order to illustrate their full extensions to the two conductors A and B of the 3D contact source model and their 3D contact asperities.

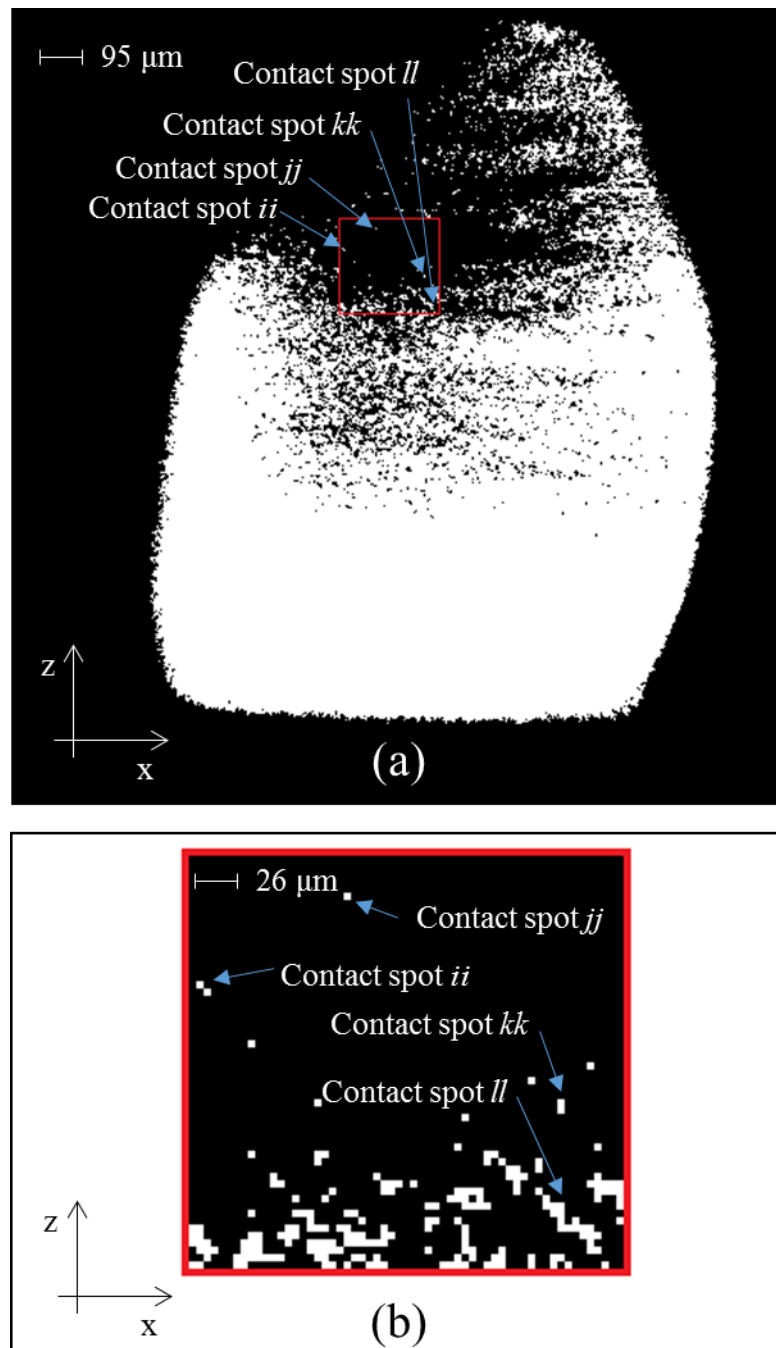


Figure 7.7. (a) 2D cross-section of x-z contact slice after the 16 A current loading test. (b) Close-up view of the red box of 2D cross-section of x-z contact slice

### 7.3.3 3D contact asperities visualisation

Figure 7.8 illustrates the 3D contact asperities of the 16 A rated AC single pole rocker switch after the four different current loading tests at 0 A, 16 A, 32 A and 64 A. The largest 3D contact asperity (the extensions above and below the largest contact spot in each 3D contact map) of the 16 A rated AC single pole rocker switch after each current loading test is not presented in Figure 7.8 because it hides the rest of the 3D contact asperities.

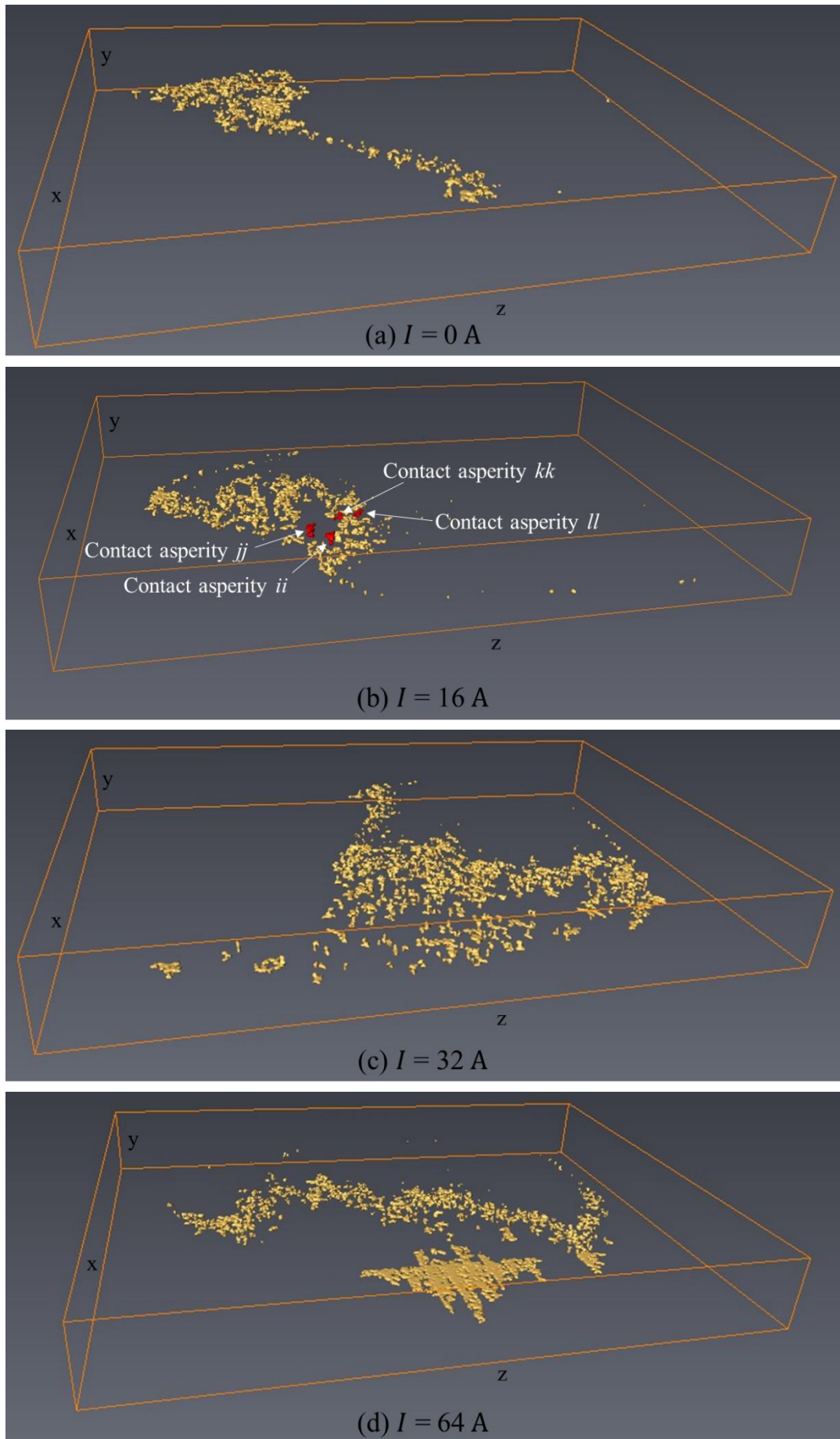


Figure 7.8. 3D contact asperities of the 16 A rated AC single pole rocker switch after four different current loading tests with bounding box dimensions of  $2.52 \times 0.31 \times 2.82 \text{ mm}$

Figure 7.9 illustrates the extensions of contact spots *ii*, *jj*, *kk* and *ll* to the two conductors of the 3D contact source model of the 16 A rated AC single pole rocker switch after the 16 A current loading test (Figure 7.6). Each of these contact spots is also shown in the 2D cross-section of the x-z contact slice of Figure 7.7(a). In addition, the 3D contact asperities of contact spots *ii*, *jj*, *kk* and *ll* are illustrated in Figure 7.10. These 3D contact asperities are the close-up view of the corresponding 3D contact asperities of Figure 7.8(b).

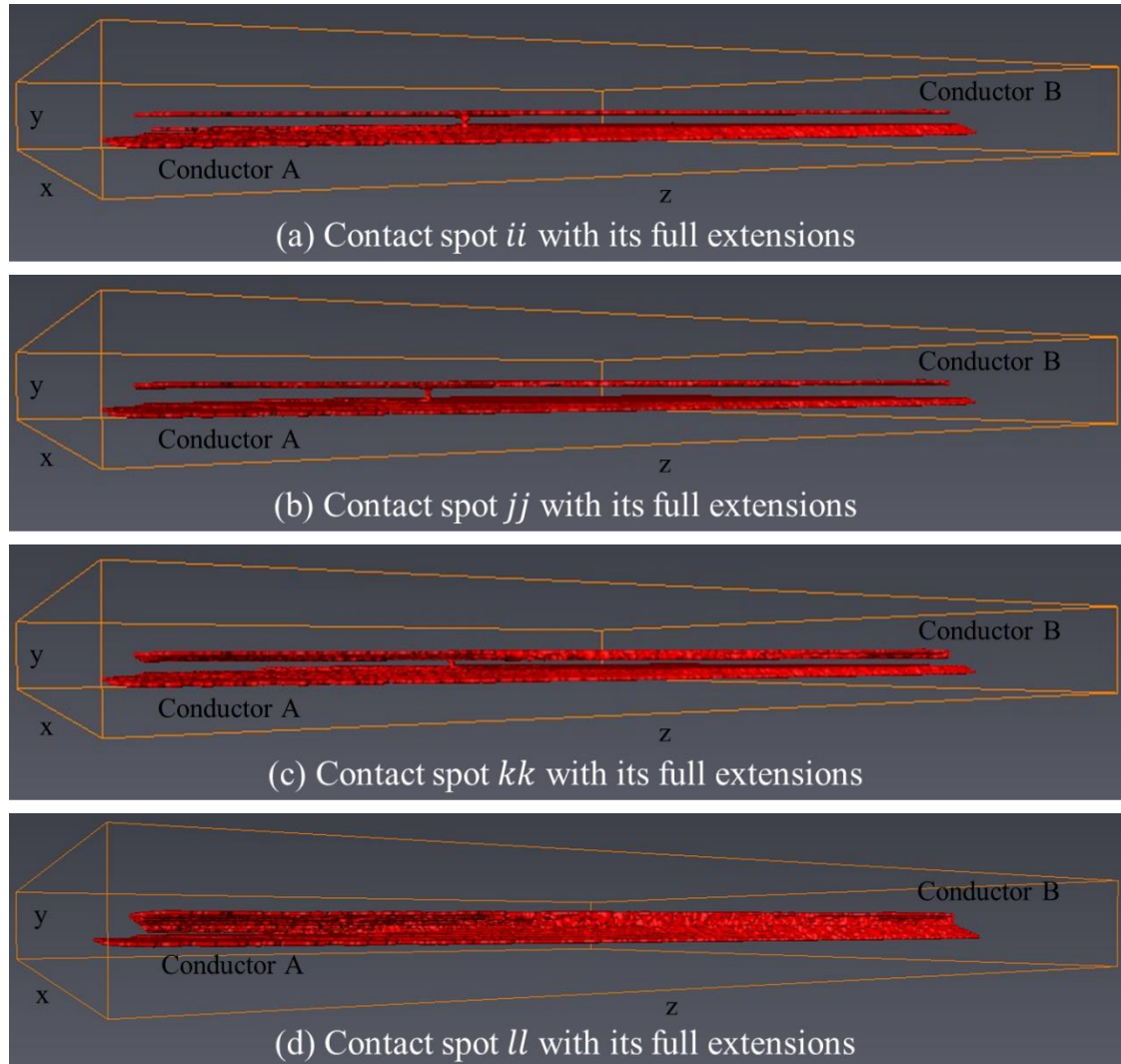


Figure 7.9. Four different contact spots of the x-z contact slice with their full extensions to the two conductors after the 16 A current loading test with bounding box dimensions of  $2.61 \times 0.25 \times 2.59$  mm

#### 7.3.4 3D contact asperities volume distribution

Figure 7.11 illustrates a set of graphs showing the 3D contact asperity volume distribution after the four different current loading tests at 0 A 16 A, 32 A and 64 A. The

data are taken and calculated from the 3D contact asperities of Figure 7.8. The volume of each 3D contact asperity is defined as the sum of voxels within the 3D contact asperity and multiplied by  $125 \mu\text{m}^3$  (volume of voxel). The smallest volume of 3D contact asperity indicated on the graphs is  $125 \mu\text{m}^3$  which is the resolution of the technique ( $1 \text{ voxel} = 125 \mu\text{m}^3$ ) and the largest 3D contact asperity ( $V_L''$ ) indicated are several thousand  $\mu\text{m}^3$  in the volume. The number of 3D contact asperities ( $n$ ) after each current loading test is counted to be equal with the number of contact spots of the corresponding 3D contact map of Figure 5.6. Where  $V_L''$ , is the largest 3D contact asperity in the volume across the fit-line.

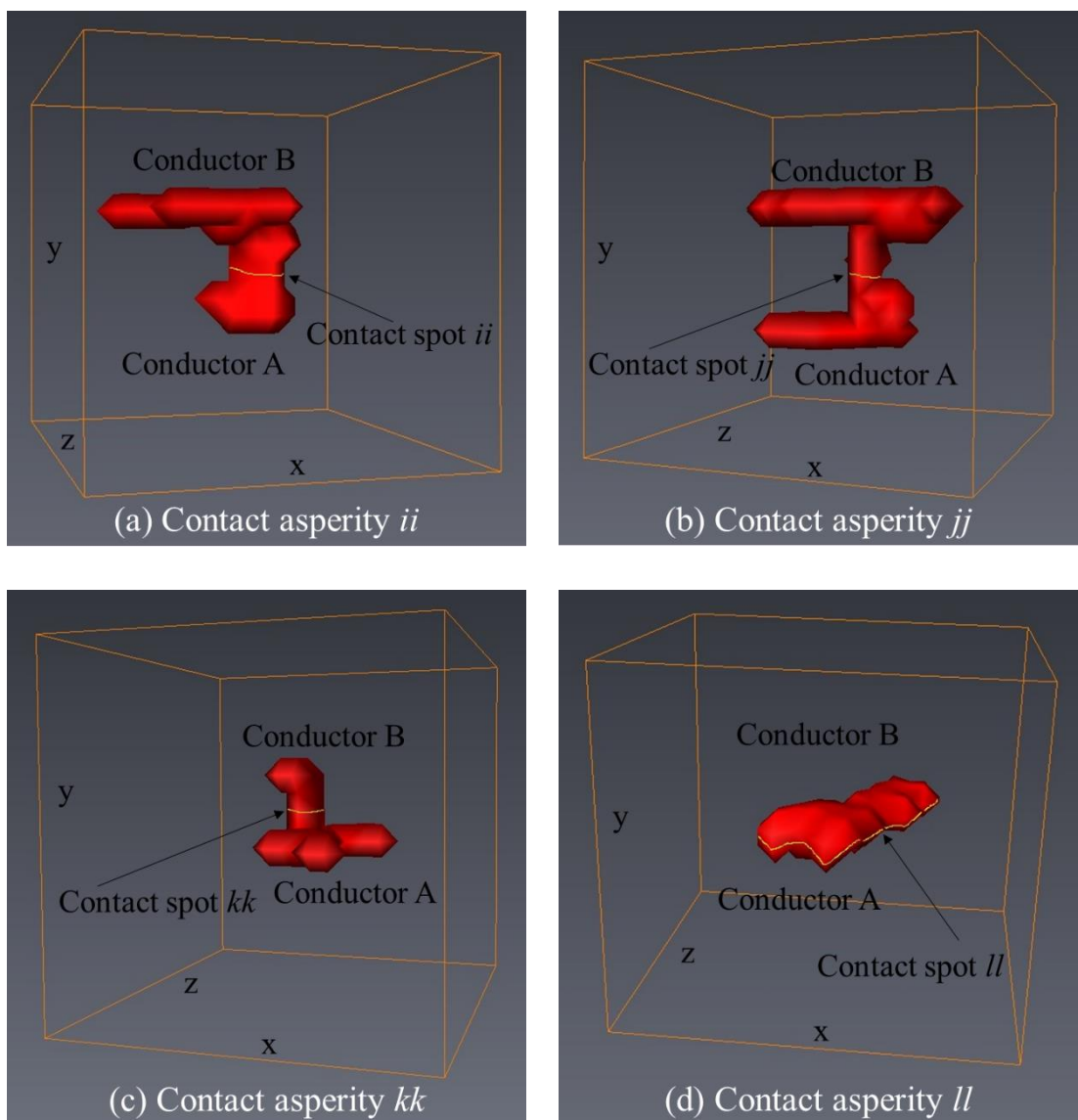


Figure 7.10. 3D contact asperities  $ii$ ,  $jj$ ,  $kk$  and  $ll$  with bounding boxes dimensions of  $0.12 \times 0.11 \times 0.11 \text{ mm}$

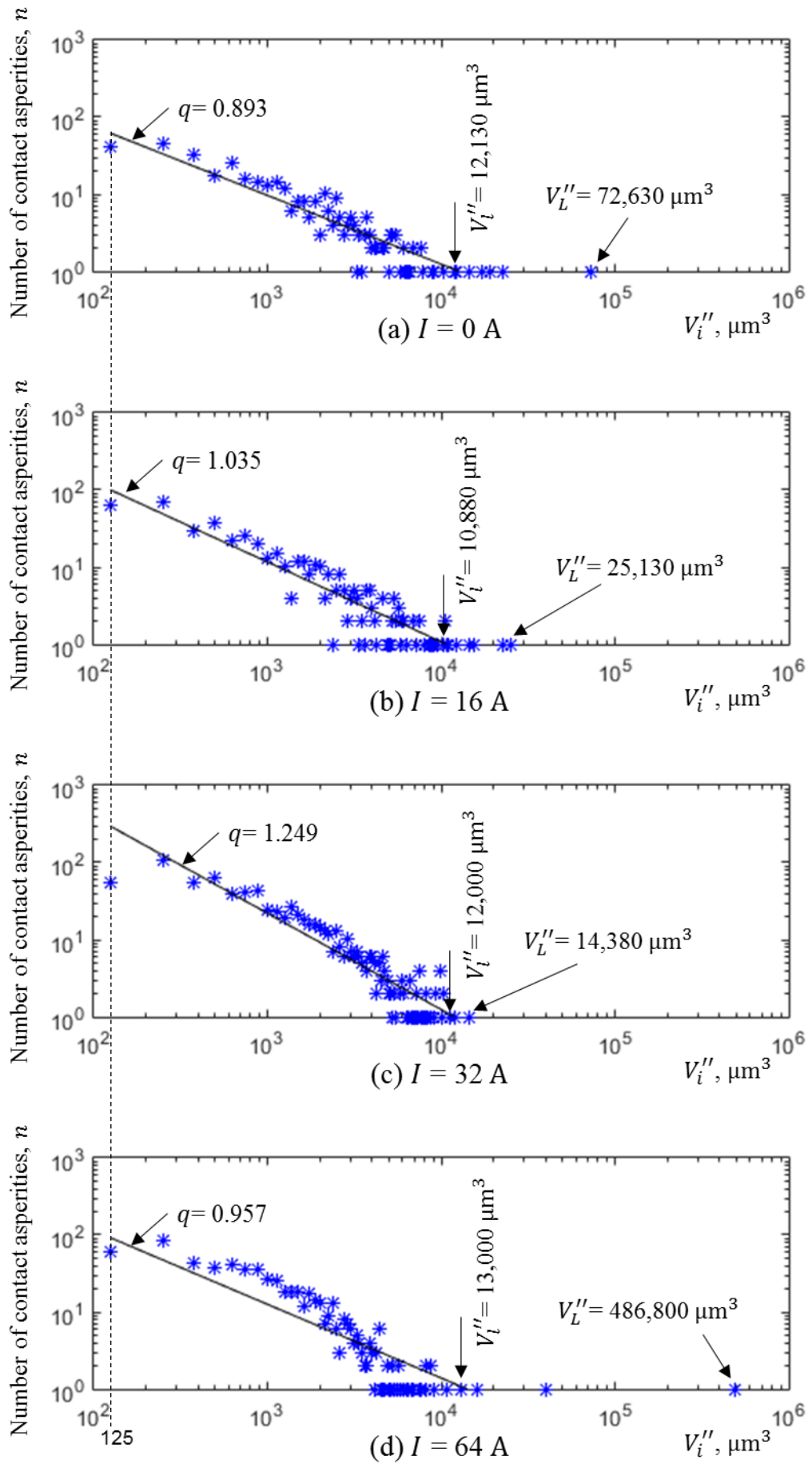


Figure 7.11. 3D contact asperities volume distribution after the four different current loading tests [195]

### 7.3.5 3D contact asperities surface area distribution

Figure 7.12 illustrates a set of graphs showing the 3D contact asperity surface area distribution after the four different current loading tests at 0 A 16 A, 32 A and 64 A. The data are taken and calculated from the 3D contact asperities of Figure 7.8. The surface area of each 3D contact asperity is defined as the sum of pixels of the 3D contact asperity which are exposed to the air and multiplied by  $25 \mu\text{m}^2$  (area of pixel). The smallest surface area of 3D contact asperity indicated on the graphs is  $100 \mu\text{m}^2$  which is four times the resolution of the technique ( $1 \text{ pixel} = 25 \mu\text{m}^2$ ,  $4 \times 1 \text{ pixel} = 100 \mu\text{m}^2$ ), and the largest 3D contact asperity ( $A_L''$ ) indicated are several thousand  $\mu\text{m}^2$  in the volume. Where  $A_L''$ , is the largest surface area exposed to the air of 3D contact asperity  $l$  across the fit-line.

### 7.3.6 Bottom surface area distribution of 3D contact asperities

Figure 7.13 illustrates a set of graphs showing the bottom surface area of the 3D contact asperity distribution after the four different current loading tests at 0 A 16 A, 32 A and 64 A. The data are taken and calculated from the 3D contact asperities of Figure 7.8. The bottom surface area of each 3D contact asperity is defined as the sum of pixels of the bottom cross-section slice image of the 3D contact asperity and multiplied by  $25 \mu\text{m}^2$  (area of pixel). The smallest bottom surface area of 3D contact asperity indicated on the graphs is  $25 \mu\text{m}^2$  (the resolution of the technique,  $1 \text{ pixel} = 25 \mu\text{m}^2$ ) and the largest bottom surface area of 3D contact asperity ( $A_{A_L}$ ) indicated is several thousand  $\mu\text{m}^2$  in the volume. Where  $A_{A_L}$ , is the largest surface area of the bottom of 3D contact asperity  $l$  across the fit-line. It is important to note that the bottom surface area of the 3D contact asperity  $i$  belongs to Conductor A of the 3D contact source model of the 16 A rated AC single pole rocker switch.

### 7.3.7 Top surface area distribution of 3D contact asperities

Figure 7.14 illustrates a set of graphs showing the top surface area of the 3D contact asperity distribution after the four different current loading tests at 0 A 16 A, 32 A and 64 A. The data are taken and calculated from the 3D contact asperities of Figure 7.8. The top surface area of each 3D contact asperity is defined as the sum of pixels of the top cross-section slice image of the 3D contact asperity and multiplied by  $25 \mu\text{m}^2$  (area of pixel). The smallest top surface area of the 3D contact asperity indicated on the graphs is



25  $\mu\text{m}^2$  (the resolution of the technique, 1 pixel = 25  $\mu\text{m}^2$ ) and the largest top surface area of 3D contact asperity ( $A_{B_l}$  respectively) indicated are several thousand  $\mu\text{m}^2$  in the volume. Where  $A_{B_l}$ , is the largest surface area of the top of 3D contact asperity  $l$  across the fit-line. It is important to note that the top surface area of the 3D contact asperity  $i$  belongs to Conductor B of the 3D contact source model of the contact system.

### 7.3.8 *Ratio of top/ bottom surface areas of 3D contact asperities distribution*

Figure 7.15 illustrates a set of graphs showing the ratio of top surface area ( $A_{B_l}$ ) and the bottom surface area ( $A_{A_l}$ ) of 3D contact asperities with their distribution after the four different current loading tests at 0 A 16 A, 32 A and 64 A. The data are taken and calculated from the 3D contact asperities of Figure 7.8. This set of graphs shows the number of 3D contact asperities with bottom surface area smaller, equal or larger than top surface area.

### 7.3.9 *3D contact asperities height distribution*

Figure 7.16 illustrates a set of graphs showing the height distribution of 3D contact asperities after the four different current loading tests at 0 A 16 A, 32 A and 64 A. The data are taken and calculated from the 3D contact asperities of Figure 7.8. The height of each 3D contact asperity is defined as the distance between the top and bottom surface areas of 3D contact asperity. The smallest height of 3D contact asperity indicated on the graphs is 5  $\mu\text{m}$  which is the height of the voxel and the largest height indicated are some dozen  $\mu\text{m}$ .

### 7.3.10 *Ratio of top/bottom surface areas with height*

Figure 7.17 illustrates a set of graphs showing the ratio of top surface area ( $A_{B_l}$ ) and the bottom surface area ( $A_{A_l}$ ) with the height ( $H_i$ ) of 3D contact asperities with their distribution after the four different current loading tests at 0 A 16 A, 32 A and 64 A. The data are taken and calculated from the 3D contact asperities of Figure 7.8. This set of graphs shows the number of 3D contact asperities with bottom surface area smaller, equal or bigger than top surface area divided by the distance (height) between them. The smallest height of 3D contact asperity indicated is 5  $\mu\text{m}$  (pixel length).

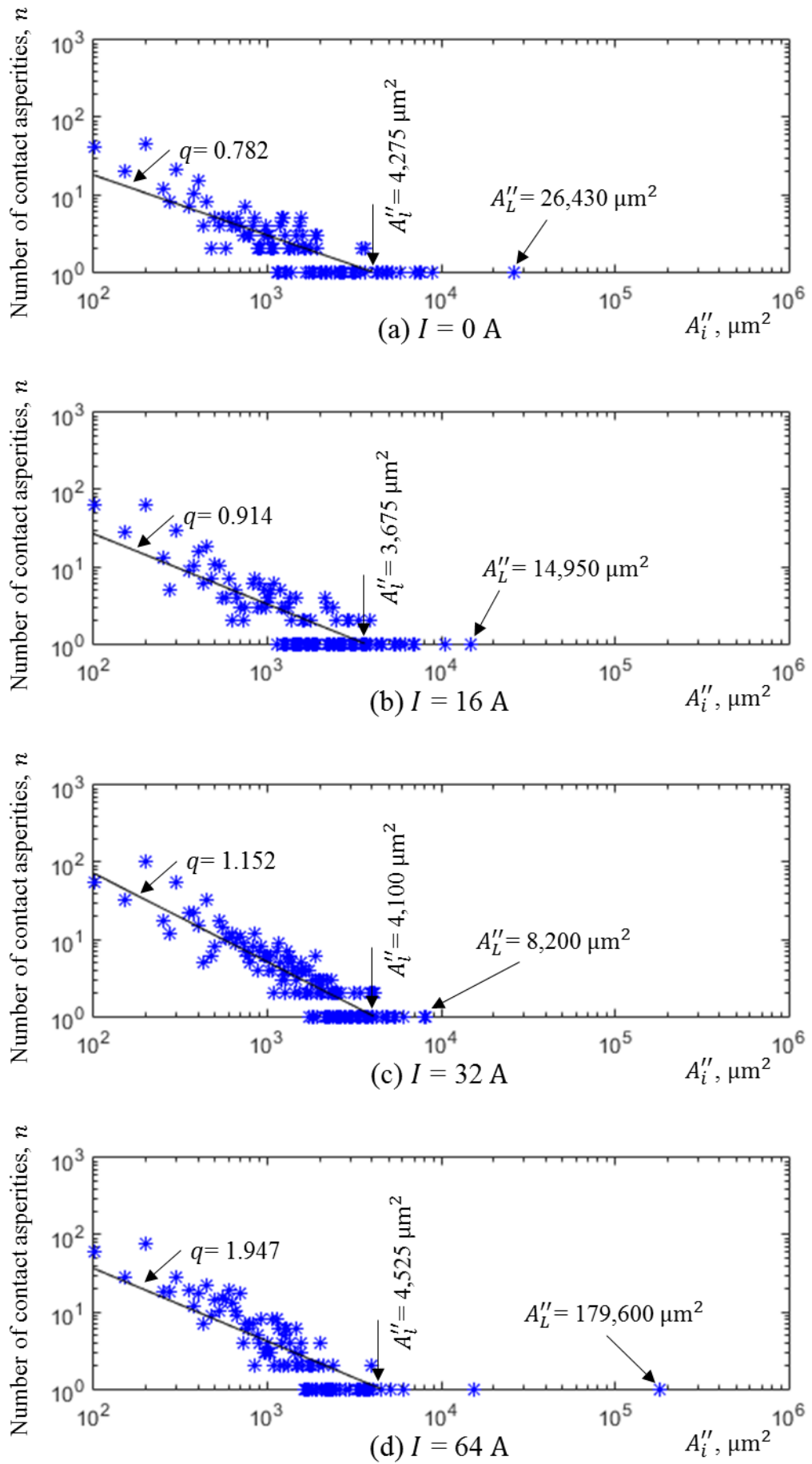


Figure 7.12. 3D contact asperities surface area distribution after four different current loading tests [195]

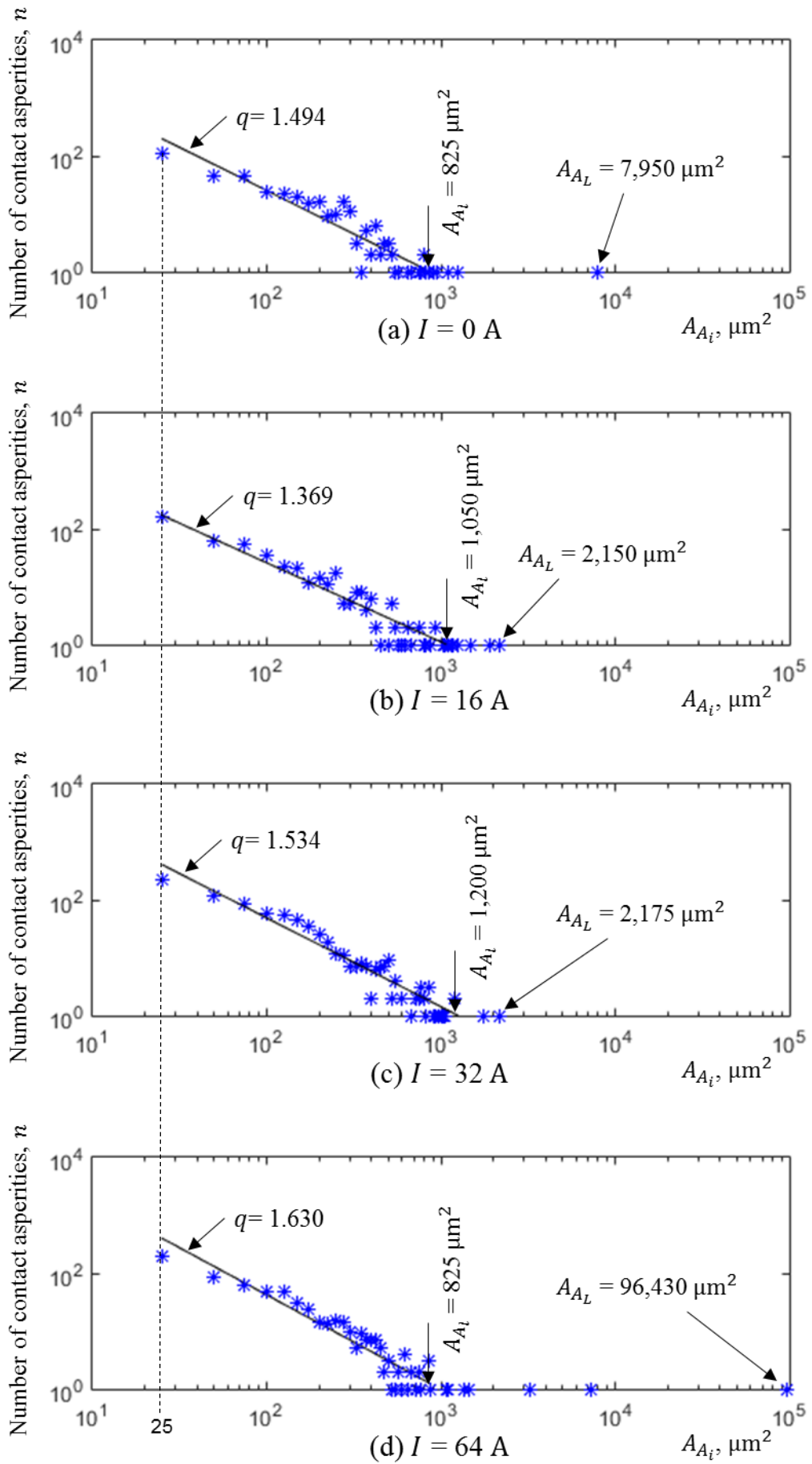


Figure 7.13. 3D contact asperities bottom surface area distribution after the four different current loading tests

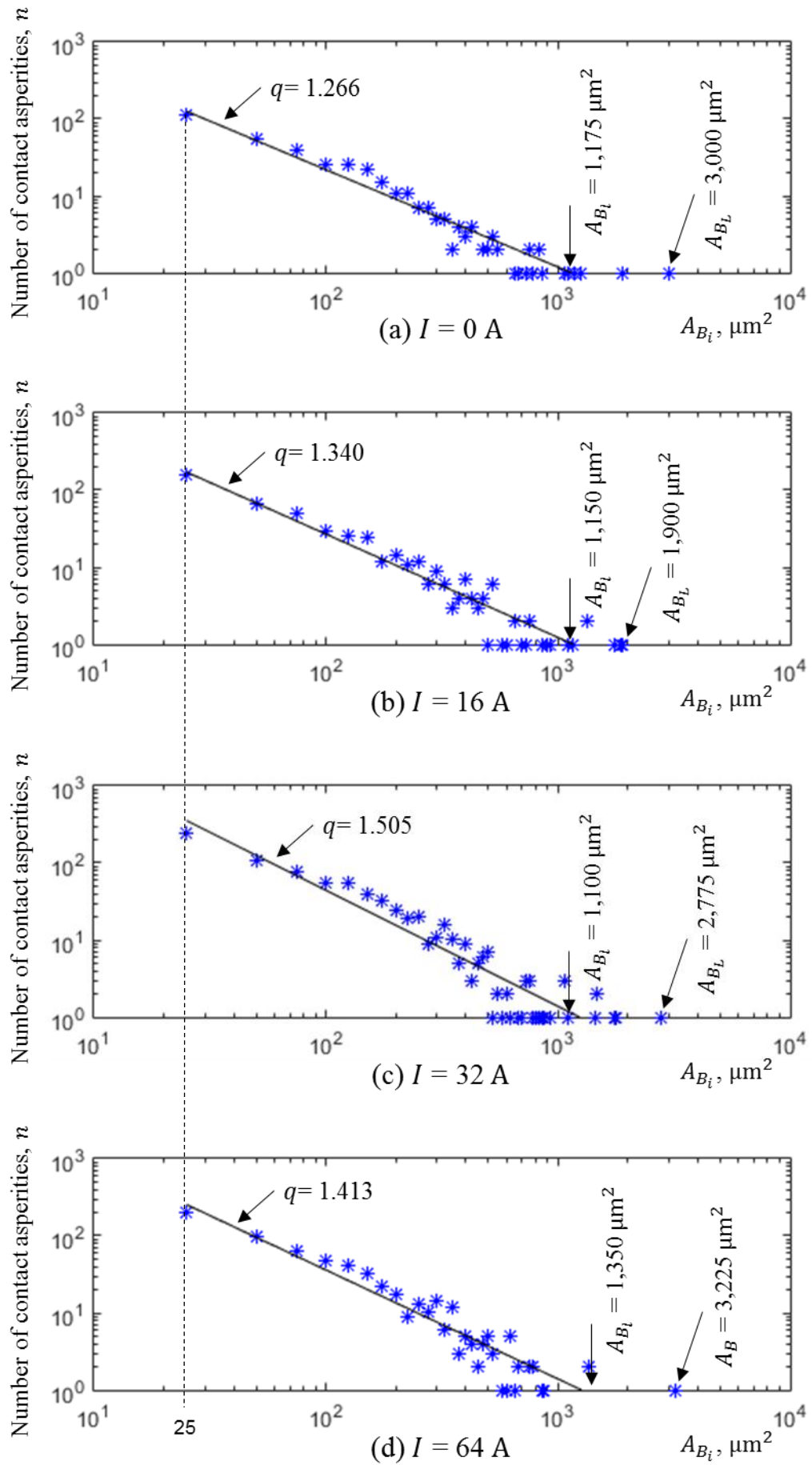


Figure 7.14. 3D contact asperities top surface area distribution after four different current loading tests

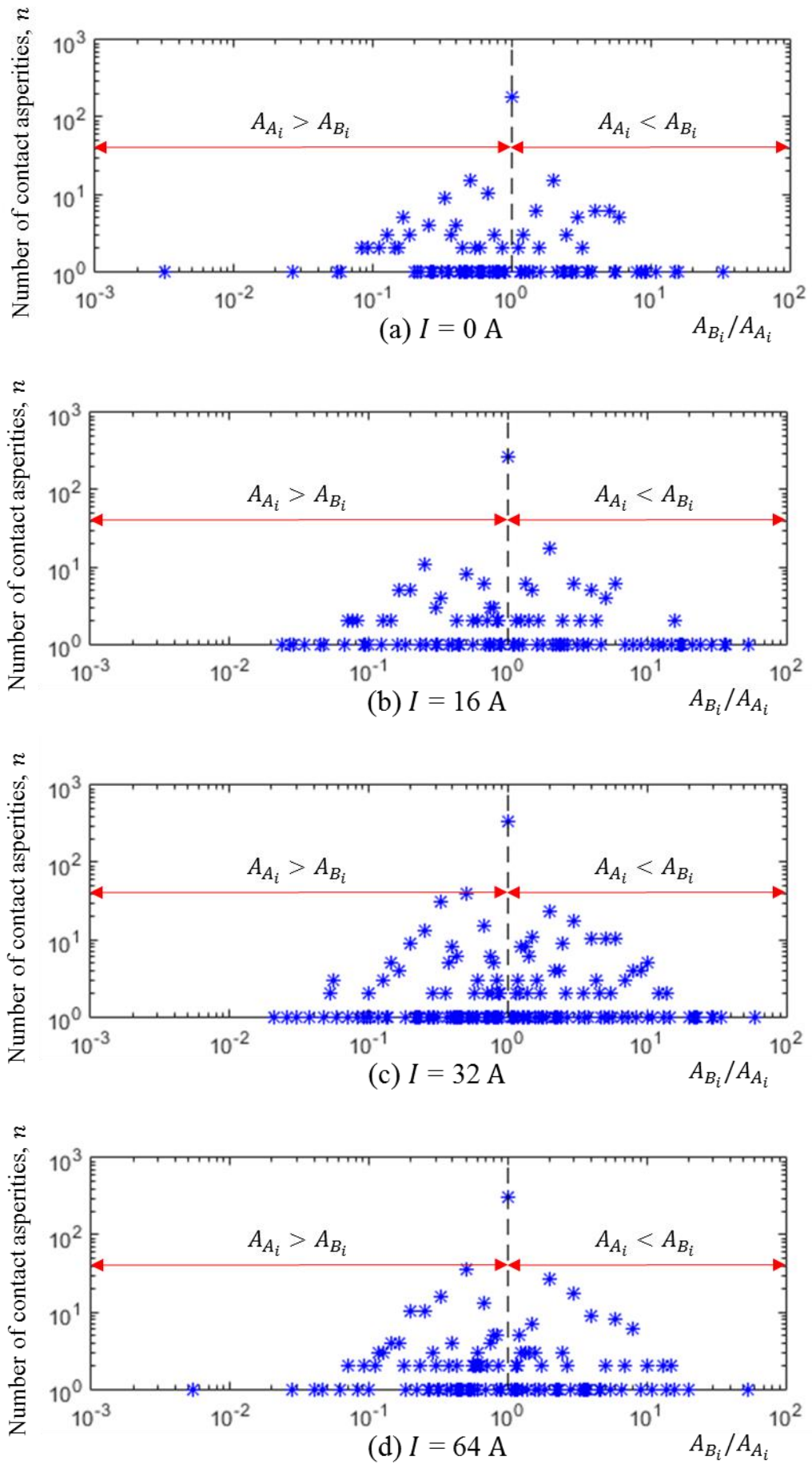


Figure 7.15. 3D contact asperities ratio of top and bottom surface area distribution after four different current loading tests

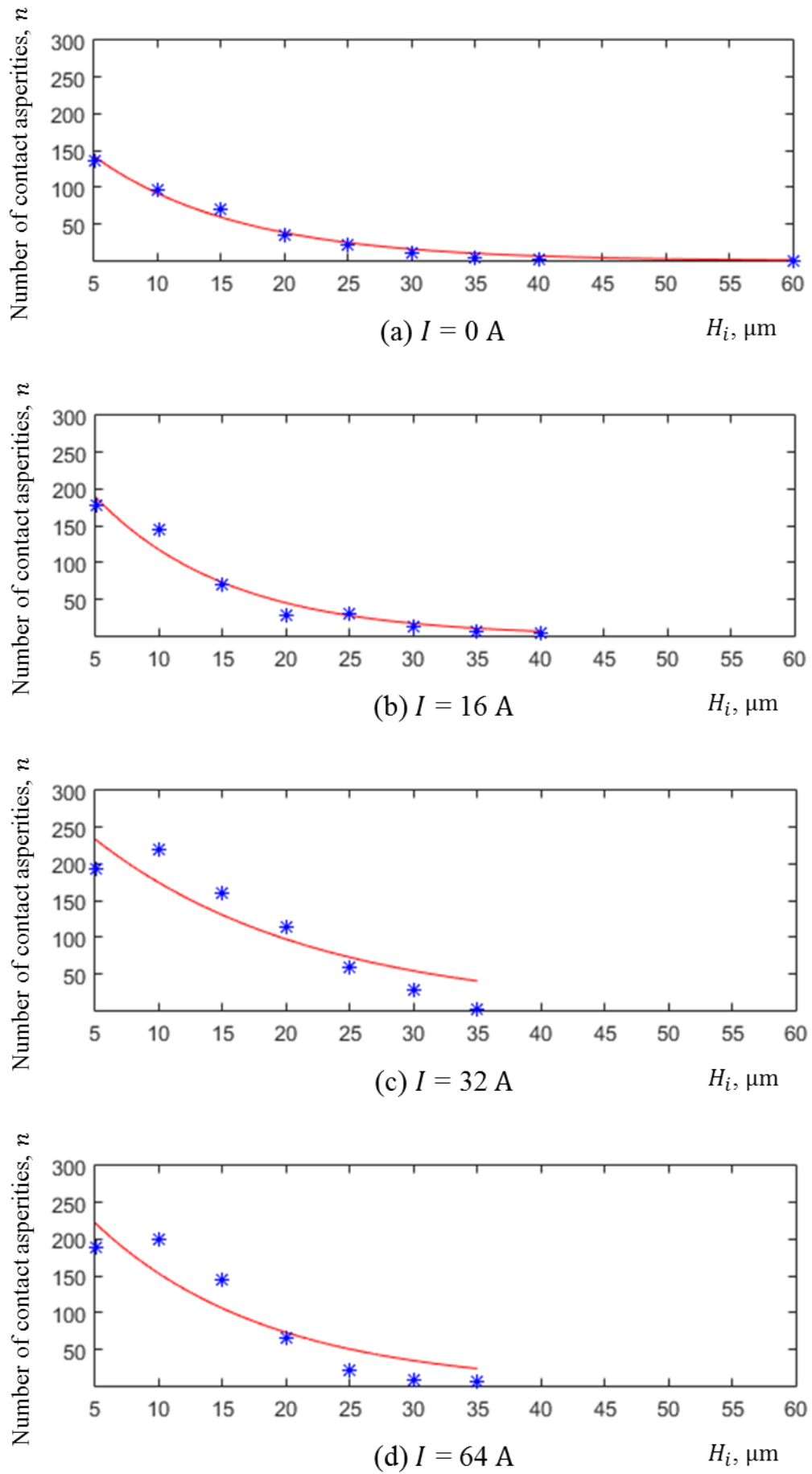


Figure 7.16. 3D contact asperities height distribution after four different current loading tests

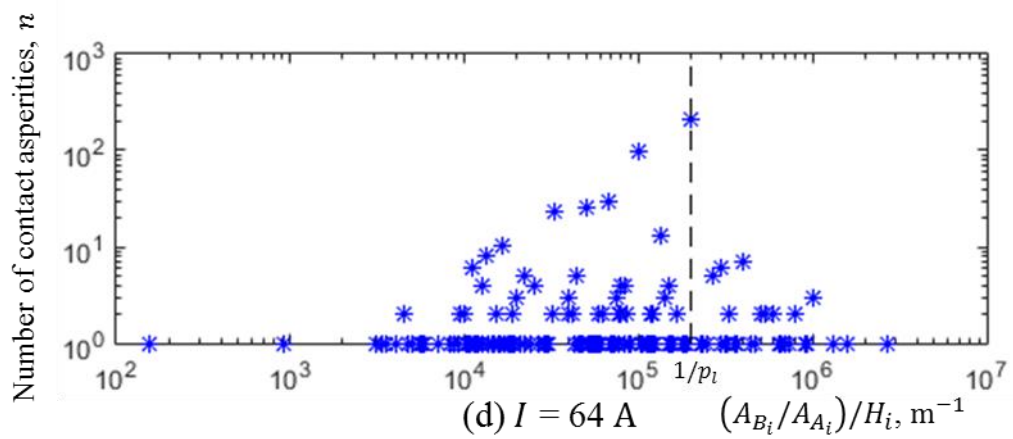
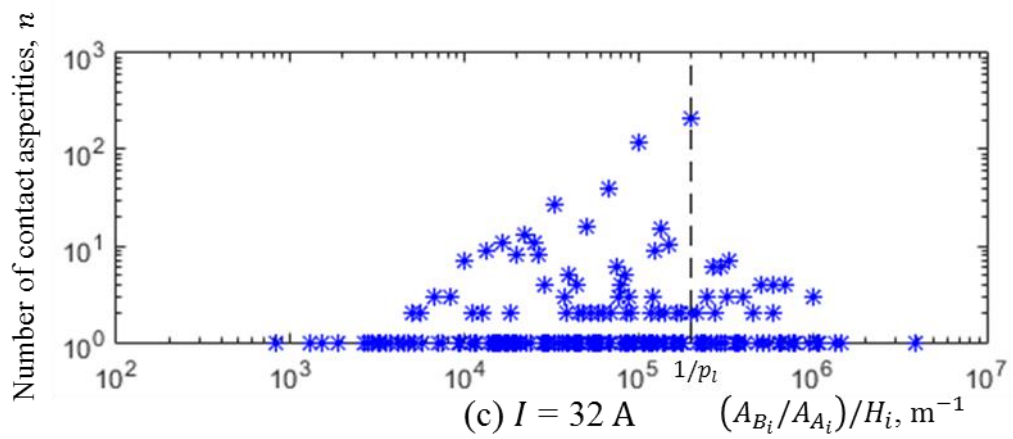
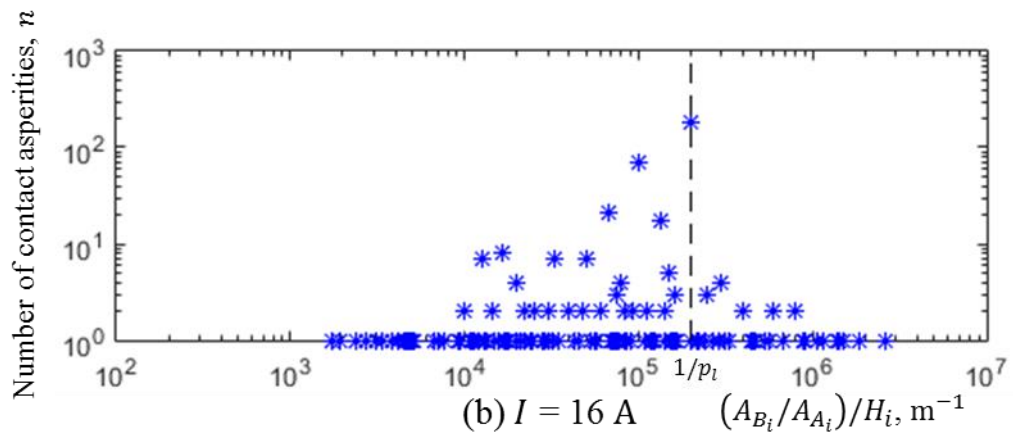
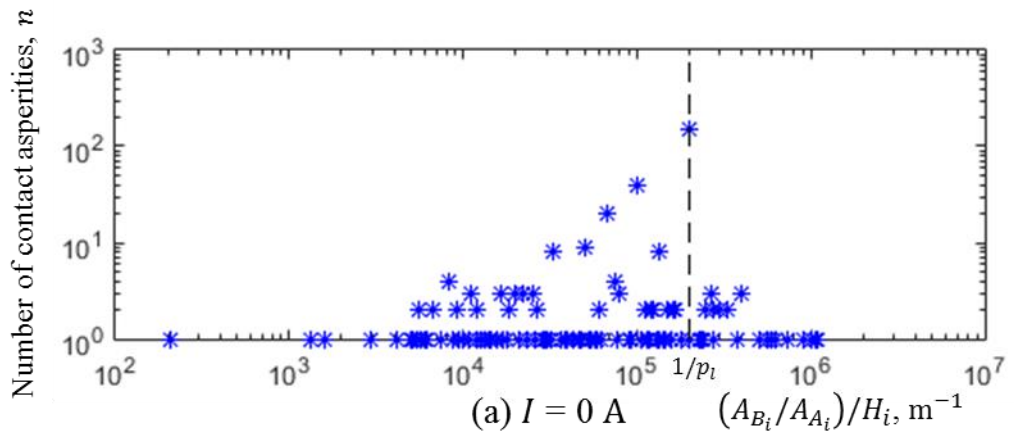


Figure 7.17. 3D contact asperities ratio of top and bottom surface area with height distribution after four different current loading tests

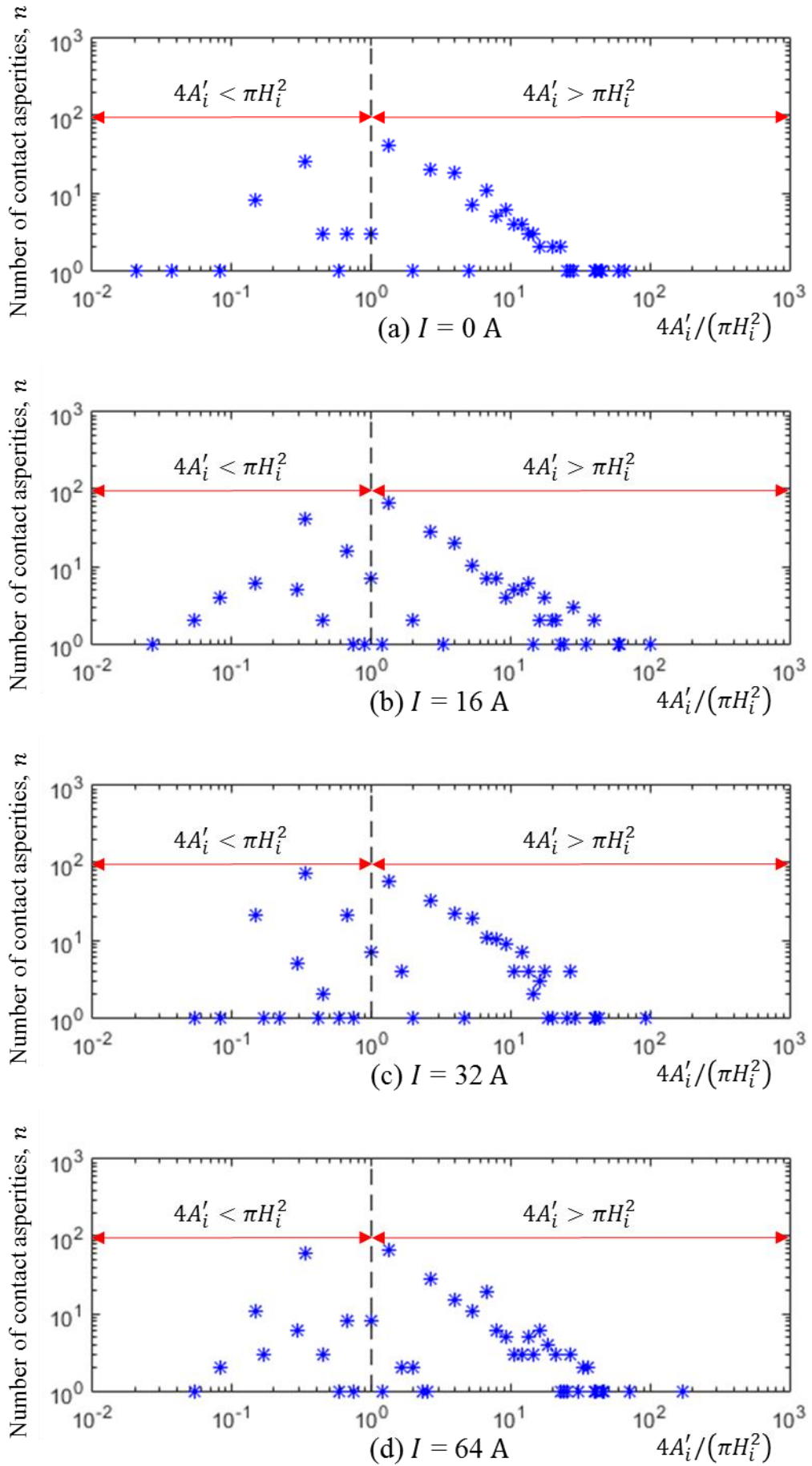


Figure 7.18. 3D contact asperities ratio distribution of equal bottom and top surface areas with height squared and multiplied by  $4/\pi$  after four different current loading tests



### 7.3.11 Hemispherical 3D contact asperities

Figure 7.18 illustrates the ratio distribution of 3D contact asperities with equal bottom and top surface areas ( $A'_i = A_{A_i} = A_{B_i}$ ) with height ( $H_i$ ) and multiplied by  $4/\pi$ . The data are taken and calculated from the 3D contact asperities of Figure 7.8. The ratio presented on the graphs of Figure 7.18 is introduced in order to investigate whether the Greenwood-Williamson [60] assumptions (the bodies of the 3D contact asperity have hemispherical shapes) meet the reality. A detailed explanation concerning the development of the ratio presented on the graphs of Figure 7.18 are given in Section 7.4.11.

## 7.4 Discussion

### 7.4.1 X-ray CT technique

The results show that the X-ray CT technique is a powerful and useful tool for viewing the contact asperities of a contact system without needing to dismantle it. The experimental data acquired using this technique with pixel resolution of  $5 \mu\text{m} \times 5 \mu\text{m}$  and voxel resolution of  $5 \mu\text{m} \times 5 \mu\text{m} \times 5 \mu\text{m}$  give the ability of examination and processing in order to investigate different characteristics which occur in the contact interface and its extension.

As mentioned and in previous sections (Section 5.8.1 and Section 6.4.1), the resolution is a very important factor for the calculation and visualization techniques. For example, for a coarse measurement (e.g.  $100 \mu\text{m}$ ) of resolution, only a few asperities of large curvature are visualized while for smaller measurement (e.g.  $0.1 \mu\text{m}$ ) of resolution, more asperities of smaller curvature are visualized [124, 181]. The smallest resolution which can be obtained by the current facility is  $3 \mu\text{m}$ . This depends on the sample dimensions and X-ray admittance of the sample materials. The resolution of  $5 \mu\text{m}$  obtained in this research is the optimum that could be achieved with the sample configuration used. However, it should be noted that the CAT\* developed and implemented within a suite of tools in this work can be used with data of finer resolution and for different visualization techniques which are producing 2D cross-section slice images. Also, the different visualization techniques, for example the MRI [143, 196-198] and Magnetic Resonance Force Microscopy (MRFM) [199-202] can be used with the suite of CAT\* developed in this chapter.

#### 7.4.2 *Contact analysis approach*

A contact analysis approach is developed and introduced in this chapter for 3D visualization of the contact asperities for contact systems. This approach uses the 2D cross-section slice images of the 3D source model of the 16 A rated AC single pole switch which have been processed as described in the previous chapter (Section 6.3.1) in order to build the 3D contact source model. From this 3D contact source model, the 3D contact asperities have been visualized. The contact analysis approach consists of contact analysis techniques (CATA, CATV and CATAC) which are developed in MATLAB using the Image Processing Toolbox.

For the 3D contact asperities visualisation a part from the 3D contact source model is used. This part of the 3D contact source model is based on the selection of the limits of the 3D contact source model in y-direction (the distance between the limits of the 3D contact source model in the y-direction equals the number of x-z cross-section slices). This selection depends on the number of slice asperities in each x-z cross-section slice above and below the 3D constriction asperities map. The first x-z cross-section slice of the 3D contact source model is the first slice which has only one contact spot below the 3D contact spots map while the last x-z cross-section slice of the 3D contact source mode is the first slice which has only one contact spot above the 3D contact spots map. The first and last x-z cross-section slices of the 3D contact source mode are the connections of all contact asperities. For example, the part of the 3D contact source model of the 16 A rated AC single pole rocker switch after the 16 A current loading test which is illustrated in Figure 7.6 consists of 12 x-z cross-section slices. The first x-z cross-section slice of this model is the last x-z cross-section slice of the first region of the Closed Circuit resistor network model (developed in Chapter 6) while the last x-z cross-section slice is the first x-z cross-section slice of the third region of the Closed Circuit resistor network model. The first and last x-z cross-section slices of the part of the 3D contact source model of the 16 A rated AC single pole rocker switch after the 16 A current loading test which is illustrated in Figure 7.6 consist of only one slice asperity (or resistor in the Closed Circuit resistor network model). The selected x-z cross-section slices of the part of the 3D contact source model of the 16 A rated AC single pole rocker switch after the 16 A current loading test which is illustrated in Figure 7.6 can be clearly seen in Figure 6.7(b) (from the 28<sup>th</sup> x-z cross-section slice to the 39<sup>th</sup> x-z cross-section slice). The same procedure used for the development of the part of the 3D contact source model of the 16 A rated AC single

pole rocker switch after the 16 A current loading test is used for the other current loading tests at 0 A, 32 A and 64 A.

In Chapter 5 the 3D contact map of an electrical contact interface is developed demonstrating the 3D nature of the contact. In this chapter, the 3D contact map is used in order to demonstrate the structures of 3D contact asperities. Figure 5.6 illustrates the 3D contact maps of the 16 A rated AC single pole switch after the four different current loading tests (0 A, 16 A, 32 A and 64 A) which are converted into the 2D contact map as presented in Figure 6.6. The 2D contact map is used as the reference x-z contact slice to make a comparison of each contact spot of the x-z contact slice with the spots of each x-z cross-section slice of the 3D contact source model of the 16 A rated AC single pole switch. The reason for this comparison is to visualize the full extensions above and below of each contact spot to the two conductors of the contact system. This result is described by the visualization of four different contact spots, *ii*, *jj*, *kk* and *ll* which are selected randomly from the 2D contact map of Figure 7.7(a). The full extensions above and below of these *ii*, *jj* and *kk* contact spots to the two conductors are illustrated in Fig. 11a, Fig. 12a and Fig.12b respectively. The full extensions above and below these *ii*, *jj*, *kk* and *ll* contact spots to the two conductors are illustrated in Figure 7.9. More visualisations of different contact spots with their full extensions above and below the two conductors are also given in a previous work [186].

#### 7.4.3 3D contact asperities findings

Figure 7.8 shows the 3D contact asperities of the 3D contact source model of the 16 A rated AC single pole rocker switch after the four different current loading tests (0 A, 16 A, 32 A and 64 A) which are visualized using the contact analysis approach. These 3D contact asperities present the extensions above and below the contact spots of Figure 5.6 to the two conductors of the contact system. In addition, the 3D contact asperities are shown to have different sizes, shapes and their contact spots vary. It is important to mention that the total number of 3D contact asperities after each current loading test is equal to the total number of contact spots of the corresponding 3D contact map of Figure 5.6. The total number of contact spots of the 3D contact maps after each current loading test is already calculated and presented in Table 5.3. Figure 7.8 illustrates one 3D contact asperity less from the total number of 3D contact asperities for each of the current loading tests. The largest 3D contact asperity of the contact system (this is the 3D contact asperity

with the largest contact spot after each current loading test) is not presented because it hides the other 3D contact asperities.

Figure 7.10 illustrates a close-up view of the actual 3D contact asperities  $ii$ ,  $jj$ ,  $kk$  and  $ll$  of Figure 7.8(b) with their contact spots  $ii$ ,  $jj$ ,  $kk$  and  $ll$  respectively. The characteristics of these 3D contact asperities are given in Table 7.1. The volume of each of these  $ii$ ,  $jj$ ,  $kk$  and  $ll$  3D contact asperities is calculated to be  $8,875 \mu\text{m}^3$ ,  $12,125 \mu\text{m}^3$ ,  $3,750 \mu\text{m}^3$  and  $6,000 \mu\text{m}^3$  respectively. This volume, is defined as the sum of voxels within the 3D contact asperity and multiplied by  $125 \mu\text{m}^3$  (volume of voxel). The contact spot area of each of these  $ii$ ,  $jj$ ,  $kk$  and  $ll$  3D contact asperities is calculated to be  $50 \mu\text{m}^2$ ,  $25 \mu\text{m}^2$ ,  $50 \mu\text{m}^2$  and  $500 \mu\text{m}^2$  respectively. This area, is defined as the sum of pixels within the 3D contact spot of 3D contact asperity and multiplied by  $25 \mu\text{m}^2$  (area of pixel). In addition, the surface area of each of these  $ii$ ,  $jj$ ,  $kk$  and  $ll$  3D contact asperities is calculated to be  $4,275 \mu\text{m}^2$ ,  $5,825 \mu\text{m}^2$ ,  $2,200 \mu\text{m}^2$  and  $2,600 \mu\text{m}^2$  respectively. The surface area of each 3D contact asperity is defined as the sum of pixels of the 3D contact asperity which are exposed to the air and multiplied by  $25 \mu\text{m}^2$  (area of pixel).

The surface area of the 3D contact asperity  $i$  with  $i \in [1, n]$  ( $n$ , is the total number of 3D contact asperities, contact spots) which is exposed to the air is described from Eq. (7.9).  $A_{sur_i}$ , is the total surface area of 3D contact asperity  $i$  and  $A_{A_i}$  and  $A_{B_i}$  are the surface areas of the bottom (Conductor A) and top (Conductor B) of the of 3D contact asperity  $i$  respectively. The bottom surface area of each of these  $ii$ ,  $jj$ ,  $kk$  and  $ll$  3D contact asperities is calculated to be  $150 \mu\text{m}^2$ ,  $475 \mu\text{m}^2$ ,  $475 \mu\text{m}^2$  and  $925 \mu\text{m}^2$  respectively. This bottom surface area, is defined as the sum of pixels of the bottom surface of the 3D contact asperity and multiplied by  $25 \mu\text{m}^2$  (area of pixel). The top surface area of each of these  $ii$ ,  $jj$ ,  $kk$  and  $ll$  3D contact asperities is calculated to be  $925 \mu\text{m}^2$ ,  $1,250 \mu\text{m}^2$ ,  $125 \mu\text{m}^2$  and  $925 \mu\text{m}^2$  respectively. This top surface area, is defined as the sum of pixels of the top surface of the 3D contact asperity and multiplied by  $25 \mu\text{m}^2$  (area of pixel). The values presented in Table 7.1 have an error of  $\pm 1.366\%$ . This error, represents the sum of the error of measured threshold values and the error of 3D volume of interest of the experimental data (see Section 4.5.2).

Furthermore, the sum of the volume of 3D contact asperities gives the total volume of 3D contact asperities ( $V_T''$ ) while the sum of the surface area exposed to the air of the

3D contact asperities gives the total surface area of the 3D contact asperities ( $A_T''$ ) exposed to the air. The total volume and the total surface area exposed to the air for the 3D contact asperities are given from Eq. (7.10) and Eq. (7.11) respectively.

Table 7.1. Characteristics of 3D contact asperities *ii*, *jj*, *kk* and *ll*

3D contact asperity	<i>ii</i>	<i>jj</i>	<i>kk</i>	<i>ll</i>
Volume ( $\mu\text{m}^3$ )	8,875	12,125	3,750	6,000
Contact spot area ( $\mu\text{m}^2$ )	50	25	50	500
Surface area exposed to air ( $\mu\text{m}^2$ )	4,275	5,825	2,200	2,600
Bottom surface area ( $\mu\text{m}^2$ )	150	475	475	925
Top surface area ( $\mu\text{m}^2$ )	925	1,250	125	925

$$A_i'' = A_{sur_i} - A_{A_i} - A_{B_i} \quad (7.9)$$

$$V_T'' = \sum_{i=1}^n V_i'' \quad (7.10)$$

$$A_T'' = \sum_{i=1}^n A_i'' \quad (7.11)$$

Table 7.2 presents the total volume and the total surface area exposed to the air of the 3D contact asperities of the 3D contact source model of the 16 A rated AC single pole rocker switch after the four different current loading tests. The calculations are made using the data presented in Figure 7.8. The values presented in Table 7.2 have an error of  $\pm 1.366\%$  (see Section 4.5.2).

Concerning the calculation of the total mechanical area of contact of the 3D contact source model after each current loading test which is given from the sum of the area of contact spots has been already introduced and presented in Table 5.3. The calculations of

volume and surface area which is exposed to air of the 3D contact asperities may be useful by researchers which are interested for the characterisation of contact systems under different factors which play important role on their reliability. These factors are the normal-force (force perpendicular to the surface) and the general contact design, the wear and the environmental and electrical parameters [6].

Table 7.2. Total volume and total surface area exposed to the air of the 3D contact asperities after the four different current loading tests

Test current (A)	0	16	32	64
Total volume ( $\mu\text{m}^3$ )	766,750	814,500	1,324,000	1,414,750
Total surface area ( $\mu\text{m}^2$ )	73,125	81,485	137,135	128,120

#### 7.4.4 3D contact asperity volume distribution findings

The graphs of 3D contact asperity volume distribution in Figure 7.11 show that the 3D contact asperities follow the same distribution after each current loading test at 0 A, 16 A, 32 A and 64 A. The results show that the volume of 3D contact asperities follow similar distribution with the area of contact spots (Figure 5.7) and voids (Figure 5.13). The smallest 3D contact asperity indicated on the graphs of Figure 7.11 is  $125 \mu\text{m}^2$ , which is the resolution of the technique (when a pixel length is  $5 \mu\text{m}$ ) and the largest 3D contact asperity indicated are several thousands  $\mu\text{m}^3$  in volume.

Moreover, it can be seen that each graph of Figure 7.11 consists of two regimes. The first where the 3D contact asperities volume distribution follows a power relationship with a slope between  $0.893 \leq q \leq 1.249$  and the second is for a small number of particular large 3D contact asperities in volume with a slope approximating equal with zero. The slope is given by Eq. (7.12).

Table 7.3 presents the slope ( $q$ ) and constant ( $C$ ) of Eq. (7.12) after each current loading test for the first regime of graphs of Figure 7.11. The constant ( $C$ ) value in log-log graphs of Figure 7.11 after each current loading test represents the number of 3D contact asperities ( $n$ ) who have volume equal to  $1 \mu\text{m}^3$ . In this research, the volume of  $1 \mu\text{m}^3$  does not exist as the smallest volume of a 3D contact asperity is  $125 \mu\text{m}^3$  (volume

of voxel). In addition, the graphs of Figure 7.11 show that the transition between the two regimes in each current loading test at 0 A, 16 A, 32 A and 64 A occurs at 12,130  $\mu\text{m}^3$ , 10,880  $\mu\text{m}^3$ , 12,000  $\mu\text{m}^3$  and 13,000  $\mu\text{m}^3$  respectively.

Moreover, from the values of Table 7.3 at normal operation (from 0 A to 16 A) and from normal to non-normal operation (from 16 A to 32 A), as the current is increased there is a tendency to have an increasing number of contact asperities with smaller volumes. At non-normal operation (from 16 A and 32 A), as the current is increased there is a tendency to have a decreasing number of contact asperities with smaller volumes.

Table 7.3. Characteristics of the first regime of the 3D contact asperities volume distribution after the four different current loading tests

Test current (A)	0	16	32	64
Slope ( $q$ )	0.893	1.035	1.249	0.957
Constant ( $C$ )	4,615	14,816	122,710	9,330

$$n(V_i'') = C(V_i'')^{-q} \quad (7.12)$$

#### 7.4.5 3D contact asperity surface area distribution findings

The graphs of 3D contact asperity surface area exposed to the air distribution in Figure 7.12 illustrate that the 3D contact asperities follow the same distribution after each current test at 0 A, 16 A, 32 A and 64 A. The smallest surface area exposed to the air of the 3D contact asperity indicated on the graphs of Figure 7.12 is 100  $\mu\text{m}^2$ , which is four times the resolution of the technique (when a pixel length is 5  $\mu\text{m}$ ) and the largest contact spots indicated are several thousands  $\mu\text{m}^2$  in the area. Moreover, it can be seen that each graph of Figure 7.12 consists of two regimes. The first where the 3D contact asperity surface area exposed to the air distribution follows a power relationship with a slope between  $0.782 \leq q \leq 1.152$  and the second is for a small number of particular large contact spots in area with a slope approximately equal to zero. The slope is given by Eq. (7.13).

Table 7.4 presents the slope ( $q$ ) and constant ( $C$ ) of Eq. (7.13) after each current loading test for the first regime of graphs of Figure 7.12. The constant ( $C$ ) value in log-log graphs of Figure 7.12 after each current loading test represents the number of 3D contact asperities ( $n$ ) who have a surface area exposed to air equal to  $1 \mu\text{m}^2$ . In this research, the surface area of a 3D contact asperity which is exposed to air and equals  $1 \mu\text{m}^2$  does not exist as the smallest surface area exposed to the air of a 3D contact asperity is  $25 \mu\text{m}^2$  (area of pixel). In addition, the graphs of Figure 7.12 show that the transition between the two regimes in each current loading test at 0 A, 16 A, 32 A and 64 A occurs at  $4,275 \mu\text{m}^2$ ,  $3,675 \mu\text{m}^2$ ,  $4,100 \mu\text{m}^2$  and  $4,525 \mu\text{m}^2$  respectively. Moreover, from the slope values of Table 7.4, as the current is increased there is a tendency to have a decreasing number of contact asperities with larger surface areas exposed to the air.

Table 7.4. Characteristics of the first regime of the 3D contact asperities surface area exposed to the air distribution after the four different current loading tests

Test current (A)	0	16	32	64
Slope ( $q$ )	0.782	0.914	1.152	1.947
Constant ( $C$ )	656	1,793	1,446	2,872

$$n(A_i) = C(A_i)^{-q} \quad (7.13)$$

#### 7.4.6 3D contact asperity bottom surface area distribution findings

The graphs of 3D contact asperity bottom surface area distribution in Figure 7.13 show that the 3D contact asperities follow the same distribution after each current loading test at 0 A, 16 A, 32 A and 64 A. The smallest surface area indicated on the graphs of Figure 7.13 is  $25 \mu\text{m}^2$ , which is the resolution of the technique (when a pixel length is  $5 \mu\text{m}$ ) and the largest surface area indicated are several  $\mu\text{m}^2$  in the volume.

Moreover, it can be seen that each graph of Figure 7.13 consists of two regimes. The first where the surface area distribution follows a power relationship with a slope between  $1.369 \leq q \leq 1.630$  and the second is for a small number of particularly large surface areas in volume with a slope approximating equal with zero. The slope is given by Eq. (7.14).



Table 7.5 presents the slope ( $q$ ) and constant ( $C$ ) of Eq. (7.14) after each current loading test for the first regime of graphs of Figure 7.13. The constant ( $C$ ) value in log-log graphs of Figure 7.13 after each current loading test represents the number of contact spots ( $n$ ) who have an area equal to  $1 \mu\text{m}^2$ . In this research, the area of  $1 \mu\text{m}^2$  does not exist as the smallest area of a contact spot is  $25 \mu\text{m}^2$  (area of pixel). In addition, the graphs of Figure 7.13 show that the transition between the two regimes in each current loading test at 0 A, 16 A, 32 A and 64 A occurs at  $825 \mu\text{m}^2$ ,  $1,050 \mu\text{m}^2$ ,  $1,200 \mu\text{m}^2$  and  $825 \mu\text{m}^2$  respectively.

Table 7.5. Characteristics of the first regime of the 3D contact asperities bottom surface area distribution after the four different current loading tests

Test current (A)	0	16	32	64
Slope ( $q$ )	1.494	1.369	1.534	1.630
Constant ( $C$ )	24,493	14,146	56,857	76,620

$$n(A_{A_i}) = CA_{A_i}^{-q} \quad (7.14)$$

#### 7.4.7 3D contact asperity top surface area distribution findings

The graphs of 3D contact asperity top surface area distribution in Figure 7.14 show that the 3D contact asperities follow the same distribution after each current loading test. The smallest surface area indicated in the graphs of Figure 7.14 is  $25 \mu\text{m}^2$ , which is the resolution of the technique (area of pixel) and the largest surface area indicated are several  $\mu\text{m}^2$  in the volume.

Moreover, it can be seen that each graph of Figure 7.14 consists of two regimes. The first where the surface area distribution follows a power relationship with a slope between  $1.266 \leq q \leq 1.505$  and the second is for a small number of particular large surface areas in volume with a slope approximating equal with zero. The slope is given by Eq. (7.15).

$$n(A_{B_i}) = CA_{B_i}^{-q} \quad (7.15)$$

Table 7.6 presents the slope ( $q$ ) and constant ( $C$ ) values of Eq. (7.15) after each current loading test at 0 A, 16 A, 32 A and 64 A for the first regime of graphs of Figure 7.14. The constant ( $C$ ) value in log-log graphs of Figure 7.14 after each current loading test represents the number of contact spots ( $n$ ) who have an area equal to  $1 \mu\text{m}^2$ . In this research, the area of  $1 \mu\text{m}^2$  does not exist as the smallest area of a contact spot is  $25 \mu\text{m}^2$  (area of pixel).

In addition, the graphs of Figure 7.14 show that the transition between the two regimes in each current loading test at 0 A, 16 A, 32 A and 64 A occurs at  $1,175 \mu\text{m}^2$ ,  $1,150 \mu\text{m}^2$ ,  $1,100 \mu\text{m}^2$  and  $1,350 \mu\text{m}^2$  respectively.

Table 7.6. Characteristics of the first regime of the 3D contact asperities top surface area distribution after the four different current loading tests

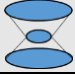
Test current (A)	0	16	32	64
Slope ( $q$ )	1.266	1.340	1.505	1.413
Constant ( $C$ )	74,224	12,826	45,299	24,081

#### 7.4.8 Ratio of top and bottom surface areas findings

The graphs of the ratio of the top and bottom surface areas of 3D contact asperities distribution in Figure 7.15 show that the 3D contact asperities follow the same distribution after each current loading test at 0 A, 16 A, 32 A and 64 A.


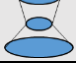
In addition, the graphs of Figure 7.15 show that the majority of 3D contact asperities have top and bottom surface area ratio equal to 1. This is because the majority of 3D contact asperities have equal bottom and top surface areas (for example, the majority of 3D contact asperities of Figure 7.13 and Figure 7.14 have area equal to  $25 \mu\text{m}^2$ , thus their ratio equals 1). Table 7.7 illustrates the number of 3D contact asperities with equal bottom and top surface areas after each current loading test (when  $A_{B_i}$  equals  $A_{A_i}$ ). The error of the calculated values of number of 3D contact asperities after each current loading test presented in Table 7.7 is  $\pm 1.366\%$ . This error, represents the sum of the error of measured threshold values and the error of 3D volume of interest of the experimental data (see Section 4.5.2).

Table 7.7. Number of 3D contact asperities with equal bottom (Conductor A) and top (Conductor B) surface areas after the four different current loading tests

Test current (A)	0	16	32	64
$n \left( \frac{A_{Bi}}{A_{Ai}} = 1 \right)$ 	186 ± 3	269 ± 4	338 ± 5	304 ± 4

Furthermore, from the graphs of Figure 7.15 the number of asperities with bottom surface area larger or smaller than the top surface area can be identified. This number of asperities is given in Table 7.8 after the four different current loading tests. The values of Table 7.8 show that the number of asperities is larger when the ratio of  $A_{Bi}$  and  $A_{Ai}$  is smaller than 1. This indicates that the majority of 3D contact asperities after each current loading test have bottom surface area (belongs to Conductor A) larger than top surface area (belongs to Conductor B). The error of the calculated values presented in Table 7.8 is ±1.366%. This error, represents the sum of the error of measured threshold values and the error of 3D volume of interest of the experimental data (see Section 4.5.2).

Table 7.8. Number of 3D contact asperities with bottom (Conductor A) surface area bigger or smaller than top (Conductor B) surface area after the four different current loading tests

Test current (A)	0	16	32	64
$n \left( \frac{A_{Bi}}{A_{Ai}} < 1 \right)$ 	123 ± 2	114 ± 2	210 ± 3	190 ± 3
$n \left( \frac{A_{Bi}}{A_{Ai}} > 1 \right)$ 	97 ± 1	108 ± 1	194 ± 3	148 ± 2

#### 7.4.9 3D contact asperity height distribution findings

The graphs of 3D contact asperity height distribution in Figure 7.16 show that the 3D contact asperities follow the same distribution after each current loading test at 0 A, 16 A, 32 A and 64 A. The smallest height indicated on the graphs of Figure 7.16 is 5 μm, which is the resolution of the technique (when a pixel length is 5 μm) and the largest surface area indicated are several μm in the volume.

Moreover, it can be seen that the fit-line of the points of each graph of Figure 7.16 follows an exponential relationship (when the height of 3D contact asperities increases

the number of 3D contact asperities decreases at a bigger rate) with an exponent between  $1.101 \leq \xi \leq 1.134$ . The exponent is given by Eq. (7.16). Table 7.9 presents the exponent ( $\xi$ ) and constant ( $C$ ) values of Eq. (7.16) for the graphs of Figure 7.16. Where  $e$ , is Euler's number (a transcendental number approximately 2.7183).

$$n(H_i) = C \cdot e^{-\xi \cdot H_i} \quad (7.16)$$

Table 7.9. Characteristics of the exponential graphs of 3D contact asperities height distribution after the four different current loading tests

Test current (A)	0	16	32	64
Exponent ( $\xi$ )	0.101	0.110	0.134	0.133
Constant ( $C$ )	234.11	349.66	869.03	644.26

#### 7.4.10 Ratio of top/bottom surface areas with height findings

The distribution graphs of the ratio of the top and bottom surface areas of the 3D contact asperities divided by the height between them in Figure 7.17 showing that the 3D contact asperities follow the same distribution after each current loading test.

In addition, the graphs of Figure 7.17 show that the majority of 3D contact asperities have ratio (top and bottom surface area divided by the height between them) equal to  $1/p_l$  or  $0.2 \text{ Mm}^{-1}$  (where  $p_l$  is the pixel length,  $5 \mu\text{m}$  in this research). Table 7.10 illustrates the number of the majority of these 3D contact asperities. These 3D contact asperities have equal bottom and top surface areas (when  $A_{B_i}$  equals with  $A_{A_i}$ ) and height between them equal to the pixel length ( $5 \mu\text{m}$  in this research).

Table 7.10. Number of 3D contact asperities with equal bottom and top surface areas divided by the minimum height ( $5 \mu\text{m}$ ) after the four different current loading tests

Test current (A)	0	16	32	64
$n\left(\frac{A_{B_i}}{A_{A_i} H_i} = \frac{1}{p_l}\right)$	$158 \pm 2$	$174 \pm 2$	$221 \pm 3$	$232 \pm 3$

Table 7.11 illustrates the result of the subtraction between the corresponding number of 3D contact asperities of Table 7.7 and Table 7.10. This result shows the number of 3D contact asperities with equal bottom and top surface areas with height between them bigger than the pixel length (5  $\mu\text{m}$  in this research).

Table 7.11. Number of 3D contact asperities with equal bottom and top surface areas with height between them bigger than 5  $\mu\text{m}$  after the four different current loading tests

Test current (A)	0	16	32	64
$n\left(\frac{A_{B_i}}{A_{A_i}} = 1\right) - n\left(\frac{A_{B_i}}{A_{A_i}H_i} = \frac{1}{p_l}\right)$	$28 \pm 0$	$95 \pm 1$	$117 \pm 2$	$72 \pm 1$

Table 7.12 illustrates the number of 3D contact asperities with volume equal with 1 voxel ( $p_l^3 = 125 \mu\text{m}^3$  in this research). The 3D contact asperities with volume of 1 voxel have equal bottom and top surface areas (when  $A_{B_i}$  equals with  $A_{A_i}$ ) and height between them equal to the pixel length (5  $\mu\text{m}$  in this research). The number of 3D contact asperities with volume equal with 1 voxel ( $125 \mu\text{m}^3$ ) after each current loading test is also given on the graphs of Figure 7.11.

Table 7.12. Number of 3D contact asperities with volume equal with 1 voxel after the four different current loading tests

Test current (A)	0	16	32	64
$n(V_i'' = p_l^3)$	$41 \pm 1$	$63 \pm 1$	$55 \pm 1$	$60 \pm 1$

Table 7.13. Number of 3D contact asperities with volume bigger than 1 voxel and height equals with 1 pixel length after the four different current loading tests

Test current (A)	0	16	32	64
$n\left(\frac{A_{B_i}}{A_{A_i}H_i} = \frac{1}{p_l}\right) - n(V_i'' = p_l^3)$	$117 \pm 2$	$111 \pm 2$	$166 \pm 2$	$172 \pm 2$

Table 7.13 illustrates the result of the subtraction between the corresponding number of 3D contact asperities of Table 7.10 and Table 7.12. This result shows the number of 3D contact asperities with equal bottom and top surface areas with height between them

equal to the pixel length  $p_l$  ( $5 \mu\text{m}$  in this research). These type of 3D contact asperities can also be labelled as slice asperities (see Figure 7.1).

#### 7.4.11 Hemispherical 3D contact asperities findings

The ratio presented on the graphs of Figure 7.18 is introduced in order to investigate whether the Greenwood-Williamson [60] model meets the reality. According to this model, the two bodies of 3D contact asperities have hemispherical shapes. This model is described from Figure 7.19(a).

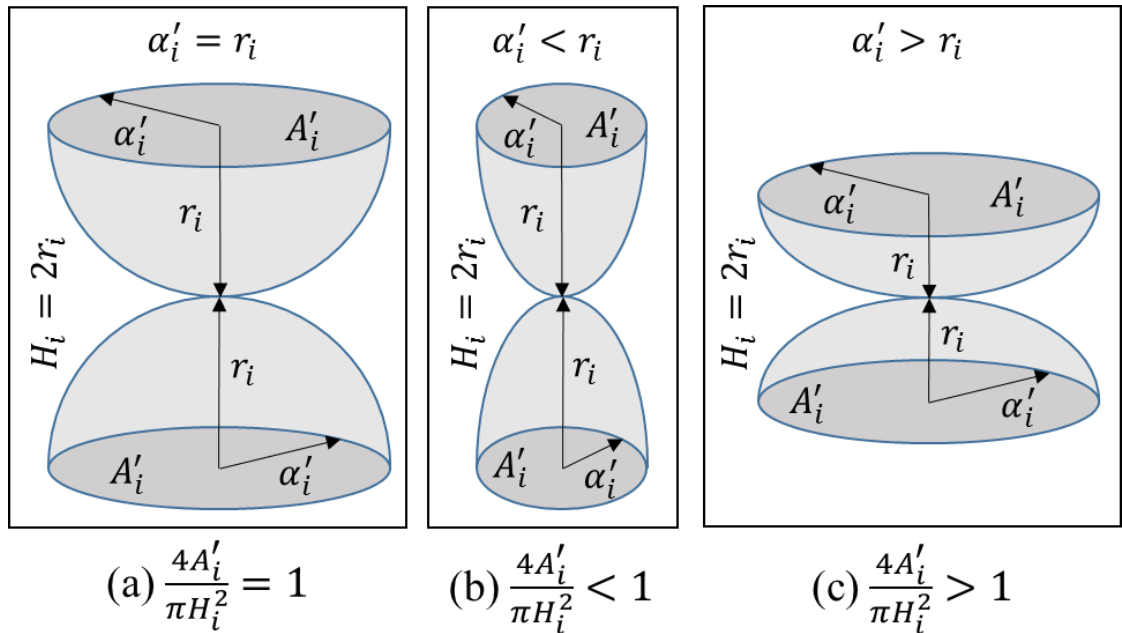


Figure 7.19. Schematic types of 3D contact asperities

Figure 7.19(a) illustrates the two hemispherical bodies of the contact asperity. Where  $A'_i$ , describes the surface areas of the bottom and the top of the contact asperity while  $\alpha'_i$  and  $r_i$  are the radii of the hemispherical bodies which are equal to this condition. The height ( $H_i$ ) of contact asperity equals  $2r_i$ . From Figure 7.19(a) it is obvious that

$$H_i = 2\alpha'_i \quad (7.17)$$

Substituting Eq. (5.7) in Eq. (7.17) the result is given by Eq. (7.18).

$$H_i = 2\sqrt{\frac{A_i'}{\pi}} \quad (7.18)$$

Rearranging Eq. (7.18), it gives

$$\frac{2\sqrt{A_i'}}{H_i\sqrt{\pi}} = \frac{4A_i'}{H_i^2\pi} = 1 \quad (7.19)$$

If the ratio of 3D contact asperity with equal bottom and top surface areas ( $A_i' = A_{A_i} = A_{B_i}$ ) with height ( $H_i$ ) multiplied by  $4/\pi$  equals 1, then the contact asperity has a shape similar with the shape of Figure 7.19(a). If this ratio is smaller than 1, the contact asperity has a shape similar with the shape of Figure 7.19(b) while if this ratio is larger than 1, the contact asperity has a shape similar with the shape of Figure 7.19(c).

The distributions of the graphs of Figure 7.18 are for the 3D contact asperities with equal bottom and top surface areas assuming that the height of each of the two conductors (bodies of contact asperity) is half of the height of each contact asperity. From the distributions of the graphs of Figure 7.18 the number of 3D contact asperities with ratio equal, smaller or larger than 1 is calculated and presented in Table 7.14.

Table 7.14. Number of 3D contact asperities with ratio equal, smaller or larger than 1 after each current loading test

Test current (A)	0	16	32	64
$n\left(\frac{4A_i'}{\pi H_i^2} = 1\right)$	$3 \pm 0$	$7 \pm 0$	$7 \pm 0$	$8 \pm 0$
$n\left(\frac{4A_i'}{\pi H_i^2} < 1\right)$	$44 \pm 1$	$79 \pm 1$	$129 \pm 2$	$95 \pm 1$
$n\left(\frac{4A_i'}{\pi H_i^2} > 1\right)$	$139 \pm 2$	$183 \pm 2$	$202 \pm 3$	$201 \pm 3$

According to the CAT\* for the visualisation of 3D contact asperities which are developed in this research and the values of Table 7.14 it is obvious that the majority of 3D contact asperities with equal bottom and top surface areas have a shape similar to the

shape of Figure 7.19(c). The number of 3D contact asperities with ratio equal to 1 represents the Greenwood-Williamson [60] assumptions for the hemispherical shapes of the two bodies which consist of the contact asperity. The values of Table 7.14 show that the contact asperities with hemispherical conductors (bodies) consist of the minority compared with the other contact asperity shapes of Figure 7.19.

## 7.5 Conclusion

The X-ray CT technique is used in order to visualize the contact system of a 16 A rated AC single pole rocker switch without the need to dismantle the sample. A contact analysis approach is developed and introduced in this chapter to show in a 3D visualization the contact asperities of a given contact system. The contact asperities consist of voxel or voxels which represent the 3D microstructures of the contact system and it is found that they have different sizes, shapes and their contact spots are variable. The 2D cross-section slice images of the contact system which are acquired with the use of X-ray CT are processed using Contact Analysis Techniques, CAT\* which are developed and implemented with a suite of tools developed in MATLAB and Image Processing Toolbox. These techniques can be used for any contact system and for any value of resolution.

The volume, the bottom surface area, the top surface area and the surface area exposed to air of each of the 3D contact asperities of the 16 A rated AC single pole rocker switch are calculated and presented with their distributions after the four different current loading tests. In the analysis of all these distributions after each current loading test it was observed that the 3D contact asperities followed a power law relationship. In addition, the total volume of the 3D contact asperities of the 16 A rated AC single pole rocker switch and their total surface area exposed to the air are also calculated and presented after the four different current loading tests at 0 A, 16 A, 32 A and 64 A.

Moreover, the height of each 3D contact asperity is calculated and presented with its distribution after the four different current loading tests. In the analysis of 3D contact asperity height distribution after each current loading test it was observed that the 3D contact asperities followed an exponential relationship (when the height of the 3D contact asperities increases the number of 3D contact asperities decreases with larger rate).



## Chapter 8 – Conclusion

### 8.1 Scope of this Research

This research is mainly an investigation of the X-ray CT technique for the visualisation and characterisation of electrical contact spots and electrical contact asperities of a conductive contact system under different current loading tests. The advantage of X-ray CT as a non-destructive visualisation technique was established to be a perfect and efficient way to investigate electrical contact spots and electrical contact asperities. Moreover, the experimental data (2D cross-section slice images of the contact system) acquired using this technique offered a good basis for better understanding the effect of electrical contact.

The visualisation and characterisation of electrical contact spots and electrical contact asperities were achieved by using Contact Analysis Techniques, CAT\* which are developed and implemented with a suite of tools developed in MATLAB and the Image Processing Toolbox. These CAT\* use as input data the 2D cross-section slice images of the contact system.

### 8.2 Novelties of this Research

The novelties of this research are summarized below:

- In Chapter 5, the 3D contact map of an electrical contact interface is developed demonstrating the 3D nature of the contact. Other researchers have visualised the contact interface in the 2D plane ignoring the scale dependency of contact interface. According to Jang and Jang [183], the scale dependency of contact interface should be considered because contact spots are formulated by rough surfaces at different scales having different morphologies.
- In Chapter 6, for the first time a resistor network model has been developed from the cross-section slice images of contact system. In this modelling process, a technique is developed which pictures any cross-section slice of the contact system and shows which voxels the electric current flows through. There are no attempts by other researchers to do this.
- In Chapter 7, the 3D contact asperities of the contact system are visualised. The contact asperities describe the structure above and below the contact interface. Other researchers have visualised only a single contact asperity.

### 8.3 Main Findings

The main findings of this research in each chapter are summarized below:

#### 8.3.1 Chapter 4

- The X-ray CT is a suitable visualisation technique for electrical contact spots and electrical contact asperities.
- The experimental data acquired using the X-ray CT technique with pixel resolution of  $5\ \mu\text{m} \times 5\ \mu\text{m}$  gives the ability of examination and processing in order to investigate different characteristics which occur in the contact interface and its extension.

#### 8.3.2 Chapter 5

- The 3D contact map of an electrical contact interface is developed demonstrating the 3D nature of the contact.
- The parameters of the 3D contact map are calculated. These parameters include the calculation of the contact resistance using two different approaches (Greenwood and Holm), the number of contact spots, the area of each contact spot and the total mechanical area of contact. In addition, the calculation of the volume of each void and the total volume of voids are conducted.

#### 8.3.3 Chapter 6

- The resistor network model of the contact system is developed from the cross-section slice images of contact system. In this modelling process, a technique is developed which pictures any cross-section slice of the contact system and shows which voxels the electric current flows through.
- The resistor network model is divided into three main regions where two regions have resistors connected in series. The third region is located between the other two regions and its resistors are connected in a nontrivial fashion of parallel and series components. For the resistance across this region an approach has been introduced by modifying the Greenwood's formula of total contact resistance. The sum of the total resistance in each region gives the total resistance across the resistor network model of the contact system. Moreover, it is found that as a cross-section slice of the resistor network model (for Closed Circuit) tends to the contact region the total number of its resistors increases. Furthermore, it is important to

note that as a cross-section slice of the resistor network model (for both circuits, Open/Closed and Closed) tends to the contact region the total cross-section area of the cross-section slice decreases. This indicates that as the cross-section slice tends to the contact region the total volume of its resistors decreases.

- The resistor network model illustrates that the constriction of electric current through the contact system shows behaviour analogous to the climate zones of earth. For example, as the electric current flows from polar zone to the tropical zone the constriction increases and when flows (the electric current) from tropical zone to the polar zone the constriction decreases.

#### 8.3.4 Chapter 7

- The visualisation of 3D contact asperities of the contact system. The contact asperities describe the structures above and below the contact spots.
- The parameters of 3D contact asperities are calculated. These parameters include the calculation of the volume of each 3D asperity and the total volume of 3D asperities as well as the surface area of each asperity which is exposed to air and the total surface area of 3D asperities which is exposed to the air.
- The 3D contact asperities are evaluated and it is found that they have different sizes, shapes and their contact spots are variable.

### 8.4 The X-ray CT Technique

Electrical contact is an important factor for the reliability of electrical devices [6]. Due to the limitation of optical imaging, methods available for the contact measurement characteristics are only suitable for open or transparent contact systems. For most of the practical situations that require contact measurement characteristics in non-transparent or enclosed contact systems, the traditional visualisation techniques are not effective [75, 187]. Based upon these requirements, a technique suitable for the electrical contact characteristics in non-transparent contact systems is developed by using the X-ray CT [7, 75]. The main advantage of this visualisation technique is the ability to acquire 2D and 3D views of the contact system keeping the features intact.

The X-ray CT system could be divided in three main parts: the X-ray source, the turntable and the detector. The sample (contact system) takes place on the turntable and illuminated with X-rays from the source. The turntable every time rotates the sample in

small equal intervals and a 2D X-ray image is acquired from the detector. This procedure is repeated until the sample makes a full rotation of 360°. In the process, the 2D X-ray images are reconstructed as 3D reconstructed volume. From this volume a software is then used in order to create 2D cross-section slice images (experimental data).

## **8.5 The Contact Analysis Techniques**

A 16 A rated AC single pole rocker switch is selected as the contact system for investigation which was scanned using X-ray Computed Tomography (CT) technique after four different current loading tests at 0 A, 16 A, 32 A and 64 A. In the process, several Contact Analysis Techniques, CAT\* are developed and implemented with a suite of tools in MATLAB and Image Processing Toolbox in order to help with the analysis of experimental data (data which are acquired from X-ray CT technique scan). These CAT\* consist of a variety of tools which are categorised into visualisation tools and calculation tools.

The visualisation tools have the ability to visualise the contact interface of the contact system (2D contact map and 3D contact map), the 2D angle contact map (show the contact spot with equal contact angle with same colour), the 3D voids between the conductors of the contact system, the 3D contact asperities (the extensions of contact spots above and below the two conductors of the contact system) and the geometric path of electric current which flows through the contact system.

The calculation tools have the ability to calculate the contact resistance using two different approaches (Greenwood and Holm), the number of contact spots, the area of each contact spot and the total mechanical area of contact of a given contact system. Moreover, the calculation tools can calculate the angle of each contact spot in 3D contact interface and the number of voids which are located between the two conductors of the contact system. In addition, the calculation of the volume of each void and the total volume of voids are conducted with the calculation tools.

Concerning the 3D contact asperities, the calculation tools have the ability to calculate the number of 3D contact asperities, the height and volume of each 3D asperity and the total volume of 3D asperities as well as the surface area of each asperity which is exposed to air and the total surface area of 3D asperities which is exposed to the air.

Another ability of the calculation tools is the calculation of the number of contact spots (number of resistors in the resistor network model, for open and closed circuits) in each cross-section slice (perpendicular to contact normal force) and indicating from which contact spots the electric current flows through and which does not.

The CAT\* give the possibility to examine and characterise the contact system under different conditions and operations. This possibility may be useful and beneficial for contact users, their suppliers and electrical device system design engineers as it visualises and characterises different features of the contact system.

## **8.6 Future Work**

The aim of future work focuses on the development of an ageing model to aid reliability prediction of electrical devices. The electrical contact is identified as the most common factor as to why electrical and electronic devices fail. According to statics, the most common cause of electrical failure is credited to connection failures. The electrical contacts fail due to a variation of factors such as film formation, corrosion, oxidation, stress relaxation, fretting and diffusion. Moreover, the high current flowing through a limited space accelerates the degradation of an electrical contact. The total contact resistance increases localised temperature at the contact interface and primarily softens the contact materials. The thermal cycling hastens stress relaxation and aging of contact materials causing failure of the electrical contact.

Visualisation of internal features in electrical components using X-ray CT visualisation technique is to be used for identifying structural defects and material migration. The main advantage of this visualisation technique is that it is non-destructive with no need of dismantling the component of interest. This leaves any features intact. The aim is to use the 3D visualisation data of contact system (e.g. in Comsol or Ansys) in order to build an ageing model examining its behaviour in different electrical (voltage, current, frequency) and physical (temperature, temperature alterations, humidity) parameters.

The ageing model could help the manufacturing companies of contact systems to develop more reliable contact systems examining their electrical and physical parameters for different contact materials under different applied forces.

## References

- [1] J. H. Kim, D. J. Srolovitz, P.-R. Cha, and J.-K. Yoon, "Capillarity and electromigration effects on asperity contact evolution in microelectromechanical systems switches," *Journal of Applied Physics*, vol. 100, pp. 054502-1-054502-8, 2006.
- [2] S. Gong, Z. H. Zhu, and E. I. Haddad, "Modeling electrical conductivity of nanocomposites by considering carbon nanotube deformation at nanotube junctions," *Journal of Applied Physics*, vol. 114, p. 074303, 2013.
- [3] N. Argibay, M. T. Brumbach, M. T. Dugger, and P. G. Kotula, "Grain boundary diffusivity of Ni in Au thin films and the associated degradation in electrical contact resistance due to surface oxide film formation," *Journal of Applied Physics*, vol. 113, p. 114906, 2013.
- [4] F. A. Chaves, D. Jiménez, A. W. Cummings, and S. Roche, "Physical model of the contact resistivity of metal-graphene junctions," *Journal of Applied Physics*, vol. 115, p. 164513, 2014.
- [5] I. H. Sung, J. W. Kim, H. J. Noh, and H. Jang, "Effect of displacement and humidity on contact resistance of copper electrical contacts," *Tribology International*, vol. 95, pp. 256-261, 2016.
- [6] P. v. Dijk, "Critical Aspects of Electrical Connector Contacts," in *2nd International Conference on Reliability of Electrical Products and Electrical Contacts (ICREPEC 2007)*, Xiamen, China, March, 2007.
- [7] A. V. Lalechos, "Evaluation of X-ray CT tomography as a means for investigating in-situ electrical contact interfaces," Electro-Mechanical Research Group, University of Southampton, Southampton, UK, 2010.
- [8] M. D. Bryant, "Resistance buildup in electrical connectors due to fretting corrosion of rough surfaces," *IEEE Transactions on Components, Packaging and Manufacturing Technology, Part A*, vol. 17, pp. 86-95, 1994.
- [9] T. S. N. S. Narayanan, P. Young Woo, and Y. L. Kang, "Fretting corrosion of lubricated tin-plated contacts," *Industrial Lubrication and Tribology*, vol. 60, pp. 233-241, 2008.
- [10] X. Luo and X. Li, "Design and characterisation of a new duplex surface system based on S-phase hardening and carbon-based coating for ASTM F1537 Co–Cr–Mo alloy," *Applied Surface Science*, vol. 292, pp. 336-344, 2014.
- [11] E. Mengotti, L. I. Duarte, J. Pippola, and L. Frisk, "Fretting corrosion: Analysis of the failure mechanism for low voltage drives applications," *Microelectronics Reliability*, vol. 54, pp. 2109-2114, 2014.
- [12] N. Wang and D. Xiong, "Superhydrophobic membranes on metal substrate and their corrosion protection in different corrosive media," *Applied Surface Science*, vol. 305, pp. 603-608, 2014.
- [13] S. Hao, L. Zhao, Y. Zhang, and H. Wang, "Improving corrosion and wear resistance of FV520B steel by high current pulsed electron beam surface treatment," *Nuclear Instruments and Methods in Physics Research Section B: Beam Interactions with Materials and Atoms*, vol. 356–357, pp. 12-16, 2015.
- [14] C. Liu, F. Su, and J. Liang, "Producing cobalt–graphene composite coating by pulse electrodeposition with excellent wear and corrosion resistance," *Applied Surface Science*, vol. 351, pp. 889-896, 2015.
- [15] M. D. Bryant, "Assessment of fretting failure models of electrical connectors," in *40th IEEE Holm Conference on Electrical Contacts*, Chicago, IL, Oct., 1994, pp. 167-175.
- [16] N. Ray, B. Kempf, T. Mützel, L. Froyen, K. Vanmeensel, and J. Vleugels, "Effect of WC particle size and Ag volume fraction on electrical contact resistance and

- thermal conductivity of Ag–WC contact materials," *Materials & Design*, vol. 85, pp. 412-422, 2015.
- [17] P. J. Tavnet, G. J. W. Van Bussel, and F. Spinato, "Machine and Converter Reliabilities in Wind Turbines," in *3rd IET International Conference on Power Electronics, Machines and Drives*, Dublin, Ireland, April, 2006, pp. 127-130.
- [18] M. Boettcher and F. W. Fuchs, "Power electronic converters in wind energy systems &#x2014; Considerations of reliability and strategies for increasing availability," in *14th European Conference on Power Electronics and Applications (EPE)*, Birmingham, UK, Aug., 2011, pp. 1-10.
- [19] W. Ren, P. Wang, Y. Fu, C. Pan, and J. Song, "Effects of temperature on fretting corrosion behaviors of gold-plated copper alloy electrical contacts," *Tribology International*, vol. 83, pp. 1-11, 2015.
- [20] R. Holm, *Electric Contacts Handbook* Third ed. Berlin: Springer Verlag, 1958.
- [21] P. G. Slade, *Electrical contacts: Principles and applications*. Florida: CRC Press, 2014.
- [22] K. L. Johnson, *Contact Mechanics*. Cambridge Cambridge University Press, 1985.
- [23] M. Braunovic, V. V. Konchits, and N. K. Myshkin, *Electrical Contacts: Fundamentals, Applications and Technology*. New York: CRC Press, 2007.
- [24] X. Yu, M. Liu, L. Meng, and L. Xiang, "Classifying cervical spondylosis based on X-ray quantitative diagnosis," *Neurocomputing*, vol. 165, pp. 222-227, 2015.
- [25] P. M. Medin, R. D. Foster, A. J. van der Kogel, J. Meyer, J. W. Sayre, H. Huang, *et al.*, "Paralysis following stereotactic spinal irradiation in pigs suggests a tolerance constraint for single-session irradiation of the spinal nerve," *Radiotherapy and Oncology*, vol. 109, pp. 107-111, 2013.
- [26] J. Ricoy, A. Ortega, and A. Cabello, "Subacute myelo-optic neuropathy (SMON): First neuro-pathological report outside Japan," *Journal of the Neurological Sciences*, vol. 53, pp. 241-251, 1982.
- [27] J. Bradfield, J. Hoffman, and F. De Beer, "Verifying the potential of micro-focus X-ray computed tomography in the study of ancient bone tool function," *Journal of Archaeological Science: Reports*, vol. 5, pp. 80-84, 2016.
- [28] M. Murata, T. Akazawa, T. Yuasa, M. Okayama, J. Tazaki, T. Hanawa, *et al.*, "Quantitative analysis on orientation of human bone integrated with midpalatal implant by micro X-ray diffractometer," *Applied Surface Science*, vol. 262, pp. 222-226, 2012.
- [29] W.-H. Yin, B. Lu, J.-B. Gao, P.-L. Li, K. Sun, Z.-F. Wu, *et al.*, "Effect of reduced x-ray tube voltage, low iodine concentration contrast medium, and sinogram-affirmed iterative reconstruction on image quality and radiation dose at coronary CT angiography: Results of the prospective multicenter REALISE trial," *Journal of Cardiovascular Computed Tomography*, vol. 9, pp. 215-224, 2015.
- [30] B. Dietl, J. Marienhagen, T. Kühnel, A. Schreyer, and O. Kölbl, "The impact of FDG-PET/CT on the management of head and neck tumours: The radiotherapist's perspective," *Oral Oncology*, vol. 44, pp. 504-508, 2008.
- [31] L. Schoeman, P. Williams, A. du Plessis, and M. Manley, "X-ray micro-computed tomography ( $\mu$ CT) for non-destructive characterisation of food microstructure," *Trends in Food Science & Technology*, vol. 47, pp. 10-24, 2016.
- [32] S. Kelkar, C. J. Boushey, and M. Okos, "A method to determine the density of foods using X-ray imaging," *Journal of Food Engineering*, vol. 159, pp. 36-41, 2015.
- [33] I. R. Donis-González, D. E. Guyer, R. Chen, and A. Pease, "Evaluation of undesirable fibrous tissue in processing carrots using Computed Tomography

- (CT) and structural fiber biochemistry," *Journal of Food Engineering*, vol. 153, pp. 108-116, 2015.
- [34] L. J. Ladani, J. Razmi, and J. Bentley, "Microstructure and mechanical strength of snag-based solid liquid inter-diffusion bonds for 3 dimensional integrated circuits," *Thin Solid Films*, vol. 518, pp. 4948-4954, 2010.
- [35] P. J. de Veen, C. Bos, D. R. Hoogstede, C. T. A. Revenberg, J. Liljeholm, and T. Ebefors, "High-resolution X-ray computed tomography of through silicon vias for RF MEMS integrated passive device applications," *Microelectronics Reliability*, vol. 55, pp. 1644-1648, 2015.
- [36] G. Liao, P. Chen, L. Du, L. Su, Z. Liu, Z. Tang, *et al.*, "Using SOM neural network for X-ray inspection of missing-bump defects in three-dimensional integration," *Microelectronics Reliability*, vol. 55, pp. 2826-2832, 2015.
- [37] E. Zschech, W. Yun, and G. Schneider, "High-resolution X-ray imaging - A powerful nondestructive technique for applications in semiconductor industry," *Applied Physics A*, vol. 92, pp. 423-429, 2008.
- [38] Y. Nikishkov, L. Airoidi, and A. Makeev, "Measurement of voids in composites by X-ray Computed Tomography," *Composites Science and Technology*, vol. 89, pp. 89-97, 2013.
- [39] A. Katunin, K. Dragan, and M. Dziendzikowski, "Damage identification in aircraft composite structures: A case study using various non-destructive testing techniques," *Composite Structures*, vol. 127, pp. 1-9, 2015.
- [40] E. J. Thoreson, J. Martin, and N. A. Burnham, "The role of few-asperity contacts in adhesion," *Journal of Colloid and Interface Science*, vol. 298, pp. 94-101, 2006.
- [41] H. J. Li, Z. Y. Jiang, D. B. Wei, J. T. Han, and A. K. Tieu, "Study on surface asperity flattening during uniaxial planar compression," *Wear*, vol. 271, pp. 1778-1784, 2011.
- [42] L. Si and X. Wang, "Nano-adhesion influenced by atomic-scale asperities: A molecular dynamics simulation study," *Applied Surface Science*, vol. 317, pp. 710-717, 2014.
- [43] S. Itoh, Y. Hamamoto, K. Ishii, K. Fukuzawa, and H. Zhang, "Detection of Asperity Contact for Precise Gap Determination in Thin-Film Nanorheometry," *Tribology Letters*, vol. 49, pp. 1-10, 2013.
- [44] B. Bhushan, "Contact mechanics of rough surfaces in tribology: multiple asperity contact," *Tribology Letters*, vol. 4, pp. 1-35, 1998.
- [45] H. T. Zhu, X. Zheng, P. B. Kosasih, and A. K. Tieu, "Tribo-surface charge and polar lubricant molecules on friction and lubrication under multiple 3D asperity contacts," *Wear*, vol. 332-333, pp. 1248-1255, 2015.
- [46] S. Wen, Y. Tan, S. Shi, W. Dong, D. Jiang, J. Liao, *et al.*, "Thermal contact resistance between the surfaces of silicon and copper crucible during electron beam melting," *International Journal of Thermal Sciences*, vol. 74, pp. 37-43, 2013.
- [47] E. Caron, K. Daun, and M. Wells, "Experimental Characterization of Heat Transfer Coefficients During Hot Forming Die Quenching of Boron Steel," *Metallurgical and Materials Transactions B*, vol. 44, pp. 332-343, 2013.
- [48] M. Seong, P. K. Singh, and S. Sinha, "Area of contact and thermal transport across transfer-printed metal-dielectric interfaces," *Journal of Applied Physics*, vol. 113, pp. 024321-024329, 2013.
- [49] C. Ji, H. Zhu, and W. Jiang, "Fractal prediction model of thermal contact conductance of rough surfaces," *Chinese Journal of Mechanical Engineering*, vol. 26, pp. 128-136, 2013.



- [50] O. Rezvanian, M. A. Zikry, C. Brown, and J. Krim, "Surface roughness, asperity contact and gold RF MEMS switch behavior," *Journal of Micromechanics and Microengineering*, vol. 17, pp. 2006–2015, 2006
- [51] B. F. Toler, R. A. C. Jr, and J. W. McBride, "A review of micro-contact physics for microelectromechanical systems (MEMS) metal contact switches," *Journal of Micromechanics and Microengineering*, vol. 23, pp. 103001-103016, 2013.
- [52] M. Kolahdoozan, M. Hamed, and M. Nikkhah-Bahrami, "A novel model for the effect of geometric properties of micro/nanoscale asperities on surface adhesion," *International Journal of Adhesion and Adhesives*, vol. 48, pp. 280-287, 2014.
- [53] H. Kim, N. H. Shaik, X. Xu, A. Raman, and A. Strachan, "Multiscale contact mechanics model for RF–MEMS switches with quantified uncertainties," *Modelling and Simulation in Materials Science and Engineering*, vol. 21, pp. 085002-085019, 2013.
- [54] M. Gaitzsch, S. Kurth, S. Voigt, S. Haas, and T. Gessner, "Analysis of Au metal–metal contacts in a lateral actuated RF MEMS switch," *International Journal of Microwave and Wireless Technologies*, vol. 6, pp. 481-486, 2014.
- [55] L. Li, W. Song, G. Zhang, and D. Jia, "An electrical contact resistance model including roughness effect for a rough MEMS switch," *Journal of Micromechanics and Microengineering*, vol. 22, pp. 115023-115030, 2012.
- [56] D. Berman, M. J. Walker, C. D. Nordquist, and J. Krim, "Impact of adsorbed organic monolayers on vacuum electron tunneling contributions to electrical resistance at an asperity contact," *Journal of Applied Physics*, vol. 110, pp. 114307-114314, 2011.
- [57] V. A. Zhuravlev, "On the question of theoretical justification of the Amontons-Coulomb law for friction of unlubricated surfaces," *Zh. Tekh. Fiz. (Journal of Technical Physics)*, vol. 10, pp. 1447–1452, 1940.
- [58] D. J. Whitehouse and J. F. Archard, "The Properties of Random Surfaces of Significance in their Contact," *Proceedings of the Royal Society of London. Series A, Mathematical and Physical Sciences*, vol. 316, pp. 97-121, 1970.
- [59] R. A. Onions and J. F. Archard, "The contact of surfaces having a random structure," *Journal of Physics D: Applied Physics*, vol. 6, pp. 289-304, 1973.
- [60] D. J. Whitehouse and M. J. Phillips, "Discrete Properties of Random Surfaces," *Philosophical Transactions of the Royal Society of London. Series A, Mathematical and Physical Sciences*, vol. 290, pp. 267-298, 1978.
- [61] D. J. Whitehouse and M. J. Phillips, "Two-Dimensional Discrete Properties of Random Surfaces," *Philosophical Transactions of the Royal Society of London. Series A, Mathematical and Physical Sciences*, vol. 305, pp. 441-468, 1982.
- [62] P. R. Nayak, "Random Process Model of Rough Surfaces," *Journal of Lubrication Technology*, vol. 93, pp. 398-407, 1971.
- [63] J. A. Greenwood and J. B. P. Williamson, "Contact of Nominally Flat Surfaces," *British Journal of Applied Physics*, vol. 295, pp. 300-319, 1966.
- [64] K. Anantheshwara and M. S. Bobji, "In situ transmission electron microscope study of single asperity sliding contacts," *Tribology International*, vol. 43, pp. 1099-1103, 2010.
- [65] S. Solhjoo and A. I. Vakis, "Single asperity nanocontacts: Comparison between molecular dynamics simulations and continuum mechanics models," *Computational Materials Science*, vol. 99, pp. 209-220, 2015.
- [66] J. A. Greenwood, "Constriction resistance and the real area of contact," *Journal of Applied Physics*, vol. 17, pp. 1621-1632, 1966.
- [67] A. Majumdar and B. Bhushan, "Fractal Model of Elastic-Plastic Contact Between Rough Surfaces," *Journal of Tribology* vol. 113, pp. 11-22, 1991.

- [68] F. M. Borodich and A. B. Mosolov, "Fractal roughness in contact problems," *Journal of Applied Mathematics and Mechanics*, vol. 56, pp. 681-690, 1992.
- [69] B. Bhushan and A. Majumdar, "Characterization and Modeling of Surface Roughness and Contact Mechanics," in *Handbook of Micro/Nano Tribology*, Second ed New York: CRC Press, 1995, pp. 109-165.
- [70] F. M. Borodich and D. A. Onishchenko, "Similarity and fractality in the modelling of roughness by a multilevel profile with hierarchical structure," *International Journal of Solids and Structures*, vol. 36, pp. 2585-2612, 1999.
- [71] J. Lopez, G. Hansal, J. C. L. Bossé, and T. Mathia, "Caractérisation fractale de la rugosité tridimensionnelle d'une surface," *Journal de Physique III*, vol. 4, pp. 2501-2219, 1994.
- [72] G. Palasantzas and J. T. M. D. Hosson, "Self-affine roughness effects on the contact area between elastic bodies," *Journal of Applied Physics*, vol. 93, pp. 898-902, 2003.
- [73] L. Kogut and K. Komvopoulos, "Electrical contact resistance theory for conductive rough surfaces," *Journal of Applied Physics*, vol. 94, pp. 3153-3162, 2003.
- [74] J. F. Archard, "Elastic Deformation and the Laws of Friction," *Proceedings of the Royal Society of London. Series A*, vol. 243, pp. 190-205, 1957.
- [75] C. Roussos and J. Swingler, "The 3D nature of a real un-dismantled electrical contact interface," *Wear*, vol. 328-329, pp. 115-122, 2015.
- [76] S. Gupta, P. Paramahans Manik, R. Kesh Mishra, A. Nainani, M. C. Abraham, and S. Lodha, "Contact resistivity reduction through interfacial layer doping in metal-interfacial layer-semiconductor contacts," *Journal of Applied Physics*, vol. 113, p. 234505, 2013.
- [77] O. Floweri, J. Kim, Y. Seo, J.-Y. Park, and N. Lee, "Characterisation of carbon nanotube pastes for field emission using their sheet resistances," *Applied Surface Science*, vol. 353, pp. 54-62, 2015.
- [78] A. R. Mirak, C. J. Davidson, and J. A. Taylor, "Characterisation of fresh surface films formed on molten Mg-Nd alloy protected by different atmospheres," *Applied Surface Science*, vol. 301, pp. 91-98, 2014.
- [79] S. Weidel and U. Engel, "Characterisation of the flattening behaviour of modelled asperities," *Wear*, vol. 266, pp. 596-599, 2009.
- [80] R. E. Johnston, "Mechanical characterisation of AlSi-hBN, NiCrAl-Bentonite, and NiCrAl-Bentonite-hBN freestanding abradable coatings," *Surface and Coatings Technology*, vol. 205, pp. 3268-3273, 2011.
- [81] X. Li, W. Wu, and H. Dong, "Microstructural characterisation of carbon doped CrAlTiN nanoscale multilayer coatings," *Surface and Coatings Technology*, vol. 205, pp. 3251-3259, 2011.
- [82] M. Novotný, J. Bulíř, P. Pokorný, J. Lančok, L. Fekete, J. Musil, *et al.*, "RF magnetron sputtering of silver thin film in Ne, Ar and Kr discharges—plasma characterisation and surface morphology," *Surface and Coatings Technology*, vol. 228, Supplement 1, pp. S466-S469, 2013.
- [83] C. Aguzzi, G. Sandri, C. Bonferoni, P. Cerezo, S. Rossi, F. Ferrari, *et al.*, "Solid state characterisation of silver sulfadiazine loaded on montmorillonite/chitosan nanocomposite for wound healing," *Colloids and Surfaces B: Biointerfaces*, vol. 113, pp. 152-157, 2014.
- [84] D. R. Nisbet, A. E. Rodda, D. I. Finkelstein, M. K. Horne, J. S. Forsythe, and W. Shen, "Surface and bulk characterisation of electrospun membranes: Problems and improvements," *Colloids and Surfaces B: Biointerfaces*, vol. 71, pp. 1-12, 2009.

- [85] S. Mitra, A. Ghanbari-Siahkali, P. Kingshott, S. Hvilsted, and K. Almdal, "Surface characterisation of ethylene–propylene–diene rubber upon exposure to aqueous acidic solution," *Applied Surface Science*, vol. 252, pp. 6280-6288, 2006.
- [86] T. Y. Hin, C. Liu, and P. P. Conway, "Surface characterisation of plasma treated flexible substrates for waveguide-on-flex application," *Surface and Coatings Technology*, vol. 203, pp. 3741-3749, 2009.
- [87] E. Buhl, M. Poelchau, G. Dresen, and T. Kenkmann, "Scaling of sub-surface deformation in hypervelocity impact experiments on porous sandstone," *Tectonophysics*, vol. 634, pp. 171-181, 2014.
- [88] S.-C. Han, W.-T. Park, and W.-Y. Jung, "A four-variable refined plate theory for dynamic stability analysis of S-FGM plates based on physical neutral surface," *Composite Structures*, vol. 131, pp. 1081-1089, 2015.
- [89] A. W. Kley, "Chapter 4 - Molecular beam scattering at metal surfaces," in *The Chemical Physics of Solid Surfaces*. vol. Volume 11, D. P. Woodruff, Ed., ed: Elsevier, 2003, pp. 79-108.
- [90] M. R. Guascito, D. Cesari, D. Chirizzi, A. Genga, and D. Contini, "XPS surface chemical characterization of atmospheric particles of different sizes," *Atmospheric Environment*, vol. 116, pp. 146-154, 2015.
- [91] J.-J. Li, H.-Q. An, J. Zhu, and J.-W. Zhao, "Improve the surface enhanced Raman scattering of gold nanorods decorated graphene oxide: The effect of CTAB on the electronic transition," *Applied Surface Science*, vol. 347, pp. 856-860, 2015.
- [92] A. Dal Corso, "Clean Ir(111) and Pt(111) electronic surface states: A first-principle fully relativistic investigation," *Surface Science*, vol. 637–638, pp. 106-115, 2015.
- [93] B. Meng and M. W. Fu, "Size effect on deformation behavior and ductile fracture in microforming of pure copper sheets considering free surface roughening," *Materials & Design*, vol. 83, pp. 400-412, 2015.
- [94] H. Kargarzadeh, R. M. Sheltami, I. Ahmad, I. Abdullah, and A. Dufresne, "Cellulose nanocrystal reinforced liquid natural rubber toughened unsaturated polyester: Effects of filler content and surface treatment on its morphological, thermal, mechanical, and viscoelastic properties," *Polymer*, vol. 71, pp. 51-59, 2015.
- [95] H. Brune and S. Rusponi, "Chapter 11 - Magnetic properties of 2D islands on single-crystal metal surfaces," in *The Chemical Physics of Solid Surfaces*. vol. Volume 12, D. P. Woodruff, Ed., ed: Elsevier, 2007, pp. 427-470.
- [96] H. R. Rajabi, H. Arjmand, S. J. Hoseini, and H. Nasrabadi, "Surface modified magnetic nanoparticles as efficient and green sorbents: Synthesis, characterization, and application for the removal of anionic dye," *Journal of Magnetism and Magnetic Materials*, vol. 394, pp. 7-13, 2015.
- [97] B. N. J. Persson, O. Albohr, U. Tartaglino, A. I. Volokitin, and E. Tosatti, "On the nature of surface roughness with application to contact mechanics, sealing, rubber friction and adhesion," *Journal of Physics: Condensed Matter*, vol. 17, pp. R1-R62, 2005.
- [98] International Organization for Standardization (ISO), ISO 4287-97: *Geometrical product specifications (GPS) - Surface texture: Profile method - Terms, definitions and surface texture parameters*, ISO, Geneva, Switzerland, 1997.
- [99] International Organization for Standardization (ISO), ISO 16610-11: *Geometrical product specifications (GPS) - Filtration - Part 21: Linear profile filters: Gaussian filters*, ISO, Geneva, Switzerland, 2011.
- [100] American Society of Mechanical Engineers (ASME), B46.1-09: *Surface Texture (Surface Roughness, Waviness, and Lay)*, ASME Publisher, New York, NY, 2009.
- [101] T. R. Thomas, *Rough Surfaces*. London: Imperial College Press, 1999.

- [102] I. M. Hutchings, *Tribology: Friction and Wear of Engineering Materials*. London: Edward Arnold, 1992.
- [103] F. d. C. Santos, A. A. d. Santos Jr, F. Bruni, and L. T. Santos, "Evaluation of subsurface contact stresses in railroad wheels using an elastic half-space model," *Journal of the Brazilian Society of Mechanical Sciences and Engineering*, vol. 26, pp. 420-429, 2004.
- [104] G. G. Adams and M. Nosonovsky, "Contact modeling — forces," *Tribology International*, vol. 33, pp. 431-442, 2000.
- [105] H. Hertz, "Ueber die berührung fester elastischer körper," *Journal für die reine und angewandte Mathematik*, vol. 1882, pp. 156-171, 2009.
- [106] T. Hisakado, "Effect of surface roughness on contact between solid surfaces," *Wear*, vol. 28, pp. 217-234, 1974.
- [107] J. A. Greenwood and J. H. Tripp, "The Elastic Contact of Rough Spheres," *Journal of Applied Mechanics*, vol. 34, pp. 153-159, 1967.
- [108] J. A. Greenwood and J. H. Tripp, "The Contact of Two Nominally Flat Rough Surfaces," *Proceedings of the Institution of Mechanical Engineers*, vol. 185, pp. 625-633, June 1, 1970 1970.
- [109] A. W. Bush, R. D. Gibson, and T. R. Thomas, "The elastic contact of a rough surface," *Wear*, vol. 35, pp. 87-111, 1975.
- [110] E. J. Abbott and F. A. Firestone, "Specifying Surface Quality—A Method based on Accurate Measurement and Comparison," *Journal of Mechanical Engineering*, vol. 55, pp. 569-572, 1933.
- [111] J. Pullen and J. B. P. Williamson, "On the Plastic Contact of Rough Surfaces," *Proceedings of the Royal Society of London. Series A*, vol. 327, pp. 159-173, 1972.
- [112] S. Kucharski, T. Klimczak, A. Polijaniuk, and J. Kaczmarek, "Finite-elements model for the contact of rough surfaces," *Wear*, vol. 177, pp. 1-13, 1994.
- [113] W. R. Chang, I. Etsion, and D. B. Bogy, "An Elastic-Plastic Model for the Contact of Rough Surfaces," *Journal of Tribology*, vol. 109, pp. 257-263, 1987.
- [114] Y. Zhao, D. M. Maietta, and L. Chang, "An Asperity Microcontact Model Incorporating the Transition From Elastic Deformation to Fully Plastic Flow," *Journal of Tribology*, vol. 122, pp. 86-93, 1999.
- [115] L. Kogut and I. Etsion, "Elastic-Plastic Contact Analysis of a Sphere and a Rigid Flat," *Journal of Applied Mechanics*, vol. 69, pp. 657-662, 2002.
- [116] R. L. Jackson and I. Green, "A Finite Element Study of Elasto-Plastic Hemispherical Contact Against a Rigid Flat," *Journal of Tribology*, vol. 127, pp. 343-354, 2005.
- [117] Horng and J. Haur, "An Elliptic Elastic-Plastic Asperity Microcontact Model for Rough Surfaces," *Journal of Tribology*, vol. 120, pp. 82-88, 1998.
- [118] J. Jamari and D. J. Schipper, "An elastic-plastic contact model of ellipsoid bodies," *Tribology Letters*, vol. 21, pp. 262-271, 2006.
- [119] Y.-R. Jeng and P.-Y. Wang, "An Elliptical Microcontact Model Considering Elastic, Elastoplastic, and Plastic Deformation," *Journal of Tribology*, vol. 125, pp. 232-240, 2003.
- [120] W. Shujuan, H. Fang, S. Bonan, and Z. Guofu, "Method for calculation of contact resistance and finite element simulation of contact temperature rise based on rough surface contact model," in *26th International Conference on Electrical Contacts (ICEC 2012)*, Beijing, China, May, 2012, pp. 317-321.
- [121] B. Bhushan, *Handbook of Micro/Nanotribology*, 2nd ed. Boca Raton, FL: CRC Press, 1999.
- [122] M. Ciavarella, G. Demelio, J. R. Barber, and Y. H. Jang, "Linear elastic contact of the Weierstrass profile," *Proceedings of the Royal Society of London. Series A*, vol. 456, pp. 387-405, 2000.

- [123] H.-O. Peitgen and D. Saupe, *The Science of Fractal Images*: Springer-Verlag, 1988.
- [124] M. Ciavarella, G. Demelio, J. R. Barber, and Y. H. Jang, "Linear elastic contact of the Weierstrass profile," *Proceedings of the Royal Society of London. Series A*, vol. 456, pp. 387-405, 2000.
- [125] Y.-F. Gao and A. F. Bower, "Elastic-plastic contact of a rough surface with Weierstrass profile," *Proceedings of the Royal Society of London. Series A*, vol. 462, pp. 319-348, 2006.
- [126] R. D. Mindlin, "Compliance of Elastic Bodies in Contact," *Journal of Applied Mechanics*, vol. 16, pp. 259-268, 1949.
- [127] R. Holm, *Theory and Applications* Fourth ed. Berlin: Springer, 1967.
- [128] F. P. Bowden and D. Tabor, "Area of Contact Between Solids," in *The friction and lubrication of solids*, ed Oxford: Oxford University Press, 2001.
- [129] J. A. Greenwood and J. J. Wu, "Surface Roughness and Contact: An Apology," *Meccanica*, vol. 36, pp. 617-630, 2001.
- [130] N. K. Myshkin, M. Braunovich, and V. V. Konchits, "The mechanics and tribophysics of electrical contacts," *Journal of Friction and Wear*, vol. 36, pp. 454-467, 2015.
- [131] N. W. Ashcroft and N. D. Mermin, *Solid state physics*. New York: Saunders College, 1976.
- [132] C. C. Roussos and J. Swingler, "Towards a 3D technique to determine the geometric path of electric current flow through a contact system," *submitted to IEEE Transactions on Components, Packaging, and Manufacturing Technology*, 2016.
- [133] J. R. Barber, "Bounds on the electrical resistance between contacting elastic rough bodies," *Proceedings of the Royal Society of London. Series A*, vol. 459, pp. 53-66, 2003.
- [134] J. G. Zhang, J. C. Gao, and C. F. Feng, "Adhesion and attaching of particles at the failed connector contacts," in *23rd International Conference on Electrical Contacts (ICEC 2006)*, Sendai, Japan, June, 2006, pp. 192-196.
- [135] D. Gagnon and M. Braunovic, "Fretting in copper-to-copper contacts under AC and DC current conditions," *IEEE Transactions on Components and Packaging Technologies*, vol. 24, pp. 378-383, 2001.
- [136] Z. Chen, W. Jang, W. Bao, C. N. Lau, and C. Dames, "Thermal contact resistance between graphene and silicon dioxide," *Applied Physics Letters*, vol. 95, pp. 161910-0 - 161910-3, 2009.
- [137] R. Holm, *Electrical Contacts*. New York: Springer, 1979.
- [138] J. I. Goldstein, D. E. Newbury, D. C. Joy, C. E. Lyman, P. Echlin, E. Lifshin, *et al.*, *Scanning Electron Microscopy and X-Ray Microanalysis*, Third ed. New York: Springer, 2003.
- [139] J. Swingler and J. W. McBride, "Micro-arcing and arc erosion minimisation using a 42 volt DC hybrid switching devices," in *50th IEEE Holm Conference on Electrical Contacts*, Seattle, WA, Sept., 2004, pp. 1-7.
- [140] J. W. McBride, "The Loaded Surface Profile: A new technique for the investigation of contact surfaces," in *23rd International Conference on Electrical Contacts (ICEC 2006)*, Sendai, Japan, June, 2006, pp. 150-156.
- [141] M. Myers, M. Leidner, and H. Schmidt, "Effect of Contact Parameters on Current Density Distribution in a Contact Interface," in *57th IEEE Holm Conference on Electrical Contacts*, Minneapolis, MN, Sept., 2011, pp. 1-9.
- [142] W. Zhu, Y. Tian, X. Gao, and L. Jiang, "A Method To Measure Internal Contact Angle in Opaque Systems by Magnetic Resonance Imaging," *Langmuir: The ACS journal of surfaces and colloids*, vol. 29, pp. 9057-9062, 2013.

- [143] J. E. Johnson, T. E. McIff, P. Leec, E. B. Toby, and K. J. Fischera, "Validation of radiocarpal joint contact models based on images from a clinical MRI scanner," *Taylor & Francis: Computer Methods in Biomechanics and Biomedical Engineering*, vol. 17, pp. 378-387, 2014.
- [144] J. Vlassenbroeck, V. Cnudde, B. Masschaele, M. Dierick, L. van Hoorebeke, and P. Jacobs, "A comparative and critical study of X-ray CT and neutron CT as non-destructive material evaluation techniques," *Geological Society, London, Special Publications*, vol. 271, pp. 277-285, 2007.
- [145] V. A. Popovich, W. Verwaal, M. Janssen, I. J. Bennett, and I. M. Richardson, "Application of X-ray computed tomography in silicon solar cells," in *35th IEEE Photovoltaic Specialists Conference (PVSC)*, Honolulu, HI, June, 2010, pp. 1759-1764.
- [146] C. W. Green, J. Farone, J. K. Briley, R. B. Eldridge, R. A. Ketcham, and B. Nightingale, "Novel Application of X-ray Computed Tomography: Determination of Gas/Liquid Contact Area and Liquid Holdup in Structured Packing," *Ind. Eng. Chem. Res.*, vol. 46, pp. 5734-5753, 2007.
- [147] A. V. Lalechos, J. Swingler, and J. Crane, "Visualisation of the Contact Area for Different Contact Forces using X-Ray Computer Tomography " in *54th IEEE Holm Conference on Electrical Contacts*, Orlando, FL, Oct., 2008, pp. 263-269.
- [148] A. V. Lalechos, J. Swingler, and J. W. McBride, "Evaluation of the X-Ray CT Visualisation Technique for Characterising Electrical Contacts," in *56th IEEE Holm Conference on Electrical Contacts*, Charleston, SC, Oct., 2010, pp. 1-6.
- [149] J. Swingler and A. Lalechos, "Visualization and size distribution of contact spots at a real un-dismantled electrical contact interface," *Journal of Physics D: Applied Physics*, vol. 42, pp. 085304-085310, 2009.
- [150] American Society for Testing and Materials (ASTM), E1441-00: *Standard Guide for Computed Tomography (CT) Imaging*, ASTM International, West Conshohocken, PA, 2000.
- [151] M. Fioravanti and R. Ricci, "Computerized tomography for wood density measurement: experimental research and methodologies," *Annali Accademia Italiana di Scienze Forestali*, vol. 40, pp. 57-59, 1991.
- [152] O. Lindgren, J. Davis, P. Wells, and P. Shadbolt, "Non-destructive wood density distribution measurements using computed tomography," *Holz als Roh-und Werkstoff*, vol. 50, pp. 295-299, 1992.
- [153] G. N. Hounsfield, "Computerized transverse axial scanning (tomography): Part 1. Description of system," *The British Journal of Radiology*, vol. 46, pp. 1016-1022, 1973.
- [154] L. A. Feldkamp, S. A. Goldstein, M. A. Parfitt, G. Jasion, and M. Kleerekoper, "The direct examination of three-dimensional bone architecture in vitro by computed tomography," *Journal of Bone and Mineral Research*, vol. 4, pp. 3-11, 1989.
- [155] R. Müller, H. Van Campenhout, B. Van Damme, G. Van der Perre, J. Dequeker, T. Hildebrand, *et al.*, "Morphometric Analysis of Human Bone Biopsies: A Quantitative Structural Comparison of Histological Sections and Micro-Computed Tomography," *Bone*, vol. 23, pp. 59-66, 1998.
- [156] P. Rügsegger, B. Koller, and R. Müller, "A microtomographic system for the nondestructive evaluation of bone architecture," *Calcified Tissue International*, vol. 58, pp. 24-29, 1996.
- [157] J. C. Elliott and S. D. Dover, "X-ray microtomography," *Journal of Microscopy*, vol. 126, pp. 211-213, 1982.
- [158] R. A. Altafim, C. R. Murakami, P. E. Cruvinel, J. M. Naime, G. O. Chierice, and S. Mascarenhas, "Computed x-ray tomography for analyzing polymer insulators,"

- in *Electrical Insulation and Dielectric Phenomena*, Kitchener, ON, Oct., 2001, pp. 149-152.
- [159] A. Beer, "Determination of the absorption of red light in coloured liquids (in German)," *Annalender Physik und Chemie*, vol. 86, pp. 78-88, 1852.
- [160] J. H. Lambert and D. L. Dilaura, *Photometry, or, The measure and gradations of light, colors and shade*. New York: Illuminating Engineering Society of North America, 2001.
- [161] W. Ludwig, "Development and Applications of Synchrotron Radiation Microtomography," Fakultät für Physik, Ludwigs Maximilians Universität München, Munich, Germany, 2001.
- [162] G. T. Herman, "Image Reconstruction from Projections," in *Fundamentals of Computerized Tomography*, Second ed London: Springer-Verlag 2009.
- [163] S. W. Smith, *The Scientist and Engineer's Guide to Digital Signal Processing*, Second ed. San Diego, CA: California Technical Publishing, 1999.
- [164] A. Rosenfeld and A. C. Kak, *Digital picture processing*, Second ed.: Academic Press, 1982.
- [165] S. R. Deans, *The Radon Transform and Some of its Applications*. New York: Wiley, 1983.
- [166] F. Natterer, *The Mathematics of Computerized Tomography*. New York: Wiley, 1986.
- [167] M. Beister, D. Kolditz, and W. A. Kalender, "Iterative reconstruction methods in X-ray CT," *Physica Medica*, vol. 28, pp. 94-108, 2012.
- [168] M. J. Paulus, S. S. Gleason, S. J. Kennel, P. R. Hunsicker, and D. K. Johnson, "High Resolution X-ray Computed Tomography: An Emerging Tool for Small Animal Cancer Research," *Neoplasia*, vol. 2, pp. 62-70, 2000.
- [169] Comet, Product: *Feinfocus FXE-160.51*, COMET GmbH, Germany, 2005.
- [170] Comet, Product: *Feinfocus FXE-160.45*, COMET GmbH, Germany, 2005.
- [171] L. Xue, H. Suzuki, Y. Ohtake, H. Fujimoto, M. Abe, O. Sato, *et al.*, "A method for improving measurement accuracy of cylinders in dimensional CT metrology," *Computer-Aided Design*, vol. 69, pp. 25-34, 2015.
- [172] G.-H. Chen and Y. Li, "Synchronized multiartifact reduction with tomographic reconstruction (SMART-RECON): A statistical model based iterative image reconstruction method to eliminate limited-view artifacts and to mitigate the temporal-average artifacts in time-resolved CT," *Medical Physics*, vol. 42, pp. 4698-4707, 2015.
- [173] S. Boudabbous, D. Arditi, E. Paulin, A. Syrogiannopoulou, C. Becker, and X. Montet, "Model-Based Iterative Reconstruction (MBIR) for the Reduction of Metal Artifacts on CT," *American Journal of Roentgenology*, vol. 205, pp. 380-385, 2015.
- [174] A. C. Kak and M. Slaney, *Principles of Computerized Tomographic Imaging*. New York: IEEE Press, 1999.
- [175] Arcoelectric Catalogue 170, Product: *1550 Standard & 1350 High Inrush Switches*, Arcoelectric a brand of Elektron Technology, England, 2008.
- [176] Volume Graphics GmbH. (2015). *Application software for visualization and documentation of industrial computer tomography / voxel data - Reference manual (myVGL Release 2.0)*. Available: <http://research.amnh.org/~debel/tomops/VGViewer/myvgl20.pdf>
- [177] Abertay University - SIMBIOS Centre. (2015). *X-ray CT equipment*. Available: <http://simbios.abertay.ac.uk/muSIMCT>
- [178] Media Cybernetics. (2015). *Technical Suport for Media Cybernetics Products*. Available: <http://support.mediacy.com/answers/showquestion.asp?faq=35&fldAuto=267>

- [179] Scientific Computing and Imaging Institute. (2015). "ImageVis3D" An interactive visualization software system for large-scale volume data. Scientific Computing and Imaging Institute (SCI). Available: <http://www.imagevis3d.org>
- [180] J. Swingler, "Clustering and the spatial distribution of contact spots at a real un-dismantled electrical contact interface," *Journal of Physics D: Applied Physics*, vol. 43, pp. 145302-145307, 2010.
- [181] J. Swingler, "The resolution dependence of measured fractal characteristics for a real un-dismantled electrical contact interface," *Wear*, vol. 268, pp. 1178–1183, 2010.
- [182] M. G. Cooper, B. B. Mikic, and M. M. Yovanovich, "Thermal Contact Conductance," *International Journal of Heat and Mass Transfer*, vol. 12, pp. 279-300, 1969.
- [183] J. Jang and Y. H. Jang, "Spatial distributions of islands in fractal surfaces and natural surfaces," *Chaos, Solitons & Fractals*, vol. 45, pp. 1453-1459, 2012.
- [184] M. T. Singer and K. Kshonze, "Electrical resistance of random rough contacting surfaces using fractal surface modeling," in *37th IEEE Holm Conference on Electrical Contacts*, Chicago, IL, Oct., 1991, pp. 73-82.
- [185] C. Roussos and J. Swingler, "Evaluation of electrical contacts using an X-Ray CT 3D visualisation technique," in *27th International Conference on Electrical Contacts (ICEC 2014)*, Dresden, Germany, June, 2014, pp. 326-331.
- [186] C. C. Roussos and J. Swingler, "A 3D contact analysis approach for the visualization of the electrical contact asperities," *submitted to AIP Advances*, 2016.
- [187] C. Roussos and J. Swingler, "Visualisation and characterisation of electrical contact spots for different current values using an X-Ray Computer Tomography," in *12th International Conference on Computational Methods and Experiments in Surface and Contact Mechanics including Tribology*, Valencia, Spain, April, 2015, pp. 59-69.
- [188] J. Swingler and A. Lalechos, "Visualization and size distribution of contact spots at a real un-dismantled electrical contact interface," *Journal of Physics D: Applied Physics*, vol. 42, pp. 1-7, 2009.
- [189] J. Swingler, "The resolution dependence of measured fractal characteristics for a real un-dismantled electrical contact interface," *Wear*, vol. 268, pp. 1178-1183, 2010.
- [190] A. R. Imre, J. Novotný, and D. Rocchini, "The Korcak-exponent: A non-fractal descriptor for landscape patchiness," *Ecological Complexity*, vol. 12, pp. 70-74, 2012.
- [191] B. B. Mandelbort, *The fractal geometry of nature*. New York: Freeman, 1982.
- [192] L. Seuront, *Fractals and multifractals in ecology and aquatic science*. Boca Raton: CRC Press, 2010.
- [193] C. C. Roussos and J. Swingler, "Calculation of the electrical parameters from 3D visualisation data of non-disassembled contact interfaces," in *61st IEEE Holm Conference on Electrical Contacts*, San Diego, CA, Oct., 2015, pp. 82-89.
- [194] W. R. Smythe, *Static and dynamic electricity*. New York: McGraw-Hili, 1950.
- [195] C. C. Roussos and J. Swingler, "Visualisation and characterisation of 3D electrical contact asperities for different current values using an X-ray computed tomography," in *28th International Conference on Electrical Contacts (ICEC 2016)*, Edinburgh, U.K., June, 2016, pp. 15-20.
- [196] C. D. Smith, A. V. Kildishev, J. A. Nyenhuis, K. S. Foster, and J. D. Bourland, "Interactions of magnetic resonance imaging radio frequency magnetic fields with elongated medical implants," *Journal of Applied Physics*, vol. 87, pp. 6188-6190, 2000.



- [197] N. Olamaei, F. Cheriet, and S. Martel, "Magnetic resonance imaging of microvessels using iron-oxide nanoparticles," *Journal of Applied Physics*, vol. 113, pp. 124701-1-124701-9, 2013.
- [198] W. Zhu, Y. Tian, X. Gao, and L. Jiang, "A Method To Measure Internal Contact Angle in Opaque Systems by Magnetic Resonance Imaging," *Langmuir: The ACS journal of surfaces and colloids*, vol. 29, pp. 9057-9062, 2013.
- [199] F. Xue, P. Peddibhotla, M. Montinaro, D. P. Weber, and M. Poggio, "A geometry for optimizing nanoscale magnetic resonance force microscopy," *Applied Physics Letters*, vol. 98, pp. 163103-1-163103-3, 2011.
- [200] C. L. Degen, M. Poggio, H. J. Mamin, C. T. Rettner, and D. Rugar, "Nanoscale magnetic resonance imaging," *Proceedings of the National Academy of Sciences*, vol. 106, pp. 1313-1317, 2009.
- [201] C. Lei, J. G. Longenecker, E. W. Moore, and J. A. Marohn, "Magnetic Resonance Force Microscopy Detected Long-Lived Spin Magnetization," *IEEE Transactions on Magnetics*, vol. 49, pp. 3528-3532, 2013.
- [202] H. J. Mamin, C. T. Rettner, M. H. Sherwood, L. Gao, and D. Rugar, "High field-gradient dysprosium tips for magnetic resonance force microscopy," *Applied Physics Letters*, vol. 100, pp. 013102-1-013102-4, 2012.